

Australian Institute of Nuclear Science and Engineering

INIS-mf--1527

AU9715743 -

AU9715815

8th
**Australian Conference
on Nuclear Techniques
of Analysis**

AINSE, Lucas Heights, N.S.W.

17-19 NOVEMBER 1993

PROCEEDINGS

ISSN 0811 - 9422

**We regret that
some of the pages
in this report may
not be up to the
proper legibility
standards, even
though the best
possible copy was
used for scanning**

SUMMARY

Wednesday, 17th November, 1993

Opening Remarks	10.00	Conference President: Prof. D. Sood (RMIT)
SESSION I	10.10	<u>Instruments</u> Chairman: MC Ridgway (ANU)
	12.30	Conference Lunch
SESSION II	1.30	<u>Surfaces and Interfaces</u> Chairman: PJ Evans (ANSTO)
	3.20	Afternoon Tea
SESSION III	3.40	<u>Instruments</u> Chairman: P Johnston (RMIT)
	6.40	BBQ

Thursday, 18th November, 1993

SESSION IV	8.30	<u>Semi-Conductors</u> Chairman: BV King (Univ of Newcastle)
	10.20	Morning Tea
SESSION V	10.40	<u>Geology</u> Chairman: JC Van Moort (Univ of Tasmania)
	12.30	Lunch
SESSION VI	1.30	<u>Materials and Semi-Conductors</u> Chairman: AG Nassibian (Univ of Western Australia)
	3.20	Afternoon Tea
SESSION VII	3.40	<u>Environmental Biology</u> Chairman: DN Jamieson (Univ of Melbourne)
	7.15	Conference Dinner

Friday, 19th November, 1993

SESSION VIII	8.30	<u>Materials</u> Chairman: R Bird (ANSTO)
	10.20	Morning Tea
SESSION IX	10.40	<u>Instruments</u> Chairman: T Ophel (ANU)
	12.20	Lunch
SESSION X	1.30	<u>New Facilities</u> Chairman: MJ Kenny (CSIRO)
	3.20	Afternoon Tea

Wednesday, 17th November, 1993

TIME

10:00 Opening Remarks - Conference President
Prof. D. Sood, RMIT

SESSION I

INSTRUMENTS

Chairman: M C Ridgway

10:10 Novel Large Area Particle Detector D Hinde (ANU)

10:40 Scanning Auger Nanoprobes - Some Current Instruments. PJK Paterson (RMIT)

11:00 Three Dimensional STIM Tomography and its Applications. M Cholewa, A Saint, S Praver, GJF Legge (Univ. Melbourne), SA Stuart (CSIRO) J Howard (ANU)

11:20 A Time of Flight Detector for High Energy Heavy Particles Z Fang DJ O'Connor (Univ. Newcastle)

11:40 Advanced Materials Analysis Facility at CSIRO HIAF Laboratory. MJ Kenny, LS Wielunski, S Sie, GF Suter, GR Baxter (CSIRO)

12:00 Poster Previews

p1 Microbeam Recoil Detection for Hydration of Minerals Studies. SH Sie (CSIRO), A Chekhmir (Inst of Experimental Mineralogy), TH Green (Macquarie Uni)

p2 Multidirectional Channelling Analysis of Epitaxial CdTe Layers using an Automatic RBS/Channeling System. LS Wielunski, MJ Kenny, (CSIRO)

p3 Numerical Studies of Triplet and Russian Quadruplet Lenses with the Maximum Beam Emittance and Given Spot Size on the Target for use in a Microprobe. AD Dymnikhov (Univ of St Petersburg, Russia) DN Jamieson, GJF Legge (Univ of Melbourne) VA Brazhnik, SA Lebed, AG Ponomarev, VE Storizhko (Ukrainian Ac of Sciences)

p4 Low Current Beam Techniques A Saint, JS Laird, RA Bardos, GJF Legge (Univ of Melbourne) T Nishijima, H Sekiguchi (ETL, Japan)

p5 A Generalized Laboratory Control System Integrated with Data Handling. G Moloney, PM O'Brien, A Scott, A Saint, GJF Legge (Univ of Melbourne)

p6 The Development of an X-ray Computerized Tomography (CT) Experimental System. G Lee, M Kijek, J Millar (RMIT)

p7 Sample Preparation and Curation at the ANTARES AMS Centre. EM Lawson, D Fink, MAC Hotchkis, GE Jacobsen, M Shying, AM Smith, C Tuniz (ANSTO)

p8 The System for High Precision and High Throughput ¹⁴C AMS Analyses at ANTARES. AM Smith, EM Lawson, D Fink, MAC Hotchkis, GE Jacobsen, M Shying, C Tuniz, J Fallon, PJ Ellis (ANSTO)

p9 A Novel Approach to Secondary Defect Reduction in Separation by Implantation of Oxygen (SIMOX) Material. SL Ellingboe, MC Ridgway (ANU)

12:30 LUNCH

SESSION II

SURFACES AND INTERFACES

Chairman: P J Evans

- 1:30 ¹⁴N Depth Profiles in Ti and Ti6Al4v Nitrided by Various Methods, Measured by Nuclear Reaction Analysis. J. Vickeridge, B Trompeter (Inst. Geological & Nuclear Sciences, NZ)
- 2:00 Surface Modification of Commercial TiN Coatings by Carbon Ion Implantation. LJ Liu, DK Sood, RR Manory (RMIT)
- 2.20 Study of CuAl(100) by Using He Ion Scattering L. Zhu, E Zur Muhlen, DJ O'Connor (Univ of Newcastle)
- 2.40 Laser Sputter Neutral Mass Spectrometry. BV King, M Clarke (Univ of Newcastle) G Betz (Technical Univ, Vienna)
- 3:00 Poster Previews
- p10 Ion Beam Mixing of Isotopic Metal Bilayers. Chris Fell (Univ of Newcastle) MJ Kenny (CSIRO)
- p11 Surface Studies by Low Energy Ion Beams: Cu/Ru(0001) and Cu/O/Ru(0001). YG Shen, DJ O'Connor, RJ MacDonald (Univ of Newcastle) K Wandelt (Germany) H Van Zee (Univ of Technology, Netherlands)
- p12 Lattice Location of Platinum Ions Implanted into Single Crystal Zirconia and Their Annealing Behaviour. DX Cao (Academia Sinica, China) DK Sood (Melbourne Inst. of Technology) IG Brown (Univ of California)
- p13 Growth of CdTe on GaAs(100) and Analysis using Ion Scattering Spectrometry. B Mitrovic, BV King (Univ of Newcastle)
- p14 Oxygen Absorption on Cu(111) Using Low Energy Ion Scattering Spectroscopy. EM Zhang, J Yao, YG Shen, BV King, DJ O'Connor (Univ of Newcastle)
- p15 Corrosion Behaviour of Ion Implanted Alloy in 0.1 M NaCl Electrolyte JW Chu, (AINSE Fellow) PJ Evans (ANSTO)
- 3:20 **AFTERNOON TEA**

SESSION III INSTRUMENTS

Chairman: P Johnston

- 3:40 The ANTARES AMS Centre and Research Program. **C.Tuniz** , D Fink, MAC Hotchkis, GE Jacobsen, EM Lawson, M Shying, AM Smith, JW Boldeman JR Bird (ANSTO)
- 4:00 The Status of the 8MV Tandem Accelerator, ANTARES. **J.Fallon**, JW Boldeman, C Tuniz, D Cohen, P Ellis (ANSTO)
- 4:20 ¹⁴C Analysis at the ANTARES AMS Centre. **MAC Hotchkis**, D Fink, GE Jacobsen, EM Lawson, M Shying, AM Smith and C Tuniz (ANSTO)
- 4:40 Ion Beam Analysis of Metal Ion Implanted Surfaces. **PJ.Evans** (ANSTO), J-W Chu (AINSE fellow), EP Johnson, JT Noorman (ANSTO)
- 5:00 Site Tour:
Tandem, Van der Graaf, SIMS, AUSANS
- 6:40 **BBQ**

Thursday, 18th November, 1993

SESSION IV SEMI CONDUCTORS

Chairman: B King

- 8:30 Lattice Location of Impurities in Semiconductors.
P Kringhoj (Arhus Univ, Denmark)
- 9:00 Identification of Defects in GaAs Induced by 1 MeV Electron Irradiation. S.T. Lai,
BD Nener, L Faraone, AG Nassibian (Univ. WA), MAC Hotchkis (ANSTO)
- 9:20 Heavy Ion Spectrometry of $\text{Si}_x\text{Ge}_{1-x}$ Thin Films. SR Walker, PN Johnston, IF Bubb
(RMIT), DD Cohen, N Dytlewski (ANSTO), M Hult, HJ Whitlow (Lund, Inst. of
Tech., Sweden), C Zahring, M Ostling (RIT, Kista, Sweden)
- 9:40 Strain Relaxation During Solid-Phase Epitaxial Crystallization of $\text{Ge}_x\text{Si}_{1-x}$ Alloy
Layers with Depth Dependent Ge Compositions. W Wong, RG Elliman,
P Kringhoj (ANU)
- 10:00 Poster Previews
- p16 Depth profile of In and As in Si measured by RBS with He and C Ions. Q Yang, Z Fang
(Univ of Newcastle) TR Ophel (ANU)
- p17 Stoichiometry, Thickness and Crystallinity of MOCVD Grown HgCdMnTe determined by
Nuclear Techniques of Analysis. WB Studd, PN Johnston, IF Bubb (RMIT) PW Leech
(Telecom Aust.)
- p18 Enhanced Relaxation of Strained $\text{Ge}_x\text{Si}_{1-x}$ Layers Induced by $\text{Co}/\text{Ge}_x\text{Si}_{1-x}$ Thermal
Reaction. MC Ridgway, RG Elliman, MR Rao (ANU Canberra)
JM Baribeau (National Research Council, Canada)
- p19 Heavy Ion Elastic Recoil Detection Analysis of Optoelectronic and Semiconductor Devices.
N. Dytlewski, DD Cohen (ANSTO) P Johnson, S Walker (Melbourne Inst of Technology)
H Whitlow, M Hult (Univ of Lund, Sweden) M Ostling C Zaring (Inst of Technology,
Sweden)
- p20 Absolute Calibration in PIXE/PIGME Analysis G.Bailey, R Bird, P Johnson (ANSTO)
- p21 First Measurements with the ANU PAC Facility AP Byrne (ANU)
- p22 A Study of Aluminium Exposed Fish Using a Scanning Proton Microprobe. M. Cholewa,
GJF Legge (Uni of Melbourne) E Eeckhaoudt, R Van Grieken
(Univ of Antwerp, Belgium)
- 10:20 **MORNING TEA**

SESSION V**GEOLOGY****Chairman:**

- 10:40 Australis: AMS for Mineralogical Application S.H. Sie, G.F. Suter (CSIRO)
- 11:10 Obsidian Sourcing Studies in Papua New Guinea using PIXE-PIGME Analysis. R. Bird, G Summerhayes, C Gosden, (La Trobe Univ), R. Bird, M Hotchkis (ANSTO) R Torrence, J Specht, R Fullagar (Australian Museum)
- 11:30 Electron Paramagnetic Resonance (EPR) Spectroscopy Supported by Particle Induced X-ray Emission (PIXE) and Particle Induced Gamma Ray Emission (PIGME) Spectroscopy in Mineral Exploration. JC Van Moort (Univ. Tasmania) M Hotchkis (ANSTO)
- 11:50 PIXE/PIGME Analysis of Arabian Bronze Silver Coins. P.Grave, D Potts, R Bird (ANSTO)
- 12:10 Poster Previews
- p23 A Back-arc Setting for Mafic Rocks of the Honeysuckle Beds, Southeastern NSW: The use of Trace and Rare Earth Element Abundances Determined by INAA. KA Dadd (UTS)
- p24 Immiscible Silicate Liquids at a High Pressure: The Influence of Melt Structure on Elemental Partitioning. TH Green (Macquarie Univ) E Vicenzi (Princeton, USA) SH Sie (CSIRO)
- p25 S/Se Ration of Pyrite from Eastern Australian VIMS deposits: Implication of Magmatic Input into Volcanogenic Hydrothermal Systems. DL Huston (Geological Survey of Canada) SH Sie, GF Suter (CSIRO) DR Cooke (Univ of TAS)
- p26 The Analysis of Thallium in Geological Materials by Radiochemical Neutron Activation and X-ray Fluorescence Spectrometry: A Comparison. P.J. McGoldrick, P Robinson (Univ of TAS)
- p27 In-situ buildingup of Cosmogenic Isotopes at the Earth's Surface: Measurement of Erosion Rates and Exposure Times. LK Fifield, GL Allan, JOH Stone, JL Evans, TR Ophel (ANU)
- p28 The Paramagnetism and Trace Element content of Auriferous Vein Quartz at Beaconsfield, Tasmania. DW Russell, JC Van Moort (Univ of Tasmania)
- 12:30 **LUNCH**

SESSION VI MATERIALS AND SEMI-CONDUCTORS

Chairman: A G Nassibian

- 1:30 **Fred Sexton, Sandia National Laboratories, Albuquerque, USA**
- 2:00 **Scanning Deep Level Transient Spectroscopy using an MeV Ion Microprobe.
JS Laird and GJF Legge (Univ. Melbourne)**
- 2:20 **Depletion Width Imaging and Interpad Charge Collection Studies of a Segmented p^+n Silicon Detector Using Scanning Ion Beam Induced Charge. RA Bardos,
J Laird, GF Moorhead, GN Taylor and A Saint (Univ Melbourne)**
- 2:40 **Seeding of Silicon by Copper Ion Implantation for Selective Electroless Copper
Plating. S Bhansali, DK Sood, RB Zmood (RMIT)**
- 3:00 **Poster Previews**
- p29 **The Effectiveness of Ti implants as Barriers to Carbon Diffusion in Ti implanted Steel
under CVD Diamond Deposition Conditions PS Weiser, S Praver (Univ of Melbourne)
A Hoffman (Technion Israel) P Evans (ANSTO)**
- p30 **Raman Microprobe Measurements of Stress in Ion Implanted Materials. KW. Nugent
S Praver, (Univ of Melbourne)**
- p31 **Ion Beam Induced Luminescence from Diamond using an MeV Ion Microprobe.
AA Bettiol, DN Jamieson, S Praver, MG Allen (Univ of Melbourne)**
- p32 **Formation of Oxides and Segregation of Mobile Atoms during SIMS Profiling with Oxygen
Ions. M Petravic, JS Williams, BG Ssvensson, M Conway (ANU)**
- p33 **The Effect of Metal Ion Implantation on the Surface Mechanical Properties of Mylar
(PET). W Zhou , DK Sood (RMIT) X Yao,
G Brown (Univ of California)**
- p34 **The Effect of Ion Implantation on the Tribomechanical Properties of Carbon Fibre
Reinforced Polymers. R Mistica, DK Sood, (RMIT) N Williams (Huck Australia)
MN Janardhana (Deakin Univ)**
- p35 **Annealing Behaviour of MeV Erbium Implanted Lithium Niobate. P Gortmaker,
JC McCallum (RMIT)**
- 3:20 **AFTERNOON TEA**

SESSION VII ENVIRONMENTAL BIOLOGY

Chairman: D N Jamiesen

- 3:40 Ion Beam Analysis Techniques Applied to Large Scale Air Pollution Studies
D. Cohen, G Bailey, J Martin, D Garton, H Noorman, E Stelcer, P Johnson
(ANSTO)
- 4:00 Sodium, Potassium and Chloride Status in Australian Foods & Diets Using Neutron
Activation Analysis. **JJ Fardy, GD McOrist, YJ Farrar, CJ Bowles** (ANSTO)
- 4:20 Detection of Submonolayer Oxygen-18 on a cold surface by Nuclear Reaction
Analysis **LS Wielunski, MJ Kenny** (CSIRO)
- 4:40 Poster Session
- 7:15 Conference Dinner

Friday, 19th November, 1993

SESSION VIII MATERIALS

Chairman: R Bird

- 8:30 Solid Phase Epitaxy in Ceramic Oxides. JC McCallum (RMIT)
- 9:00 RBS Analysis of Electrochromic Layers. DC Green, JM Bell (UTS), MJ Kenny, LS Wielunski (CSIRO)
- 9:20 Selective Rutherford Backscattering Techniques in the Study of Transition-Metal Implanted $\text{YBa}_2\text{Cu}_3\text{O}_{7-x}$. J.W. Martin, G.J. Russell (UNSW), DD Cohen (ANSTO)
- 9:40 Ion Beam Modification of Thermal Shock Resistance Characteristics of Brittle Materials. VN Gurarie (Univ of Melbourne) JS Williams (RMIT)
- 10:00 Determination of the Flow Rates of Oil, Water and Gas in Pipelines. JS Watt, G Roach, HW Zastawny (CSIRO)
- 10:20 **MORNING TEA**

SESSION IX INSTRUMENTS

Chairman: T Ophel

- 10:40 Advances of the IBIC Technique. MBH Breese, JS Laird, DN Jamieson (Univ of Melbourne)
- 11:10 A New Method for True Quantitative Elemental Imaging Using PIXE and the Proton Microprobe. CG Ryan (CSIRO) DN Jamieson (Univ of Melbourne) CL Churms JV Pilcher (National Accelerator Centre, S.Africa)
- 11:30 Applications of Focused MeV Light Ion Beams for High Resolution Channeling Contrast Imaging. DN Jamieson, MBH Breese (Univ of Melbourne)
- 11:50 The Australian/Swedish Collaboration on Ion Beam Time-of-Flight H Whitlow (Lund Institute of Tech, Sweden)
- 12:10 Nonlinear Dynamics for Charged Particle Beams with a Curved Axis in the Matrix Recursive Model. AD Dyminkov (Univ of St Petersburg, Russia)
- 12:30 **LUNCH**

SESSION X**NEW FACILITIES**

Chairman: M J Kenny

- 1:30 The Combined Application of Ion and Raman Microprobe Techniques.
S Praver, KW Nugent, A Orlow, L Kostidis (Univ of Melbourne)
- 2:00 AMS at the ANU including Biomedical Applications. LK Fifield, S King, GL Allan,
TR Ophel (ANU)
- 2:20 EXAFS and Microprobe Analysis at the Australian National Beamline Facility.
RF Garrett, DJ Cookson, G Foran (ANSTO), CD Creagh (UNSW), D Balaic,
SW Wilkins (CSIRO-DMST), K Nugent, Z Barnea, M Chowela (Univ of Melbourne)
- 2:40 Program for upgrade of Neutron Scattering facilities at HIFAR. JW Bolderman
(ANSTO)
- 3:00 Closing Remarks: J S Williams
- 3:20 **AFTERNOON TEA**

CONTENTS

CONTENTS

<u>Papers</u>	<u>Page</u>
Novel Large Area Particle Detector. D HINDE (ANU)	1
Scanning Auger Nanoprobes - Some Current Instruments. PJK PATERSON (RMIT)	2
Three Dimensional STIM Tomography and its Applications. M CHOLEWA, A SAINT, S PRAWER, GJF LEGGE (UNIV. MELBOURNE), SA STUART (CSIRO) J HOWARD (ANU)	3
A Time of Flight Detector for High Energy Heavy Particles. Z FANG, DJ O'CONNOR (UNIV OF NEWCASTLE)	6
Advanced Materials Analysis Facility at CSIRO HIAF Laboratory. MJ KENNY, LS WIELUNSKI, S SIE, GF SUTER, GR BAXTER (CSIRO)	9
Microbeam Recoil Detection for Hydration of Minerals Studies. SH SIE (CSIRO), A CHEKHMIR (INST OF EXPERIMENTAL MINERALOGY), TH GREEN (MACQUARIE UNI)	12
Multidirectional Channelling Analysis of Epitaxial CdTe Layers using an Automatic RBS/Channeling System. LS WIELUNSKI, MJ KENNY (CSIRO)	15
Numerical Studies of Triplet and Russian Quadruplet Lenses with the Maximum Beam Emittance and Given Spot Size on the Target for use in a Microprobe. AD DYMNIKHOV,(UNIV OF ST PETERSBURG, RUSSIA) VA BRAZHNIK, SA LEBED, AG PONOMAREV, VE STORIZHKO (UKRAINIAN AC OF SCIENCES) GJF LEGGE, DN JAMIESON (UNIV OF MELBOURNE)	18
Low Current Beam Techniques. A SAINT, JS LAIRD, RA BARDOS, GJF LEGGE (UNIV OF MELBOURNE)	21
A Generalized Laboratory Control System Integrated with Data Handling. G MOLONEY, PM O'BRIEN, A SCOTT, A SAINT, GJF LEGGE (UNIV OF MELBOURNE)	24
The Development of an X-ray Computerized Tomography (CT) Experimental System. G LEE, M KIJEK, J MILLAR (RMIT)	25
Sample Preparation and Curation at the ANTARES AMS Centre. EM LAWSON, D FINK, MAC HOTCHKIS, GE JACOBSEN, M SHYING, AM SMITH, C TUNIZ (ANSTO)	28

<u>Papers</u>	<u>Page</u>
The System for High Precision and High Throughput ^{14}C AMS Analyses at ANTARES. EM LAWSON, D FINK, MAC HOTCHKIS, GE JACOBSEN, M SHYING, AM SMITH, C TUNIZ, J FALLON, PJ ELLIS (ANSTO)	29
A Novel Approach to Secondary Defect Reduction in Separation by <u>Implantation</u> of <u>Oxygen</u> (SIMOX) Material. SL ELLINGBOE, MC RIDGWAY (ANU)	30
^{14}N Depth Profiles in Ti and Ti6Al4v Nitrided by Various Methods, Measured by Nuclear Reaction Analysis. I VICKERIDGE, B TROMPETTER (INST. GEOLOGICAL & NUCLEAR SCIENCES, NZ)	33
Surface Modification of Commercial TiN Coatings by Carbon Ion Implantation. LJ LIU, DK SOOD, RR MANORY (RMIT)	37
Study of CuAl(100) by Using He Ion Scattering. L ZHU, E ZUR MUHLEN, DJ O'CONNOR (UNIV OF NEWCASTLE)	40
Laser Sputter Neutral Mass Spectrometry. BV KING, M CLARKE (UNIV OF NEWCASTLE) G BETZ (TECHNICAL UNIV, VIENNA)	43
Ion Beam Mixing of Isotopic Metal Bilayers. C FELL (UNIV OF NEWCASTLE) MJ KENNY (CSIRO)	46
Surface Studies by Low Energy Ion Beams: Cu/Ru(0001) and Cu/O/Ru(0001). YG SHEN, DJ O'CONNOR, RJ MACDONALD (UNIV OF NEWCASTLE) K WANDEL (GERMANY) H VAN ZEE (UNIV OF TECH, NETHERLANDS)	49
Lattice Location of Platinum Ions Implanted into Single Crystal Zirconia and Their Annealing Behaviour. DX CAO (ACADAMIA SINICA, CHINA) DK SOOD (RMIT) IG BROWN (UNIV OF CALIFORNIA)	52
Growth of CdTe on GaAs(100) and Analysis using Ion Scattering Spectrometry B MITROVIC, BV KING (UNIV OF NEWCASTLE)	55
Oxygen Absorption on Cu(111) Using Low Energy Ion Scattering Spectroscopy. FM ZHANG, J YAO, YG SHEN, BV KING, DJ O'CONNOR (UNIV OF NEWCASTLE)	59
Corrosion Behaviour of Ion Implanted Alloy in 0.1 M NaCl Electrolyte. JW CHU, (AINSE FELLOW) PJ EVANS (ANSTO)	62

<u>Papers</u>	<u>Page</u>
The ANTARES AMS Centre and Research Program. C.TUNIZ , D FINK, MAC HOTCHKIS, GE JACOBSEN, EM LAWSON, M SHYING, AM SMITH, JW BOLDEMAN, JR BIRD (ANSTO)	65
The Status of the 8MV Tandem Accelerator, ANTARES. JW BOLDEMAN, C TUNIZ, D COHEN, P ELLIS, J FALLON (ANSTO)	66
¹⁴ C Analysis at the ANTARES AMS Centre. MAC HOTCHKIS, D FINK, GE JACOBSEN, EM LAWSON, M SHYING, AM SMITH, C TUNIZ (ANSTO)	67
Ion Beam Analysis of Metal Ion Implanted Surfaces. JW CHU (AINSE FELLOW), EP JOHNSON, JT NOORMAN, PJ EVANS (ANSTO)	68
Lattice Location of Impurities in Semiconductors. P KRINGHOJ (ARHUS UNIV, DENMARK)	72
Identification of Defects in GaAs Induced by 1 MeV Electron Irradiation. S.T. LAI, BD NENER, L FARAONE, AG NASSIBIAN (UNIV. WA), MAC HOTCHKIS (ANSTO)	76
Heavy Ion Spectrometry of Si _x Ge _{1-x} Thin Films. SR WALKER, PN JOHNSTON IF BUBB (RMIT), DD COHEN, N DYTLEWSKI (ANSTO) M HULT, HJ WHITLOW (LUND, INST. OF TECH, SWEDEN), C ZHRING, M OSTLING (RIT, KISTA, SWEDEN)	80
Strain Relaxation During Solid-Phase Epitaxial Crystallization of Ge _x Si _{1-x} Alloy Layers with Depth Dependent Ge Compositions. W WONG, RG ELLIMAN, P KRINGHOJ (ANU)	83
Depth profile of In and As in Si measured by RBS with He and C Ions. Q YANG, Z FANG (UNIV OF NEWCASTLE) TR OPHEL (ANU)	86
Stoichiometry, Thickness and Crystallinity of MOCVD Grown HgCdMnTe determined by Nuclear Techniques of Analysis. WB STUDD, PN JOHNSTON, IF BUBB (RMIT) PW LEECH (TELECOM AUST.)	89
Enhanced Relaxation of Strained Ge _x Si _{1-x} Layers Induced by Co/Ge _x Si _{1-x} Thermal Reaction. MC RIDGWAY, RG ELLIMAN , MR RAO (ANU CANBERRA) JM BARIBEAU (NATIONAL RESEARCH COUNCIL, CANADA)	92

<u>Papers</u>	<u>Page</u>
Heavy Ion Elastic Recoil Detection Analysis of Optoelectronic and Semiconductor Devices. N. DYTLEWSKI, DD COHEN (ANSTO) P JOHNSON, S WALKER (RMIT) H WHITLOW, M HULT (UNIV OF LUND, SWEDEN) M OSTLING C ZARING (INST OF TECHNOLOGY, SWEDEN)	95
Absolute Calibration in PIXE/PIGME Analysis. G.BAILEY, R BIRD, P JOHNSON (ANSTO)	98
First Measurements with the ANU PAC Facility AP BYRNE (ANU)	99
A Study of Aluminium Exposed Fish Using a Scanning Proton Microprobe. M. CHOLEWA, GJF LEGGE (UNI OF MELBOURNE) E EECKHAUDT, R VAN GRIEKEN (UNIV OF ANTWEERP, BELGIUM)	100
Australis: AMS for Mineralogical Application S.H. SIE, G.F. SUTER (CSIRO)	103
Obsidian Sourcing Studies in Papua New Guinea using PIXE-PIGME Analysis. G.SUMMERHAYES, C GOSDEN,(La TROBE UNIV) R BIRD, M HOTCHKISS (ANSTO) R TORRENCE, J SPECHT R FULLAGAR (AUST. MUSEUM)	107
Electron Paramagnetic Resonance (EPR) Spectroscopy Supported by Particle Induced X-ray Emission (PIXE) and Particle Induced Gamma Ray Emission (PIGME) Spectroscopy in Mineral Exploration. JC VAN MOORT (UNIV. TASMANIA) M HOTCHKIS (ANSTO)	111
PIXE/PIGME Analysis of Arabian Bronze Silver Coins. P GRAVE, D POTTS, R BIRD (ANSTO)	112
A Back-arc Setting for Mafic Rocks of the Honeysuckle Beds, Southeastern NSW: The use of Trace and Rare Earth Element Abundances Determined by INAA. KA DADD (UTS)	113
Immiscible Silicate Liquids at a High Pressure: The Influence of Melt Structure on Elemental Partitioning. TH GREEN (MACQUARIE UNIV) E VICENZI (PRINCETON, USA) SH SIE (CSIRO)	116
S/Se Ration of Pyrite from Eastern Australian VIMS deposits: Implication of Magmatic Input into Volcanogenic Hydrothermal Systems. DL HUSTON (GEOLOGICAL SURVEY OF CANADA) SH SIE, GF SUTER (CSIRO) DR COOKE (UNIV OF TAS)	119
The Analysis of Thallium in Geological Materials by Radiochemical Neutron Activation and X-ray Fluorescence Spectrometry: A Comparison. P.J. M ^C GOLDRICK, P ROBINSON (UNIV OF TAS)	121

<u>Papers</u>	<u>Page</u>
In-situ buildingup of Cosmogenic Isotopes at the Earth's Surface: Measurement of Erosion Rates and Exposure Times. LK FIFIELD, GL ALLAN, JOH STONE, JL EVANS, TR OPHEL (ANU)	124
The Paramagnetism and Trace Element content of Auriferous Vein Quartz at Beaconsfield, Tasmania. DW RUSSELL, JC VAN MOORT (UNIV OF TASMANIA)	126
Scanning Deep Level Transient Spectroscopy using an MeV Ion Microprobe. JS LAIRD AND GJF LEGGE (UNIV. MELBOURNE)	127
Depletion Width Imaging and Interpad Charge Collection Studies of a Segmented p^+n Silicon Detector Using Scanning Ion Beam Induced Charge. RA BARDOS, J LAIRD, GF MOORHEAD, GN TAYLOR AND A SAINT (UNIV MELBOURNE)	130
Seeding of Silicon by Copper Ion Implantation for Selective Electroless Copper Plating. S BHANSALI, DK SOOD, RB ZMOOD (RMIT)	131
The Effectiveness of Ti implants as Barriers to Carbon Diffusion in Ti implanted Steel under CVD Diamond Deposition Conditions. PS WEISER, S PRAWER (UNIV OF MELBOURNE) A HOFFMAN (TECHNION ISRAEL) P EVANS (ANSTO)	134
Raman Microprobe Measurements of Stress in Ion Implanted Materials S PRAWER, KW. NUGENT (UNIV OF MELBOURNE)	137
Ion Beam Induced Luminescence from Diamond using an MeV Ion Microprobe. AA BETTIOL, DN JAMIESON, S PRAWER, MG ALLEN (UNIV OF MELBOURNE)	140
Formation of Oxides and Segregation of Mobile Atoms during SIMS Profiling with Oxygen Ions. M PETRAVIC, JS WILLIAMS, BG SSVENSSON, M CONWAY (ANU)	143
The Effect of Metal Ion Implantation on the Surface Mechanical Properties of Mylar (PET). W ZHOU , DK SOOD (RMIT) X YAO, G BROWN (UNIV OF CALIFORNIA)	146

<u>Papers</u>	<u>Page</u>
The Effect of Ion Implantation on the Tribomechanical Properties of Carbon Fibre Reinforced Polymers. R MISTICA (RMIT) N WILLIAMS (HUCK AUSTRALIA) MN JANARDHANA (DEAKIN UNIV) DK SOOD (RMIT)	149
Annealing Behaviour of MeV Erbium Implanted Lithium Niobate. P GORTMAKER, JC MCCALLUM (RMIT)	152
Ion Beam Analysis Techniques Applied to Large Scale Air Pollution Studies D. COHEN, G BAILEY, J MARTIN, D GARTON, H NOORMAN, E STELCER, P JOHNSON (ANSTO)	155
Sodium, Potassium and Chloride Status in Australian Foods & Diets Using Neutron Activation Analysis. JJ FARDY, GD MCORIST, YJ FARRAR, CJ BOWLES (ANSTO)	158
Detection of Submonolayer Oxygen-18 on a cold surface by Nuclear Reaction Analysis LS WIELUNSKI, MJ KENNY (CSIRO)	161
Solid Phase Epitaxy in Ceramic Oxides. JC McCALLUM	164
RBS Analysis of Electrochromic Layers. DC GREEN, JM BELL (UTS), MJ KENNY, LS WIELUNSKI (CSIRO)	165
Selective Rutherford Backscattering Techniques in the Study of Transition-Metal Implanted YBa ₂ Cu ₃ O ₇₋₈ . J.W. MARTIN, G.J. RUSSELL (UNSW), DD COHEN (ANSTO)	168
Ion Beam Modification of Thermal Shock Resistance Characteristics of Brittle Materials. VN GURARIE (UNIV OF MELBOURNE) JS WILLIAMS (RMIT)	171
Determination of the Flow Rates of Oil, Water and Gas in Pipelines. G ROACH, JS WATT, HW ZASTAWNY (CSIRO)	172
Advances of the IBIC Technique. MBH BREESE, JS LAIRD, DN JAMIESON (UNIV OF MELBOURNE)	175
A New Method for True Quantitative Elemental Imaging Using PIXE and the Proton Microprobe. CG RYAN (CSIRO) DN JAMIESON (UNIV OF MELBOURNE) CL CHURMS JV PILCHER (NATIONAL ACCELERATOR CENTRE, S.AFRICA)	178
Applications of Focused MeV Light Ion Beams for High Resolution Channeling Contrast Imaging. DN JAMIESON, MBH BREESE (UNIV OF MELBOURNE)	181

<u>Papers</u>	<u>Page</u>
The Australian/Swedish Collaboration on Ion Beam Time-of-Flight. H WHITLOW (LUND, INST. OF TECH, SWEDEN)	184
Nonlinear Dynamics for Charged Particle Beams with a Curved Axis in the Matrix Recursive Model. AD DYMINKOV (UNIV OF ST PETERSBURG, RUSSIA)	185
The Combined Application of Ion and Raman Microprobe Techniques. S PRAWER, KW NUGENT, A ORLOW, L KOSTIDIS (UNIV OF MELBOURNE)	188
AMS at the ANU including Biomedical Applications. LK FIFIELD, S KING, GL ALLAN, TR OPHEL (ANU)	189
EXAFS and Microprobe Analysis at the Australian National Beamline Facility. RF GARRETT, DJ COOKSON, G FORAN (ANSTO), CD CREAGH (UNSW), D BALAIC, SW WILKINS (CSIRO-DMST), K NUGENT, Z BARNEA, M CHOWELA (UNIV OF MELBOURNE)	191
Program for upgrade of Neutron Scattering facilities at HIFAR. JW BOLDERMAN (ANSTO)	192

ABSTRACTS

NOVEL LARGE AREA PARTICLE DETECTOR

D. Hinde
Australian National University

(Paper to be handed out at Conference)



Scanning Auger Nanoprobes Some Current Instruments

Peter J K Paterson, Surface Physics Group, Applied Physics Department, RMIT

Recent developments in the surface analysis technique of Auger Electron Spectroscopy (AES) have produced instruments with higher counting rates at smaller electron beam diameter, even at low beam voltage. This means that elemental analysis and some chemical analysis can be carried out on areas < 50 nm in size.

The best of these new instruments use high brightness cold field emission sources which are x 50 times brighter than LaB6 filaments. Their beam energy is typically variable from 25kV down to 1kV with associated spatial resolution of 25 nm to about 150 nm (1kV) for elemental analysis. In addition they have high sensitivity detectability with some having superior energy resolution for chemical state determination. Modern software control of the sample stage allows high sample throughput and provides continuous azimuthal rotation of the sample to remove topographic artifacts during depth profiling. The addition of supplementary techniques such as XPS (X-ray Photoelectron Spectroscopy) and SIMS (Secondary Ion Mass Spectroscopy) further enhance the chemical state analysis ability of the instrument.

In carrying out materials analysis the above features provide new benefits. At low beam voltage (< 3 kV) the excitation volume is small thereby reducing scattering and increasing microanalytical accuracy. In addition specimen charging on insulators is easier to control, and beam damage to delicate samples is reduced.

High energy resolution enables direct determination of chemical states particularly in many binary compounds which enables the plotting of AES linescans and chemical maps. The addition of XPS and/or SIMS increases the analytical capability for more complex compounds.

The three field emission scanning Auger microprobes on which analyses were carried out were:

- (i) The Perkin-Elmer PHI 670xi Nanoprobe,
- (ii) The CAMECA Nanoscan 100,
- (iii) The Fisons Instruments Surface Science (VG) Microlab 310-F

Examples of analyses carried out with these instruments will mostly concern materials which are electrical insulators and will include: fibres - optical and fibre glass surfaces :carbon films- diamond , graphite and amorphous carbon :ceramics -catalysts.

Three-Dimensional STIM Tomography and its Applications



AU9715745

M. Cholewa, A. Saint, S. Prawer, G.J.F. Legge

Micro Analytical Research Centre (MARC), School of Physics, The University of Melbourne, Parkville, Vic. 3052, AUSTRALIA

S-A. Stuart

CSIRO, Forest Product Division, Clayton, Vic. 3169, AUSTRALIA

J. Howard

Plasma Research Laboratory, Research School of Physical Sciences and Engineering, ANU, Canberra, Australia.

Since Cormack [1] published his first work on computer assisted tomography (CAT) the idea found a large number of applications. The mathematical principles required for image reconstruction were first developed by Radon in 1917, when he defined the Radon and inverse Radon transforms. The CAT process reconstructs a two dimensional distribution of a physical property pertaining to an object's cross-section from measurements of line integrals of that property in the cross-sectional plane. For x-ray CAT, the property is the linear attenuation coefficient and for STIM Tomography [2] the energy loss of an ions. Ions are relatively easy to manipulate and there now exist many ion microprobes that can focus MeV ion beams down to micron and submicron dimensions.

To maintain submicron resolution in the tomographic data several factors need to be considered: (a) precise sample manipulation, (b) control of the quality of a detector, (c) beam spreading while traversing the sample and (d) change of the stopping power with the energy. The influence of these factors would be addressed in this paper.

In an attempt to study problems associated with reconstruction of our data we used data from isolated chemical vapour deposited (CVD) diamonds to map density variations within the formed diamond particles. Production of diamond particles from hydrocarbons using Microwave Plasma Chemical Vapour Deposition (CVD) is now a well established technique [3, 4]. Large isolated CVD diamond particles up to 50 μm in diameter have been deposited on tungsten wire tips using Microwave Plasma CVD [4].

For STIM Tomography with the Melbourne Ion microprobe, each projection was made by magnetically scanning the beam of 3.6 MeV H^+ across the diamond particle using a computer controlled digital scanning system. An unencapsulated Hamamatsu PIN S1223-01 Photodiode, placed 3 cm behind the specimen, was used to measure the residual energy of each ion which passed through the specimen. Although STIM resolutions of 50 nm are obtainable with this specimen, for this work the beam resolution had to be made comparable with the pixel resolution of 500 nm. At each sample point the beams dwelt until 7 ions had been recorded, before moving on to the next point in the scan. The median filtered image was then stored on disc and the computer reset for the next projection.

After each projection had been recorded, the specimen was rotated 1° about an axis that is parallel to the plane of projection, and the next projection was measured. The process was repeated until data had been collected for a full 180° rotation of the specimen. Each projection consisted of 256×256 sample points and the time required to measure each projection was typically two minutes. Following collection, the projection data were pre-processed to correct for imperfect specimen movement upon rotation. Individual slices through the specimen were reconstructed using a filtered backprojection algorithm. The density data from the individual slices were then combined to form a three-dimensional density image of the diamond particle using available software and hardware at the Australian National University.

In our present system sample was mounted about 300 mm from the motor which rotated a specimen. Small change in position there caused a large movements (up to a few microns) in both horizontal and

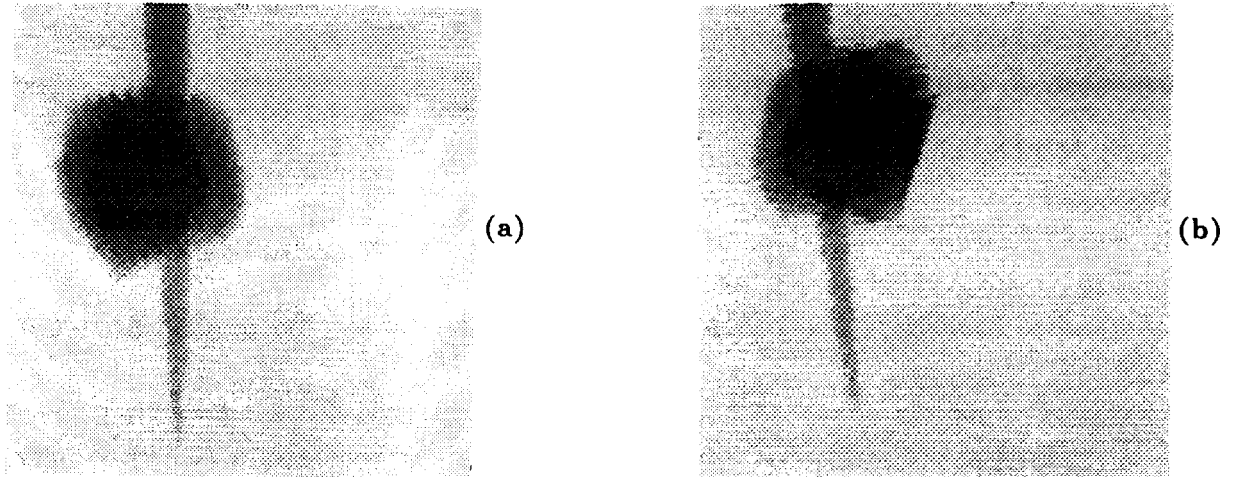


Fig.1 A typical 2-D projection (256×256 pixels) of median energy detected by the particle detector for (a) 0° and (b) 90° projection of $90 \times 120 \mu m^2$

vertical directions between different projections. Figure 1 shows the projection at 0° (a) and at 193° (b) respectively. Movements as well as a change in angle of the tungsten wire could be easily observed when comparing these two projections. We need to develop a data preprocessing system to compensate, if possible, for effects responsible for our problems. Apart from problems with sample movements, local detector damage would cause a small (up to 3 channels) shift in full energy peak. To have faith in the reconstructed images an influence of the above effects need to be found.

Following collection, the projection data were pre-processed to correct for imperfect specimen motion upon rotation. Individual $x - y$ slices through the specimen were tomographically reconstructed using various algorithms developed under the IDL programming language at the Australian National University. The density data from the individual slices were then combined to form a three-dimensional density image of the diamond particle.

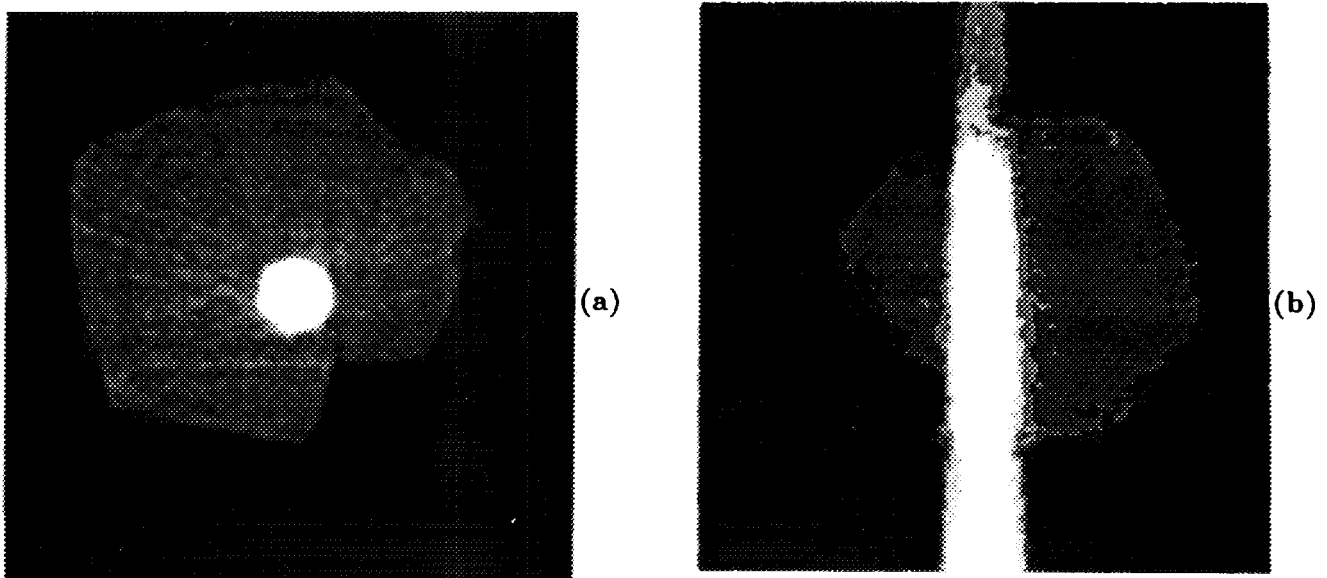


Fig.2 Reconstructed vertical ($x-y$) (a) and horizontal (b) slices through the diamond particle.

During the analysis of the tomography data a great care was taken to discover and, if possible, to compensate for any problems related with the sample manipulation. The major problem is caused by sudden jumps (up to a few μm) of the specimen field-of-view ($90 \times 120 \mu m^2$) from one view angle to the next. Since the tungsten tip supporting the crystal is approximately parallel with the z -axis in the field-of-view we correct for random rotations by bringing into common vertical alignment the tip and centre-of-mass of the tungsten tip base for all view angles. The 2-d projections are compensated for relative vertical misalignments by correlating with z_k the energy loss profiles $\sum_i G(t_i, \phi_j; z_k)$ for all view angles ϕ_j . t -dislocations (for different z_k) are corrected by demanding that the centre of mass of the individual slices (fixed ϕ_j, z_k) be consistent with $x - y$ centre-of-mass of the cross section (at fixed z_k) as determined by the set of all pairs of orthogonal views. We are presently exploring more general methods, based on consistency conditions which the projections must satisfy [5] to compensate for the problems associated with sample manipulation.

Having corrected for these image inconsistencies, we perform the reconstructions on the separate slices z_k using filtered back-projection technique. We routinely used this method for the reconstructions because of its slightly superior performance when reconstructing test phantoms. The test reconstructions indicate that variations of order 2% of the diamond density should be distinguishable given the STIM experimental geometry and data signal to noise ratios. Unfortunately, the images show some blurring of the tungsten tip, while the density distribution appears to decrease in a monotonic way outwards from the tip. This is unexpected behaviour, and we suspect that the effects may be in part due to energy dependence of the energy loss rate and beam broadening while traversing the sample.

STIM Tomography is a very useful technique for characterizing bulk density variations in CVD diamonds. STIM Tomography has been shown to be capable of coping with large and small density variations within the one specimen. These density variations have been shown to vary between disordered carbon ($\sim 2 \text{ g/cm}^3$), diamond ($\sim 3.2 \text{ g/cm}^3$) and tungsten ($\sim 19.6 \text{ g/cm}^3$), all in the one specimen. Large variations in density within the sample makes it difficult to determine density with a very high precision in this preliminary experiment.

This work was supported by a grant from Australian Research Council.

REFERENCES

- [1] **A.M. Cormack**
J. Appl. Phys., **34** (1963)2772.
- [2] **A.E. Pontau, A.J. Antolak, D.H. Morse, A.A. Ver Berkmoes, J.M. Brase, D.W. Heikkinen, H.E. Martz and I.D. Proctor**
Nucl. Instrum. & Meth., **B40/41** (1989)646.
- [3] **A.V. Hetherington, C.J.H. Worth and P. Southworth**
J. Mater. Res., **5(8)** (1990)1591.
- [4] **S.-A. Stuart, S. Prawer, A. Hoffman, A. Moodie and P. Weiser**
Mater. Res. Soc. Symp. Proc., **202** (1991)217.
- [5] **J. Howard**
J. Opt. Soc. Am. A, **5** (1988) 999.

A Time of Flight detector for high energy heavy particles

Z. Fang and D.J. O'Connor

Department of Physics, University of Newcastle, NSW 2308, Australia

As a commonly used method to measure the energy of a particle with known mass, the flight time of the particle travelling over a certain distance is measured. A detector based on this principle is called a time-of-flight (TOF) detector which has attracted interests constantly during the last 15 years^[1-4]. For high energy heavy particle energy detection, TOF detector is an appropriated choice and such a system developed recently is described in this paper.

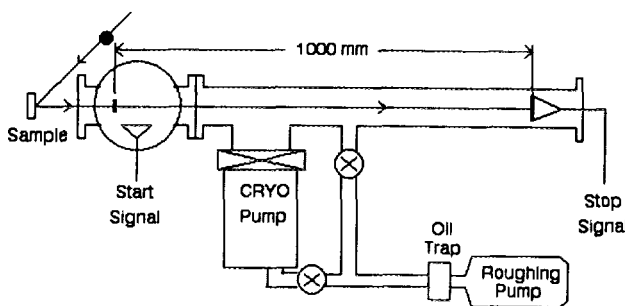


Fig.1 Simplified structure of the TOF system

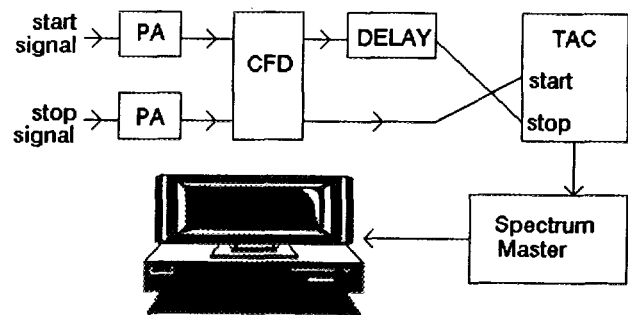


Fig.2 The electronics processing the timing signals

The basic structure of the system is simplified and illustrated in Fig.1. Two timing detectors measure the flight time of the particles passing through a 1 meter separation. The back detector consists of a set of chevron assembled multichannel plates(MCPs) on top of a $\sim 50\Omega$ anode which ensured smooth signal transformation. The front detector is described elsewhere^[5] in detail and here it is simply represented by a $\phi 10\text{mm}$ carbon foil which functioned as the detector acceptance aperture. The secondary electrons generated from the carbon foil are collected by the bottom MCPs-anode assembly therefore the timing signal is produced.

The output signals from the MCPs are negative pulses with various pulse height and sub-nanosecond leading edge. Suitable electronics modulars are selected to deal with these signals. A fast quad constant fractional discriminator

(ORTAC 935) is used to transfer these signals into well defined pulses that minimised the time walk. As shown in Fig.2, reversed timing technique is used to reduce the dead time on the time to amplitude converter (ORTAC 567). The time spectrum is collected by a spectrum master (ORTAC 921) with maximum 16k channels and the data are finally transferred and stored in a computer.

The resolution of a TOF system depends on many parameters. generally it is written as the sum of three terms, $(\Delta E)^2 = (\Delta E)_L^2 + (\Delta E)_T^2 + (\Delta E)_{\text{foil}}^2$. The first term $(\Delta E)_L$ is related to geometric arrangement since even particles from an ideal point source may travel a slightly different path due to the finite detector solid angle. $(\Delta E)_L$ is minimised by having the flight path perpendicular to the acceptance apertures of the detectors^[6]. The second term $(\Delta E)_T$ represented the timing uncertainty which comes from the intrinsic timing resolution of the detectors and the timing uncertainty in the electronics. The last term $(\Delta E)_{\text{foil}}$ comes from the different energy loss and energy loss straggling when the particle pass through a non-uniform carbon foil. Although most limits to the energy resolution are difficult to control, such as the timing uncertainty in electronics and energy loss straggling in carbon foil, they all fell in the same order. For example, timing uncertainty in electronics is about 50ps. So the

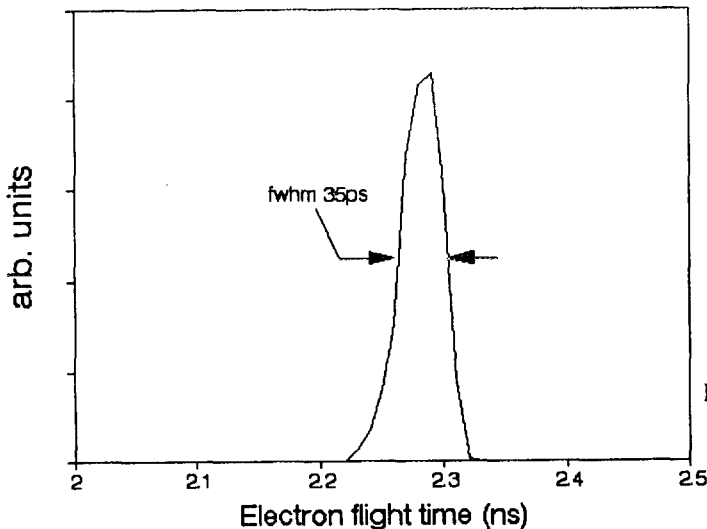


Fig.3 The timing spread for secondary electron transportation from carbon foil to MCPs-anode. total 10,000 electrons are simulated.

overall energy resolution is minimised if comparable value from the timing detector is obtained. A computer simulation result is shown in Fig.3 which revealed that the intrinsic timing resolution for the front timing detector is about 30ps^[5]. To minimise the total timing resolution, the shape of the anode, the voltages applied on each terminals and the threshold and delay for the CFD are carefully considered and practiced.

Compared with other timing detectors already been designed, the front timing detector has several new features. In this new design, the magnetic field is produced by two carefully arranged coils rather than by permanent magnets. The arrangement of the coils are carefully chosen that a uniform field is

produced. The whole structure of the detector is compact and all the components are fitted into a standard 6" stainless steel crosspiece. Other than that, the secondary electrons generated from the carbon foil are accelerated and deflected at the same time rather than using the accelerate meshes which may introduce some suspicious signals. As shown in Fig.1, all the components are designed to satisfy UHV requirements, the system can be baked and clean sample surface can be maintained. The UHV comparability of this system also made it possible to link other surface analysis techniques to perform in situ surface analysis.

The whole system is firstly tested by a 4MeV radioactive α -source. Further calibration is taken using the beam from accelerators. The parameters used in electronics and the voltages applied on each HV terminals are selected that the detector works on the optimise condition. The application of this system is basically to perform heavy ion RBS with improved depth and mess resolution. A two dimensional goniometer controlled by electric motors makes it possible for high energy heavy ion channelling analysis. As demonstrated by H.Whitlow et.al.^[7,8], a powerful TOF-E system can be set up to measure the velocity and energy of the particle simutanously. Particles with unknown mass can be identified. The TOF-E system will have more wide applications in material analysis.

References

- [1] A.Chevarier and N.Chevarier, Nucl. Instr. and Meth., 218(1983)1.
- [2] R.H.Kraus, Jr., D.J.Vieira, H.Wollnik and J.M.Wouters, Nucl. Instr. and Meth., A264(1988)327.
- [3] J.D.Bowman and R.H.Heffner, Nucl. Instr. and Meth., 148(1978)503.
- [4] F.Busch, W.Pfeffer, B.Kohlmeyer, D.Schüll and F.Pühlhoffer, Nucl. Instr. and Meth., 171(1980)71.
- [5] Z.Fang and D.J.O'Conner, to be published.
- [6] T.Mizota, K.Yuasa-Nakagawa, S.M.Lee, T.Nakagawa, Nucl. Instr. and Meth., A305(1991)125.
- [7] H.J.Whitlow, in: Proc. High Energy and Heavy Ion Beams in Materials Analysis, Albuquerque, 1989, eds. J.R.Tesmer, C.J.Maggiore, M.Nastasi, J.C.Barbour and J.W.Mayer (Materials Research Society, Pittsburgh, PA) p73(1990).
- [8] Harry J.Whitlow, Bo Jakobsson and Lars Westerberg, Nucl. Instr. and Meth., A310(1991)636.



Advanced Materials Analysis Facility at CSIRO HIAF Laboratory.

M.J.Kenny¹, S.H.Sie², L.S.Wielunski¹, G.F.Suter² and G.R.Baxter¹

(1) CSIRO Division of Applied Physics, PO Box 218 Lindfield, 2070

(2) CSIRO Division of Exploration and Mining, Delhi Road, North Ryde, 2113

Introduction

The HIAF facility at North Ryde, based on a 3 MV Tandetron accelerator has been operating for several years⁽¹⁾. Initially three ion sources were in operation:- conventional duoplasmatrons for proton and helium beams and a sputter ion source for heavy ions. An electrostatic focussing system was designed and built in-house for providing microbeams⁽²⁾. The research emphasis has been largely on microbeam PIXE with particular reference to the mining industry⁽³⁾.

An AMS system was added in 1990 which prevented the inclusion of the charge exchange canal required for helium beams. The facility has been operated by CSIRO Division of Exploration and Mining.

At the beginning of 1992, the Ion Beam Technology Group of CSIRO Division of Applied Physics was relocated at Lindfield and became a major user of the HIAF facility. Because the research activities of this group involved Rutherford Backscattering and Channelling, it was necessary to add a helium ion source and a new high vacuum beam line incorporating a precision goniometer. These facilities became operational in the second quarter of 1992. Currently a PIXE system is being added to the chamber containing the goniometer, making the accelerator an extremely versatile one for a wide range of IBA techniques.

Ion Source

Conventionally in a tandem accelerator, negative ions are extracted from the ion source and accelerated to the positively charged terminal. There they are stripped of a number of electrons and become positively charged. They then receive an acceleration away from the terminal and the final energy is $(n+1)eV$ where n is the number of positive charge states on the outgoing ion and V is the terminal voltage. Although this procedure works well for many ions, there are a number of elements which do not easily allow an electron to be added to form a negative ion. Helium is one such element. The method adopted in such cases is to produce a positive ion by conventional means and to pass it through a charge exchange canal containing an element such as lithium or rubidium which have a high affinity for giving up an electron.

In this case an evaluation of available ion sources from commercial manufacturers showed that the Alphasross RF source produced by National Electrostatic Corporation in the USA was the most suitable for installation in this

accelerator with minimum disruption to existing facilities, in particular the optical path lengths associated with the microbeam system. Specifications called for an analysed beam of 1 μA at a terminal voltage of 1.0 MV and to be stable for a period of one hour. This was achieved with minimal trouble on the first attempt.

The system initially takes about forty five minutes to get going because of the need to heat the charge exchanger chamber to about 50° C to melt the rubidium. At the conclusion of a run it takes an equivalent time to cool down, during which time the helium plasma is kept running. The source has run for several hundred hours over the eighteen month period and has required only one cleaning and rubidium replacement (10g). The electronics has operated without fault.

Target Station

The specifications called for a precision goniometer with two rotational degrees of freedom and two translations within the rotation and an operating vacuum of 10^{-6} torr or better. The system was to be computer controlled with facility for automatic channel location and multi sample data collection. Complete software for data analysis was also required. The backlash for rotation was required to be $\pm 0.01^\circ$ and for translation $\pm 20 \mu\text{m}$ or better. From evaluation of available systems it was decided to purchase a goniometer hardware / software package from Charles Evans and Associates, Redwood City, California, USA and to fabricate the chamber locally.

The system is based on a Klinger stepper motor controlled goniometer. Although the motors are contained within the vacuum system, the required vacuum specification has been met. Samples are loaded on a 50 mm diameter puck which can be loaded and unloaded through an air-lock. A laser beam coincident with the beam spot is used to determine sample coordinates for the computer. Three detectors are mounted in the chamber. The first is at 160° for back angle RBS, the second is variable from 95° to 130° for glancing angle RBS and the third is at 20° for Hydrogen Forward Scattering. Data acquisition options include fixed position, auto channelling, rotating random. Upto forty samples can be queued for analysis at the one time. Interactive analysis of the data can be carried out using user friendly software at the same time as further data is being accumulated. The system has operated satisfactorily with only minimal software bugs. The chamber vacuum is provided by a 15 cm Edwards cryopump and a 10 cm cryopump is used on the beam line. Typical beam currents are in excess of 100 nA He^{++} and beam spot is about 1.5 mm diameter. Currently a PIXE system is being added to improve sensitivity for elements whose masses are similar.

The entire accelerator facility is such that switching from one ion source to another is quite simple and so hydrogen beams can also be used. This makes it possible to carry out a variety of Nuclear Reaction Analysis reactions such as $^{15}\text{N}(p,\alpha)^{12}\text{C}$ and $^{18}\text{O}(p,\alpha)^{15}\text{N}$ with respective proton energies of 1.0 and 0.83 MeV.

Performance

The entire system has operated reliably since installation and has been used to analyse composition and structure of a wide range of thin films and crystals. Some of these are:

RBS

Electrochrome WO_3/ITO layers

Gold films on glass for Gated Ion Channel Sensors

Optical surfaces- Ta_2O_5

RBS/ Channelling

Compound semiconductors - $\text{Hg}_x\text{Cd}_{1-x}\text{Te}$

Compound superconductors $\text{YBa}_2\text{Cu}_3\text{O}_x$

Nickel Crystals

HFS

Water uptake on Pt/Ir surfaces

NRA

Measurement of wear in Ion Irradiated Carbon Surfaces by

$^{15}\text{N}(p,\alpha)^{12}\text{C}$

The role of oxygen in formation of Gated Ion Channel Sensors by

$^{18}\text{O}(p,\alpha)^{15}\text{N}$

The Alphatross helium ion source and the new chamber and goniometer system have made the HIAF facility extremely versatile for a wide range of Ion Beam Analysis techniques and can provide accurate quantitative data very quickly.

References

- (1) S.H.Sie, Nucl. Instr. and Meth. in Phys. Reserach B10/11 (1985) 664
- (2) C.G.Ryan, Nucl. Instr. and Meth. in Phys. Reserach B15 (1986) 664
- (3) C.W.L.Griffin, C.G.Ryan,G.S.Souter and D.R.Cousens, Nucl. Instr. and Meth. in Phys. Reserach B54 (1991) 284.



Microbeam Recoil Detection for Hydration of Minerals Studies

S.H. Sie, G.F. Suter (HIAF, CSIRO Exploration and Mining, North Ryde, NSW)

A. Chekhir (Institute of Experimental Mineralogy, USSR Acad. of Science, Moscow and
Macquarie University, North Ryde, NSW)

T.H. Green (Macquarie University, North Ryde, NSW)

ABSTRACT

The glancing angle geometry is chosen to enable application of the elastic recoil detection micro-analysis on thick geological samples, for hydrogen content determination. Simultaneous PIXE measurements can be used to eliminate the problem of uncertainties in beam charge collection. The method is applied to determine the hydration characteristics of silicates, produced experimentally at high pressure and temperature simulating the lower crust and upper mantle conditions. Preliminary results show that the technique can be applied readily on a microscopic (<100 μm) scale for determination of H at fraction of atomic percent level.

1. Introduction

Solubility of water in minerals is of fundamental importance in understanding the behaviour of melts on quenching, and thus for modelling of magma genesis and evolution. A number of techniques have been used to determine water content on macroscopic samples or as bulk analyser, for example infra red spectroscopy [1] and weight loss on ignition [2]. These methods are prone to errors when bubbles (often microscopic) are present in the sample, and are generally unsuitable when the samples themselves are microscopic, such as monomineralic constituents of natural rocks and most experimental petrological samples. Microbeam techniques such as the ion microprobe and the nuclear microprobe can be used to determine the water content through H determination [3]. Quantitative analysis is more readily achieved using nuclear microprobes, whereas the matrix effect in ion microprobe can be problematic. The inverse resonant reactions induced by microbeams of F^{19} or N^{15} can be used to determine H content, but the shorter range of the beam and high energy imply high energy deposit density which often results in thermal damage to the samples [4]. The forward recoil is an alternative method with generally higher cross section and thus can be carried out with low beam intensities to reduce specimen damage.

In this paper we report preliminary results of application of the forward recoil technique using microbeams of alphas to determine the H content of some experimental petrological samples. The use of simultaneous PIXE helps to eliminate some of potential problem in quantification.

2. Experimental set-up

In an elastic collision, the recoil energy E_r of the target nucleus is given by

$$E_r = E_o \frac{4m_1m_2}{(m_1 + m_2)^2} \cos^2 \theta$$

where m_1, m_2 are the incident and recoiling atomic mass, E_o the incident energy and θ the laboratory recoil angle. From this equation it is obvious that maximum recoil energy will be obtained for when $m_1=m_2$, decreasing monotonically as with increasing m_1 . For easy discrimination of incident and recoils $m_1 \neq m_2$, and thus for hydrogen the first practical beam will be alpha beams since the reactivity of deuterons is not desirable, and He^3 is not as readily available. The formula also indicates that the smallest angle θ the higher the recoil energy, coinciding with the cross section for Rutherford scattering. Thus the desired geometry is either a transmission geometry $\theta = 0^\circ$ or a glancing angle as close as possible to 0° . The transmission geometry requires a thin sample to enable the recoils to be detected. For 3-4 MeV alpha beam this requires sample thickness below 20-30 microns which can be a problem if the sample has to be self supporting as well. For limited sample size this can be achieved

readily [5]. The glancing geometry presents a more convenient alternative, in terms of simpler sample preparation, although the effective depth of analysis is shallow at ~ 0.8 - $1 \mu\text{m}$, to be compared with 2 - $4 \mu\text{m}$ (depending on the sample thickness) for transmission geometry for a matrix of silicates. The shallow depth requires the sample to be polished to a good surface finish ($<0.1 \mu\text{m}$), comparable to that required for electron probe analysis. To minimise the effect of surface roughness, the sample surface should not be too oblique with respect to the beam direction. In the present measurements, 3 MeV alpha beam was used and the incident and exit angle were symmetrically set at 16 deg with respect to the sample surface. This represents an acceptable compromise between the need for larger angle to minimise the effect of surface roughness and to increase effective depth of analysis, and the higher cross section for smaller recoil angles. The recoiling protons were detected in a surface barrier detector, subtending an angle of 1.2 msr at the sample, and covered with a $15 \mu\text{m}$ thick mylar foil to absorb the scattered alpha beam. The absorber attenuates the proton maximum recoil energy of 1.38 MeV to $\sim 0.92 \text{ MeV}$.

The scattering cross section of alpha on protons deviates from Rutherford scattering, and is accountable in terms of phase shift analysis of the partial waves [6-8]. Extensive compilation of phase shifts for proton-alpha scattering required for cross section calculations for the regime applicable to the present work has been published [8], and tested experimentally. Enhancement over the Rutherford cross section increases with the incident alpha beam energy and decreasing recoil angles. A computer code "RECOIL" has been written, incorporating this cross section parametrised appropriately, that calculates the shape of the recoiling proton spectrum for given experimental conditions, and a uniform hydrogen distribution with depth. The hydrogen depth profile of the sample can be obtained in the first order by comparing the measured data and the calculated shape.

To test the program and calibrate the experimental geometry, polymer foils (polyethylene, kapton) were irradiated with a defocused (diameter 1.0 mm), low intensity ($<0.2 \text{ nA}$) beam in order to prevent hydrogen loss from the sample. In addition the sample was continuously translated to further minimise this effect, with dwell time at each new spot of 5 seconds . Doubling the beam density and dwell time produced the same result, and thus it can be assumed that thermal damage and other causes of H loss were averted. Figure 1 shows the data and calculated spectrum, from polyethylene. Straggling and multiple scattering effect are included in the calculation, although the effect of the latter is negligible. The dominant contribution to straggling is the absorber in front of the detector. For example the calculated Bohr's estimate for total straggling effect on protons recoiling from a silica (SiO_2) matrix is $\sim 30 \text{ keV}$ at the surface, increasing to $\sim 40 \text{ keV}$ at the maximum depth analysed (representing $\sim 4\%$ energy spread), which are to be compared with $\sim 16 \text{ keV}$ detector resolution. The mean r.m.s. spread in angle at its maximum at this depth is only $\sim 3^\circ$, giving a mean spread in energy of $<0.1\%$.

3. Results

The samples consist of experimental petrological trial samples, consisting of a mixture of anorthite and diopside with various amounts of water added. The mixture is sealed, and fused at high pressure (up to 10 kb) and temperature (up to 1200°C) and quenched into glass. Measuring between 0.5 - 1 mm , the samples were set in epoxy and polished. After initial trials where surface charging was found to present a severe problem in beam charge integration, a thin coating of Au ($\sim 10 \text{ nm}$) was deposited on the samples to conduct the beam charge, and also to provide additional handle on normalisation of the data through the Au X-rays (L and M lines) collected simultaneously in a Si (Li) detector. Measurements were carried out initially with low beam ($<0.5 \text{ nA}$) to avoid the possibility of thermal damage, and later increased to 1 - 2 nA focused to 30 microns . A few initial runs were carried out with the beam defocused to 200 microns , with similar results.

The sample were scanned in discrete steps, starting from outside the perimeter. The PIXE spectra collected simultaneously indicate unambiguously when the beam is on the sample, through the presence of the Ca and Si (including unresolved minor components of Al and Mg) peaks (Fig. 2). Two contrasting spectra of the recoil protons are shown in Fig. 2, showing a sample with a relatively high level of H with uniform bulk distribution, and another with lower H level that enables the observation of the typical surface peak due to adsorption of moisture on the specimen surface. Several spot analyses were carried out on each sample which indicated homogeneity. In the present trial, samples

H content varies from 0.3% to 2.5%. For the higher ranges (>1%, corresponding to >9% water content), the agreement with estimates from electron probe analysis is good.

4. Conclusion

From the present measurements it can be concluded that for uniformly distributed H, a detection limit as low as 10 ppm can be obtained, corresponding to a single count in the range of 0.2-0.9 MeV, for 0.3 mm Coulomb charge, which in turn can be collected in ~5 minutes with a 1 nA beam. There is virtually no background count in this energy range. In contrast, using the inverse resonant reaction $F19(p,\alpha)$ at 6.417 MeV a net yield of ~5 counts is expected for 1% H content, and comparable beam charge using close to 2π sr detection geometry. But more importantly, the limit is set by the cosmic ray background, which defines a lower limit of detection at ~ 50 ppm. The forward recoil technique is thus more suitable for applications for microanalysis, where lower level of beam currents can be used.

References.

- [1] D.L. Hamilton and S. Oxtoby, *J. Geol.* **94** (1986) 525.
- [2] S. Newman et al., *Amer. Miner.* **71** (1986) 1527.
- [3] J.L. Karsten et al. *Earth Plan. Sci. Lett.* **59** (1982) 420.
- [4] S.H. Sie, unpublished.
- [5] M. Mosbah et al., *Nucl. Inst. Meth.* **B54** (1991) 298.
- [6] C.L. Critchfield and D.C. Dodder, *Phys. Rev.* **76** (1949) 602.
- [7] P.D. Miller and G.C. Phillips, *Phys. Rev.* **112** (1958) 2043.
- [8] D.C. Dodder et al, Los Alamos Report LA-6389-MS, 1976.
- [9] R.E. Benenson et al, *Nucl. Inst. Meth.* **B15** (1986) 453.

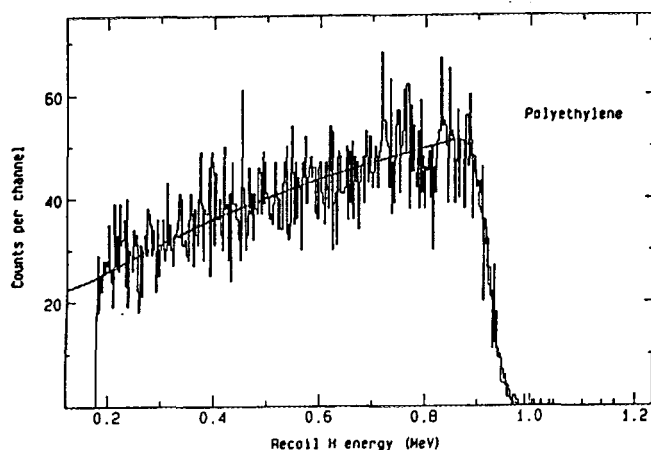


Fig. 1. H recoil spectrum from polyethylene

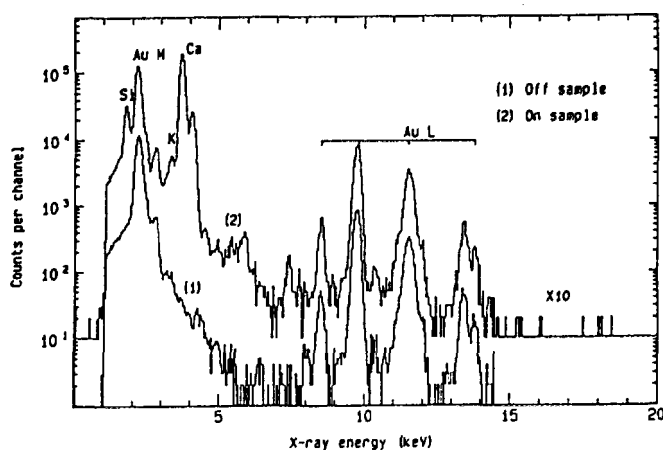


Fig. 2. PIXE spectra collected simultaneously with the recoil spectra. The microbeam was scanned across the sample. The PIXE spectrum indicates unambiguously when the beam is on sample, and is used to deduce the beam charge from the known sample major element composition (Ca in this case).

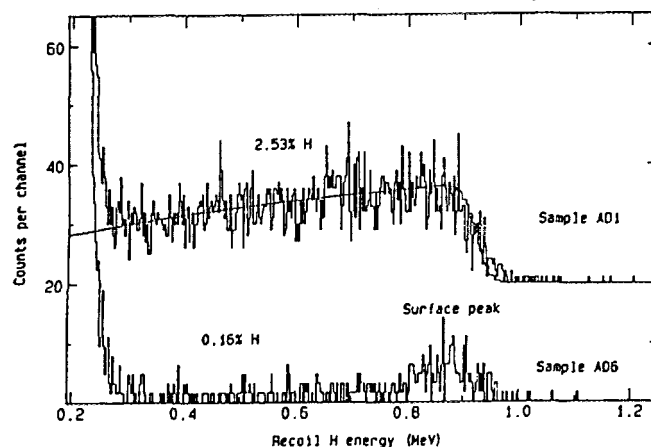


Fig. 3. Recoil spectra from two of the samples, with contrasting shapes. For the sample with lower H content, the surface peak due to moisture adsorption is evident.

MULTIDIRECTIONAL CHANNELING ANALYSIS OF EPITAXIAL CdTe LAYERS USING AN AUTOMATIC RBS/CHANNELING SYSTEM

L.S. Wielunski and M.J. Kenny

CSIRO, Division of Applied Physics, P.O.Box 218 Lindfield, NSW 2070, Australia.

Rutherford Backscattering Spectrometry (RBS) is an ion beam analysis technique used in many fields. The high depth and mass resolution of RBS make this technique very useful in semiconductor material analysis [1]. The use of ion channeling in combination with RBS creates a powerful technique which can provide information about crystal quality and structure in addition to mass and depth resolution [2]. The presence of crystal defects such as interstitial atoms, dislocations or dislocation loops can be detected and profiled [3,4]. Semiconductor materials such as CdTe, HgTe and $\text{Hg}_x\text{Cd}_{1-x}\text{Te}$ generate considerable interest due to applications as infrared detectors in many technological areas.

The present paper demonstrates how automatic RBS and multidirectional channeling analysis can be used to evaluate crystal quality and near surface defects.

The CdTe epitaxial layers have been grown on 50 mm diameter (211) GaAs wafers in a Cambridge Instruments Quantax 226 MOCVD system. Structure analysis has been performed using a 2 MeV He beam from the HIAF accelerator and Klinger stepper motor controlled goniometer with Charles Evans software [5]. The system is designed to automatically collect RBS data in fixed position and/or rotational random and/or channeling position for up to forty individual samples without operator assistance, providing that all samples are mounted within the 50mmX50mm sample holder. The whole goniometer can be rotated to any angle around the vertical axis and the sample manipulator can be tilted up to 45° in either direction around the horizontal axis. The angular precision of these two angles is $\pm 0.01^\circ$. The samples are mounted on the top of two orthogonal linear translation mechanisms which allow any point of the 50mmX50mm sample surface to coincide with crossing of the above mentioned axes of rotations. The linear precision of translations is better than $\pm 0.02\text{mm}$. All translations and rotations are computer controlled with stepping motors and digital encoders installed directly on the goniometer in the vacuum chamber. The vacuum in the chamber during operation is better than 10^{-6} torr.

The automatic channeling procedure is very effective and is based on automatic two dimensional angular scanning for channeling in steps 0.5° within $\pm 5^\circ$ around the direction recorded in the initial parameter set. When multidirectional channeling analysis is required a separate initial parameter set must be created for each channeling direction and the direction recorded in each initial parameter set must be within $\pm 5^\circ$ of the expected channeling axis.

Fig 1 shows typical results from a CdTe epitaxial layer on a (211) GaAs single crystal. The layer thickness is more than the RBS depth analysis range (2000nm) and the substrate signal is not recorded. The (211) channeling spectrum recorded in the direction near to the normal to the sample surface shows a reasonable channeling level, however this is not a good channeling axis and it is advisable to record the channeling spectrum in one of the major channeling directions for example (110) or (111). The (110) axis is 30° from the (211) direction and when a proper 30° tilt of the sample has been recorded in the second initial parameter set, the automatic channeling procedure located the (110) channel and produced the (110) channeling spectrum with the $\chi_{\min}=5\%$ shown on Fig 1. This spectrum clearly shows that the sample is a good quality epitaxial layer.

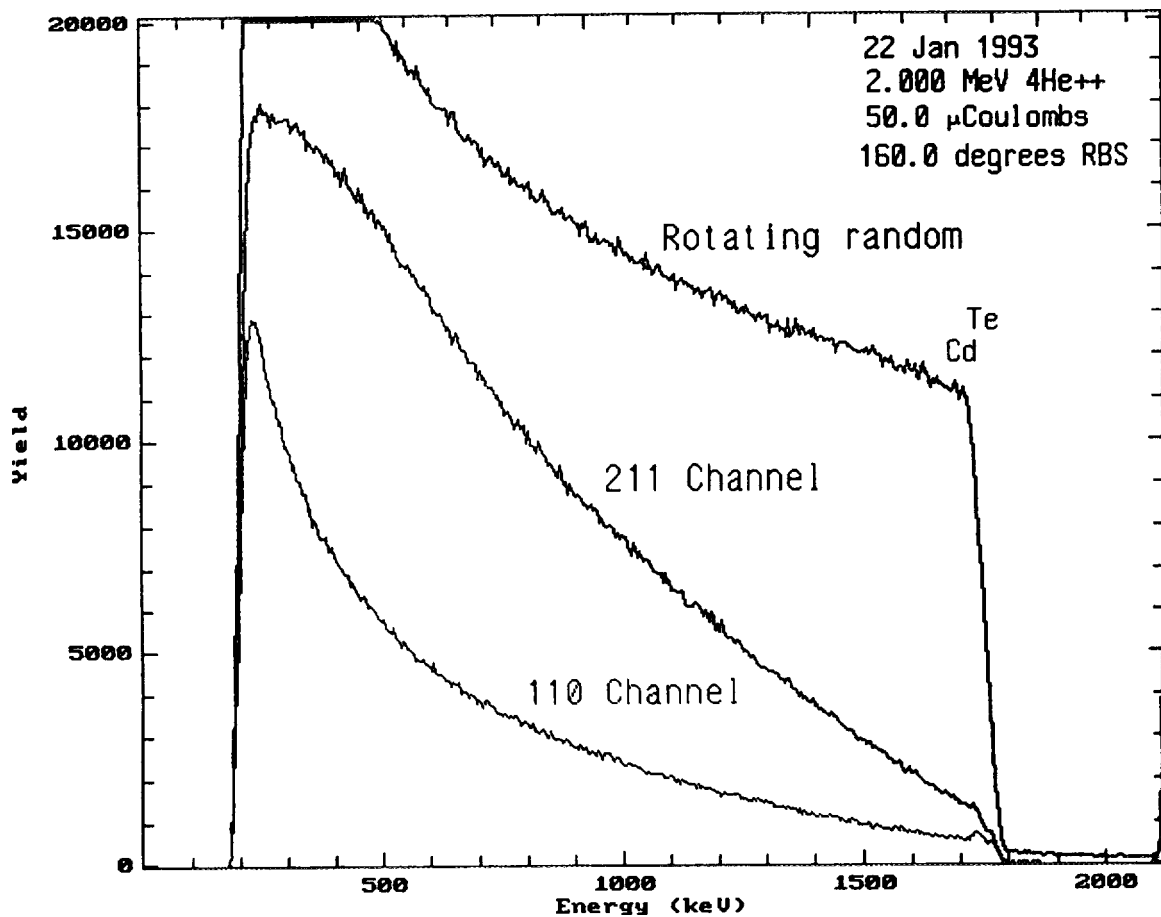


Fig 1. 2MeV He RBS spectra collected automatically in rotating random, (211) and (110) channeling directions.

The above results demonstrate how multidirectional channeling analysis can be done automatically without tedious operator assistance normally required in such complex measurements. For example the automatic RBS/channeling system substantially simplifies the structural analysis of an epitaxial (111) CdTe twin multilayer on (100) GaAs previously reported by manual channeling [6].

References

- [1] W.K. Chu, J.W. Mayer and M.-A. Nicolet, Backscattering Spectrometry (Academic Press, New York, 1978).
- [2] L.C. Feldman, J.W. Mayer and S.T. Picraux, Materials Analysis by Ion Channeling (Academic Press, New York, 1982).
- [3] L.S. Wielunski, S. Hashimoto and W.M. Gibson, Nucl. Instr. and Meth. B13 (1986) 65.
- [4] A. Turos, L. Wielunski, M. Wielunski and B. Wojtowicz-Natanson, Nucl. Instr. and Meth. 149 (1978) 421.
- [5] M.J. Kenny, S.H. Sie, L.S. Wielunski, G.F. Suter and G.R. Baxter, Advanced Materials Analysis Facility at CSIRO HIAF Laboratory, (this conference).
- [6] L.S. Wielunski, M.S. Kwietniak, G.N. Pain and C.J. Rossouw, Nucl. Instr. and Meth. in Phys. Res. B45 (1990) 455.

NUMERICAL STUDIES OF TRIPLET AND RUSSIAN QUADRUPLLET QUADRUPOLE LENS SYSTEMS WITH THE GIVEN SPOT SIZE ON THE TARGET, FOR USE IN A MICROPROBE.

V.A. Brazhnik¹, A.D. Dymnikov^{2,3}, D.N. Jamieson³, S.A. Lebed¹, G.J.F. Legge³, A.G. Ponomarev¹ and V.E. Storizhko¹.

¹Applied Physics Institute of the Ukrainian Academy of Sciences, 244007 Sumy, UKRAINE.

²Institute of Computational Mathematics and Control Processes, University of St Petersburg, Stary Petergof, RUSSIA.

³MARC, School of Physics, University of Melbourne, Parkville, 3052, AUSTRALIA.

INTRODUCTION.

In a nuclear microprobe the focusing system is an essential component which determines the beam spot size, i.e. the microprobe resolution. A small beam cross section at the target is the most important of the many conflicting requirements imposed on the beam. The second most important factor is the current of the beam which at the given brightness is proportional to the phase volume (or emittance) of the beam.

Existing microprobes frequently use a triplet or a Russian quadruplet as the focusing systems. This paper describes the numerical studies of some optimal quadrupole lens systems consisting of three or four lenses suitable for use in a nuclear microprobe taking into account geometrical aberrations of third order. The maximum emittance of changed particle beams for these systems has been found. It is shown how the maximum emittance depends on the spot size.

The Description of the Optimal Systems.

We investigated four different Quadruplets and one Triplet. All five systems have the same total length l (the distance between the object diaphragm and the target), the same effective lengths L of the quadrupole lenses and the same working distance $g = t_{n+1} - \frac{1}{2}L$, where t_{n+1} is the difference between the centre of the last lens and the position of the target. For the triplet $n = 3$ and for the quadruplet $n = 4$. The physical parameters of the systems appear in the table below.

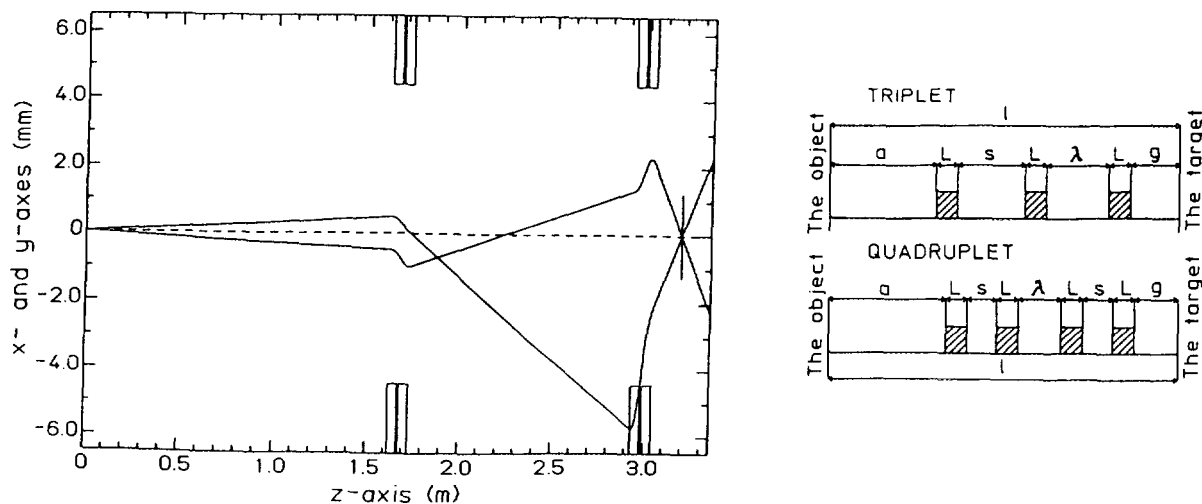


Figure 1: (left) System M showing the separated doublet configuration, The ray intially above (below) the axis is in the xoz ($yo z$) plane. (right) The physical parameters of the systems (see table).

System J has the highest demagnification $D = D_x = D_y$ for negative D and the system M has the highest D for positive D . The system M has one intermediate crossover, see figure 1.

To include the chromatic aberrations we introduce the coefficient α given by:

$$\alpha = D_x D_y / C_{px} C_{py},$$

where C_{px} and C_{py} are the chromatic coefficients, given by:

$$C_{px} = \langle x | \theta \delta \rangle, \quad C_{py} = \langle y | \phi \delta \rangle, \quad \delta = \Delta p / p$$

The coefficient α is proportional to the optimum acceptance (the greatest possible acceptance for fixed δ and the beam spot size on the target), i.e. to the highest microprobe current.

The system K has the maximum α for negative D and the system B has the maximum α for positive D (one intermediate crossover). The system T, triplet, has the positive D_x and the negative D_y . More details concerning these systems can be found in reference [1].

We have been solving the inverse problem: for the given spot size to find the maximum phase volume (4-dimensional) of the beam which gives this spot size and appropriate optimum sizes of the object and aperture diaphragms, assumed rectangular. The results of these calculations have been fulfilled for different spot sizes and are shown on figure 2. We assume that the shape of the spot on the target is a square. The number of the different points for the initial phase set was 85. We have also calculated the reduced parasitic sextupole and octupole aberration coefficients. In all systems the first lens has the smallest values of these coefficients and the last but one has the greatest values. It is possible to see that the contribution of parasitic aberrations for the system M can be considerably less than for the system K if the system has the optimum collimation diaphragms.

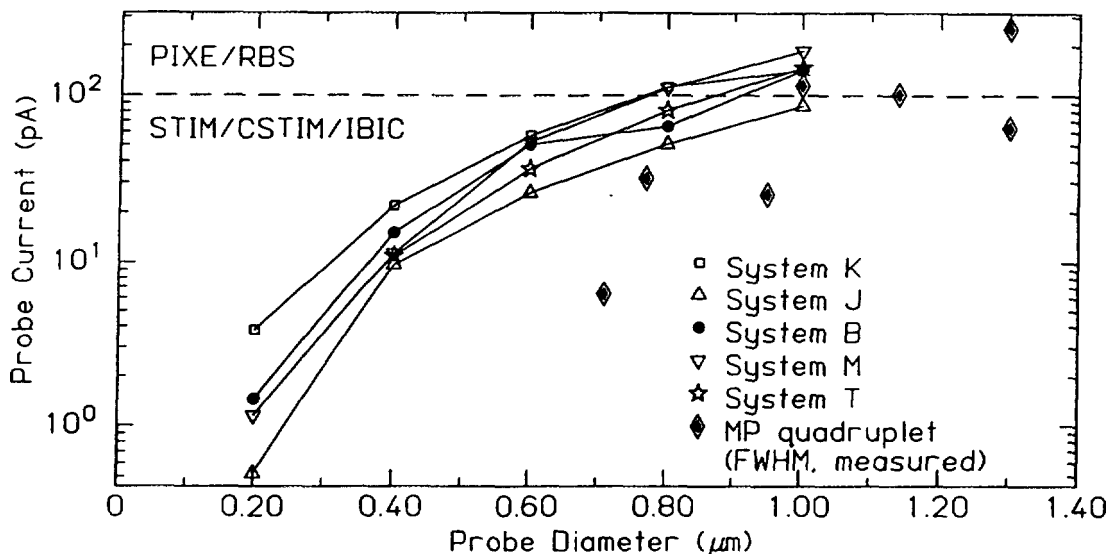


Figure 2: The probe current as a function of probe diameter of each system assuming an ion source/accelerator brightness of $5.3 \text{ pA}/(\mu\text{m}^2 \text{mrad}^2 \text{MeV})$ for a 3 MeV H^+ beam provided by the Melbourne Pelletron accelerator.

CONCLUSION.

We conclude that the optimal systems discussed here have great promise for the next generation of probe forming lens systems. It is planned to test these systems experimentally in the near future.

The Physical Parameters of the Optimal Systems:

System:		T	K	J	B	M
Total length l	(m)	3.19	3.19	3.19	3.19	3.19
Quad. length $L1$	(m)	0.05	0.05	0.05	0.05	0.05
Quad. length $L2$	(m)	0.05	0.05	0.05	0.05	0.05
Quad. length $L3$	(m)	0.05	–	–	–	–
Object distance a	(m)	1.52	0.02	2.82	0.72	1.62
Working distance g	(m)	0.15	0.15	0.15	0.15	0.15
Bore radius	(m)	0.0065	0.0065	0.0065	0.0065	0.00635
Drift space λ	(m)	0.01	2.8	0.0	2.1	1.2
Drift space s	(m)	1.36	0.01	0.01	0.01	0.01
Quad. field $B1$	(T)	0.0926	0.464	0.176	0.474	0.491
Quad. field $B2$	(T)	-0.364	0.350	0.528	0.358	0.376
Quad. field $B3$	(T)	0.860	–	–	–	–
Demagnification (dimensionless)						
D_x		31.6	-91.	-11.0	30.7	47.7
D_y		-22.9	-9.1	-11.0	30.7	47.7
Chromatic Aberration ($\mu\text{m}/\text{mrad}/\%$)						
$\langle x \theta\delta \rangle$		-14	80	54	-284	-488
$\langle y \phi\delta \rangle$		248	20	66	-72	-125
Spherical Aberration ($\mu\text{m}/\text{mrad}^3$)						
$\langle x \theta^3 \rangle$		32	-13	-17	540	2300
$\langle x \theta\phi^2 \rangle$		154	-6.6	-56	260	1050
$\langle y \phi^3 \rangle$		-240	-0.7	-30	29	110
$\langle y \theta^2\phi \rangle$		-212	-6.6	-56	262	1050
Selected reduced parasitic sextupole aberration coefficients ($\text{m}/\text{rad}^2/\%$)						
$\langle x \phi^2 S2 \rangle$		-140	0	-70	0.27	1.5
$\langle y \theta\phi S2 \rangle$		400	0	-130	0.5	2.8
$\langle x \theta^2 S3 \rangle$		-120	-86	-74	-1000	-2700
$\langle y \theta\phi S3 \rangle$		-170		54	130	300
$\langle x \theta^2 S4 \rangle$		–	10	5.5	120	304
$\langle x \phi^2 S4 \rangle$		–	-9.6	-5.4	110	280
$\langle y \theta\phi S4 \rangle$		–	-18	-11	210	-530
Selected reduced parasitic octupole aberration coefficients ($\text{mm}/\text{mrad}^3/\%$)						
$\langle y \phi^3 O2 \rangle$		-650	0	-71	0.70	-1.0
$\langle x \theta^3 O3 \rangle$		-130	36	44	-1500	-6400
$\langle x \theta\phi^2 O3 \rangle$		55	-9.7	-19	380	1500
$\langle y \theta^2\phi O3 \rangle$		-76	-9.7	-19	380	1500
$\langle y \phi^3 O3 \rangle$		–	-2.9	-1.3	115	450

S2, O2 are for the % parasitic sextupole or octupole pole tip field contamination in quadrupole lens 2, etc. See [2] for more details.

The work at Melbourne has been partially supported by a grant from the Australian Research Council.

References.

- [1] V. Brazhnik, A. Dymnikov, R. Hellborg, S. Lebed, J. Pallon and V. Storizhko, Nucl. Instr. Meth. B77 (1993) 29-34.
[2] D.N. Jamieson and G.J.F. Legge, Nucl. Instr. Meth. B34 (1988) 411-422.

Low Current Beam Techniques

A.Saint, J.S.Laird, R.A.Bardos and G.J.F. Legge

Microanalytical Research Centre (MARC), School of Physics, The University of Melbourne, Parkville, 3052, Australia.

T.Nishijima and H.Sekiguchi

Electrotechnical Laboratory (ETL), Tsukuba, Japan.

1 Introduction

Since the development of STIM imaging in 1983 [1-2] many low current beam techniques have been developed for the scanning (ion) microprobe. These include STIM tomography, Ion Beam Induced Current, Ion Beam Micromachining and Microlithography and Ionoluminescence [3]. Most of these techniques utilise beam currents of 10^{-15} A down to single ions controlled by beam switching techniques.

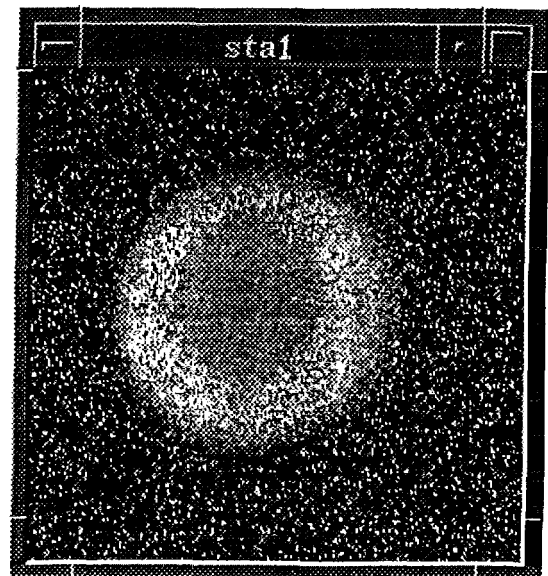
This paper will discuss some of the low beam current techniques mentioned above, and indicate some of their recent applications at MARC. A new STIM technique will be introduced that can be used to obtain Z-contrast with STIM resolution.

2 Simultaneous STIM and IBIC

Recently, experiments to investigate the structural and electrical properties of microwave diodes were undertaken at the Electrotechnical Laboratory (ETL), Tsukuba, Japan. In these experiments a thinned Silicon P-N diode of $30\mu\text{m}$ diameter was electrochemically thinned to $5\mu\text{m}$. The sample was biased to 1.3V and the IBIC signal was collected directly from the diode. A STIM detector was placed behind the specimen. Using the TQSA multi-station data acquisition system at ETL both IBIC signals and STIM signals could be collected simultaneously in separate stations. The specimen was irradiated with 2MeV protons. The STIM and IBIC images are both shown in figures 1a and 1b respectively. The STIM image provides information on the physical structure of the device. The Al contact can clearly be seen in this image. The IBIC image contains information on the electrical activity of the device. This image indicates that the device is not fully depleted at the centre of the diode at this bias potential.



1a



1b

Figure 1 - Simultaneous STIM and IBIC

3 Charge Sharing in IBIC

The Experimental Particle Physics group at Melbourne University have been engaged in the development of solid state pad detectors to be incorporated into one of the large detector arrays at CERN. Knowledge of the electrical properties is essential to optimise both energy and spatial resolution.

A detector array of 16 X 16 1mm^2 pads was mounted in the microprobe chamber. A focussed beam of 2MeV alpha-particles was scanned over an area of 500 X 500 μm around the corners of 4 of these pads. The top two pads, of the four, are connected together and to station 1 of the data acquisition system. The bottom right hand pad is connected to station 2 and the fourth pads is floating. Figure 2a shows the IBIC image of the top two pads at 20V bias. The incomplete depletion region between the two pads can be clearly seen. Figure 2b shows the charge collected on the lower right hand pads when a pulse is present on the upper two pads. This represents charge leakage from the upper two pads to the lower pads and gives interesting information on the position resolution of these detectors.

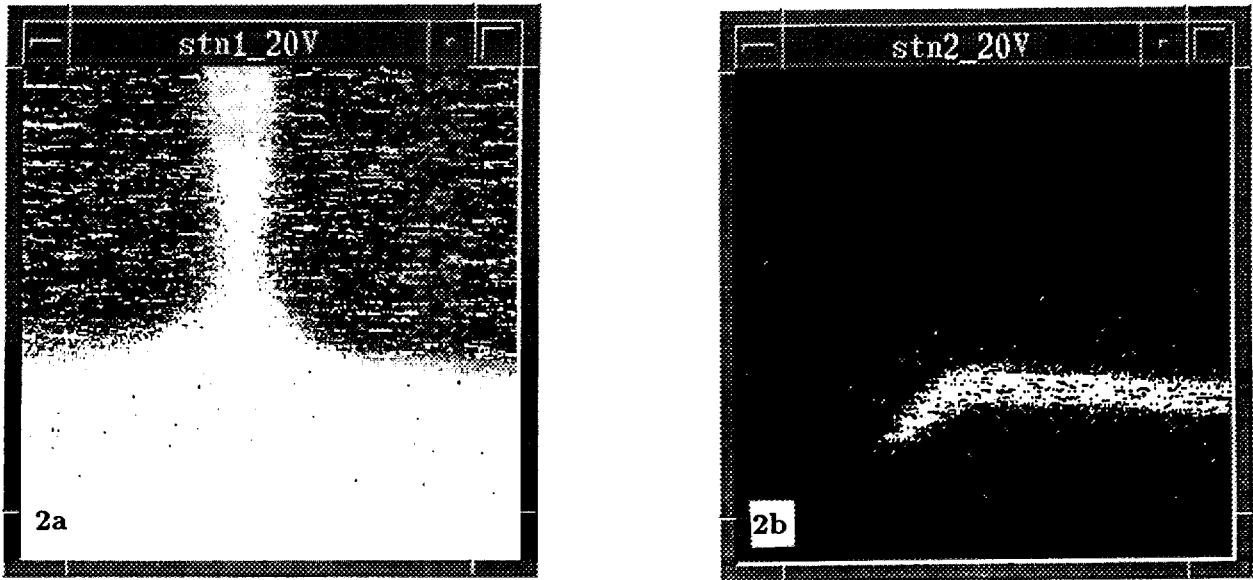


Figure 2 - Charge Sharing in IBIC

4 STIM imaging with Molecular Hydrogen

Lefevre [4] pointed out that increased energy contrast could be obtained in an energy loss STIM experiment using molecular ions.

In this work a STIM detector of limited solid angle is used, so that there is a relatively high probability that one of the protons in a molecule will be scattered out of the detector. Care must be taken that the solid angle is not too small or Coulomb explosion effects will dominate. The unscattered proton is still detected, but only deposits 1/2 the energy of the original molecule (minus the energy lost in traversing the specimen). All these events have, therefore, been tagged as being from a scattering event (i.e. its partner H^+ ion has been scattered out of the detector). The number of these events is a measure of the amount of scattering in any given region of the specimen. This means that in a single data set we have information on both the scattering and energy loss of particles in given region of a scanned specimen.

From the well known Rutherford and Bethe-Bloch equations for nuclear scattering and electronic energy loss, it can be seen that the amount of scattering is proportional to $(Z_2/E)^2$ and the amount of energy loss (electronic) is proportional to (Z_2/E) . Both the amount of scattering and the energy loss are linearly dependent on areal density. Thus the ratio of scattering to energy loss yields a quantity that is independent of areal density and proportional to (Z_2/E) .

From figure 3 it can be shown that -

$$(1 - P) = \left(\frac{A}{A + 2B} \right) \quad (1)$$

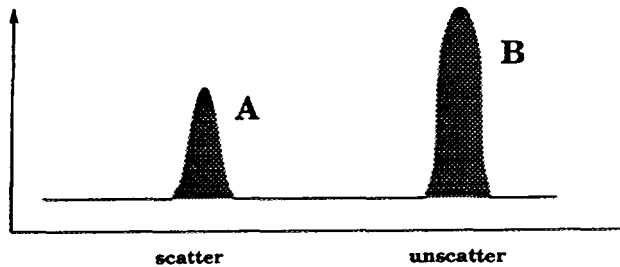
where, P = the probability that a proton is detected and A and B are the areas shown in figure 3.

Therefore if we take the ratio

$$C_Z = \left(\frac{(1 - P)}{\Delta E} \right) \quad (2)$$

,where ΔE = energy loss in same region as scattering, then the parameter C_Z is dependent on (Z_2/E) and not on areal density.

To show the independence of the parameter C_Z to changes in areal density, a thin (nominally $1\mu m$) niobium foil was scanned with a beam of 3 MeV H_2^+ ions. The scan was 300 microns square. The foil varies in areal density over the region of the scan. Spectra were extracted from six regions in the E loss map, where each region had fairly uniform areal density (but a different density to the other 5). From these spectra the parameter C_Z was calculated and these results are shown in figure 3. The parameter C_Z remains approximately constant for the foil even though the areal density is varying widely.



A	B	E loss (channels)	$\left(\frac{A}{A+2B} \right) = X$	$\frac{X}{E \text{ loss}} = C_z$
14604	27485	83	0.2099	2.529
9495	6999	147	0.4042	2.749
11040	14360	103	0.2776	2.695
35186	22381	157	0.4401	2.803
16826	18230	112	0.3157	2.818
10325	9976	121	0.3418	2.825

Figure 3 - Z-Contrast STIM

5 references

1. H.W. Lefevre, R.C. Connolly, G. Sieger and J.C. Overley Nucl. Instr. Meth. 218 (1983) 39-42
2. R.M. Sealock, A.P. Mazzolini and G.J.F. Legge Nucl. Instr. Meth. 218 (1983) 217-220
3. Proceedings of the Third International Conference on Nuclear Microprobe Technology and Applications - Nucl. Instr. Meth. B77 (1993)
4. H.W. Lefevre, R.M.S. Schofield, J.C. Overley and J.D. MacDonald Scanning Micros. 1987, vol.3



A GENERALIZED LABORATORY CONTROL SYSTEM INTEGRATED WITH DATA HANDLING

G. Moloney, P.M O'Brien, A. Scott, A. Saint and G.J.F. Leqqe

Micro Analytical Research Centre (MARC), School of Physics,
University of Melbourne, Parkville, Vic 3052.

A system has been developed to control multiple operations associated with complex accelerator experiments. The system is used to control specimen and beam positions and scanning rates, the variation and stabilization of ion beam lens currents and other operations. It runs in a PC, controlling operations via the PC bus and GPIB. An ethernet link to the data handling workstation allows control there from the command line or via a Graphical User Interface. This link also allows interaction between the multiparameter data collection program and the control system program.



The Development of an X-Ray Computerized Tomography (CT) Experimental System

Lee G.N., Kijek M.M. and Millar J.J.

Department of Applied Physics, Royal Melbourne Institute of Technology,
P.O. Box 2476V, Melbourne, Vic 3001.

Abstract - This paper describes a prototype experimental CT system that has been recently developed at Applied Physics, RMIT/ Physics, La Trobe UCNV. The system incorporates the scanning mode of the first generation CAT-scanner and is designed to perform the scanning of small objects. A microcomputer is used to control the scanning motions and data collection. The performance of the system was examined by scanning a ball-point pen.

1. X-Ray Computerized Tomography

Computerized tomography (CT) [1] is a non-destructive technique used to obtain images of the internal structures of objects which are opaque to visible light. The first CT-scanner was developed by Hounsfield [2] (who shared the Nobel Prize with Cormack [3] in 1979) in 1971. The images produced are two-dimensional distributions of linear attenuation coefficients. By stacking successive images, three-dimensional details of internal structures can be obtained. Radiation such as X-rays, gamma rays, ultra-sound, microwaves, seismic waves, neutrons and electrons have been used for CT. Until recently, unscattered transmitted radiation was primarily used. CT using scattered X-rays has been investigated [4]. The work presented in this paper was performed with transmitted X-rays.

The fundamentals of X-ray computerized tomography are based on the interaction between X-rays and the specimen. Consider a monochromatic collimated X-ray beam of intensity I_0 passing through a non-homogeneous object. The transmitted beam has intensity I as in Eq. 1 where $\mu(x,y)$ is the linear attenuation coefficient along the X-ray path.

$$-\ln \frac{I}{I_0} = \int_{-\infty}^{\infty} \mu(x,y) dx \quad (1)$$

The values of the line integral, also referred to as ray sums, can be determined by measuring I and I_0 . The mathematical foundation to reconstruct the image is provided by the Radon transform [5]. The inverse Radon transform retrieves the original function from all of its line integrals and was defined as

$$\mathfrak{R}^{-1} P(r, \phi) = \frac{1}{2\pi^2} \int_0^{\pi} \int_{-\infty}^{\infty} \frac{\partial / \partial \ell [P(\ell, \theta)]}{r \cos(\theta - \phi) - \ell} d\ell d\theta \quad (2)$$

where ℓ and θ are the coordinates in Radon space and r and ϕ are the polar coordinates in object space. \mathfrak{R}^{-1} is the inverse Radon operator and $P(\ell, \theta)$ represents the line integral of the original function in Radon space.

2. Description of the System

The system is designed to perform CT scans of small objects. It consists of an X-ray source, a collimation system, a sample holder, a data acquisition system and a microcomputer to control the scanning motions and data collection as shown in Figure 1.

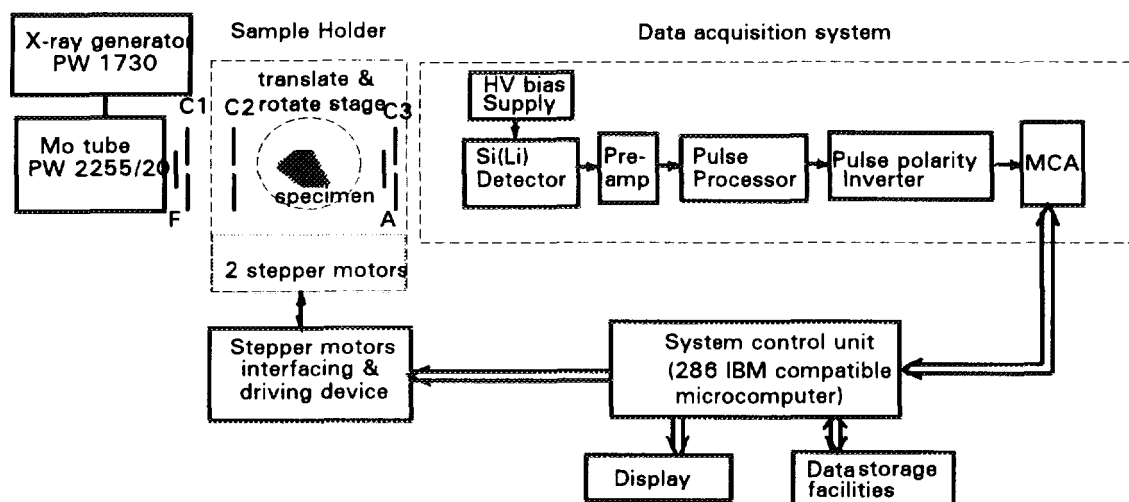


Figure 1. A schematic diagram of the experimental CT system.

2.1 The X-ray Source, collimation, filter and absorber

A Philips 2.7 kW water-cooled broad focus Mo target XRD tube PW2255/20 is used to provide characteristic X-rays with energy 17.44 keV. The tube, operated with a Philips constant potential generator PW1730 at 35kV and 35-40 mA, provides a point source of dimensions 2 mm x 1.2 mm. An approximately parallel X-ray beam of 0.5 mm diameter is achieved by using three 0.5 mm circular apertures C1-C3 (Fig. 1). The apertures are used to define the beam geometry and minimize scattered X-rays. The aperture C1 is placed at 5 mm in front of the source while C2 and C3 are placed 70 mm and 125 mm from C1 respectively. In order to suppress the Bremsstrahlung and the Mo K β peak, a 0.12 mm Zr filter (F) is used. Due to the non-linear input and output count rate characteristic of the pulse processor used, an optimal maximum input rate of 7000 counts/ sec, which corresponds to an output rate of 3000 counts/ sec, is selected and is achieved by attenuating the beam with 0.4 mm Zr and 4 mm Mylar (A).

2.2 The Sample Holder

The system incorporates the scanning mode of the first generation CT-scanner [6] (i.e. the sample is translated and rotated). The movements are provided by the sample holder, equipped with two stepper motors. A Philips 4-phase unipolar permanent magnet stepper motor 9904 112 31004 together with a 25:3 reduction gear and a shaft with 1 mm pitch thread are used to provide the translational movement of 2.5 μ m per pulse. Another Philips 4-phase unipolar permanent magnet stepper motor 9904 112 06101 is used with a 60:1 reduction worm-wheel driven stage to provide rotational movement of 0.125 $^\circ$ per pulse. Only one direction is required for the rotational motion and data is collected with the sample always translating in the same direction. The angular and linear accuracies were measured to be better than 0.06 $^\circ$ and 25 μ m respectively.

2.3 The data acquisition system

A Link Si(Li) Energy Dispersive Detector Model 5070-5081 is used to detect the transmitted X-rays. The signal is amplified and processed by using a Link 2030 Pre-Amplifier and 2010 Pulse Processor. The polarity of the signal pulse was then inverted with an Ortec inverter 433A before passing on to the Ortec ACE2-BI multi-channel analyser (MCA).

2.4 The system control

A 286 IBM compatible microcomputer was used as the system control unit. A program was written in C to control the sample movements and the data collection, and to interface the microcomputer to the MCA and the stepper motors. An electronic device, including two stepper motor driver board RS 332-098 was designed and built to take in the signal via the parallel port and drive the stepper motors.

3. Experimental Results

The performance of the system has been demonstrated by using a ball-point pen (Fig. 2). The pen has an outer plastic case which is hexagonal on the outside and circular on the inside. The centres of the hexagon and the circle are not common, hence the wall is thinner on one side and thicker on the other. Inside the case is the refill which consists of a plastic tube filled with ink. A total of 60 projections (3° interval), each with 53 ray sums (0.25 mm interval) were recorded. With the energy selection facility in the MCA, 25 channels (20 eV/ channel) around the Mo $K\alpha$ peak were selected. The integral counts in all the 25 channels over a period of 30 sec live time were recorded.

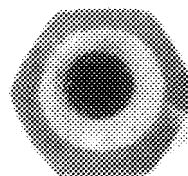


Fig.2. A photograph of the cross-section.

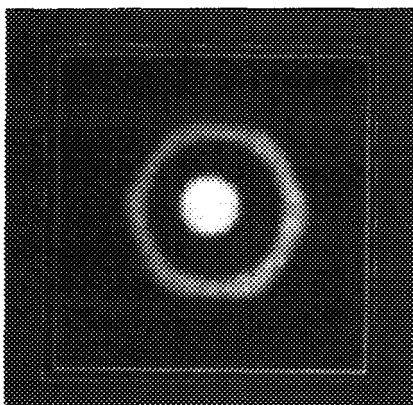


Fig.3. Image reconstructed using C1 only.

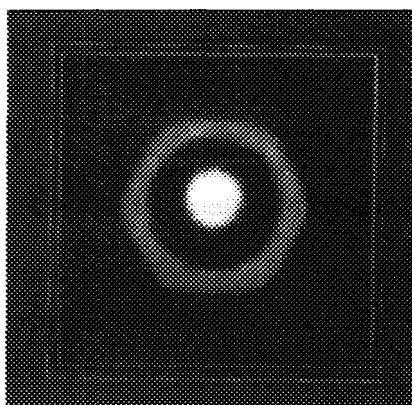


Fig.4 Image reconstructed using C1, C2 & C3

Figure 3 is an image reconstructed using only a circular aperture C1 of 0.5 mm diameter. Figure 4 is an image reconstructed using C1, C2 and C3, all of 0.5 mm diameter. Centroid correction, area normalisation and correction of the background slope in each projection were performed on the data prior to reconstruction. The images were then reconstructed by using the filtered backprojection method [7] and the Ramachandran-Lakshminarayanan filter [8]. The four layers of differing density, the outer plastic case, the air gap, the plastic tube of the refill and the ink, are clearly shown. Differing thicknesses in the outer plastic case are also noticed in both of the images. Note figure 4 has sharper edges than figure 3.

Acknowledgments

The authors wish to express their indebtedness to the 'Computer Imaging Group' of Monash University for their assistance with image reconstruction and the access to their backprojection reconstruction program. The authors also wish to acknowledge the help given by Mr G. Sergeant for constructing the sample holder. One of the authors G. Lee would like to thank the following: T. Baker, B Robinson, A. Russo, P. Smith, and J. Taylor for their assistance in many ways.

References

- [1] G. N. Hounsfield (1973) Br.J. Radiol. 46, 1016-1022.
- [2] A. M. Cormack (1963) J. Appl. Phys. 34, 2722-2727.
- [3] J. R. Davis et al (1986) Austr. Phys. 23, No. 10, 245-247.
- [4] P. Wells et al (1993) Nucl. Instrum. Meth. B 72, 261-272.
- [5] J. Radon (1917) Ber. Verb. Saechs. Akad. Wiss., Leipzig, Math. Phys. K1 69, 262-277.
- [6] H.H.Barrett and W.Swindell (1981) Radiological Imaging, Vol.2, Chap.7, Wiley, New York.
- [7] G. T. Herman (1980) Image Reconstruction from Projections, Academic Press, New York.
- [8] G. N. Ramachandran and A. V. Lakshminarayanan (1971), Proc. Nat. Sci., USA 66, 2236.



SAMPLE PREPARATION AND CURATION at the ANTARES AMS CENTRE

*G.E. Jacobsen, D. Fink, MA.C. Hotchkis, E.M. Lawson, M. Shying,
AM. Smith and C. Tuniz*

Australian Nuclear Science and Technology Organisation PMB 1, Menai, NSW
2234. Australia.

The high throughput and high precision requirements for ^{14}C AMS analyses at ANTARES make vital the role of maintaining a sample preparation and curation laboratory of the highest standard. Automatic computer logging of processing parameters and ready access to sample ownership, history and status is essential when dealing with thousands of samples from diverse sources. At Ansto two high quality clean rooms are near completion, one for low-level environmental samples and the other for modern or enriched samples for industrial and biomedical research projects.

In the first phase, for ^{14}C samples, we have concentrated on simple pre-treatment procedures such as stripping inorganic carbon from water, dissolution of carbonate samples and oxidising organic fractions. Graphitization rigs for reduction of CO_2 to solid graphite is carried out using Fe as a catalyst resulting in carbon AMS targets giving up to $50\mu\text{A}$ of ^{12}C and with a chemistry processing background equivalent to 0.3% modern while unprocessed commercial graphite shows an accelerator background of 0.1% M. Graphitisation is now automatically monitored and logged, and a fully computerised and automated system producing 8 graphite samples is under construction. Sample curation and quality control will make use of a site-wide data base system.

In addition to carbon sample preparation, we have commenced preparing aluminium oxide targets from biological samples for AMS of ^{26}Al . Dual treatment of quartz in rocks and sediments for ^{10}Be and ^{26}Al for Quaternary science projects related to geomorphology and in-situ production studies is also being planned for early 1994.



**THE SYSTEM for HIGH PRECISION and HIGH THROUGHPUT
¹⁴C AMS ANALYSES AT ANTARES**

*A.M. Smith, D. Fink, M.A.C. Hotchkis, G.E. Jacobsen, E.M. Lawson,
M. Shying, C Tuniz, J. Fallon and P.J. Ellis*

Australian Nuclear Science and Technology Organisation
PMB 1, Menai, NSW 2234, AUSTRALIA

High precision measurements of isotopic ratios are performed at the ANTARES AMS facility by sequentially injecting stable isotopes and the radioisotope of interest sufficiently rapidly that variations in ion-source output and transmission can be both allowed for and assessed. The equipment includes enlarged image chambers for the injection and analysing magnets incorporating both high and low mass off-axis Faraday cups, a novel arrangement of electrodes to modulate the injected beam energy, an isotope sequencer to provide timing and gating signals for the data acquisition interface and Faraday cup integrators. A custom built high voltage operational amplifier provides the sequencer with the required voltage waveforms. The isotope sequencer has been designed for flexibility of operation, with bounce periods adjustable from 2 μ s to 8 sec and repetition rates of up to 50 Hz. A description of the equipment set-up, software and operation methodology will be presented.

Accelerator computer control and logging of essential settings is accomplished by two 68030 CPUs operating under OS-9 in a VME environment. Each CPU, one dedicated to low-energy beam transport, the other to the high-energy, communicates via thin-wire ethernet to a central control DEC workstation 5000/PX running a process management program that presents graphic images of accelerator components and status for user access. Multiparameter singles and coincidence data are acquired through a VME front-end interface using a dedicated 68030 CPU to collect and arrange data buffers from VME compatible peak-sensing ADCs manufactured by CAEN, Italy (model V419). Buffers are transferred to a parent data acquisition process running in a second DEC workstation for real-time analysis and presentation of user-defined I-D and 2-D spectra.

Ansto has purchased a 60 sample high-intensity 846 ion source from HVEE to facilitate high throughput ¹⁴C measurements with low background. This ion source has been mounted on a new injection platform and can be raised to 100 kV above ground, making possible a maximum total injection energy of 150 kV. The turbo molecular and roughing pumps and sample changing mechanisms are all at high voltage, and an electrostatic beam attenuator has been added for precise reduction of beam currents when necessary. Our experience with this system will be discussed.



A NOVEL APPROACH TO SECONDARY DEFECT REDUCTION IN SEPARATION BY IMPLANTATION OF OXYGEN (SIMOX) MATERIAL

S. L. Ellingboe and M.C. Ridgway

Department of Electronic Materials Engineering
Research School of Physical Sciences and Engineering
Australian National University, Canberra, ACT 2601, Australia

INTRODUCTION

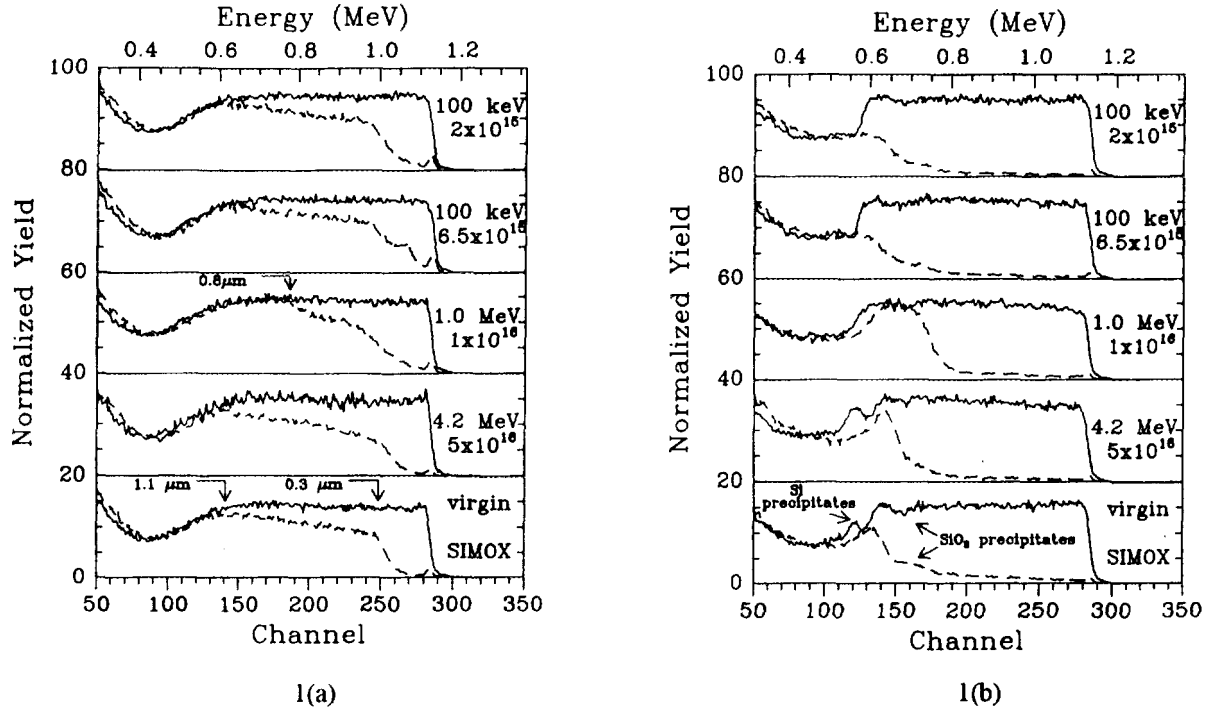
The formation of a buried SiO₂ layer in Si for increased radiation hardness, dielectric isolation, and/or higher operating speeds in Si devices has been studied extensively. In the present report, a novel method for improving the final defect structure of SIMOX material is demonstrated for the first time. The concept of ion-beam-defect-engineering (IBDE) introduced by Wang et al [1] has been utilised. If defects are introduced at a depth R₁ by irradiation with energetic ions into samples which were previously damaged at a depth R₂, it is possible to alter the properties of the defects at R₂, reduce or eliminate damage at R₂, and/or create gettering sites for defects at R₁. By implanting with Si prior to the annealing of As-implanted Si, Wang et al demonstrated that the secondary defect formation near the As projected range (R_p) was decreased. With high-energy Si implantation (where Si R_p > As R_p), the Si interstitials created from the As implant were gettered to the deep disorder created from the Si implant and consequently, secondary defect formation near As R_p was reduced. Similarly, Lu et al [2] used low-energy Si implantation (where Si R_p < B R_p) to create a band of damage near the surface. Lu et al claim that during high temperature annealing, the gradient in the concentration of interstitial defects (created by the Si implant) caused an enhancement in the diffusion of defects to the surface region. Again, a reduction in the secondary defect concentration at B R_p was observed.

In a previous report [3], we showed the beneficial effects of a pre-anneal, high-energy Si implant on unannealed SIMOX material as a function of Si dose and implant temperature. To elucidate the mechanisms responsible for this secondary defect reduction in annealed SIMOX material, we have implanted unannealed SIMOX material with Si ions at various energies (i.e. various Si ion ranges) while keeping the nuclear energy deposition constant at two depths, the front Si/SiO₂ interface or the near-surface region. Si (100) wafers implanted at 300°C with 1 MeV O ions to a dose of 2.18x10¹⁸ cm⁻² were used as the starting material. Pre-anneal Si implants were then performed at an implant temperature of 150°C and at various doses and energies as outlined in the table below. All wafers were annealed at 1300°C for 2 hours.

Ion and Energy	Ion Range (μm)	Dose (cm ⁻²)	Dose Rate (cm ⁻² /sec)	Relative Defect Production/ Ion:	
				@ 1.0 μm	@ 0.15 μm
4.2 MeV Si	3.24	5x10 ¹⁶	1.58x10 ¹³	1.5	1.0
1.0 MeV Si	1.31	1x10 ¹⁶	3.16x10 ¹³	10.25	5.0
100 keV Si	0.15	6.5x10 ¹⁵	9.47x10 ¹²	0.0	25.0
100 keV Si	0.15	2x10 ¹⁵	3.16x10 ¹²	0.0	25.0

RESULTS AND DISCUSSION

Figure 1(a) is the RBS/C spectra of unannealed SIMOX material which has been implanted with Si ions which had R_p greater than, equal to, or less than that of the O R_p. All channelled spectra show a surface peak as well as a thin, well-channelled region at the surface separated from the amorphous layer near the O R_p by a damaged layer. The most significant change in defect structure appears in the 1.0 MeV Si-implanted sample. First, the width of the amorphous layer has increased, moving toward the surface ~0.3μm. Second, channelling measurements indicate a more gradual increase in defect density, as opposed to the sudden increase in all other samples at ~0.3μm. For the 100 keV Si-implanted samples, a level of intermediate damage between the well-channelled surface and the increased damage level at 0.3μm is apparent, especially at the higher dose of 6.5x10¹⁵ cm⁻². Finally, the 4.2 MeV Si implant has not altered the defect depth distribution, but has lowered the minimum channelling yield (χ_{min}) throughout the Si overlayer indicating reduced defect concentrations.



NOTE: The depth scale is $\sim 80 \text{ \AA}/\text{channel}$.

After annealing, even greater changes in the defect structure are evident. Figure 1(b) shows RBS/C spectra of the annealed, Si-implanted SIMOX material. In addition to the lowered χ_{\min} throughout the Si overlayer in all Si-implanted SIMOX samples, the height of the residual damage peak near the front Si/SiO₂ interface varies widely from sample to sample. The virgin SIMOX material indicates the presence of SiO₂ precipitates in the Si overlayer near the front Si/SiO₂ interface and the SiO₂ layer appears to have a band of trapped Si precipitates. The 4.2 MeV, 5×10^{16} Si/cm² sample is the most similar to the virgin material. The front Si/SiO₂ interface appears to have moved slightly towards the surface, indicative of the incorporation of more O or Si into the SiO₂ layer. Also, the band of Si precipitates (confirmed by XTEM) within the buried SiO₂ has widened. In both the 1.0 MeV and the 100 keV Si-implanted SIMOX samples, these Si precipitates are not apparent from RBS/C analysis. XTEM analysis on the 4.2 MeV Si-implanted SIMOX indicates the SiO₂ precipitate concentration in the Si overlayer near the front Si/SiO₂ interface is reduced, and the back Si/SiO₂ interface has greater planarity.

The 100 keV samples differed the most from the virgin material. The front Si/SiO₂ interface appears much more abrupt than in any of the other samples. The channelled RBS spectra indicates the presence of SiO₂ precipitates in the Si overlayer, but in smaller concentrations than were observed in the virgin SIMOX material. Compared with virgin SIMOX material, the lower dechannelling rate at the front Si/SiO₂ interface is indicative of a reduction and/or change in the nature of dechannelling centres. Further examination by XTEM showed twinning at the front Si/SiO₂ interface and a very low concentration of SiO₂ precipitates in the Si overlayer. In comparison, the back interface does not appear to have been affected by the shallow Si implant. The Si dose at 100 keV did not affect the damage peak height apparent in the RBS/C spectra.

The defect band created in the near-surface region by low energy Si irradiation before annealing in O-implanted Si attracts interstitial-type defects because of the available annihilation sites. When a sufficiently large number of interstitial type defects diffuse from the damage at the depth of the original O implant, the formation of secondary defects will be reduced. We saw that the SiO₂ precipitate concentration near the front Si/SiO₂ interface was reduced in the 100 keV Si-implanted SIMOX material and that there was no longer a band of Si within the buried SiO₂ layer. This is consistent with an enhanced diffusion of Si towards the surface caused by the low-energy Si implantation. Furthermore, the remaining Si precipitates in the SiO₂ are smaller in size indicating a lower concentration of trapped Si. Since it is clear the shallow implant reduced the damage level at

the front Si/SiO₂ interface, the defect production in the near-surface region must play an important role in the secondary defect reduction.

Still, the 100 keV, 2×10^{15} Si/cm² sample had approximately the same peak vacancy concentration at 0.15 μm as the 4.2 MeV, 5×10^{16} Si/cm² implant. This infers the 100 keV implant had ~25 times the defect production per ion at 0.15 μm. However, only the 100 keV Si implant resulted in reduced damage levels at the front interface. One possible explanation lies in the direction of the damage gradient created by the Si implants. The annihilation of defects (particularly in the huge concentrations of this study) is presumably more efficient at the surface rather than in the bulk. Therefore, a gradient causing an attraction towards the surface would be more desirable. The blocking effect of the SiO₂ layer (the diffusion coefficient of Si in SiO₂ is very small) once it has formed must also be considered. Even if the high-energy Si implant did attract interstitial type defects at the front Si/SiO₂ interface, the defects would be blocked by the SiO₂ layer. The energy of the Si implant will determine the direction of the damage gradient and consequently, where secondary defect reduction will take place.

Finally, we see that the previously amorphised Si region of the 1.0 MeV Si-implanted sample has epitaxially recrystallised over depths of 0.8 μm to 0.88 μm but that the formation of polySi is apparent at depths greater than 0.88 μm. Both RBS and XTEM show that the front Si/SiO₂ interface is also much more diffuse than in any of the other SIMOX samples. The increased width of the amorphous layer in unannealed SIMOX material after the 1 MeV versus the 4.2 MeV Si implant (which had the same peak vacancy concentration at 1.0 μm) is attributable to a different defect production per ion and dose rate effects. The 1.0 MeV implant succeeded in preventing the formation of a band of Si within the SiO₂ layer indicating that the damage sites created near the Si/SiO₂ interface did influence the distribution of Si in the oxide. Presumably, this damage created more nucleation sites which in turn promoted more homogeneous SiO₂ formation. However, the 1.0 MeV Si implant was only moderately successful in reducing the SiO₂ precipitate concentration within the Si overlayer. The use of a lower implant temperature during O implantation was more beneficial in keeping SiO₂ precipitate formation in the Si overlayer to a minimum.

CONCLUSION

It has been shown that pre-anneal Si irradiation in O-implanted Si can reduce secondary defect formation. Both the depth and amount of damage created are crucial to the success of the Si implantation. Low-energy Si implantation, which creates damage in the near-surface region and hence, a damage gradient towards the surface, attracts interstitial defects and annihilates them. A Si implant whose projected range is the same as the O Rp creates extra nucleation sites at the a/c interface which promotes homogenous SiO₂ formation. However, if the damage level at this depth is too high and the width of the amorphous layer is increased (as in our experiments), the quality of the front Si/SiO₂ interface will be degraded since solid phase epitaxy (SPE) is inhibited in O-rich Si. Consequently, random nucleation and growth (RNG) becomes the dominant recrystallisation mechanism [4,5] and polySi is formed which leads to very undesirable electrical characteristics in SIMOX material. Finally, the high-energy Si implant increased the incorporation of O and/or Si into the buried SiO₂ layer and reduced the SiO₂ precipitate density within the Si overlayer. Long range effects were also evident in that the back Si/SiO₂ interface was planarized.

REFERENCES

- 1) Zhong-lie Wang, Bo-xu Zhang, Qing-tai Zhao, Qi Li, L.R. Liefting, R.J. Schreutelkamp, and F.W. Saris, *J. Appl. Phys.* **71**, 3780 (1992).
- 2) W.X. Lu, Y.H. Qian, R.H. Tian, Z.L. Wang, R.J. Schreutelkamp, J.R. Liefting, and F.W. Saris, *Appl. Phys. Lett.* **55**, 1838 (1989).
- 3) S. Ellingboe and M.C. Ridgway, *Mater. Res. Soc. Symp. Proc.* 1992 *in press*.
- 4) E.F. Kennedy, L. Csepregi, J.W. Mayer, T.W. Sigmon, *J. Appl. Phys.* **48**, 4241 (1977).
- 5) G.L. Olson, J.A. Roth, *Mat. Sci. Rep.* **3**, 1 (1988).

^{14}N Depth profiles in Ti and Ti6Al4V nitrided by various methods, measured by Nuclear Reaction Analysis.

By

Ian Vickridge¹, Bill Trompeter¹ and Ian Brown²

Introduction

Titanium alloys have desirable mechanical properties for applications in many areas, but their surface properties, such as friction coefficient, hardness, and wear and corrosion resistance often need to be enhanced. This may be accomplished by forming a thin layer of titanium nitride on the surface, by such methods as thermal nitriding, Ion Beam Assisted Deposition (IBAD), sol-gel technology, or ion implantation. Ion Beam Analysis is assuming an increasing importance for characterising the composition of the outer few microns since it is the only technique that can rapidly yield quantitative concentration depth profiles of ^{14}N with minimal disruption of the analysed region.

IBA Methodology

Rutherford Backscattering Spectrometry (RBS) may be used to depth profile the outer micron of a nitrided metal with depth resolution of about $0.01\ \mu\text{m}$ [1] by measuring the reduction of the plateau height of the metal component of the spectrum, however often the composition at depths greater than $1\ \mu\text{m}$ is of interest. Nuclear Reaction Analysis (NRA) allows depth profiling to greater depths, at the expense of depth resolution. Previous work has applied the $^{14}\text{N}(d,p_{1+2})$ reaction [1]; $^{14}\text{N}(\alpha,\gamma)$ resonance profiling [2]; inelastic alpha scattering at 6 MeV incident energy [3]; and $^{14}\text{N}(d,\alpha_1)$ [4]. We have found the $^{14}\text{N}(d,\alpha_1)$ reaction to be ideal for depth profiling the outer few microns of nitrided Ti.

All measurements were made in the new Institute of Geological and Nuclear Sciences general purpose IBA chamber, on a new beamline from the 3MV KN Van de Graaff accelerator at Lower Hutt. The chamber is electrically isolated and is used as a Faraday cup for current integration. A $100\ \mu\text{m}$ $300\ \text{mm}^2$ partially depleted ruggedised silicon surface barrier detector at 150° is used with a $13\ \mu\text{m}$ mylar absorber in front of it. The mylar stops the high flux of elastically scattered deuterons, but allows the passage of the more energetic protons and alphas. Protons of energy less than 3 MeV, and alphas of energy less than about 12.5 MeV are fully stopped by the detector. After experiments with a pressed TiN powder target we chose an incident beam energy of 1400 keV since this exploits the wide and

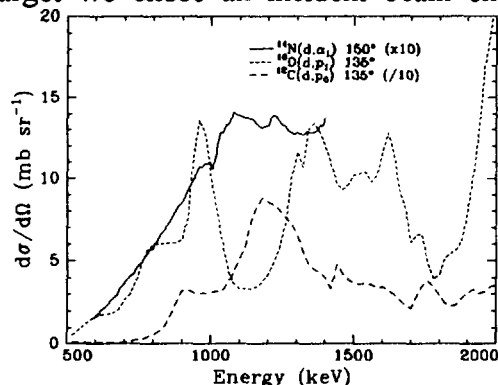


Figure 1 $^{14}\text{N}(d,\alpha_1)$ cross section taken from the literature. Also shown for comparison are $^{12}\text{C}(d,p_0)$, and $^{16}\text{O}(d,p)$.

relatively flat plateau in the $^{14}\text{N}(d,\alpha_1)$ cross section (figure 1). Our choice of incident beam energy was also dictated in part by the available cross section data. We used an uncollimated detector of 2 cm diameter, at a distance of 52 mm from the 1 to 2 mm diameter beam impact point on the target. Under these conditions, the depth resolution is limited to about $0.25\ \mu\text{m}$ by the kinematic spread of the alpha particles. We could use a slit collimator to improve the depth resolution at the expense of solid angle. We used $0.5\ \mu\text{s}$ shaping time in the main amplifier, and kept the beam current below 30 nA in order to avoid pileup from the high intensity proton groups

¹Institute of Geological and Nuclear Sciences Ltd, P.O. Box 31312, Lower Hutt, New Zealand

²Industrial Research Ltd, P.O. Box 31310, Lower Hutt, New Zealand

interfering with the α_1 group. In 4 to 5 minutes, 10 μC of incident charge gave about 2500 counts per 20 keV channel on the plateau of the α_1 spectrum from pure TiN. Such a spectrum is shown in figure 2.

We extracted the concentration depth profiles of nitrogen from these alpha spectra by using the simulation program SENRAS [5]. We used the cross sections of ref [6], furnished with SENRAS, and also available on the SigBase anonymous ftp sites [7], and then iteratively modified the assumed concentration profile until an acceptable comparison was obtained between the simulated and measured spectra. We have confirmed that the spectra from thick pure TiN targets are adequately simulated by this program (figure 2). Once the experimental parameters had been determined from the spectrum of pure TiN, the only adjustable parameter for fitting was the assumed concentration profile.

The protons from $^{12}\text{C}(d,p_0)$ and $^{16}\text{O}(d,p_1)$ may also be exploited to gain further information about the sample being analysed. In principle, they could also be used for depth profiling, so long as one knows the cross sections (and those of the numerous interfering proton groups from ^{14}N), however except on thin samples, we have used them in only a qualitative way to estimate whether oxygen and carbon in the samples are purely in the surface regions, or appear to be deep in the sample too. But these, and also the incompletely stopped p_0 and other peaks from ^{14}N contribute significantly to the count rate, and in the case of the $^{14}\text{N}_{p_{1+2}}$ peak also limit the explorable depth. It would be advantageous to be able to rid ourselves of these peaks (allowing higher beam currents without incurring significant pileup and dead time). One way of improving the explorable depth is to use a thinner depletion zone in the detector [8]. The depletion layer thickness of the detector may be adjusted by varying the applied bias until, say, the $^{14}\text{N}_{p_{1+2}}$ peaks are reduced in energy, but the α_0 peak remains well clear of the α_1 peak. This is demonstrated in figure 3, where the bias (full depletion at 100 volts) was reduced in steps right down to 5 volts. However the effect sought for is not as great as might at first be expected, since the p_{1+2} peak broadens as it moves down in energy. This is probably due to inhomogeneity in depletion layer thickness [8]. Our observations of the pulse shapes from the preamplifier, however, suggest that it may be possible to exploit the long rise time of pulses from incompletely stopped particles to eliminate them electronically from the spectrum.

Application to Thermal Nitrides

Our main results pertain to thermal nitrides, although some work has commenced on plasma nitriding, and on Ion Beam Assisted Deposition. Thermal nitriding was performed in flowing instrument grade nitrogen, further scrubbed with a commercial catalyst (BASF), at atmospheric pressure.

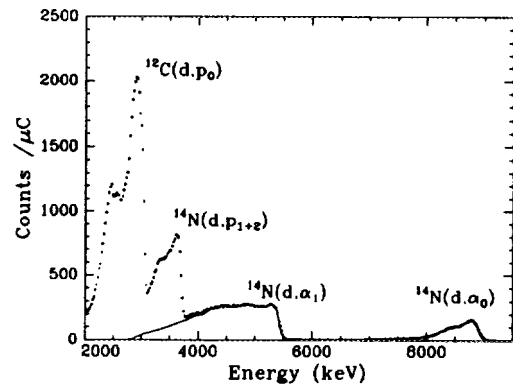


Figure 2 A typical charged particle spectrum from TiN. Solid line is a fit to the two alpha peaks, as described in the text.

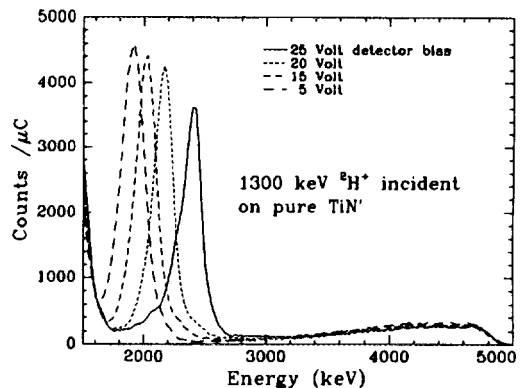


Figure 3 The $^{14}\text{N}(d,p_{1+2})$ peak is moved to lower energy by reducing the thickness of the depletion layer on the detector.

Nitridation at 850°C

The temperature 850°C is below the phase change in commercially pure (CP) titanium from the hexagonal close-packed (hcp) structure to the body centred cubic (bcc) form at 882°C. In figures 4 and 5, we show the particle spectra, the assumed nitrogen concentration profiles, and the simulated spectra corresponding to these profiles for the thermal nitriding of CP Ti, and for Ti6Al4V alloy. The obvious plateaux in these profiles correspond to a

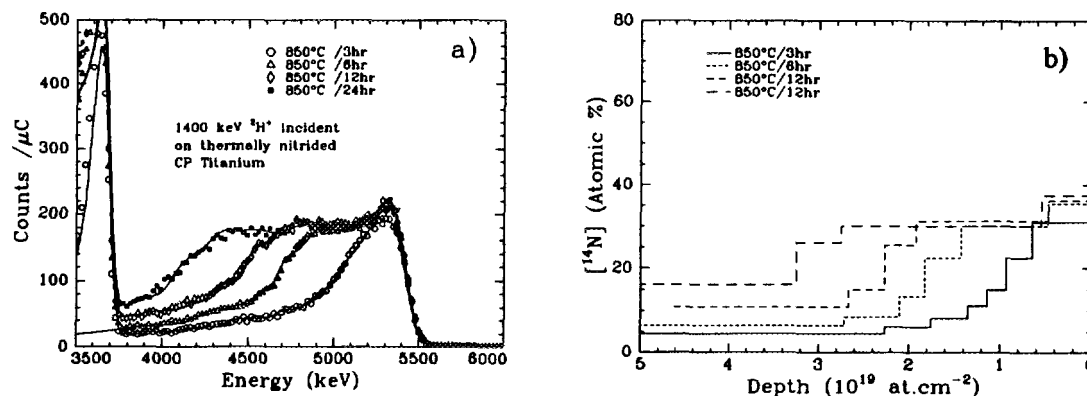


Figure 4 CP Ti nitrided at 850°C for varying durations. a) Measured α_1 energy spectra (points) and simulations (solid lines), assuming the concentration depth profiles shown in b).

composition of Ti_2N , and we observe slight enrichment at the surface. There is a significant difference between the nitrogen concentration profiles in the alloy and CP Ti. In the CP Ti, the

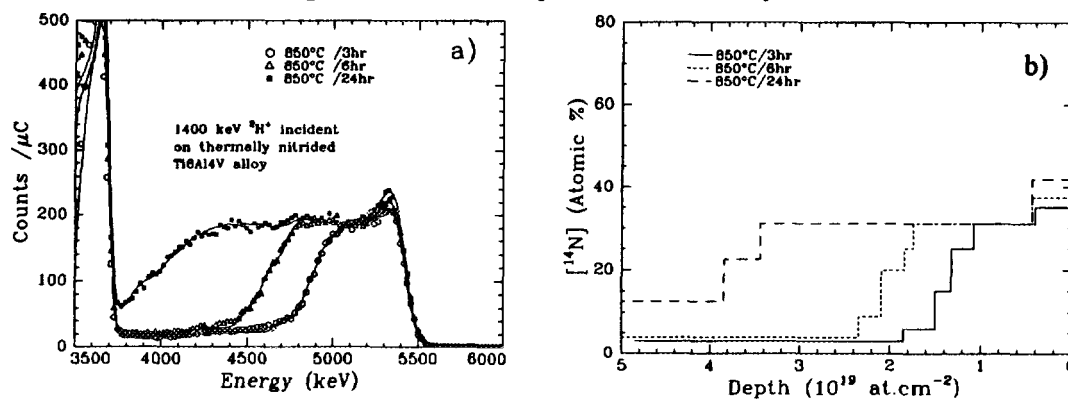


Figure 5 Ti6Al4V alloy nitrided at 850°C for varying durations. a) Measured α_1 energy spectra (points) and simulations (solid lines), assuming the concentration depth profiles shown in b).

nitrogen has a stronger deep diffusion tail than in the corresponding alloy case, suggesting a fast diffusion mechanism in CP Ti, possibly by grain boundaries, that is less active in the alloy. XRD of these samples shows no significant differences, and the most abundant phase in both cases is Ti_2N , highly oriented with respect to the surface, as has also been observed in glow-discharge nitrided samples [1]. A small amount of randomly oriented TiN is also observed.

Alloy behaviour above the 882°C hcp/bcc phase transition.

High temperature isochronal nitridation of the alloy has revealed a curious behaviour, in which nitrogen penetrates deeper at 1000°C than at 1100°C and 1200°C. At 1300°C the nitrogen once again penetrates deeply. The total nitrogen contents of the 1200°C and 1300°C films are very similar, although the depth distributions are markedly different. This anomalous behaviour is also observed in the XRD measurements, shown in figure 7. At 1000°C Ti_2N is observed, highly oriented with respect to the substrate, along with TiN. Above 1000°C, only TiN is observed. Although the plateau in the nitrogen profile of the 1200°C sample corresponds quite closely to a composition of Ti_2N , we do not see this as a crystalline phase

via XRD. Our working hypothesis to understand these results involves a nitrogen-rich phase (TiN, possibly superstoichiometric in nitrogen) on the surface, in which nitrogen has a low diffusion coefficient. At 1000°C, this phase is formed slowly, allowing nitrogen to traverse the

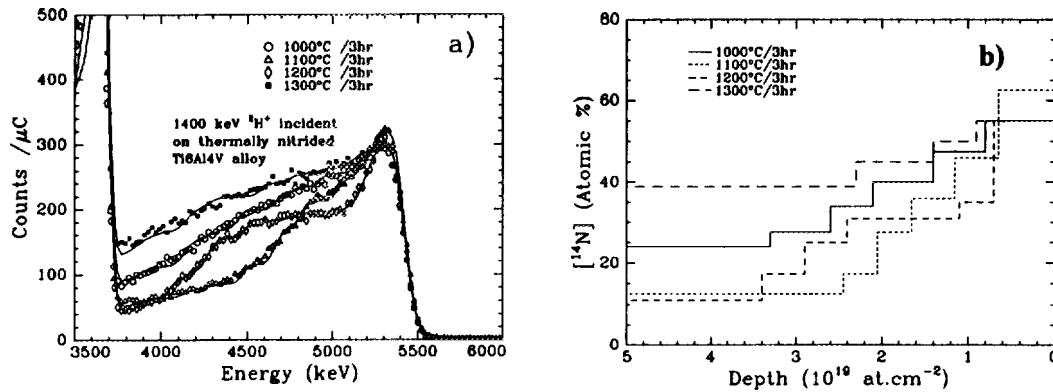


Figure 6 Ti6Al4V alloy thermally nitrated for 3hrs at various (high) temperatures. a) Measured α_1 energy spectra (points) and simulations (solid lines), assuming the concentration depth profiles shown in b).

surface region and diffuse into the substrate. At 1100°C this phase is formed much more quickly, and blocks the nitrogen flux through the surface region. At 1200°C, the nitrogen that has penetrated in the initial phases is redistributed with little further additional nitrogen

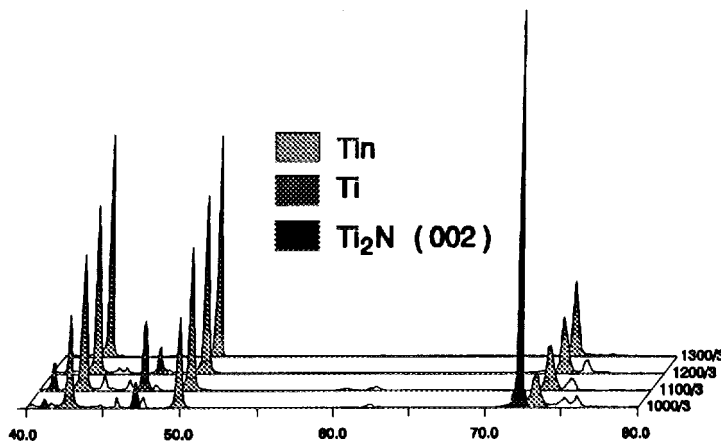


Figure 7 XRD pattern of the high temperature Ti6Al4V isochronal nitrides.

entering the system. By 1300°C the nitrogen can diffuse relatively freely once more through all of the phases. To improve our understanding of this system we could observe the concentration profiles for shorter nitridation times, use ^{15}N as an isotopic tracer, and observe the modification of existing nitrogen profiles after annealing in vacuum or inert gas.

References

- 1) Brading H.J., Morton P. H., Bell T. and Earwaker E. *The structure and Composition of Plasma Nitrided Coatings on Titanium*. Nucl. Instr. and Meth. B66 (1992) pp.230-236.
- 2) Gossett C.R. *Very high resolution profiling of nitrogen by the $^{14}\text{N}(\alpha,\gamma)^{18}\text{F}$ reaction*. Nucl. Instr. and Meth. B10/11 (1985) pp.722-726
- 3) Artigalas H., Chevarier A., Chevarier N., El Bouanani M., Gerlic E., Moncoffre N., Roux B., Stern M. and Tousset J. *Nitrogen profiling in nitride films and nitrogen-implanted samples using the $^{14}\text{N}(\alpha,\alpha)$ and $^{14}\text{N}(\alpha,p)$ reactions at 6 MeV incident energy*. Nucl. Instr. and Meth. B66 (1992) pp.237-241
- 4) Kenny M.J., Wielunski L.S., Tendys J. and Collins G.A. *A comparison of plasma immersion ion implantation with conventional ion implantation*. Nucl. Instr. and Meth. B80/81 (1993) pp.262-266.
- 5) Vizkelethy G. *Simulation and Evaluation of Nuclear Reaction Spectra*. Nucl. Instr. and Meth. B45 (1990) pp.1-5.
- 6) Amsel G. and David D. *La microanalyse de l'azote par l'observation directe de réactions nucléaires*. Revue de Physique Appliquée, 4(1969), 383
- 7) The SigBase is accessible via anonymous FTP to lhn.gns.cri.nz (IP 131.203.40.1) or to physics.isu.edu (IP 134.50.3.6). Further information is available by E-mail from srlnicv@lhn.gns.cri.nz (I.C. Vickridge), or from vizkel@physics.isu.edu (G. Vizkelethy).
- 8) Amsel G., Paszti F., Szilagy E. and Gyulai J. *p, d, and α particle discrimination in NRA: thin adjustable sensitive zone semiconductor detectors revisited*. Nucl. Instr. and Meth. B63 (1992) pp.421-433.



SURFACE MODIFICATION OF COMMERCIAL TiN COATINGS BY CARBON ION IMPLANTATION

L. J. LIU^{1,2}, D. K. SOOD¹ AND R. R. MANORY^{1,2}

Microelectronics & Materials Technology Centre¹, and Department of Chemical & Metallurgical Engineering², Royal Melbourne Institute of Technology, 124 LaTrobe Street, Melbourne, VIC 3000, AUSTRALIA

ABSTRACT

Commercial TiN coatings of about 2 μm thickness on high speed steel substrates were implanted at room temperature with 95 keV carbon ions at nominal doses between 1×10^{17} - 8×10^{17} ions cm^{-2} . Carbon ion implantation induced a significant improvement in ultra-microhardness, friction coefficient and wear properties. The surface microhardness increases monotonically by up to 115% until a critical dose ϕ_{crit} is reached. Beyond this dose the hardness decreases, but remains higher than that of unimplanted sample. A lower friction coefficient and a longer transition period towards a steady state condition were obtained by carbon ion implantation. The changes in tribomechanical properties are discussed in terms of radiation damage and possible formation of a second phase rich in carbon.

INTRODUCTION

In recent years, more interest has been directed towards possibility of using ion beam techniques to modify TiN hard coatings [1-4]. Our previous work [4] shows that argon ion implanted TiN produces improvements in hardness, friction, wear and apparent adhesion at all doses. Roos *et al.* [2] observed a low friction coefficient during break-in corresponding to a lower fretting wear damage related to the carbon ion implantation. They reported that part of the implanted carbon had diffused out from the gaussian-like distribution towards the surface. Until now however, a complete understanding of the dominating mechanism has not been achieved despite extensive studies in this area. In this work, we investigate the effect of ion damage and report tribomechanical properties of TiN after carbon ion implantation.

EXPERIMENTAL PROCEDURE

About 2 μm thick TiN films were deposited on high speed steel substrate by PVD method using a Balzers evaporation process. Carbon ion implantation was performed at room temperature using 95 keV energy and with nominal doses of 1, 3, 5 and 8×10^{17} ions cm^{-2} . Hardness measurements were carried out using a UMIS-2000 apparatus with a Berkovitch pyramid of 0.2 μm tip radius. Friction and wear tests were made using a pin-on-disc machine (CSEM Tribometer) with a 3 mm sapphire ball sliding on the sample under a load of 1 N. The sliding velocity was kept constant at 0.1256 m s^{-1} , while the test was carried on till 25,000 cycles. The friction coefficient and wear measurements were performed under the ambient of air at 51% relative humidity and the temperature of 22°C. The wear tracks were analysed using a Tencor Alphastep-250 instrument. The influences of carbon implantation were confirmed using Rutherford back scattering (RBS). RBS was performed in RMIT using 2 MeV He^+ at a scattering angle of 110°.

RESULTS AND DISCUSSION

The ultra-low load microhardness indentation technique was used to study the mechanical

properties in the near-surface region of TiN coatings. The results of microhardness (measured at plastic penetration region ~ 100 nm) as a function of ion dose show an increase by 40% to 115% after ion implantation (Fig. 1). Two hardness regimes are observed as the implantation dose is increased. In region I, the hardness increases monotonically with increasing dose. Above a critical dose ϕ_{crit} , the hardness starts to decrease, but still remains higher than the original unimplanted surface (region II). This may be explained by the formation of an amorphous region as a sub-surface zone enclosed within the crystalline but damaged substrate. This hardening behaviour as a function of dose appears to be consistent with the model proposed by Burnett and Page [5]. The increase in hardness in region I can be explained as radiation hardening: two major classes of defect (the implanted ions themselves and radiation damage *e.g.* interstitial/vacancy pairs) are introduced to hinder dislocation motion. The decrease in hardness in region II from the maximum level observed at lower dose can be explained by two possible mechanisms. One explanation is that the effect is similar to the decrease in hardness observed in the late stages of precipitation hardening, *i.e.*, the increased dose causes growth of second phase (non-coherent) precipitates. Another possible explanation involves radiation damage, the level of which rises as a result of displacements occurring in response to "knock-on" collisions, which result in the formation of displacement spikes whose cores may be amorphous. Each such spike will behave like a small second-phase particle in an otherwise damaged matrix and interact with dislocations [6]. According to this model the two mechanisms co-exist and complement each other.

Friction and wear measurements revealed remarkable differences between the unimplanted and ion implanted TiN (Fig. 2). Three characteristic stages can be seen from unimplanted sample (Fig. 2a): A running-in period in the first stage where the wear rate is very high and the friction also changes rapidly due to a flat formation on the sapphire ball. In the second stage, the wear rate is relatively small because of the changes in contact area; After 7,200 cycles (136 m) the wear process reaches the third stage, a steady state regime. In contrast to the steep running-in transition for unimplanted TiN, the sample implanted at the lower dose (Fig. 2b) has a running-in period extended over a larger number of cycles (about 3,000) and shows a lower friction coefficient value of 0.5. For the highest dose sample, the running-in transition generating wear debris was delayed and extended to 16,000 cycles, showing very low friction coefficient of 0.2. The modified behaviour is most probably due to the carbon over-layer and the transition occurs after the over-layer start removing [2]. Wear measurements taken after 25,000 cycles under identical conditions show that after implantation the wear was reduced to 25% of the unimplanted value (data not shown here). This measurement is consistent with the friction data shown above.

The shift to lower energy of titanium edge from carbon implanted sample can be seen from RBS spectra in Fig. 3. It revealed that the TiN surface is covered with carbon or stabilised hydrocarbon layer as also suggested by Roos *et al.* [2] under totally different conditions. RUMP simulation shows that an ultra-thin carbon layer of about 80 Å is present on the surface and that part of the implanted carbon has diffused from the Gaussian-like profile towards the carbon-covered surface, forming a diffusion tail that extends from the depth of implanted layer to the surface layer, so the high ability of wear resistance can be partly attributed to this top-layer formation. The carbon atoms contained at the region concentrated as a Gaussian-like profile make the implantation region amorphous, these make the TiN surface hardening as mentioned above. In Fig. 3, the spectrum of implanted sample shows much higher signal at channel 120. RUMP simulation indicated that it is the overlap of substrate and TiN, and some mixed layers existed between them. That means ion bombardment made TiN film thin (about 1.8 μm).

SUMMARY

In conclusion, these results indicate that carbon implantation into TiN leads to an overall improvement in tribological properties which is manifest in an increase in hardness by up to 115%, a lower friction coefficient and a longer transition towards a steady state condition. These improvements are due to the radiation damage and amorphous layer (second-phase) formation. The presence of a carbon over-layer (80Å thickness) and the carbon distribution were also shown to influence the wear behaviour.

REFERENCES

1. M. Braun, *Nucl. Instr. Meth.*, **B59** (1991) 914.
2. J.R. Roos, J.P. Celis and M. Franck, *Surf. Coat. Technol.*, **45** (1991) 89.
3. A.V. Kulkarni, N. Mate, S.M. Kanetkar and S.B. Ogale, *Surf. Coat. Technol.*, **54/55** (1992) 508.
4. L.J. Liu, W. Zhou, D.K. Sood and R.R. Manory, *MRS Symposia Proceedings*, Vol. **279**, (1993) (in press).
5. P.J. Burnett and T.F. Page, *Radiation Effects*, **97** (1986) 123.
6. L.A. Christel, J.F. Gibbons and T.W. Sigmon, *J. Appl. Phys.*, **52** (1981) 7143.

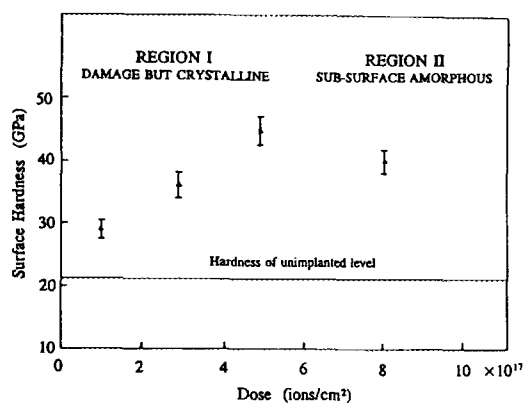


Fig. 1 Surface hardness vs dose of carbon ion implantation.

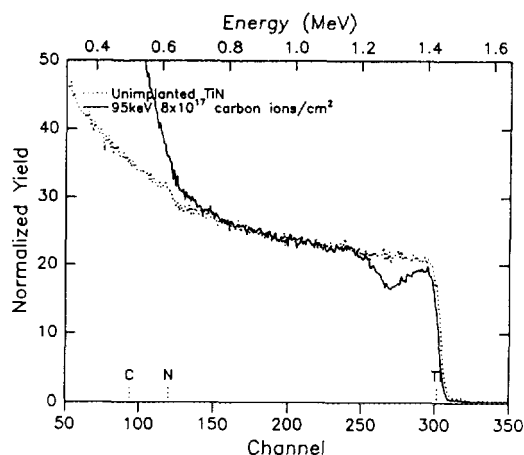


Fig. 3 RBS spectra measured on a carbon ion implanted TiN (8×10^{17} ions cm^{-2}) and the unimplanted TiN.

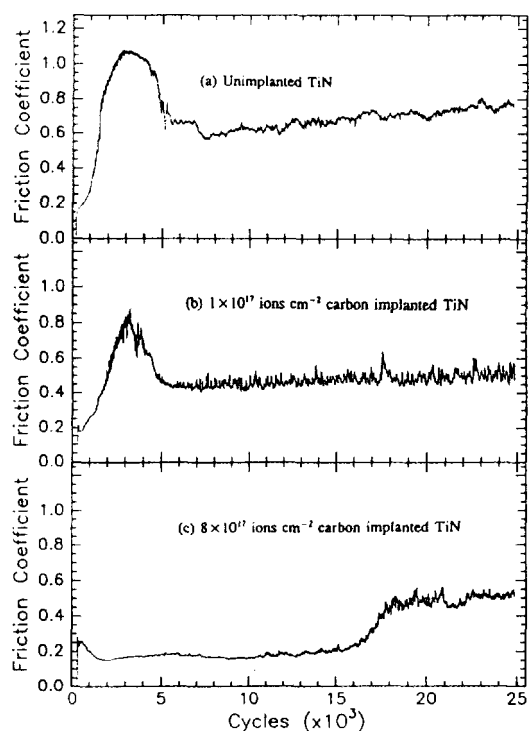


Fig. 2 Friction coefficient vs number of cycles in pin-on-disc tests.



STUDY OF CuAl(100) BY USING He ION SCATTERING

L. Zhu, E. Zur Muhlen, and D.J.O'Connor
DEPARTMENT OF PHYSICS, UNIVERSITY OF NEWCASTLE
N.S.W. 2308

ABSTRACT

The clean CuAl(100) surface has been investigated by using He⁺ ion scattering. The polar scans show that Al atoms randomly replace the Cu atoms but sit (0.15 ± 0.05) Å higher than the Cu atoms. The outmost layer concentration of Al is about $(17 \pm 3)\%$. The Al concentration on the outmost layer is sensitive to the sample temperature up to 300°C.

INTRODUCTION

The \bar{A} -phase CuAl alloy has been recently investigated by using AES and XPS to study the clean surface and oxygen adsorption [1]. In this work, He ion scattering is used to study clean CuAl(100) with the advantage of its outmost layer sensitivity for the determination of surface structure and composition .

EXPERIMENTAL

The experimental setup is a Leybold-Heraeus UHV system equipped with an electrostatic energy analyser. The base pressure of the system is better than 1×10^{-10} mbar. A He⁺ beam was produced by a low energy (0.1-10keV) accelerator equipped with a Colutron ion source. The CuAl(100) sample was supplied by A. Hoffman from the Technion Institute and was checked with X-ray diffraction which showed that the difference between the surface normal and the <100> direction is less than 0.5°. The clean and ordered surface was obtained after several treatments of 2keV Ar⁺ sputtering and annealing at 300°C.

RESULTS AND DISCUSSION

The azimuthal scan at an incident angle of 7° to the surface in fig.1 clearly shows shadowing in the <011>, <001> and <013> directions. An increase in the Al intensity along the <011> direction might result from the buckling of the Al atoms on the surface or wedge focusing. This intensity enhancement changes with the incident angle. Fig.2 and fig.3 are polar scans for 2keV He⁺ scattering at an angle of 135° in the <011> and <010> directions. The Cu critical angle is in good agreement with the calculation using a ZBL potential [2]. Different critical angles

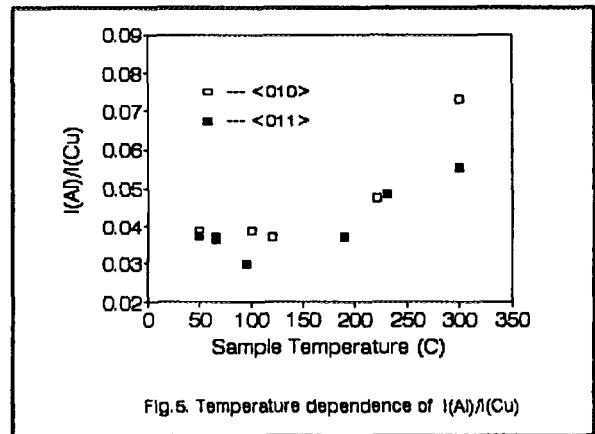
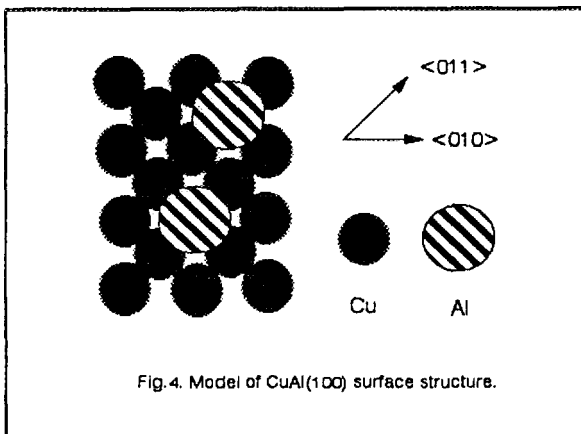
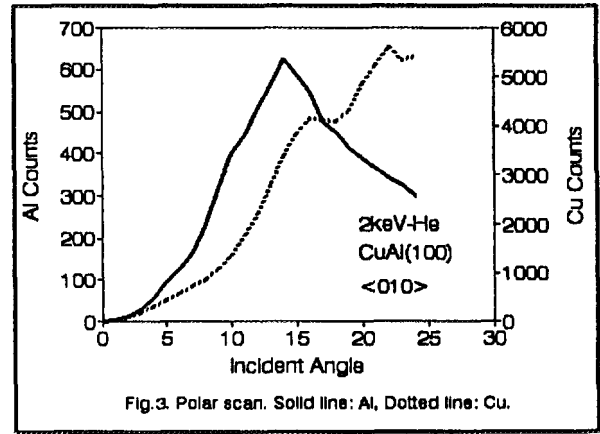
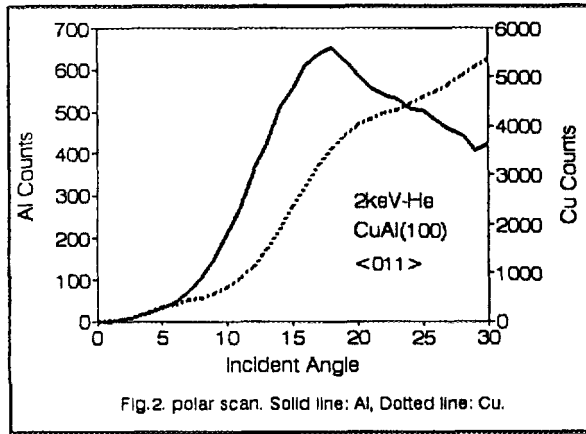
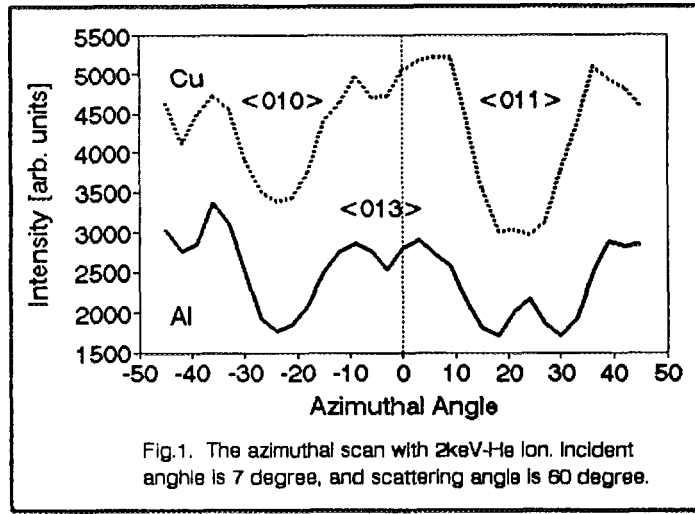
for Cu and Al were obtained, which correspond Al ditting $0.15 \pm 0.05 \text{ \AA}$ above the Cu position. Similar polar scans have obtained for the beam energy of 2.4keV. The surface structure model for the clean CuAl(100) is proposed in fig.4, in which the Al atoms randomly replace Cu atoms instead of forming islands. Several experiment results do not support the possibility of Al island formation. Similar buckling has been observed on NiAl(110) [3] and $\text{Fe}_3\text{Al}(100)$ [4].

The outmost layer composition of the clean surface at room temperature was investigated under different experimental conditions. It was found to be $17 \pm 3\%$ Al which is almost the same as the Al bulk composition (18%). The composition was not sensitive to the scattering geometries and beam energies in the range 1-2keV. The experimental results are in good agreement with the calculation based on Haff's model [5]. The small surface energy difference between pure Al (316 mJ/m^2) and pure Cu (323 mJ/m^2) may suggest a weak segregation of Al on the surface.

The temperature dependence of the ratio of the intensities of the signal from Cu and Al $I(\text{Cu})/I(\text{Al})$ is shown in fig.5. Al segregates when the sample is heated above 200°C . Up to 200°C , the ISS intensity ratio of Al to Cu seems to be constant. A energy barrier for the Al segregation may exist on this surface. According to the Gibbsian theory [6], Al will segregate at higher temperatures. The entropy and enthalpy of Al in this process is determined to be $0.453k$ and $0.049 \pm 0.004 \text{ eV}$ respectively where k is the Boltzmann constant. The enthalpy is very close to the thermal energy (0.041 eV) corresponding to the temperature 200°C , at which $I(\text{Al})/I(\text{Cu})$ starts to increase. Similar results have been obtained by using the radiation-induced segregation theory [7].

REFERENCES

- [1] A. Hoffman, T. Maniv and M. Folman, Surf. Sci. 193 (1988) 57.
- [2] J.F. Zeigler, J.P. Biersack and U. Littmark, The Stopping and Range of Ions in Solids, Vol. 1 (Pergamon, Newyork, 1985)
- [3] H.L. Davis and J.R. Noonan, Phys. Rev. Lett. 54 (1985) 566.
- [4] D. Voges, Diploma thesis.
- [5] P.L. Haff. Appl. Phys. Lett. 31 (1977) 259
- [6] N.Q. Lam and H.A. Hoff, Surf. Sci. 193 (1988) 353
- [7] H. Wiedersich, P.R. Okamoto and N.Q.Lam, J. Nucl. Mater. 83 (1979) 98.





LASER SPUTTER NEUTRAL MASS SPECTROMETRY

B.V. King, M. Clarke, H. Hu and G. Betz*

Department of Physics, University of Newcastle, Callaghan 2308

* Permanent address : Institut für Allgemeine Physik, Technische Universität Wien, A-1040 Wien, Austria

Laser sputter neutral mass spectrometry (LSNMS) is an emerging technique for highly sensitive surface analysis. In this technique a target is bombarded with a pulsed beam of keV ions. The sputtered particles are intercepted by a high intensity pulsed laser beam above the surface and ionised with almost 100% efficiency. The photoions may then be mass analysed using a quadrupole or, more commonly, using time of flight (TOF) techniques. In this method photoions are extracted from the ionisation region, accelerated to a known energy E_0 and strike a channelplate detector a distance d away (figure 1). The flight time t of the photoions is then related to their mass by $d = \sqrt{m} / \sqrt{2E_0}$, so measurement of t allows mass spectra to be obtained.

LSNMS is capable of achieving very high sensitivities, due to the high ionisation efficiency. The useful yield, defined as the ratio of the number of atoms detected to those sputtered, may approach 0.1 allowing quantitative analysis of sub ppm concentrations in the top monolayer of a surface. Typically two or more photons are required to ionise a ground state atom or molecule. For example, KrF (248nm) excimer lasers produce photon energies of 5eV. Two photons are then required to ionise Fe (IP 7.9eV) but 3 photons are required to ionise Xe (IP 12.1eV). LSNMS may be performed in two modes. In resonant LSNMS, one or more dye laser photons are used to excite atoms through long lived excited states to the ionisation continuum. Only moderate intensities are required (10^5Wcm^{-2}) so the laser can be defocussed to produce large ionisation volumes. In addition the laser ionisation is species selective so no subsequent mass analysis is required. Very high useful yields and therefore high sensitivities may then be obtained. For example, a detection limit of 9ppt has been found for ^{113}In in Si using 2 colour resonant ionisation [1].

In nonresonant LSNMS [2], sputtered particles are excited through virtual states in a multiphoton process. Much higher laser intensities are required to saturate ionisation, typically 10^{10}Wcm^{-2} , but all elements may be simultaneously ionised. To achieve the higher power densities, the laser must be more tightly focussed, resulting in lower ionisation volumes. Subsequent mass analysis of the photoions is also required, lowering the useful yield of NRLSNMS to about 10^{-3} . This value is comparable to the useful yield of secondary ion mass spectrometry (SIMS). SIMS signals are however dominated by the variation of at least 3 orders of magnitude in the secondary ion yield. Quantitation is therefore difficult in SIMS unless dilute impurities are profiled and calibration samples are available using the same matrix. In contrast, relative elemental sensitivities (RES) determined using NRLSNMS are much more uniform. For example, RES for Fe, Cr, Co, and Ni are independent of matrix composition to within 20% [3]. A major factor in the deviation of RES from one element to another is the contribution of photodissociated molecules to the observed atomic ion signal. Typically, 10% of the particles sputtered from a surface are molecules. The photoionisation cross-sections for molecules are however typically much higher than for atoms, because they have a higher density of

excited levels and so quasi-resonant excitation through such levels is much more likely. Fragmentation of the molecular ions is also likely at the high power levels used for NRLSNMS [4], so that the observed atomic photoion signal, e.g. Ni^+ may be entirely due to dissociation of photoionised molecules.

The LSNMS instrument at Newcastle uses the frequency tripled output (355nm, 3.5eV photon energy) of a Spectra Physics GCR5 35W Nd:YAG laser to pump a dye laser to produce tunable UV photons for RLSNMS. The 3.5eV photons may also be directly used for NRLSNMS. The laser beam is transported into a UHV vacuum system which includes a pulsed ion source and TOF analyser. Typically 33mJ pulses of 355nm laser light are focussed to a diameter of 0.25mm, 5mm above the target, resulting in a peak intensity of 10^{10}Wcm^{-2} . The sample is bombarded with 0.5 μs pulses of 0.2 μA 4keV Ar^+ . The ions are pulsed at the same rate as the laser, 30Hz, but the laser pulse is delayed by 14 μs to allow for the primary ion flight time (12.5 μs) and the sputtered neutral flight time from the sample surface to the ionisation volume (1.5 μs). The resultant TOF spectra (figure 2) contains peaks due to laser desorption and ion sputtering as well as true LSNMS peaks. The peaks may be distinguished by changing the delay between the ion and laser pulses - the peaks due to the ion beam alone will be shifted in time whereas the LSNMS peaks will only change in magnitude due to the different part of the sputtered neutral energy distribution probed by the ionising photon beam. This effect may be used to plot out time of flight spectra for sputtered particles, enabling their origin (sputtered atoms or molecules) to be determined. For example, the flight time from the sample surface to the ionisation volume of the species which produces Zr^+ under laser postionisation, can be well modelled by assuming that Zr is being sputtered as an atom rather than as a molecule (figure 3). If the laser ionised signal is due to sputtered atoms the energy spectrum of the sputtered species should follow a Thompson distribution with a E^{-2} decrease at high energy. This is indeed found for the Zr^+ signal.

In conclusion, LSNMS is an emerging technique of great sensitivity and flexibility, useful for both applied analysis and to investigate basic sputtering processes.

- [1] D.L. Pappas, D.M. Hrubowchak, M.H. Ervin, N. Winograd, *Science* 243 (1989) 64.
 [2] C.H. Becker and K.T. Gillen, *Anal.Chem.* 56 (1984) 1671.
 [3] G. Kampwerth, M. Terhorst, E. Niehuis, A. Benninghoven, *Proc. SIMS VIII*, eds A. Benninghoven, K.T.F. Janssen, J. Tumpner and H.W. Werner (J. Wiley, Chichester 1992) 563
 [4] J.B. Pallix, U Schuhle, C.H. Becker, D.L. Huestis, *Anal.Chem.* 61 (1989) 805.

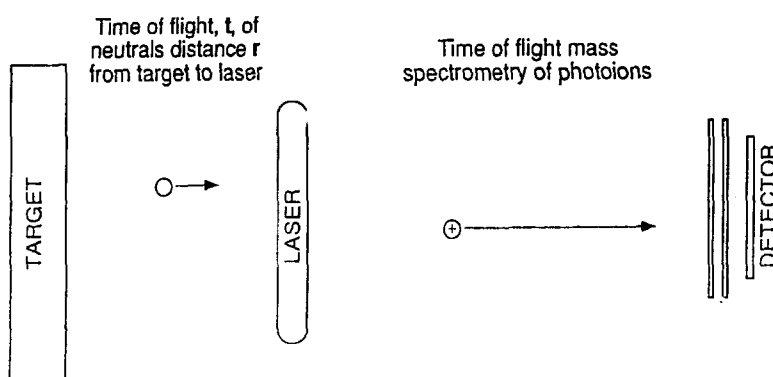


Figure 1 Schematic diagram of a LSNMS experiment.

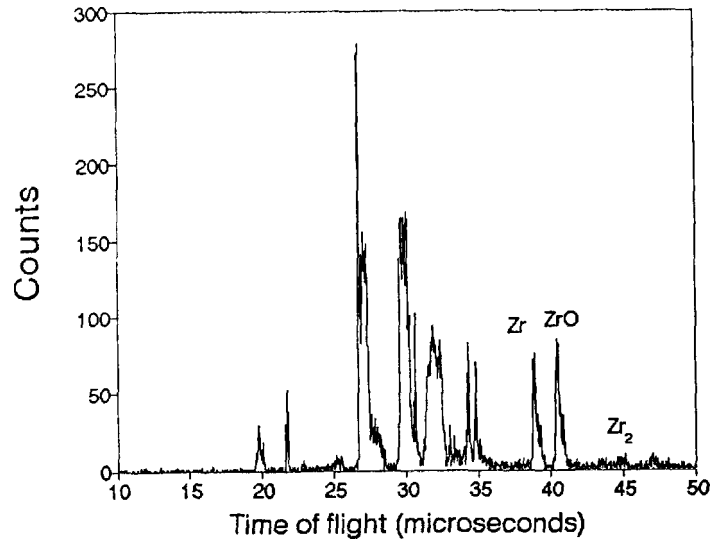


Figure 2 LSNMS TOF spectrum for Zr irradiated with 180pC 4keV Ar⁺. The peaks at flight times of 39 μ s and 45 μ s correspond to postionised Zr and Zr₂ respectively.

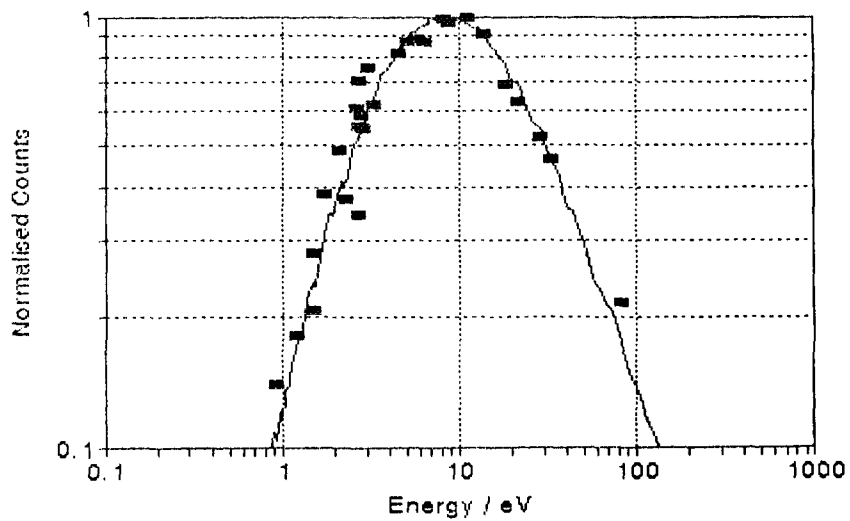


Figure 3 Energy spectrum of laser ionised Zr⁺ (squares) compared to that expected from the Thompson distribution for sputtered Zr atoms (line).

ION BEAM MIXING OF ISOTOPIC METAL BILAYERS

C J Fell,

Dept. of Physics, University of Newcastle, Callaghan, 2308

M J Kenny,

CSIRO Div. of Applied Physics, Lindfield, 2070

Since the 1960's the use of ion beams for modification of materials has had ever growing industrial applications, from the miniaturisation of electronic devices to corrosion and wear resistance. Studies of irradiation induced atomic relocation at interfaces (ion beam mixing) can elucidate the basic principles upon which this technology is based, as well as contributing to the general understanding of ion-solid interactions. These experiments usually examine the extent to which an interface or marker layer is broadened (magnitude of mixing) and how this magnitude depends on physical, mechanical, thermal and electronic properties of the target, as well as on different ion beam parameters.

The collision cascade leads to atomic mixing via ballistic relocation, followed by a 'thermal spike' in which chemical properties of the target play an important role. The variation of mixing magnitude with target properties such as cohesive energy and heat of mixing has been widely documented eg. [1]. A phenomenological model exists which attempts to predict the amount of mixing, taking into account these chemical driving forces [2]. In order to obtain a more fundamental insight into the mechanisms of ion-solid interactions, bilayer targets can be prepared from two different single isotopes. Mixed atoms thus remain identifiable by mass, but experience no chemical interactions with surrounding atoms. Isotopic bilayers also simplify depth profile analysis by Secondary Ion Mass Spectrometry, due to similar sputter yields and ion yields for the two components.

A mixing study using SIMS is to be carried out using specially grown monocrystalline bilayers of ^{58}Ni / ^{60}Ni . Good crystallinity of the layers is essential to eliminate grain boundary diffusion as well as sputter-induced roughness, which is caused by grain structure and degrades SIMS depth resolution. SIMS results will then reveal the inherent depth resolution of the sputter profiling technique, which is limited by atomic mixing effects. Further experiments will involve SIMS analysis of pre-implanted targets, examining the variation of mixing magnitude with implantation conditions such as dose, dose rate and target

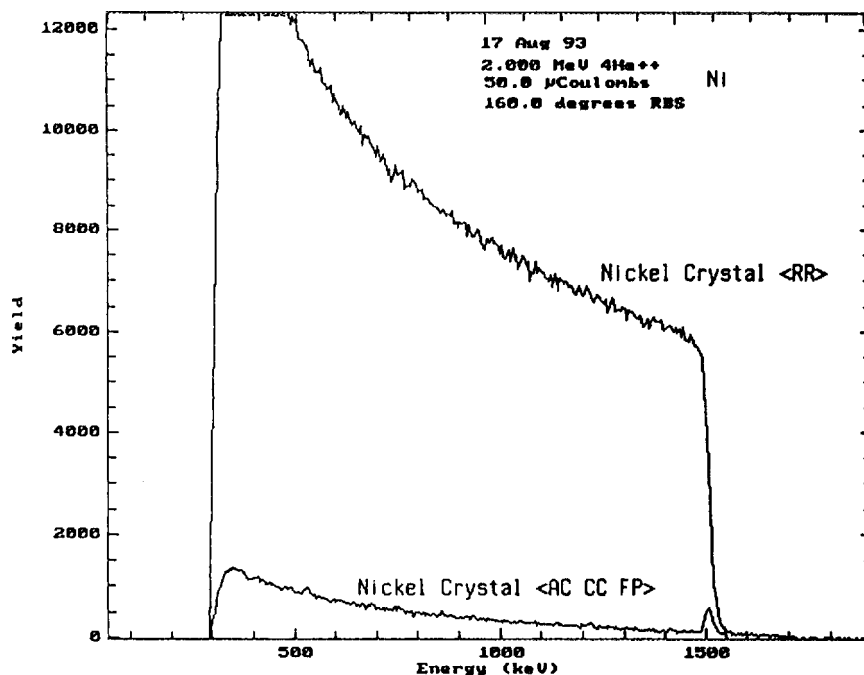
temperature. Variations of mixing magnitude with target temperature offer important information about atomic transport mechanisms. eg. if diffusion is limited by defect recombination at clusters or sinks then the dissolution of these features should result in a variation in mixing at a well defined temperature [3]. Experiments at low temperatures can yield information about mixing in the absence of radiation enhanced diffusion, providing an even more fundamental view of the effect of the collision cascade.

Recent reports [4,5,6] describe mixing as strongly dependent on the cooling rate of the collision cascade and that this in turn depends on the rate at which heat is transferred from the lattice to the electronic system. In particular, Koponen and Hautala [4] predict considerably less mixing in Ni, Pd and Pt as compared with Cu, Ag and Au respectively, due to a stronger electron-phonon coupling in each of the former and hence greater cascade cooling rates. Results of the intended work on Ni will thus be compared with published results for Cu [7,8]. The study will then be repeated using $^{106}\text{Pd} / ^{108}\text{Pd}$ bilayer targets, with these results being comparable with published results for Ag [9].

An important aspect of the work is the preparation of high quality single-crystal thin films. The Ni layers will be grown on the (110) surface of pure Ni and verified for crystallinity using Reflection High-Energy Electron Diffraction and Rutherford Backscattering channelling analysis. The Pd bilayers will be grown on a Pd (100) surface. RHEED will be used to confirm the two-dimensional crystallinity of the surface before and after deposition of each layer, and channelling used to confirm bulk film crystallinity.

Single crystal substrates are currently being prepared. Analysis of the Ni (110) surface using RHEED at 9 kV shows a streak spacing which corresponds to a lattice spacing of $2.47 \pm 0.09 \text{ \AA}$. This value is consistent with an unreconstructed Ni surface along the $\langle \bar{1}10 \rangle$ direction, which has a row spacing of 2.49 \AA . Results of channelling analysis on a Ni (110) substrate using 2 MeV $^4\text{He}^{++}$ shows a χ_{min} value of 0.027, which agrees with the theoretically attainable value of 0.020.

CSIRO Ion Beam Technology HIAF



RBS spectrum for 2 MeV ${}^4\text{He}^{++}$ along $\langle 110 \rangle$ channel for Ni
Rotating random spectrum is included for comparison

References:

- [1] Y.-T. Cheng, M. van Rossum, M.-A. Nicolet, W.L. Johnson. *App. Phys. Lett.* **45** (1984) 185
- [2] W.L. Johnson, Y.-T. Cheng, M. van Rossum, M.-A. Nicolet. *Nucl. Inst. Meth.* **B7/8** (1985) 657
- [3] Y.-T. Cheng. *Mat. Sci. Reports* **5(2)** (1990) 45
- [4] I. Koponen, M. Hautala. *Nucl. Inst. Meth.* **B69** (1992) 182
- [5] C.P. Flynn, R.S. Averback. *Phys. Rev.* **B38** (1988) 7118
- [6] M.W. Finnis, P. Agnew, A.J.E. Foreman. *Phys. Rev.* **B44** (1991) 567
- [7] R.S. Averback, D. Peak, L.J. Thompson. *App. Phys.* **A39** (1986) 59
- [8] B.M. Paine, R.S. Averback. *Nucl. Inst. Meth.* **B7/8** (1985) 666
- [9] B.V. King, R.P. Webb. *SIMS VIII*. eds. A. Benninghoven, K.T.F. Janssen, J. Tumpner, H.W. Werner. Wiley (1992) 363

Surface Studies by Low Energy Ion Beams: Cu/Ru(0001) and Cu/O/Ru(0001)

Y.G. Shen¹, D.J. O'Connor¹, K. Wandelt², H. van Zee³ and R.J. MacDonald¹

¹ Department of Physics, University of Newcastle, New South Wales 2308, Australia

² Institut für, Physikalische und Theoretische Chemie der Universität Bonn, Wegelerstrasse 12, D-5300 Bonn 1, Germany

³ Department of Physics, Eindhoven University of Technology, 5600 MB Eindhoven, The Netherlands

The surface structure of Cu on Ru(0001) has been studied by low energy Li⁺ ion scattering. It was found that Cu forms pseudomorphic islands for two layers. The effects of Cu on an O-precovered Ru(0001) surface has also been investigated using keV He⁺ ions. The results show that during the deposition of Cu, O is displaced from the Ru surface and migrated onto the top of the surface of the growing overlayer. The floated out O has been tested, showing a disordered overlayer.

1. Introduction

In recent years there has been a growing interest in the properties of bimetallic and alloy surfaces due to the fundamental importance of these systems in both heterogeneous catalysis and materials science. A typical example is the growth of Cu on the close-packed hexagonal Ru(0001) surface, for which it was shown that Cu grows on the Ru(0001) surface forming pseudomorphic films up to two layers [1]. Further growth forms a Cu(111)-like structure, which can be confirmed up to many layers [2]. It has been also known that there exists a continuous displacement of the oxygen to the surface during Cu deposition on Ru(0001) for a wide range of experimental conditions [3].

In this study, low energy ion scattering (LEIS) techniques were used to investigate the surface structure of Cu on Ru(0001) and the growth mechanism of Cu on an O-precovered Ru(0001) surface.

2. Experimental

The experimental apparatus used in this study has been described in detail previously [4]. High purity Cu was evaporated onto the Ru(0001) surface from a Cu basket melted to a W wire. The source was carefully outgassed prior to Cu evaporation. The deposition rate was controlled by the voltage difference across the W filament. By joint use of Li⁺ and He⁺ ion scattering we established the relationship between the voltage difference, the time of deposition and the Cu coverage. The Ru(0001) surface was cleaned by using a standard procedure [5].

3. Li⁺ scattering from clean Ru(0001) and Cu(111)

The intensities of 1 keV Li⁺ ions scattered off clean Ru(0001) and Cu(111) surfaces as a function of incident angle α are shown in fig. 1. The typical incident angle dependences were taken along two different orientations at a scattering angle of $\Theta = 130^\circ$. The most important feature in fig. 1 is that there are three shadowing edges ($\alpha_c = 15^\circ, 29^\circ$ and 74°) for the $[\bar{1}2\bar{1}]$ azimuth in Cu(111), while there are four shadowing edges ($\alpha_c = 15^\circ, 29^\circ, 54^\circ$ and 74°) along the $[10\bar{1}0]$ azimuth in Ru(0001). Similarly, there are two critical angles ($\alpha_c = 15^\circ$ and 53°) for the $[11\bar{2}]$ azimuth in Cu(111), while there are three critical angles ($\alpha_c = 15^\circ, 54^\circ$ and 74°) along the $[\bar{1}010]$ azimuth in Ru(0001). The critical angles for Ru and Cu patterns in Fig. 1 reflect directly the position of atoms in the first, second, and possible third layers. These features are consistent with the structures and expected differences between hcp (0001) and fcc (111) surfaces.

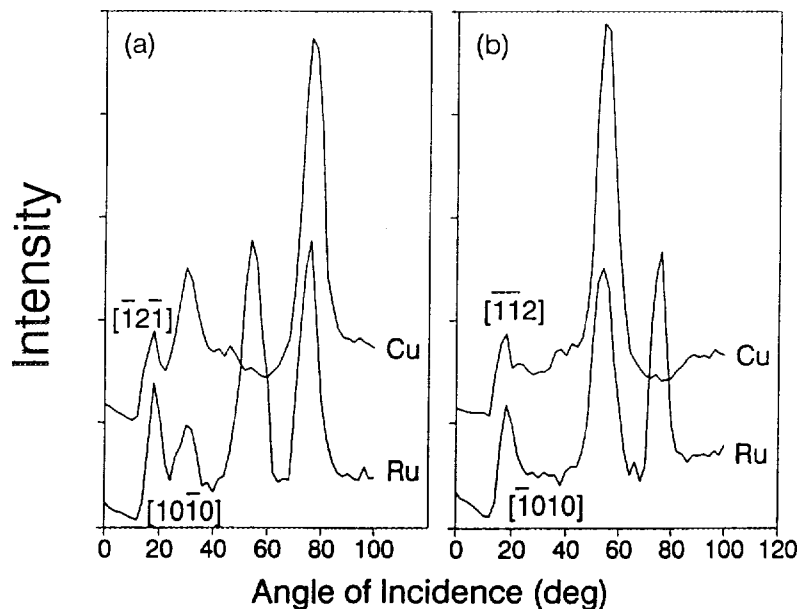


Fig. 1 Intensities of 1 keV Li^+ ions scattered from clean Ru(0001) and Cu(111) as a function of incident angle α at a scattering angle of $\Theta = 130^\circ$ along two different azimuthal orientations.

4. Cu/Ru(0001)

The growth of the Cu thin films on Ru(0001) at room temperature was performed for various film thickness range from 0.2 to 10 ML. However, our main interest concentrated on the low coverage regime (≤ 2 ML). The coverage of the Cu overlayer was determined with the low energy Li^+ ion scattering using selected scattering geometries.

The coverage dependence of the Cu signal was taken at $\alpha = 30^\circ$ along the $[10\bar{1}0]$ azimuth (not shown). The first linear increase of the Cu signal up to 1 ML corresponds to simple overlayer growth. However, the second linear increase up to about 2.2 ML was also observed, indicating pseudomorphic growth of Cu. After the 2 ML, the growth mode is very difficult to ascertain from the LEIS data alone.

Fig. 2 shows the incident angle dependences of the Ru signals along the $[10\bar{1}0]$ azimuth at a scattering angle of $\Theta = 130^\circ$, collected as a function of Cu coverage. From these spectra the following two statements can be made: first, Cu deposition causes the attenuation of the Ru signal where scattering occurs from only the first layer atoms. This confirms pseudomorphic growth of Cu; second, the fact that the Ru showing two peaks at higher incident angles due to second and third layer scattering remain prominent for coverage up to 2 ML indicates that the Cu atoms are in a normal registry position (i.e. there is a continuation of the hcp stacking sequence). Further analysis regarding the Cu atom sites will be reported in detail somewhere.

The structure of the Cu overlayers up to 5 ML have also been probed by measuring the incident angle dependences. The result is consistent with an epitaxial Cu(111) structure by comparing with the results of Cu(111) although the distorted incident angle dependences were observed.

5. He^+ scattering from Cu/O/Ru(0001)

The adsorption of Cu on an O-precovered Ru(0001) has been also studied, with the goal of understanding the differences in growth mechanisms on clean and modified Ru substrate. Results of these measurements in this section were obtained using keV He^+ ion beams. The use of noble gas projectiles, which have an extremely high rate of neutralisation during scattering events, ensures a high degree of surface sensitivity.

Cu deposition at room temperature onto 20 L O/Ru(0001) surfaces leads to the variation in the Cu and O signals are shown in fig. 3. The He^+ spectra were taken after successive Cu deposition. In this experiment, the scattering geometry was chosen along the $[10\bar{1}0]$ azimuth at an incident angle of

$\alpha=55^\circ$ and a scattering angle of $\Theta=90^\circ$ where the shadowing and/or blocking effects are suppressed. These results show that the majority amount of oxygen (about 70%) originally on the clean Ru(0001) surface is still present following large amounts of Cu deposition on the top of the oxygen layer. This displacement process could be observed up to Cu coverages of 10 ML. It clearly shows that facile migration of O atoms from the Ru to the Cu overlayers has occurred. This behaviour has been explained on the basis of the "compress model" [3]. The displaced O has been tested by the azimuthal scan at grazing incidence, showing a disordered overlayer.

6. Conclusion

In summary, Cu/Ru(0001) and Cu/O/Ru(0001) have been studied by low energy Li^+ and He^+ ion scattering. The results show that Cu forms well ordered islands which are pseudomorphic for two layers. Cu deposition onto an O-precovered Ru(0001) surface leads to about 70% migration or float out of the oxygen from the Ru to the Cu.

References:

1. J.E. Houston, C.H.F. Peden, D.S. Blair and D.W. Goodman, *Surf. Sci.* 167 (1986) 427.
2. C. Park, E. Bauer and H. Poppa, *Surf. Sci.* 187 (1987) 86.
3. K. Kalki, M. Schick, G. Ceballos and K. Wandelt, *Thin Solid Films*, 1993, in press.
4. Y.G. Shen, D.J. O'Connor and R.J. MacDonald, *Surf. Interface Anal.* 17 (1991) 903; 19 (1992) 729.
5. J.W. Niemandsverdriet, P. Dolle, K. Markert and K. Wandelt, *J. Vac. Sci. Technol.* A5 (1987) 875.

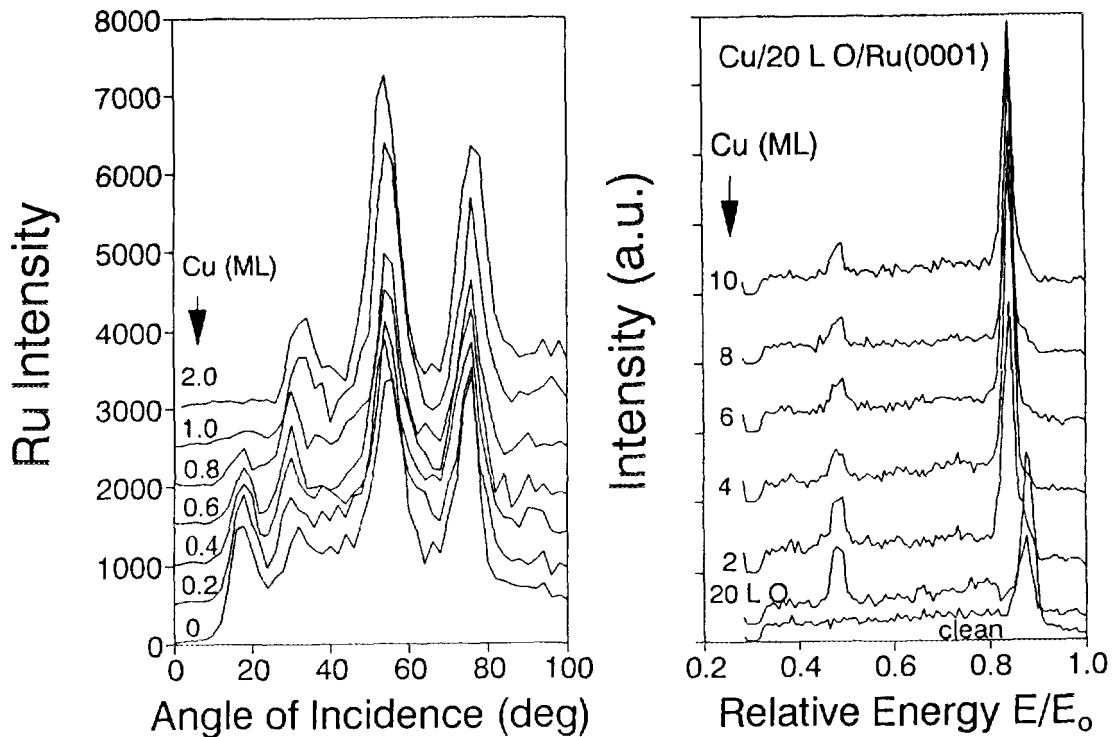


Fig. 2 Intensities of 1 keV Li^+ ions scattered from the Ru atoms as a function of incident angle α are shown for various coverages of evaporated Cu.

Fig. 3 Energy spectra of 1 keV He^+ ions scattered from clean and various coverages of Cu evaporated onto 20 L O-precovered Ru(0001) surface at room temperature.



LATTICE LOCATION OF PLATINUM IONS IMPLANTED INTO SINGLE CRYSTAL ZIRCONIA AND THEIR ANNEALING BEHAVIOUR

D.X.Cao⁺, D.K.Sood and I.G.Brown*

Microelectronics and Materials Technology Centre, Royal Melbourne Institute of Technology, 124 La Trobe Street, Melbourne 3000 (Australia)

+Permanent address: Institute of Nuclear Research, Academia Sinica, P.O.Box 800-204, Shanghai 201800 China

*Accelerator and Fusion Research Division, Lawrence Berkeley Laboratory, University of California, Berkeley, CA 94720 (USA).

Single crystal samples of (100) oriented cubic zirconia stabilised with 9.5 mol % yttria were implanted with platinum ions, using a metal vapour vacuum arc (MEVVA) high current ion implanter, to a nominal dose of 1×10^{17} ions/cm². The implanted samples were annealed isothermally in air ambient at 1200°C, from 1-24 hours. Rutherford Backscattering Spectrometry and Channelling (RBSC) of 2 MeV He ions are employed to determine depth distributions of ion damage, Pt ions and substitutionality of Pt ions before and after annealing. The damage behaviour, Pt migration and lattice location are discussed in terms of metastable phase formation and solid solubility considerations.

1. INTRODUCTION

Surface modification of ceramics by ion beam techniques is already being used to create novel mechanical, optical, chemical, electrical and tribological properties in the surfaces of alumina, silicon nitride, magnesia and titanium borides and carbides[1]. However, comparatively little work has been reported on the surface modification of zirconias by ion beam methods [2,3]. Zirconia is an important oxide ceramic with several applications based upon its unique mechanical properties and its high oxygen ion conductivity. We have undertaken a systematic research program [4] to explore and understand little known fundamental aspects of ion bombardment induced phenomena on zirconia surfaces. This work presents our study on platinum implantation into zirconia. Platinum was chosen since it is used in thin film form as a typical electrochemical contact material on zirconia based electrochemical devices such as oxygen sensors and fuel cells [5]. A dispersed layer of dense precipitates of Pt formed by implantation to high doses, can be of considerable interest as an alternative conducting layer with large "three phase" (zirconia, Pt and oxygen) volume within the layer.

2. EXPERIMENTAL

Single crystal samples of (100) oriented cubic zirconia stabilised with 9.5 mol % yttria were obtained from Ceres Corporation, USA. Ion implantation was carried out using a metal vapour vacuum arc (MEVVA) high current ion implanter at LBL. A nominal dose of 1×10^{17} ions/cm² was

implanted without any cooling of the target mount leading to an implantation temperature of about 200° C. The extraction voltage was 75 kV. The implanted samples were annealed isothermally in air ambient at 1200°C, from 1-24 hours. Rutherford Backscattering Spectrometry and Channelling (RBSC) of 2 MeV He ions were employed for analysis. Some samples were studied with RHEED (reflection high energy electron diffraction) to determine their surface structure.

3. RESULTS AND DISCUSSION

MEVVA source produces ions with multiple charge states leading to effectively multi-energy implants. For our experiment, the average charge state of Pt was 2.1 [6] corresponding to an average energy of 158 keV for the Pt ions extracted at 75 kV. The observed RBSC spectra for as implanted samples[Figs. 1&2] showed the Pt depth profiles to be non-Gaussian with peak concentration close to the surface. When fitted with the results of the PROFILE code, they were found to be sputter limited with a retained dose of only 0.35×10^{17} ions/cm² corresponding to an effective sputtering yield of 1.1 atoms/ion. The aligned spectra show high damage but no evidence of any amorphisation (confirmed by RHEED data), and a substitutionality of 0 %. Virgin zirconia crystals contained in bulk about 0.5 mol% Hf which was almost totally substitutional.

On annealing at 1200°C (Fig.1) much of the damage peak anneals out during the first hour leaving behind a small surface peak which vanishes at higher anneal time of 24 h. With increasing anneal time, the damage recovers rather slowly and the dechannelling

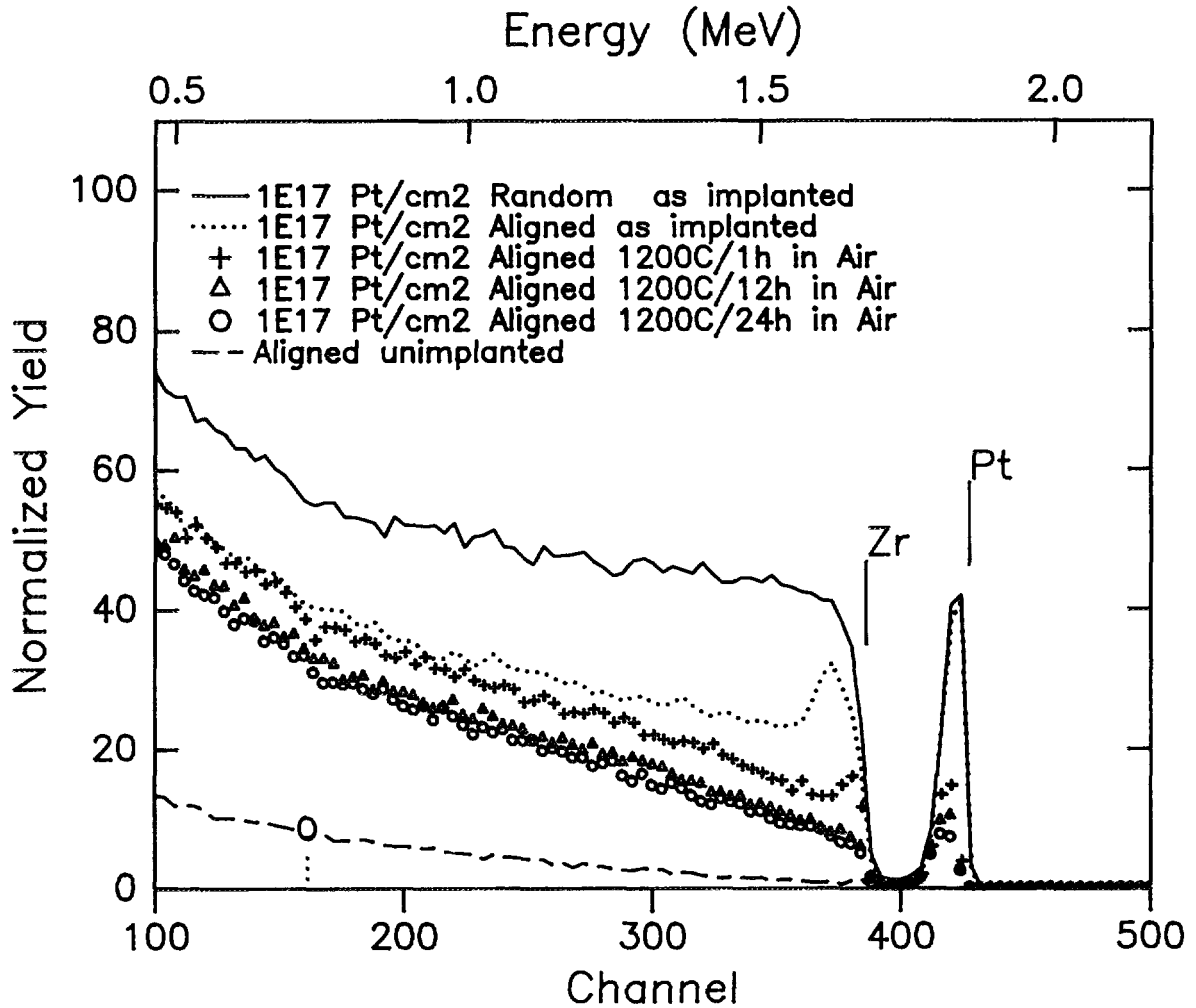


Fig. 1. RBSC spectra showing the annealing behaviour at 1200°C for the indicated annealing times. The scattering angle was 170°

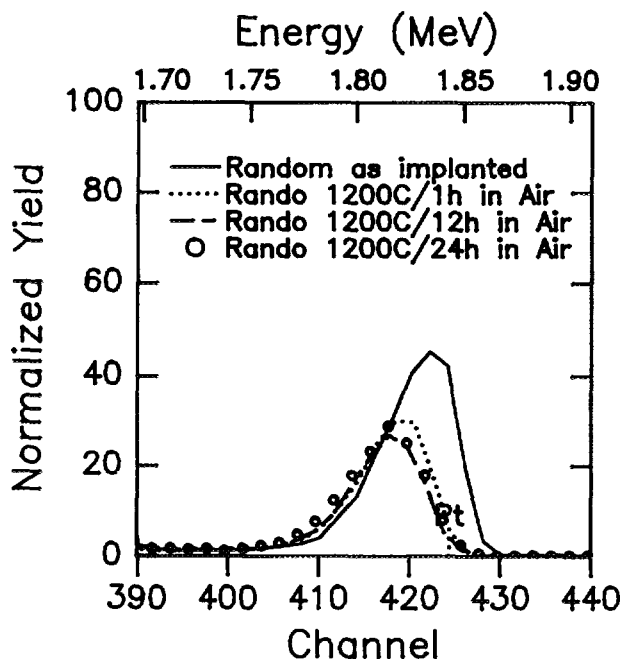


Fig. 2. Random RBS spectra showing the migration of Pt on annealing.

yield drops at all depths but remains higher than that in a virgin crystal. This shows incomplete recovery of the ion damage. Pt atoms undergo substantial migration concurrently (Fig. 2). After the first hour of annealing, a substantial amount of Pt originally present at the surface is lost leaving behind a near Gaussian distribution of Pt with a peak located at a depth of about 25 nm. This depth is close to the peak damage depth of 22 nm calculated from TRIM91 code for 158 keV Pt ions. This indicates the possibility of "damage getting" of Pt ions, since the TRIM projected range is 34 nm. With increasing anneal time, the Pt depth profile does not change much but the substitutional fraction keeps increasing from an initial value of 0% to 72% after a 24 hour anneal. The peak in the as implanted random spectrum corresponds to a peak concentration of about 29 mol% Pt. After annealing for 24 h at 1200°C, the peak concentration in the random spectrum reduces to about 18 mol% Pt corresponding to a measured solubility of about 13 mol% Pt in zirconia.

A further insight into the relationship between the residual damage and Pt atoms is

provided by the angular scans about $\langle 100 \rangle$ axis after annealing, as shown in Fig.3. The angular scans for Zr and Pt were obtained from the same depth intervals. After annealing (Figs. 3a, 3b) at 1200°C (1, 24 h), Pt clearly occupies different sites as seen from the different critical angles observed for Zr (0.72, 0.53°) and Pt (1.04, 1.13°). As the annealing time increases, the critical angles for Zr decrease while those for Pt increase marginally. Now the lattice parameters for cubic Pt and cubic zirconia are 0.39231 and 0.507 nm respectively[7]. Since the critical angle is proportional to inverse square root of the lattice spacing, Pt precipitates in zirconia can therefore be expected to lead to a higher critical angle than that for Zr in zirconia. Our measurements therefore indicate the formation of precipitates of Pt which may be partially coherent with the matrix. As the annealing time increases, the angular scans (Figs. 3a and 3b) indicate further growth and greater coherence of the platinum precipitates with the

surrounding zirconia matrix. These observations are also consistent with the dechanneling behaviour in Fig. 1 discussed earlier.

4. SUMMARY

a) Pt implantation at about 200 C to high doses, does not produce an amorphous phase

b) Retained dose is small (35%) and Pt depth profiles are sputter limited. An effective sputtering yield is 1.1 atoms /incident ion.

c) Ion damage begins recovers quite well at 1200°C, leading to formation of partially coherent precipitates of Pt.

d) Pt shows a solid solubility of at least 13 mol% in zirconia at 1200°C

5. ACKNOWLEDGMENTS

We thank A.P.Pogany for assistance with RHEED measurements.

REFERENCES

1. "Structure Property Relationship in Surface Modified Ceramics", eds. C.J.McHargue et al (Kluwer Academic,1989).
2. W. Wei et al, *Surface Coatings Tech.* 37 (1989)179.
3. E.L. Fleischer et al, in "Beam Solid Interactions; Physical Phenomena", eds. P. Borgesen et al, MRS (1990) 537; and *J. Mater. Res.* 5 (1990) 385.
4. D.X.Cao, D.K.Sood and I.G.Brown, *Proc. IUMRS-ICAM-93 conference, Symposium U, September 1993, Elsevier, Amsterdam.*
5. S.P.S. Badwal, F.T. Ciacchi and D.K. Sood, *Solid State Ionics*, 18/19 (1986)1033-37.
6. I.G.Brown and X.Godechot, *IEEE Trans. Plasma Sci.* 19(1991)713.
7. "Crystallographic Data on Metals and Alloy Structures", Eds. A. Taylor and B.J.Kagle (Dover, New York, 1963).

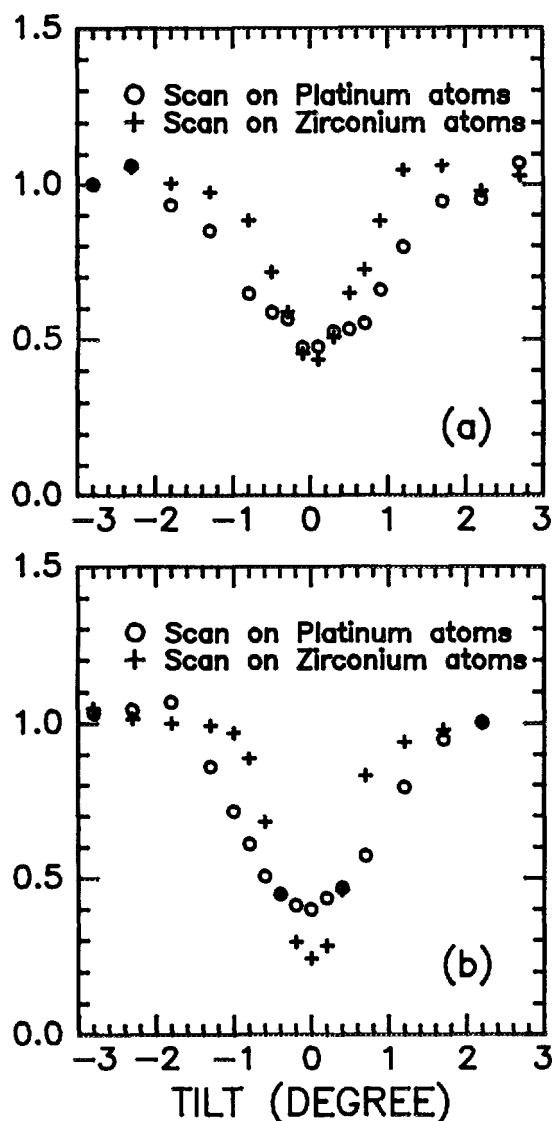


Fig. 3. Angular scans about $\langle 100 \rangle$ axial channel, after annealing in air at (a) 1200°C, 1h, (b) 1200°C, 24 h .

Growth of CdTe on (100) GaAs and Analysis
using Ion Scattering Spectrometry

B.Mitrovic*, B.V.King*

*)Department of Physics, University of Newcastle, Newcastle 2308,
New South Wales, Australia.

A brief review of CAICISS has been presented as well as its advantages in studies of semiconductor surfaces and interfaces. The results that we have gained from SABRE simulation are graphically presented as an incident angular spectrum. The plausible interpretation for the large anomalous peak at 60° is given.

1. INTRODUCTION

Since its first announcement [1], CAICISS (Coaxial Impact-Collision Ion Scattering Spectrometry) has appeared to be powerful and promising tool for quantitative study of atomic geometry of semiconductor surfaces and related systems.

In reality CAICISS is just a modification of ICISS (Impact-Collision Ion Scattering Spectrometry) [2],[3],[4] which is again a subset of ISS (Ion Scattering Spectrometry) [5],[6]. Technically a pulsed-beam low energy ion source and a time-of-flight ion energy analyser are placed coaxially so as to take the experimental scattering angle at 180° [7].

The advantages of CAICISS [8],[9],[10],[11],[12] can be summarised as follows:

1. It can be performed during film deposition (In Situ monitoring) with negligible damage or to be applied in dynamical, time resolved, surface studies. In both cases it gives real space picture opposite to the diffraction methods (RHEED etc.) which give Fourier transform or reciprocal space picture

2. Analysis of spectra is relatively simplified because the influence of the multiple scattering and charge exchange processes is mostly prevented by the particular experimental geometry. Both processes are usually considered as drawbacks in ISS [13], although some authors underline the different point of view [14]

3. Using the Time-of-Flight detection technique we can choose to selectively detect only ions or both ions and neutrals scattered from the surface.

4. By proper choice of a type of projectile (noble gases, alkaline metals) we are able control (up to certain limit) the diameter of the shadow-cone and on that way to execute shallow or deeper sensitive measurements (up to 10 monolayers). From the point of view of exploitation of the shadowing effect this technique is more similar to RBS rather than to conventional LEIS.

2. RESULTS

The computer program SABRE has been used to simulate CAICISS of 2 keV Ne⁺ on the bulk-terminated As-stabilised surface of (100) GaAs. 4 million trajectories were run, uniformly distributed over the surface unit cell. Thermal vibrations and electronic energy loss have been excluded to enable faster computation and to obtain the model-spectrum which includes only geometrical effects. These also may be related to the initial temperature conditions prior to growth.

The spectrum shown, Fig.1, is for particles incident along [011] crystallographic direction. Trajectories have been calculated for angles of incidence to the surface of 5° to 90° in 5° steps. On the other side we have calculated the shadow cones using Oen's model and determine the critical angles by precise delineation. The purpose of this was to compare the results with those from simulation.

The peak at 19° is due to the Ne ions being focussed onto the As surface atoms and then being backscattered. A similar smaller peaks occurs at 70° degree due to focussing onto second layer Ga. A large peak at 60° is, as yet, unexplained but may be due to a double focussing sequence onto subsurface atoms.

3. CONCLUSION

The basic features of CAICISS have been presented. Simulation using fast computer code - SABRE has revealed an angle-resolved spectrum with several well defined peaks. Some of

them are in good accordance with the prediction of the qualitative theory. For large anomalous peak the interpretation is proposed.

References

1. M.Katayama, E.Nomura, N.Kanekama, H.Soejima, M.Aono, Nucl.Instr. and Meth. B33, (1988), 857-861.
2. M.Aono, C.Oshima, S.Zaima, S.Otani, Y Ishizawa, Jpn.J.Appl.Phys.20, (1981), L829-L832.
3. M.Aono, R.Souda, Jpn.JAppl.Phys, 24, (1985), 1249-1262.
4. Th.Fauster, Vacuum, 38, (1988), 129-142.
5. D.J.O'Connor, in "Surface Analysis and Methods in Material Science" (edited by J.O'Connor, B.Sexton, R.Smart, Springer Series in Surface Science 23, p.245-261.
6. E.Taglauer, in "Ion Spectroscopies for Surface Analysis" (edited by A.Czanderna, D.Hercules), Methods of Surface Characterization, v.2, p.363-416.
7. M.Aono, M.Katayama, E.Nomura, Nucl.Instr. and Meth.B64, (1992), 29-37.
8. B.V.King, M.Katayama, M.Aono, R.S.Daley, R.S.Williams, Vacuum, 41, (1990), 938-940.
9. N.Sugiyama, A.Hashimoto, M.Tamura, Jpn.J.Appl.Phys., 29, (1990), L1922-L1925.
10. A.Hashimoto. N.Sugiyama, M.Tamura, Jpn.J.Appl.Phys., 30, (1991), 3755-3758.
11. T.Saitoh, A.Hashimoto, M.Tamura, J.Appl.Phys.71, (1992), 3802-3805.
12. I.Chakarov, B.V.King, R.P.Webb, R.Smith, Nucl.Instr. and Meth. B67, (1992), 332-334.
13. H.Niehus, R.Spitzl, Surf. and Interf.Anal.17, (1991), 287-307.
14. O.Grizzi, M.Shi, H.Bu, J.W.Rabalais, P.Hochmann, phys.rev.B40, (1988), 10127-10180.

Ne 2.000kev on (100) GaAs

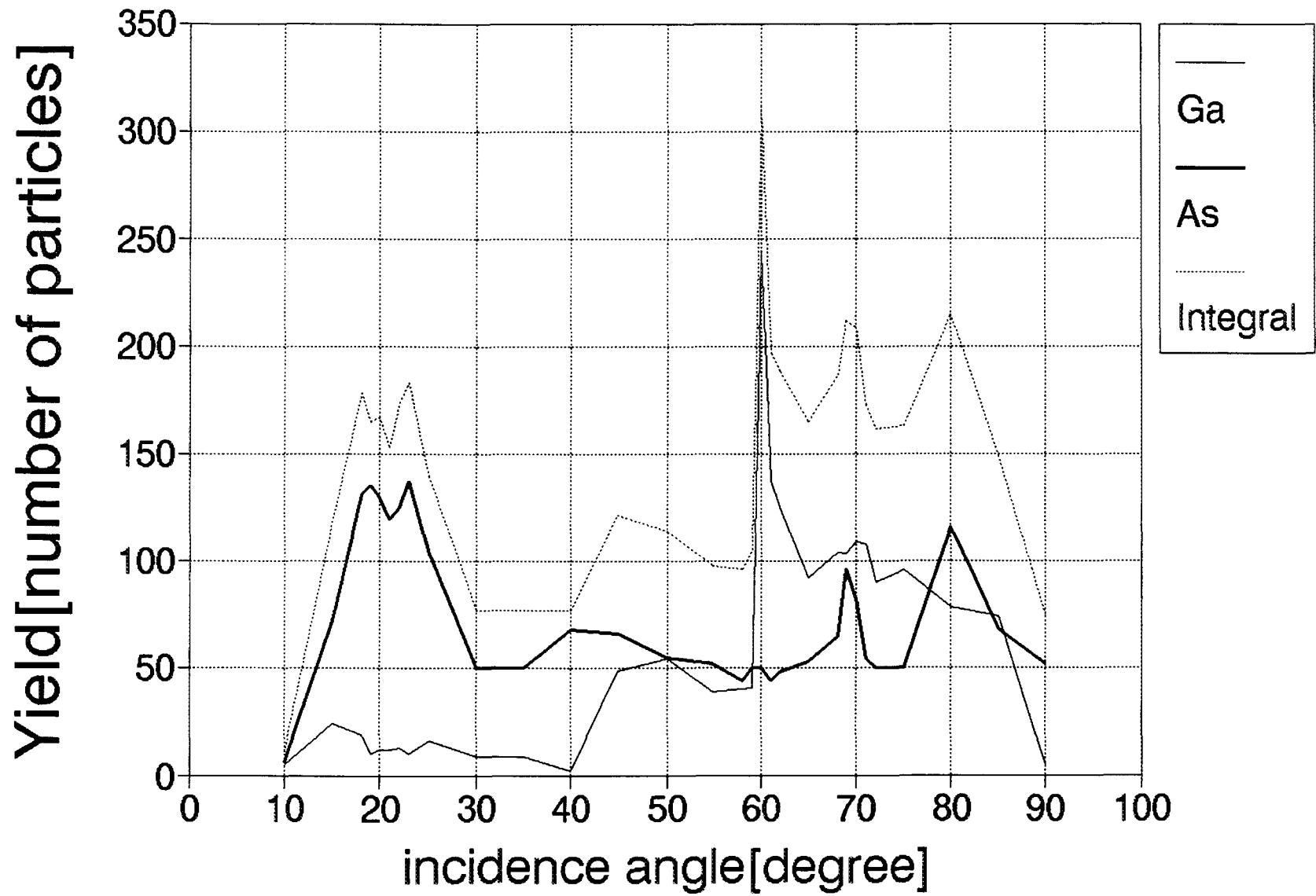


FIG 1

Oxygen Adsorption on Cu(111) Using Low Energy Ion Scattering Spectroscopy

F.M. Zhang, J. Yao, Y.G. Shen, B.V. King and D.J. O'Connor

Department of Physics, The University of Newcastle,
Newcastle, NSW 2308, Australia

Abstract

The surface structure and oxygen adsorption of Cu(111) have been studied by 2 keV Li^+ , He^+ and Ar^+ ion scattering. Incident and azimuthal dependences were measured for the clean and O-covered surfaces, and the surface geometry was analysed on the basis of the shadowing features. Experimental results under different oxygen exposures at room temperature showed that the Cu(111) surface undergoes a roughening transition and results in a reconstruction where Cu atoms are vertically displaced by about 0.23 Å.

Introduction

The structure of the clean and the oxygen exposed Cu surfaces have been extensively studied^[1-2]. Recently, more attention has been paid to the Cu(111) surface because its oxygen adsorption behaviour is different to that of the Cu(100) and Cu(110) surfaces, and is still under debate^[3].

Experimental

The experimental conditions essential to the present study are briefly summarized as follows: (a) the base pressure was 2×10^{-10} mbar; (b) the Cu(111) cleaning and O dosing were achieved by conventional procedures; and (c) oxygen was adsorbed at room temperature and the surface structure was checked by LEED.

Results and discussion

The azimuthal angle of the Cu(111) surface with respect to the beam direction was calibrated by both observing the LEED pattern position and monitoring the Cu signals obtained at grazing incidence. The results of the azimuthal scan at grazing incidence of $\alpha = 12^\circ$ for 2 keV Ar^+ ions are shown in figure 1. The inset shows the top view of the Cu(111) surface, which also illustrates the angular orientation used in this study. The symmetry of the crystal structure can be obtained directly from these features, which contain information of the surface periodicity.

The structure of the clean Cu(111) surface (sharp 1×1 LEED pattern) has been determined using low energy Li^+ ion scattering. The main experimental procedures were to collect data by varying the incident angle α along low-index directions or by varying the azimuthal angle ϕ at fixed incident angle α . Results obtained were compared to the shape of the calibrated shadow cone (because of the scattering angle $\Theta < 180^\circ$) or to calculations based on the ZBL scattering potential.

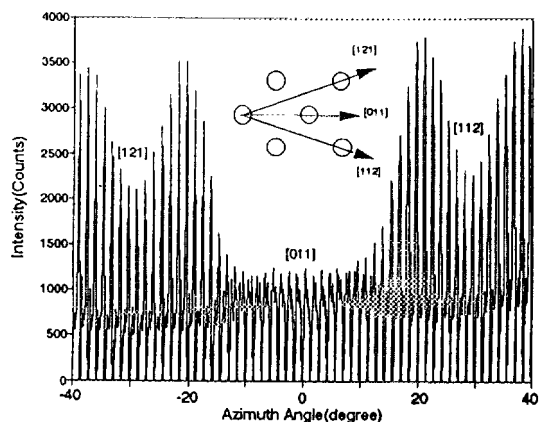


Fig. 1 The dependence of Cu signal on azimuthal angle.

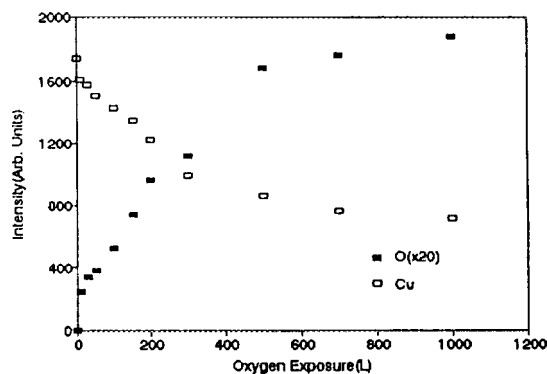


Fig. 2 The dependence of Cu signal on oxygen exposure.

From the incident angle dependences along the $[\bar{1}\bar{1}2]$, $[1\bar{2}1]$ and $[0\bar{1}1]$ three main low-index crystallographic directions (not shown), the results show that there is no reconstruction of the top-most layer and no contraction in the first-second layer spacing within the detection uncertainty of 0.05 Å.

The oxygen adsorption measurements on Cu(111) were carried out with He^+ ions. The reason for using He^+ instead of using Li^+ is two-fold. Firstly, He^+ ions have an extremely high rate of neutralisation during scattering events, ensuring that the detected signal mainly comes from the top-most layer; secondly, for Li^+ scattering, oxygen single scattering peaks are superimposed on a large background signal owing to multiple, inelastic scattering of Li^+ ions from the subsurface. However, care has been taken to include the possible orientation-dependent neutralisation of He^+ ions in the interpretation of the experimental data. Typical oxygen adsorption results are shown in figure 2. In this experiment, the scattering geometry was chosen along the $[0\bar{1}1]$ azimuth at $\Theta = 2\alpha = 90^\circ$, where the shadowing and/or blocking effects are minimised. As oxygen is adsorbed, the O signal increases while the Cu signal decreases. At an exposure of 500 L, the O signal has almost reached saturation.

In order to obtain further structural information, intensity data as a function of incident angle α for the clean and O-covered Cu(111) surfaces were collected. Typical experimental data along the $[0\bar{1}1]$ azimuth are shown in figure 3. The critical angles were 16.5° and 21.5° for clean and O-covered Cu(111) surfaces, respectively, at $\Theta = 90^\circ$. Here, the experimentally determined critical angle corresponding to 80% of maximum intensity was used to define the position of the critical angle α_c ^[4]. Attributing this change in critical angle to a horizontal displacement would require a movement of near 1 Å. Such a large displacement is unlikely because the first layer is not laterally reconstructed based on our LEED observation during O adsorption. After considered all possible explanations to the change in critical angle, we think the most possible situation is that some of the Cu atoms on O-covered Cu(111) surface were displaced vertically. Figure 4 shows the calculated

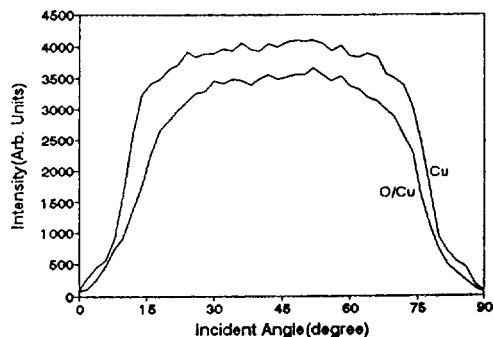


Fig. 3. The incident angle dependence of Cu signal intensity from clean and O-covered Cu(111) surfaces.

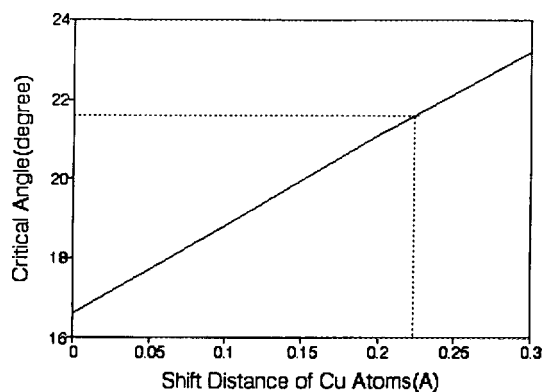


Fig. 4 The relationship between critical angle and shift distance of Cu atoms for ZBL potential.

critical angle α_c of the Cu shadowing edge as a function of the vertical displacement of the Cu atoms along the $[0\bar{1}1]$ azimuth using the ZBL potential. From the figure, we can calculate that oxygen adsorption induced a vertical reconstruction, where the Cu atoms were displaced by about 0.23\AA . This is in good agreement with the value of 0.3\AA obtained by Niehus^[2]. Due to the complex process of oxygen adsorption on Cu(111) surface, no consensus has been reached about the surface structure induced by oxygen adsorption. A recent study by STM showed that two new oxygen induced reconstructions of Cu(111) with unit cells being 29 and 44 times larger than the 1×1 surface unit cell^[3].

Conclusion

In conclusion, we have presented the low energy ion scattering results from clean and oxygen covered Cu(111) surface. It was shown that the clean Cu(111) surface has a 1×1 surface without reconstruction. With oxygen adsorption at room temperature, the Cu atoms on the Cu(111) surface possibly undergoes a reconstruction with a vertical 0.23\AA displacement of Cu atoms.

References:

1. L. McDonnell and D. P. Woodruff, Surf. Sci. 46 (1974) 503
2. H. Niehus, Surf. Sci. 130 (1983) 41.
3. F. Jensen, F. Bensenbacher, E. Laasgaard and I. Stensgaard, Surf. Sci. Lett. 259 (1991) L774-L780.
4. Y. G. Shen, D. J. O'Connor and R. J. MacDonald, Nucl. Instr. Meth. B66 (1992) 441.



Corrosion Behaviour of Ion Implanted Aluminum Alloy in 0.1 M NaCl Electrolyte

J.W.Chu* and P.J.Evans

Australian Nuclear Science and Technology Organisation, Private Mailbag 1, Menai 2234, NSW. Australia.

D.K.Sood

Microelectronics and Materials Technology Centre, Royal Melbourne Institute of Technology, P.O.Box 2476, Melbourne, Vic 3001, Australia.

Introduction

Aluminum and its alloys are widely used in industry because of their light weight, high strength and good corrosion resistance which is due to the formation of a protective oxide layer. However, under saline conditions such as those encountered in marine environments, this group of metals are vulnerable to localised degradation in the form of pitting corrosion. This type of corrosion involves the adsorption of an anion (ie. Cl^-) at the oxide solution interface. Ion implantation of metal ions has been shown to improve the corrosion resistance of a variety of materials. This effect occurs when the implanted species reduces anion adsorption thereby decreasing the corrosion rate [1,2]. In this paper we report on the pitting behavior of Ti implanted 2011 Al alloy in dilute sodium chloride solution.

Experimental

Aluminum alloy (type 2011-T3), containing about 5.5%Cu, 0.5% Pb/Bi and trace amounts of Fe, was machined into circular discs (16mm ϕ x 3mm thick). One surface of each specimen was mechanically polished, with the final polish performed using a 0.25 μm diamond paste. Secondary electron microscope examination of the as-polished specimens revealed the presence of scratches. The polished samples were implanted with Ti ions using a metal vapour vacuum arc (MEVVA) ion source. For these implantations, the source was operated at an extraction potential of 25 kV and an ion beam current (pulsed) of 80 mA. The average charge state of MEVVA generated Ti ions is 2.1 [3], which combined with the above extraction potential yielded a mean ion energy of approximately 50 keV. At this energy, the projected range as calculated by TRIM [4] was found to be about 430 Å. The bulk temperature rise of the samples during implantation was less than 150°C as determined by a non-contact thermometer (OPTEX Q185). Samples were analyzed by Rutherford backscattering (RBS) before and after corrosion testing. The implanted doses were determined by RUMP [5] simulation of the RBS spectra.

Electrochemical tests were conducted in de-aerated 0.1 M NaCl solution, and the test temperature was 20-25°C. A saturated calomel electrode (SCE) was used for reference. Al specimens were mounted in a specially designed electrode such that only the test surface was in contact with the electrolyte. Samples were immersed in the solution for either 2 or 18 hours prior to polarization. Anodic polarization curves were obtained by stepping the potential at a rate of 2 mV/min from the corrosion potential in the anodic direction.

Results and discussion

Anodic polarization experiments for both virgin and Ti implanted samples have been carried out. The pitting potentials of Ti implanted surfaces were shifted to a higher value (ie. more positive) which represented an increase in resistance to pitting corrosion. Some divergence in pitting potential values was observed and this was attributed to variations in the quality of the final polish. The typical value for unimplanted samples was -0.630V and -0.580V for

* AINSE Post-doctoral Fellow.

Ti implanted samples. The data also showed that the increase of pitting potential is not proportional to the implanted dose. These results indicate that Ti implantation increased the pitting corrosion resistance of 2011 Al alloy. However, the improvement was limited, which could be due to the defects such as scratches on the surface.

RBS spectra were measured for specimens prior to and following corrosion tests. Fig.1 shows the RBS spectra of samples which had been immersed in the solution for 1 day. In this case the oxygen peak in the spectrum of the as-polished surface is larger than that of the Ti implanted sample. Fig.2 shows the RBS spectra after polarization. Compared with the Ti implanted sample, the aluminum concentration at the surface of the virgin 2011 Al is reduced significantly and a large oxygen peak is evident. The results indicated that Ti implantation has reduced the uptake of oxygen and increased the surface resistance to the corrosion.

Fig.3(a) and (b) show scanning electron micrographs of the aluminum 2011 alloy and Ti implanted samples after polarization tests. The precipitates of constitutional elements such as CuAl_2 (round inclusion) and Cu_2FeAl_7 (long crystal) are present on both sample surfaces. Mechanical scratches can also be seen on both samples. For unimplanted material, the surface shows grain boundaries and pits of small size. For the Ti implanted specimen, the surface is generally smooth, grain boundaries are not visible, and there are fewer pits but these are of relatively larger size. These results imply that Ti implantation has reduced the density of pits by removing some of the surface defects, but that pitting of the implanted surface occurs at the remaining defects. Corrosion products on the implanted surface were analysed by energy dispersive X-ray spectroscopy and found to contain large amounts of chlorine.

Summary

The oxygen uptake and resistance to pitting of Ti implanted Al 2011 alloy in 0.1 M NaCl solution were examined and compared with that of unimplanted material. The Ti implanted surfaces exhibited an increased pitting potential and a reduced oxygen uptake. The extent of improvement is limited by two factors. One is the large number of surface defects produced in the polishing process, and the other was related to the concentration of implanted Ti at the surface which is low compared with that at the peak of the implant distribution.

Acknowledgments

This work was supported by Australian Institute of Nuclear Science and Engineering in the form of AINSE Post-doctoral Fellowship.

References

1. P.M. Natishan, E. McCafferty and G.K. Hubler, J. Electrochem. Soc., 135, 321 (1988).
2. P.M. Natishan, E. McCafferty and G.K. Hubler, Nucl. Instrum. Methods, B59/60, 841 (1991).
3. I.G. Brown, B. Feinberg and J.E. Galvin, J. Appl. Phys. 63 (1988) 4889
4. J.F. Ziegler, J.P. Biersack and U. Littmark, The stopping and Range of Ions in Solids (Pergamon, New York, 1985)
5. L.R. Doolittle, Nucl. Instr. and Meth. B9 (1985) 334

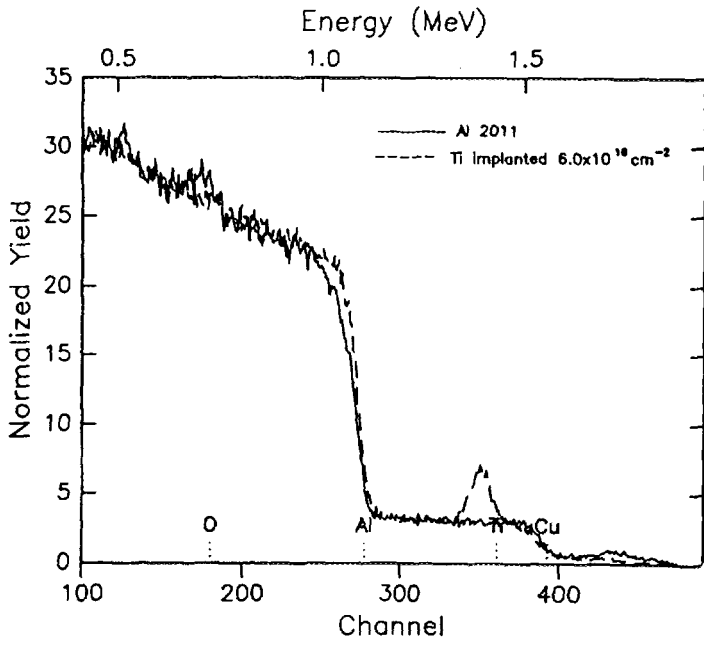


Fig.1 RBS spectra of samples (after 18 hr immersion in solution).

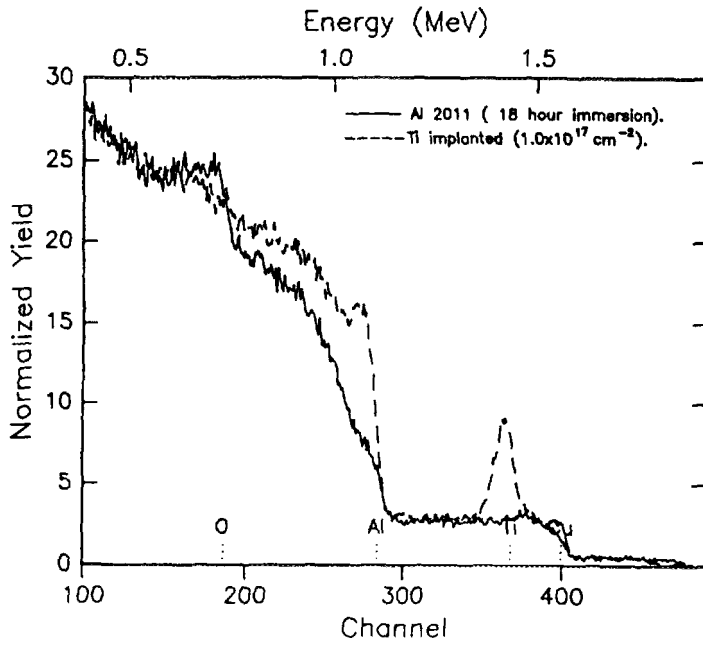
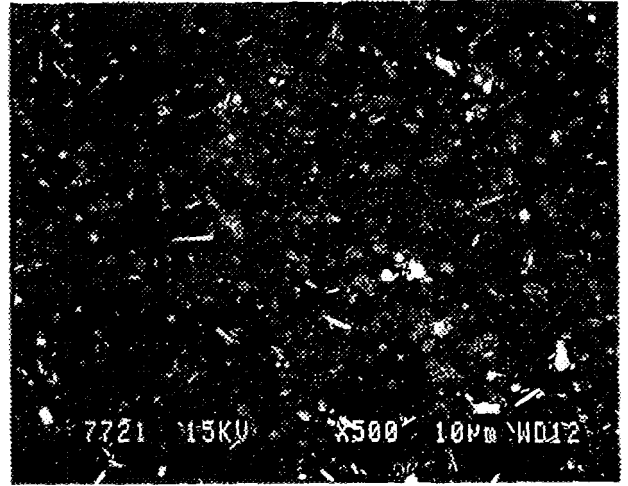
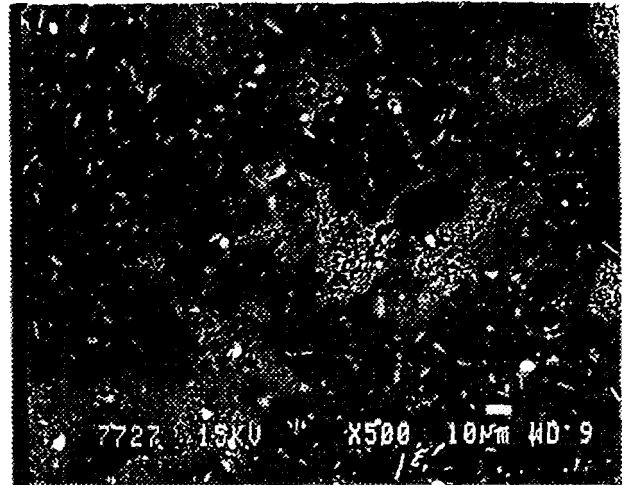


Fig.2 RBS spectra of electrochemical tested samples (18 hr immersed in solution prior to the tests).



(a)



(b)

Fig.3 Scanning electron micrographs of electrochemical tested samples, (a) Al 2011, (b) Ti implanted Al 2011.



THE ANTARES AMS CENTRE AND RESEARCH PROGRAM

*C.Tuniz, D.Fink, M.A.C. Hotchkis, G.E. Jacobsen, E.M. Lawson, M. Shying,
A.M. Smith, J.W. Boldeman, J.R. Bird*

Australian Nuclear Science and Technology Organization
Private Mail Bag 1, Menai, NSW 2234, Australia

The ANTARES tandem accelerator is now operational at Lucas Heights Research Laboratories with excellent terminal voltage stability and beam transmission [1]. All the components required for the AMS spectrometer have been installed, including the 60-sample ion source and the fast isotope cycling system [2]. AMS analysis with state-of-the-art precision and sensitivity have been demonstrated. Two beamlines on the switching magnet are dedicated to the measurement of ^{14}C [3] and other long-lived cosmogenic radioisotopes such as ^{10}Be , ^{26}Al , ^{36}Cl and ^{129}I [4, 5]. A national research program on Quaternary science has been funded for 1993 by the Australian Research Council and the Australian Institute of Nuclear Science and Engineering (AINSE). About 30 projects from more than 10 Australian universities have been selected by the AINSE-AMS Specialist Committee. These projects, requiring the analysis of ^{14}C in about 400 archaeological and geological samples, include the study of past atmospheric ^{14}C variations from analysis of tree rings of Tasmanian pines, dating of prehistoric aboriginal rock art painting and dating of human-megafauna associations in Australia. Sample processing of the AMS samples is performed at Lucas Heights Research Laboratories [6] at the Quaternary Research Centre (Australian National University) and at the NWG Macintosh Centre for Quaternary Dating (University of Sydney).

- [1] J.W. Boldeman *et al.*, this conference.
- [2] A.M. Smith *et al.*, this conference.
- [3] M.A.C. Hotchkis *et al.*, this conference.
- [4] D. Fink *et al.*, this conference.
- [5] E.M. Lawson *et al.*, this conference.
- [6] G.E. Jacobsen *et al.*, this conference.



THE STATUS OF THE 8MV TANDEM ACCELERATOR, ANTARES

J Fallon, JW Boldeman, C Tuniz, D Cohen, P Ellis

Australian Nuclear Science and Technology Organisation
Private Mail Bag1, Menai, NSW 2234, Australia

ANTARES is now reliably used in a variety of Accelerator Mass Spectrometry applications, as a tool in Ion Beam Analysis and to produce small amounts of radioisotopes such as ^{18}F . To satisfy these needs, dedicated beam lines have been developed and the accelerator upgraded in many ways.

These developments, along with a pictorial study will be presented.

14C Analyses at the ANTARES AMS Centre

M.A.C. Hotchkis, D. Fink, G.E. Jacobsen, E.M. Lawson, M. Shying,
A.M Smith and C. Tuniz

Australian Nuclear Science and Technology Organisation
Private Mail Bag 1, Menai, NSW 2234, Australia

Since becoming fully operational earlier this year, the ANTARES AMS Centre has performed many ^{14}C - measurements on a variety of samples. Numerous measurements have been made using standards, to assess precision, accuracy and reproducibility over different time periods. For example, repeated isotope ratio measurements with a statistical error of 0.58% resulted in a standard error in the mean of 0.62%. From these results, calibration and accelerator beam tuning procedures have been established to minimise uncertainties in the final results. ^{14}C blanks obtained from different stages of sample preparation have been measured; an ultimate sensitivity corresponding to a $^{14}\text{C} / ^{12}\text{C}$ ratio of 10^{-15} has been demonstrated. These data will be presented, along with results for unknowns.

Current projects for which measurements have been made include dating of archaeological sites in Australia and SE Asia, and experiments to evaluate methods of carbon extraction from highly degraded wood and bone. Of particular interest has been our dating of material from the egg of an Elephant Bird. This species of flightless bird has been extinct for several hundred years and was a native of Madagascar. The egg, which is intact, was found recently by children playing in sand dunes on the coast of Western Australia.



ION BEAM ANALYSIS OF METAL ION IMPLANTED SURFACES

by

P.J. Evans^a, J.W. Chu^{a,*}, E.P. Johnson^a, J.T. Noorman^a and D.K. Sood^b

**^a Australian Nuclear Science and Technology Organisation
PMB 1, Menai NSW, 2234, Australia**

**^b Royal Melbourne Institute of Technology,
GPO Box 2746V, Melbourne, VIC, 3001**

ABSTRACT

Ion implantation is an established method for altering the surface properties of many materials. While a variety of analytical techniques are available for the characterisation of implanted surfaces, those based on particle accelerators such as Rutherford backscattering (RBS) and nuclear reaction analysis (NRA) provide some of the most useful and powerful for this purpose. Application of the latter techniques to metal ion implantation research at Ansto will be described with particular reference to specific examples from recent studies. Where possible, the information obtained from ion beam analysis will be compared with that derived from other techniques such as Energy Dispersive X-ray (EDX) and Auger spectroscopies.

ION BEAM ANALYSIS OF METAL ION IMPLANTED SURFACES

INTRODUCTION

Ion beam analysis (IBA) offers a number of powerful diagnostic tools for the characterisation of modified surfaces. By means of Rutherford backscattering (RBS), nuclear reaction analysis (NRA) and elastic recoil detection (ERD), it is possible to determine the elemental composition of the near surface region as a function of depth. This capability makes them particularly useful for the analysis of thin films and implanted surfaces.

In 1989, Ansto's Applications of Nuclear Physics Program commenced a project on metal ion implantation (MII) research, primarily directed at engineering materials. The stimulus for this undertaking was the success achieved, in the years immediately preceding it, by several groups in developing high current metal ion sources. One such source, first described by Brown and co-workers¹ was that based on a metal vapour vacuum arc (MEVVA). This type of source, which appeared to offer both simplicity and reliability, is capable of generating ions of a wide range of metallic materials together with some semiconductors (i.e. Si and Ge) and non-metals (i.e. C). In addition, its high ion beam currents make it particularly suitable for high dose applications. For these reasons, the MEVVA ion source was selected for our work.

The initial phase of the MII project involved development of an ion implanter equipped with a MEVVA ion source. The completion of this phase in early 1991 marked the beginning of our applications oriented research which has included detailed studies on the MII of several systems. During this latter phase, IBA has been extensively used to determine implant distributions and to characterise surfaces subjected to post implantation testing. The purpose of the present note is to illustrate this work with particular reference to studies on specific systems.

EXPERIMENTAL

The implantation system and experimental procedure have been described in detail previously^{2,3}. Specimens were polished to 1/4 μ diamond and ultrasonically cleaned prior to implantation. The ion source was operated at ion beam currents (pulsed) of 40 - 100 mA, pulse repetition frequencies of 1 - 10 Hz and extractor voltages of 20 or 25 kV. The latter in conjunction with the average ion charge states⁴ yielded mean ion energies in the range 40 - 60 keV. Ion doses ranged from 3.5×10^{14} - 1.5×10^{17} cm⁻² for tungsten implanted GC and between 1×10^{15} - 2×10^{17} cm⁻² type 2011 Al alloy implanted with Ti and Cr ions.

RBS spectra of implanted substrates were obtained using a 2 MeV $^4\text{He}^+$ incident beam, which was normal to the target, and a scattering angle of 169°. The oxidation of metal surfaces has been monitored by measuring the alpha particle yield from the reaction $^{16}\text{O}(^3\text{He},\alpha)^{15}\text{O}$. A beam of 2.4 MeV ^3He ions was directed onto the targets which were inclined at 45° to the incident beam and the charged particle spectra measured at 90°. Further details of the oxygen measurements appear elsewhere³. Finally, elastic recoil detection (ERD) of the hydrogen distribution in specimens exposed to an rf plasma was performed using a 2.5 MeV ^4He beam.

RESULTS AND DISCUSSION

Recently, we have investigated the implanted of glassy carbon (GC) with tungsten ions focussing on both the wear properties and surface characterisation of the modified material. In an extension of this work, W implanted GC has been exposed to an rf hydrogen plasma for varying times. The hydrogen content of the exposed surfaces was then determined by ERD. For W implanted GC, the

hydrogen content after a 1 hour exposure was found to be $10 \pm 10\%$. In contrast, C^+ implanted GC yielded a corresponding increase of $30 \pm 15\%$. The lower hydrogen content in the tungsten modified material suggested the observed inhibition was due to a chemical effect which slowed the formation of hydrocarbons thereby reducing surface erosion.

Aluminium and its alloys are one of the most widely used group of metals. While generally exhibiting good corrosion resistant properties, specific alloys are susceptible to corrosion in some applications. For this reason, various protective treatments, including ion implantation, have been investigated as a means of improving the operational performance of these metals. In alloys of the 2000 series, copper is the main alloying element with percentage compositions by weight in the range 5.0 - 6.0%. Recently, we investigated the oxidation of this alloy implanted with Ti and Cr ions³. The oxygen uptake as a function of time at 500°C was monitored using nuclear reaction analysis. RBS analysis was also performed on both the as-implanted and oxidised specimens. Typical RBS spectra for Ti and Cr implanted substrates, prior to and after oxidation for 1 hour, are shown in Figs. 1 and 2 respectively. The main features of note here are the redistribution of particular alloying elements (Pb/Bi and Cu) and differences in the behaviour of the implant ions following high temperature oxidation. In order to distinguish between purely thermal effects and those associated with the oxidation process, Ti and Cr implanted specimens were vacuum annealed at 500°C for 1 hour. RBS spectra of the as-implanted and annealed surfaces are presented in Figs. 3 and 4 for Ti and Cr respectively. These spectra indicate that the redistribution of Cr, Cu and Pb/Bi apparent in the oxidised samples (Figs. 1 and 2) is largely due to thermal effects. Furthermore, comparison of the results in Figs. 3 and 4 with the spectrum of a vacuum annealed virgin sample of 2011 Al shown in Fig. 5 suggests that the redistribution of Cu and Pb/Bi occurred to a greater extent in the implanted material. This is attributed to the presence of ion beam induced damage in the implanted layer which promotes diffusion or segregation of particular alloying elements.

CONCLUSION

In the foregoing, we have described the application of IBA techniques to the characterisation of ion implanted surfaces. Either individually or in conjunction with other surface analytical methods, techniques such as RBS, NRA and ERD are capable of providing key information on the nature of modified surfaces. Our studies of 2011 Al oxidation and annealing offer a good illustration of this approach. In this instance, RBS measurements were combined with scanning electron microscopy and EDX analysis to distinguish between different oxidative and thermal processes from which we were able to propose a model for the structure of the oxidised implanted surface.

ACKNOWLEDGEMENTS

The award of an AINSE Post-doctoral Fellowship to J.-W. Chu and the support of AINSE are gratefully acknowledged.

REFERENCES

1. I.G. Brown, J.E. Galvin, B.F. Gavin and R.A. MacGill, *Rev. Sci. Instrum.*, **57**, 1069 (1986).
2. A. Hoffman, P.J. Evans, D.D. Cohen and P.J.K. Paterson, *J. Appl. Phys.*, **72**, 5687 (1992).
3. J.W. Chu, N. Dytlewski, P.J. Evans and D.K. Sood, *Nucl. Instrum. Meth. B*, **B80/81**, 289 (1993).
4. I.G. Brown, B. Feinberg and J.E. Galvin, *J. Appl. Phys.*, **63**, 4889 (1988).

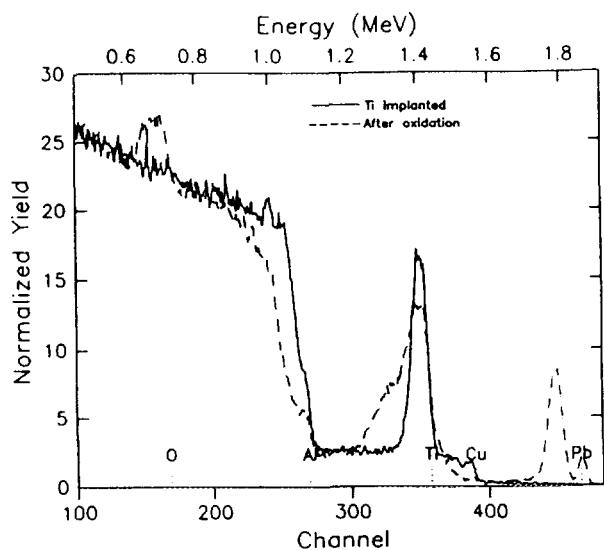


Figure 1 - RBS spectra of Ti implanted (dose = $2 \times 10^{17} \text{ cm}^{-2}$) 2100 Al specimen prior to (solid line) and after 1 hour oxidation at 500°C (broken line).

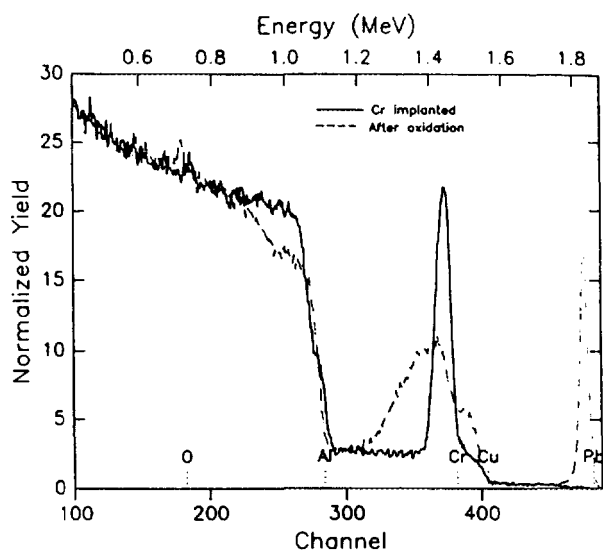


Figure 2 - RBS spectra of Cr implanted (dose = $2 \times 10^{17} \text{ cm}^{-2}$) 2100 Al specimen prior to (solid line) and after 1 hour oxidation at 500°C (broken line).

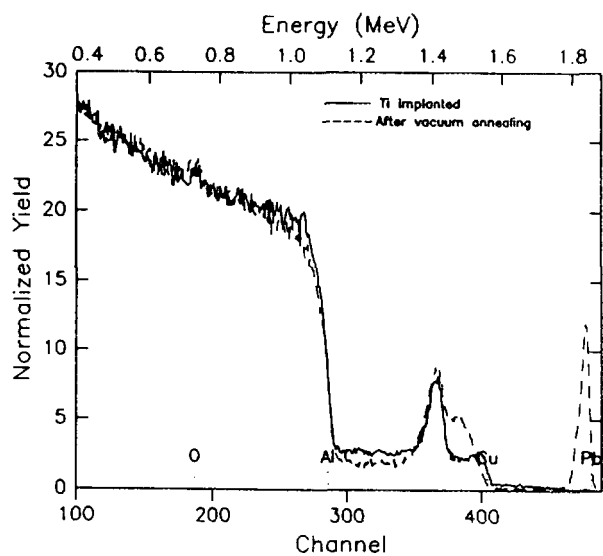


Figure 3 - RBS spectra of Ti implanted (dose = $1 \times 10^{17} \text{ cm}^{-2}$) 2100 Al specimen prior to (solid line) and after 1 hour vacuum anneal at 500°C (broken line).

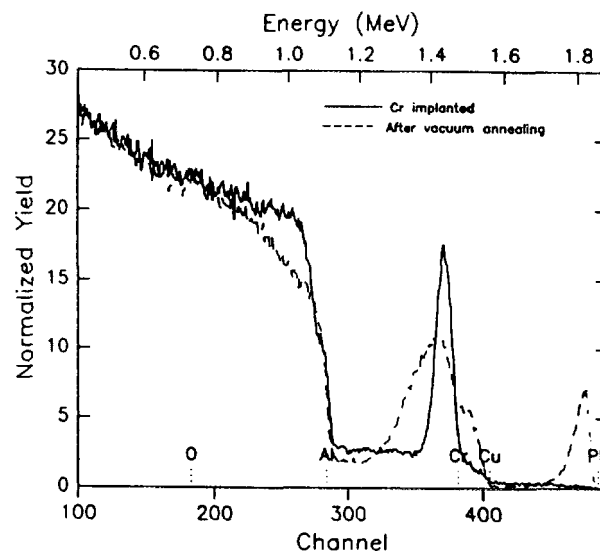


Figure 4 - RBS spectra of Cr implanted (dose = $1.5 \times 10^{17} \text{ cm}^{-2}$) 2100 Al specimen prior to (solid line) and after 1 hour vacuum anneal at 500°C (broken line).

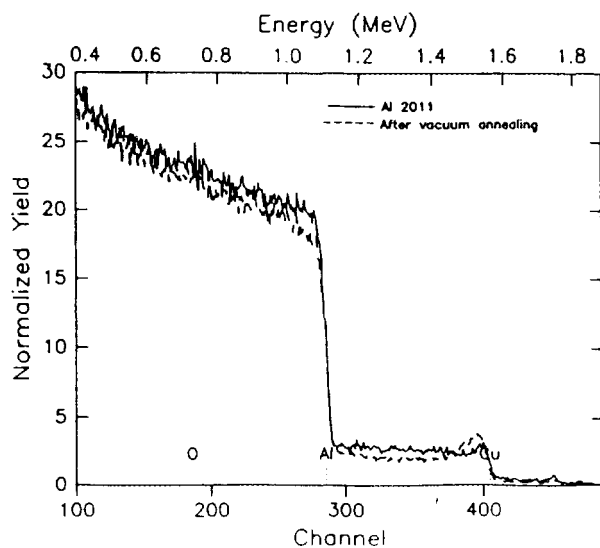


Figure 5 - RBS spectra of polished virgin 2100 Al specimen prior to (solid line) and after 1 hour vacuum anneal at 500°C (broken line).



Lattice Location of Impurities in Semiconductors: A RBS/Channeling and Proton-Induced X-Ray Emission Study

Per Kringhøj

Department of Electronic Materials Engineering, Research School of Physical Sciences and Engineering, The Australian National University, Canberra, ACT, 0200, Australia.

Rutherford backscattering spectrometry (RBS)/channeling and proton-induced x-ray emission (PIXE) are two well established and characterised techniques. Over the last three decades RBS/channeling measurements has been performed to extract the substitutional fraction of impurities in both elemental and compound semiconductors. However, due to the limitation of RBS, only elements heavier than the host crystal can be examined (except for a few elements, where a nuclear reaction or a resonance can be used). In silicon this limitation is acceptable, due to the low mass of Si, but in the III-V compounds (e.g. InP), the technique is limited to a few elements of hardly no technological or fundamental interest. One can overcome this by combining RBS/channeling with PIXE, where PIXE is applied to detect elements with a mass lower than the host crystal.

In the present work, the lattice location of Ge in InP has been studied and compared to the group-III impurity Ga, and the group-VI impurity Se which is known to be a donor [1-4]. The (RBS)/channeling technique has been used to detect not only the substitutional fraction, but also the relative population of the two sublattices. The half-width is approximately equal to the characteristic angle, ψ_1 [5]:

$$\psi_1 = \left(\frac{2Z_1 Z_2 e^2}{Ed} \right)^{1/2} \quad (1)$$

where Z_1 and Z_2 are the atomic number of the ion and the crystal atoms, respectively, E is the ion energy, and d is the atomic spacing in the row. In a direction, where the two species of the compound form separate rows (e.g. $\langle 110 \rangle$), the characteristic angle is different for the two types of strings due to the large difference in Z . By comparing the channeling angular width for the impurity and the host atoms, the substitutional site may be identified. In the $\langle 111 \rangle$ direction, where the string consists of alternating In and P atoms, the characteristic angle for the two compound species is equal and the angular widths are consequently also equal.

LEC-grown p-type InP doped with Zn to a level of $2 \cdot 10^{16} \text{ cm}^{-3}$ was multiple-energy ion implanted with either Ga, Ge, or Se. The samples were kept at 200°C during implantation and the total dose implanted was $3.8 \cdot 10^{15} \text{ cm}^{-2}$, resulting in a flat profile with a peak concentration of $1 \cdot 10^{20} \text{ cm}^{-3}$ over a depth of $\sim 400 \text{ nm}$, as deduced from secondary-ion mass spectrometry (SIMS). Ge implanted samples were also co-implanted with P to the same dose, in order to overlap the Ge profile. Subsequently the samples were annealed using rapid thermal annealing (RTA). The annealing was done at 880°C for one sec. The RBS/channeling-PIXE setup is shown schematically in Fig. 1 together with a typical x-ray spectrum. In contrast to the RBS technique, the PIXE technique provides no depth resolution. Hence, in order to compensate for this in a comparison between channeling dips from PIXE and RBS, the RBS signal for In is integrated over a depth corresponding to the depth distribution of the impurity. The carrier concentration and mobility profiles were obtained by differential Hall/resistivity measurements using the Van der Pauw technique. Chemical depth distribution of the dopants was obtained by SIMS.

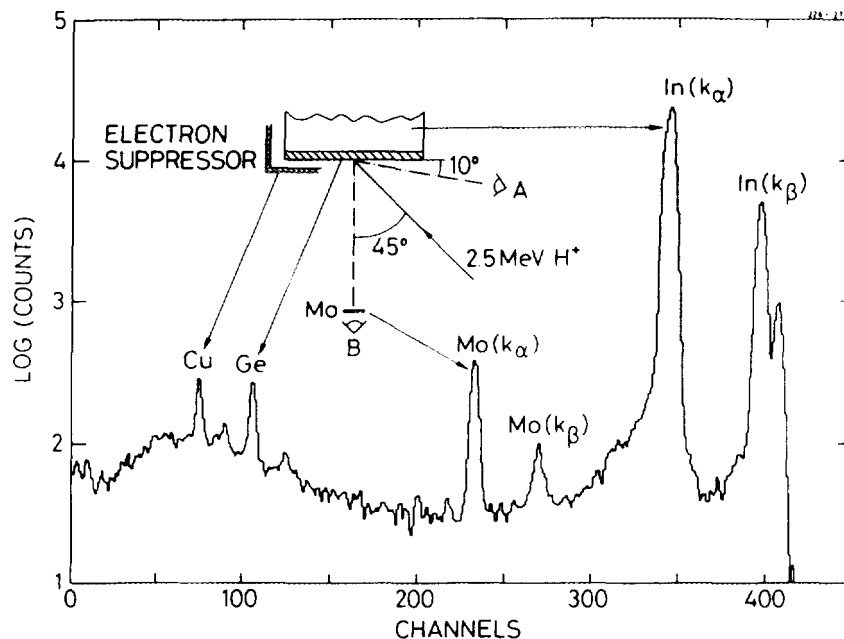


Fig.1. Schematic outline of the RBS/channeling-PIXE setup. A represents the RBS detector and B the Si(Li) detector for x-ray.

The overall substitutional fraction of Se, Ge, and Ga can be extracted from the angular scans in the $\langle 111 \rangle$ direction. The $\langle 111 \rangle$ angular scans for Se, Ge, and Ga are shown in Fig.2. The figure shows the normalised signal from the impurity together with the RBS In signal. The half-width, $\psi_{1/2}$ and the minimum yield, χ_{\min} for the impurities and In are shown in Table 1 together with the substitutional fraction, f_{eq} . The substitutional fraction corresponding to the three impurities is observed to be $\sim 100\%$. The half-width of the In yield and the impurity yield are observed to be identical, demonstrating the following: i) The impurity is positioned on substitutional sites; ii) the x-ray channeling dip is identical to the RBS channeling dip. Also shown are the angular scans in the $\langle 110 \rangle$ direction for the three dopants. The angular scans for Ga and In in the $\langle 110 \rangle$ direction are almost identical, as seen in Fig.2(c), thus demonstrating that Ga is occupying the In position.

The half-width of the angular scan for P cannot be measured in our setup, and it is therefore not possible to compare the half-widths for Se and Ge, to the half-width of P. However, as the half-width is proportional and almost equal to the critical angle, the value can be estimated by using the value for $\psi_{1/2}(\text{In})$ and Eq.(1):

$$\psi_{1/2}(\text{P}) = \psi_{1/2}(\text{In}) \sqrt{\frac{Z_{\text{P}}}{Z_{\text{In}}}} \quad (2)$$

This results in a value of 0.24 for $\psi_{1/2}(\text{P})$ which is identical to the measured value of $\psi_{1/2}(\text{Se})$ (see Table 1). This leads to the conclusion that the angular half-widths for the P and Se yields are equal and, thus, that the Se atoms are preferentially occupying P-lattice positions. The channeling angular scan for Ge is shown in Fig.2(b) and indicates that the Ge atoms are distributed between both types of lattice sites as the value of the angular width is midway between the values of P and In. The relative site population, x of the two sublattices can be extracted from the following formula:

$$\psi_{1/2}(\text{Ge}) = x \cdot \psi_{1/2}(\text{In}) + (1 - x) \cdot \psi_{1/2}(\text{P}) \quad (3)$$

The relative site population for Ge extracted is $x = 0.50 \pm 0.08$! Where, instead of $\psi_{1/2}(P)$, the value for $\psi_{1/2}(Se)$ has been used. The channeling angular scan for samples co-implanted with P is relatively higher and shows that the substitutional Ge fraction is situated on the In lattice position, however the substitutional fraction is only $\sim 80\%$ in the Ge plus P case.

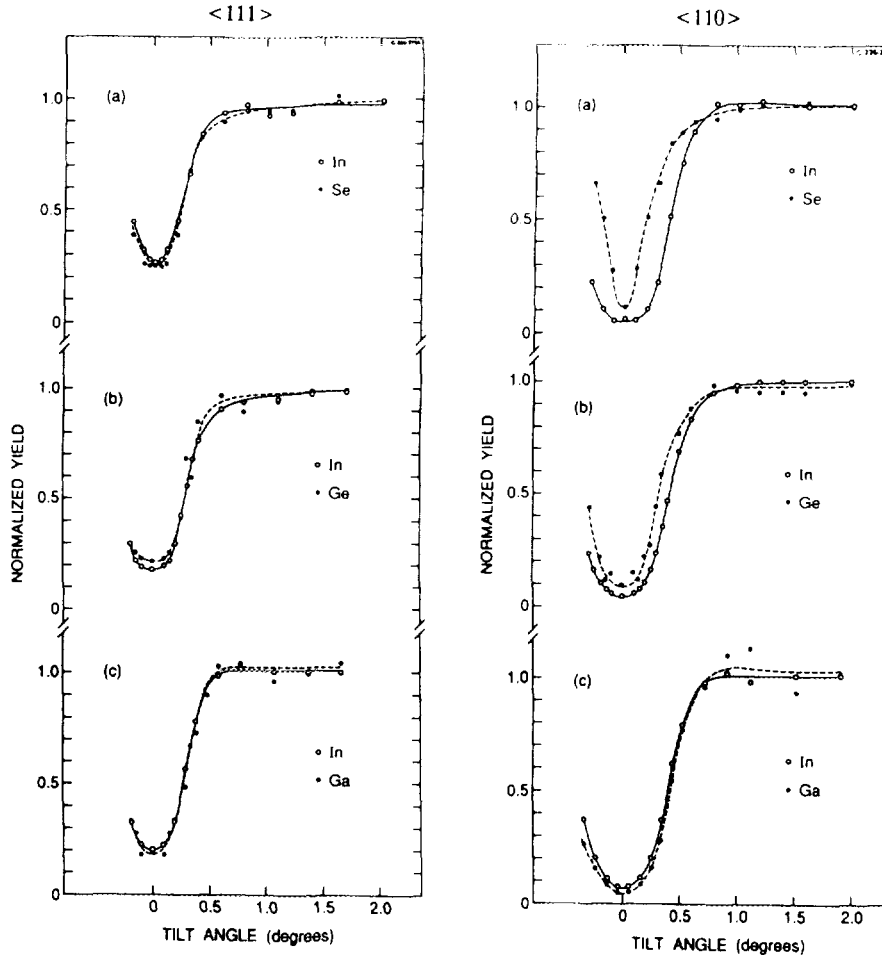


Fig. 2. The $\langle 111 \rangle$ and $\langle 110 \rangle$ channeling angular scans from samples implanted with Se (a), Ge (b), and Ga (c) together with the In signal.

Table 1. Channeling angular half-widths together with χ_{\min} values obtained for the two indicated directions. For the $\langle 111 \rangle$ direction, f_{eq} is also given.

	$\langle 110 \rangle$		$\langle 111 \rangle$		f_{eq}
	$\psi_{1/2}$	$\chi_{\min}(\%)$	$\psi_{1/2}$	$\chi_{\min}(\%)$	
In	0.43 ± 0.01	7.9 ± 0.1	0.32 ± 0.01	20.2 ± 0.3	...
Ga	0.44 ± 0.01	5 ± 3	0.32 ± 0.01	18 ± 5	1.03 ± 0.06
In	0.44 ± 0.01	5.1 ± 0.1	0.31 ± 0.01	19.1 ± 0.2	...
Ge	0.43 ± 0.01	10 ± 2	0.32 ± 0.01	21 ± 4	0.98 ± 0.05
In	0.43 ± 0.01	5.2 ± 0.1	0.30 ± 0.01	26 ± 1	..
Se	0.24 ± 0.01	11 ± 2	0.30 ± 0.01	25 ± 6	1.01 ± 0.08
In	0.43 ± 0.01	5.0 ± 0.1	0.31 ± 0.01	13 ± 2	..
Ge+P	0.44 ± 0.01	23 ± 3	0.32 ± 0.01	28 ± 6	0.83 ± 0.08

In order to investigate the electrical characteristics of the Ga-, Ge-, and Se-implanted samples, differential Hall/resistivity measurements were performed. The carrier concentration and mobility profiles of Ge- and Se-implanted samples are shown in Fig.3, together with the chemical profile of Se measured with SIMS. The carrier concentration profiles follow the chemical profile, but a fraction of the dopants is electrically inactive. The mobility profiles also reflect the chemical profile, illustrating that the main scattering mechanism is due to the ionised dopants, as also predicted theoretically by [6].

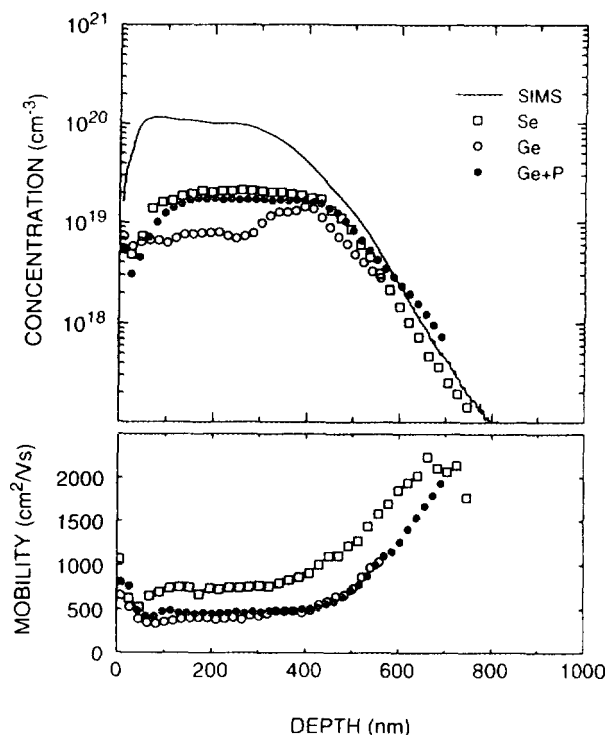


Fig.3 Carrier concentration and mobility profiles for Ge, Ge plus P, and Se.

The maximum carrier concentration is $2 \cdot 10^{19}$ and $1 \cdot 10^{19} \text{ cm}^{-3}$, respectively, for Se and Ge. Despite the lower carrier concentration in the Ge case, the mobility is a factor of two lower. This can only be due to a higher concentration of ionised scattering centres in the case of Ge, indicating that Ge is acting as both acceptor and donor. Co-implantation of P, however leads to a significant improvement in the electrical activity, with almost identical mobility profile (see Fig.3). The differential Hall/resistivity data for Ge-single and Ge plus P implanted samples are in good agreement with the channeling result, where amphoteric behaviour is seen only in the Ge-single case. From the channeling data presented above, it can be unambiguously concluded that all three dopants are located exclusively on substitutional sites, and that Ga is occupying the In position, Se the P position, and that Ge is distributed equally between both sublattices. Thus, Ge has amphoteric behaviour. This phenomenon can be reduced by co-implanting P, however, this leads to a decrease in the solubility of Ge in InP.

References

- (1) S.S. Gill, B.J. Sealy, *J. Appl. Phys.* **56**, 1189 (1984).
- (2) J.D. Woodhouse, J.P. Donnelly, P.M. Nitishin, E.B. Owens, and J.L. Ryan, *Solid State Electron.* **27**, 677 (1984).
- (3) J.P. Donnelly, C.E. Hurwitz, *Solid State Electron.* **23**, 943 (1980).
- (4) T. Inada, S. Tako, and Y. Yamamoto, *J. Appl. Phys.* **52**, 4863 (1981).
- (5) J. Lindhard, *K. Dan. Vidensk. Selsk. Mat. Fys. Medd.* **34**, No 14 (1965).
- (6) D.A. Anderson, N. Apsley, P. Davies, and L. Giles, *J. Appl. Phys.* **58**, 3059 (1985).



Identification of Defects in GaAs Induced by 1 MeV Electron Irradiation

S.T.Lai, B.D.Nener, L.Faraone, and A.G.Nassibian
Department of Electrical and Electronic Engineering
The University of Western Australia, Nedlands, WA 6009.
M.A.C.Hotchkis
ANSTO, Private Mail Bag 1, Menai, NSW 2234.

Abstract

This paper shows that (i) 1 MeV electron irradiation on n-type vapor phase epitaxial (VPE) GaAs creates three electron traps E1, E2 and EL6, and results in the splitting of the EL2 center into two levels EL2-A and EL2-B, and (ii) a 15 min. isochronal anneal results in the annihilation of the E1 and E2 traps, a reduction in EL6 trap concentration, and the return of EL2 to a single level EL2-A. A defect model is outlined which correlates with the observed results.

Introduction

Defect studies have become an important subject for both semiconductor material and device researchers mainly because of the dominant effect they have on the performance of semiconductor devices. To understand the origin of these defects, the first step is to create known defects and then identify them by determining their characteristics. Several methods such as plastic deformation, quenching and irradiation with electrons, protons, neutrons, ions, and gamma rays have been used to create defects in semiconductor materials. In this paper, we present capacitance-voltage (C-V) and deep-level transient spectroscopy (DLTS) results on a nonirradiated control sample, and 1 MeV electron irradiated samples, both before and after isochronal annealing. A detailed description of the sample fabrication, measurement set-up, and C-V and DLTS analysis are outlined in earlier publications [1-3].

Experimental Results and Conclusions

Electron irradiation is found to create acceptor traps, which act as recombination centers and compensate the shallow donors in the n-GaAs sample, and thus decreasing the free carrier concentration with increasing electron fluence. Eventually, at high electron fluence, the free carrier concentration reduces to such an extent that the whole $4.27 \mu\text{m}$ of upper n-active layer is fully depleted even at zero bias at room temperature.

Figures 1 and 2 show the DLTS Arrhenius plots from 20 K to 300 K for the control sample (N-1) and an irradiated sample (I-1), respectively. Three electron traps E1, E2 and EL6, and an additional level EL2-B were observed in the irradiated samples. The trap parameters of samples N-1, and I-1 to I-4 are tabulated in Table 1. A higher defect introduction rate was obtained for E1, E2 and EL6 as compared to the EL3 trap and EL2 center.

15 min. and 50°C step isochronal anneals were carried out on a high fluence (8.0×10^{14} e cm⁻²) sample (I-5). An increase in free carrier concentration was observed after 250°C annealing. Figure 3 shows the effect of annealing on the free carrier concentration versus temperature of sample I-5, while Table 2 indicates the trap parameters of sample I-5 with annealing. From these results, it is evident that E1 and E2 are annihilated after a 290°C anneal, the EL6 trap concentration rapidly decreases with annealing temperature but stays constant after 270°C, and EL2 returns back to a single level after a 270°C anneal. Based on these results, E1 and E2 appear to be intrinsic defects related to V_{As} (arsenic vacancy) and As_i (arsenic interstitial) in close proximity with each other, known as a correlated or Frenkel pair. These defects are annihilated by the mobile As_i recombining with the V_{As} . This model is supported by the fact that (i) the V_{Ga} and Ga_i are unstable and they recombine immediately after their creation even at low temperature [4], (ii) E1 and E2 traps are annihilated together by first order kinetics, (iii) the 270°C annealing temperature corresponds to the temperature at which the As_i becomes mobile, and (iv) the activation energies and capture cross sections remain constant during annealing. The complex EL2 defect created by the electron irradiation is probably an $As_{Ga}-As_i$ (arsenic antisite and arsenic interstitial) defect because during irradiation some of the As_i becomes mobile and is trapped by the As_{Ga} present in the sample. The annealing causes the complex $As_{Ga}-As_i$ to dissociate and the mobile As_i starts to migrate and eventually recombines with the V_{As} , likely to be EL6, in the sample.

References

1. S.T. Lai, B.D. Nener, L. Faraone, A.G. Nassibian and M.A.C. Hotchkis, *J. Appl. Phys.*, **73**, 640, (1993).
2. S.T. Lai, B.D. Nener, L. Faraone and A.G. Nassibian, (submitted to *J. Appl. Phys.* for publication).
3. B.D. Nener, S.T. Lai, L. Faraone and A.G. Nassibian, *IEEE Trans. Instru. and Meas.*, (August 1993).
4. D. Pons and J.C. Bourgoin, *J. Phys. C*, **18**, 3839, (1985).

Table 1: Characteristics of deep-level defects in n-type GaAs induced by electron irradiation (N stands for nonirradiated or control sample and I stands for irradiated samples with the electron fluence given in $e\text{ cm}^{-2}$).

Defects	Parameters	N-1	I-1 1.1×10^{14}	I-2 1.5×10^{14}	I-3 2.1×10^{14}	I-4 3.1×10^{14}
EL2 or EL2-A	$\Delta E(\text{meV})$ $\sigma_n(10^{-12}\text{ cm}^2)$ N_t/N_d	(815±2) 0.125 0.0521	(821±8) 0.271 0.0230	(810±7) 0.147 0.0225	(819±4) 0.235 0.0347	(820±4) 0.243 0.0352
EL2-B	$\Delta E(\text{meV})$ $\sigma_n(10^{-12}\text{ cm}^2)$ N_t/N_d	— — —	(843±14) 3.41 0.0359	(843±13) 2.47 0.0384	(840±7) 2.29 0.0371	(849±3) 3.08 0.0527
EL3	$\Delta C(\text{meV})$ $\sigma_n(10^{-15}\text{ cm}^2)$ N_t/N_d	(419±2) 0.394 0.0013	(422±3) 0.427 0.0017	(418±5) 0.342 0.0019	(426±1) 0.576 0.0023	(425±4) 0.610 0.0025
EL6	$\Delta E(\text{meV})$ $\sigma_n(10^{-15}\text{ cm}^2)$ N_t/N_d	— — —	(335±2) 2.03 0.0617	(325±3) 1.00 0.0651	(334±3) 2.54 0.1300	(336±5) 2.50 0.2260
E2	$\Delta E(\text{meV})$ $\sigma_n(10^{-14}\text{ cm}^2)$ N_t/N_d	— — —	(130±2) 4.80 0.2620	(131±2) 4.60 0.3045	* * *	* *
E1	$\Delta E(\text{meV})$ $\sigma_n(10^{-16}\text{ cm}^2)$ N_t/N_d	— — —	(34±1) 1.80 0.3865	(33±1) 0.95 0.4688	* *	* *

Table 2: Isochronal annealing characteristics of deep-level defects in n-type GaAs induced by electron irradiation (sample I-5).

Annealing Temperature	Parameters	EL2 Center	EL3 Trap	EL6 Trap	E2 Trap	E1 Trap
250°C	$\Delta E(\text{meV})$	A: (821±3) B: (870±5)	(418±12) —	(358±2) —	* *	* *
	$\sigma_n(\text{cm}^2)$	A: 1.34×10^{-13} B: 0.65×10^{-11}	0.03×10^{-14} —	0.56×10^{-14} —	— —	— —
	N_t/N_d	0.0750	0.0018	0.1790	—	—
260°C	$\Delta E(\text{meV})$	A: (826±2) B: (891±1)	(456±6) —	(356±2) —	(129±1) —	* *
	$\sigma_n(\text{cm}^2)$	A: 1.82×10^{-13} B: 2.00×10^{-11}	0.15×10^{-14} —	0.59×10^{-14} —	4.44×10^{-14} —	— —
	N_t/N_d	0.0670	0.0015	0.0300	0.1490	—
270°C	$\Delta E(\text{meV})$	A: (824±1)	(489±6)	(396±3)	(128±2)	(32±1)
	$\sigma_n(\text{cm}^2)$	A: 1.51×10^{-13}	0.95×10^{-14}	5.31×10^{-14}	3.48×10^{-14}	1.47×10^{-16}
	N_t/N_d	0.0557	0.0016	0.0110	0.1120	0.1630
280°C	$\Delta E(\text{meV})$	A: (829±1)	(500±5)	(403±2)	(128±1)	(32±1)
	$\sigma_n(\text{cm}^2)$	A: 1.83×10^{-13}	1.63×10^{-14}	4.00×10^{-14}	3.17×10^{-14}	1.08×10^{-16}
	N_t/N_d	0.0555	0.0020	0.0090	0.0063	0.0066
290°C	$\Delta E(\text{meV})$	A: (825±1)	(510±3)	(395±1)	+	+
	$\sigma_n(\text{cm}^2)$	A: 1.64×10^{-13}	3.00×10^{-14}	5.15×10^{-14}	+	+
	N_t/N_d	0.0545	0.0040	0.0087	+	+
300°C	$\Delta E(\text{meV})$	A: (825±1)	—	(394±3)	+	+
	$\sigma_n(\text{cm}^2)$	A: 1.52×10^{-13}	—	4.18×10^{-14}	+	+
	N_t/N_d	0.0530	—	0.0087	+	+

* Cannot be measured experimentally since the extrinsic donors are fully compensated by the acceptor traps induced by electron irradiation.

+ The defects are annihilated by annealing.

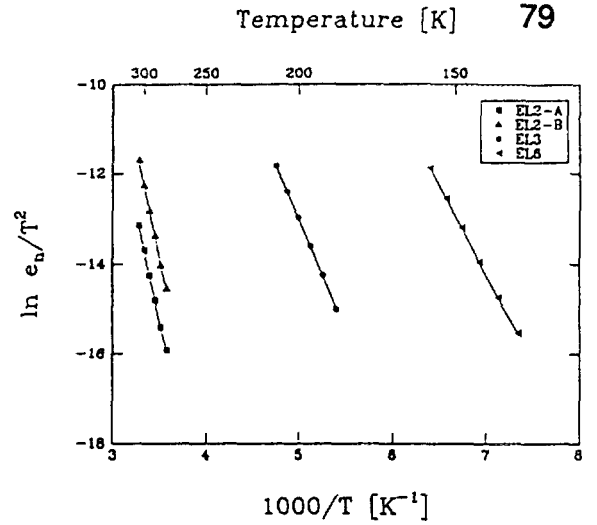
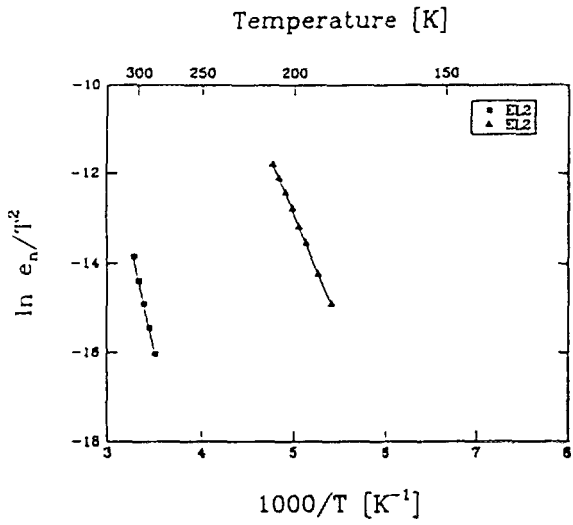


Figure 1. Arrhenius plot showing the deep levels of sample N-1.

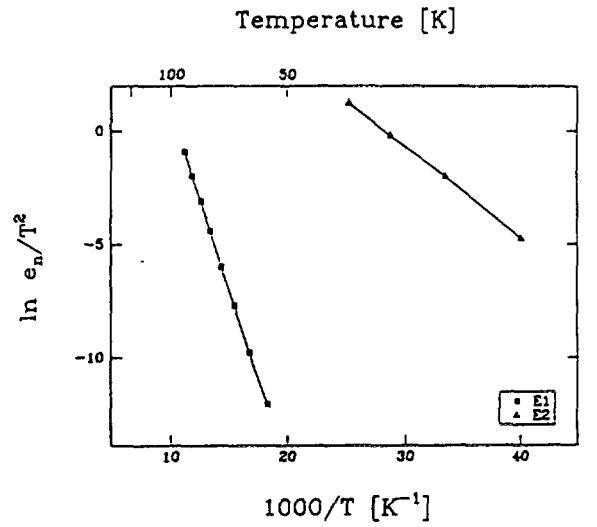
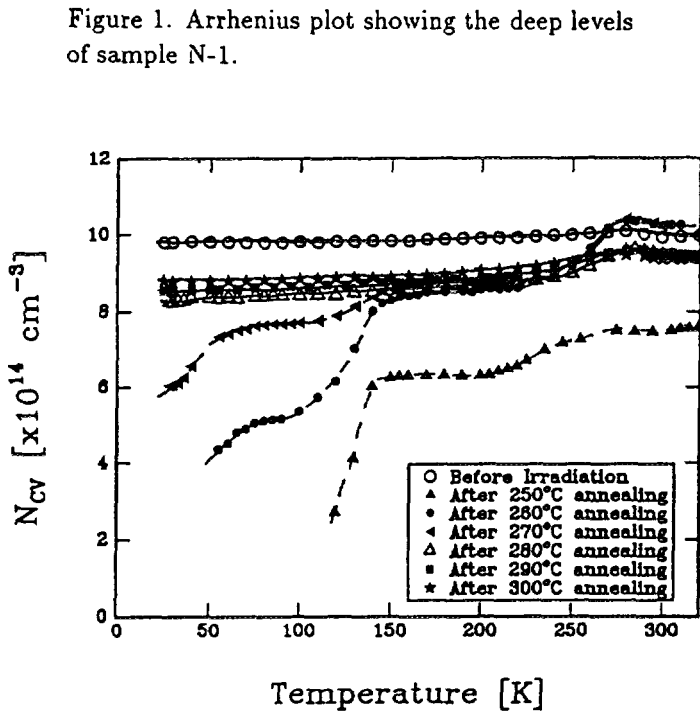


Figure 2. Arrhenius plots showing the deep levels of sample I-1.

Figure 3. Plots of free carrier concentration (N_{CV}) versus temperature of sample I-5 after 15 min. isochronal annealing.

HEAVY ION RECOIL SPECTROMETRY OF $\text{Si}_x\text{Ge}_{1-x}$ THIN FILMS

Scott R. Walker¹, Peter N. Johnston¹, Ian F. Bubb¹, David D. Cohen², Nick Dytlewski², Mikael Hult³, Harry J. Whitlow³, Carina Zahring⁴ and Mikael Östling⁴

¹Department of Applied Physics, Royal Melbourne Institute of Technology, GPO Box 2476V, Melbourne 3001, Australia

²Australian Nuclear Science and Technology Organisation, PMB 1, Menai 2234, Australia

³Department of Nuclear Physics, Lund Institute of Technology, Sölvegatan 14, S-223 62, Lund, Sweden

⁴Department of Solid State Electronics, The Royal Institute of Technology, Box 1298, S-164 28, Kista, Sweden

ABSTRACT

Mass and energy dispersive recoil spectrometry employing 77 MeV ^{127}I ions from ANTARES (FN Tandem) facility at Lucas Heights has been used to examine the isotopic composition of samples of $\text{Si}_x\text{Ge}_{1-x}$ grown at the Australian National University by Electron Beam Evaporation (EBE). The recoiling target nuclei were analysed by a Time Of Flight and Energy (TOF-E) detector telescope composed of two timing pickoff detectors and a surface barrier (energy) detector. From the time of flight and energy, the ion mass can be determined and individual depth distributions for each element can be obtained. Recoil spectrometry has shown the presence of oxygen in the $\text{Si}_x\text{Ge}_{1-x}$ layer and has enabled the separate determination of energy spectra for individual elements.

INTRODUCTION

Over the past few decades Rutherford Backscattering Spectrometry (RBS) has been used extensively to study the composition of semiconductor device materials. However, RBS is not easily applied to situations involving light element impurities in heavier elements. The determination of light element concentration and distribution, whether dopant or impurity, is an important problem in many semiconductor compounds. Mass and energy dispersive Recoil Spectrometry (RS) has recently found application in such situations where RBS is inapplicable, e.g. [1]. The technique involves the use of a high energy heavy ion beam and employs a Time of Flight and Energy (TOF-E) detector to extract mass and depth

information from the recoiling target nuclei. Amorphous layers of

$\text{Si}_x\text{Ge}_{1-x}$ were grown for potential optoelectronic device applications by Electron Beam Evaporation (EBE) at the Australian National University. It was suspected that oxygen was present as an impurity in significant quantities in these layers. Recoil Spectrometry has enabled the separation of the oxygen, silicon and

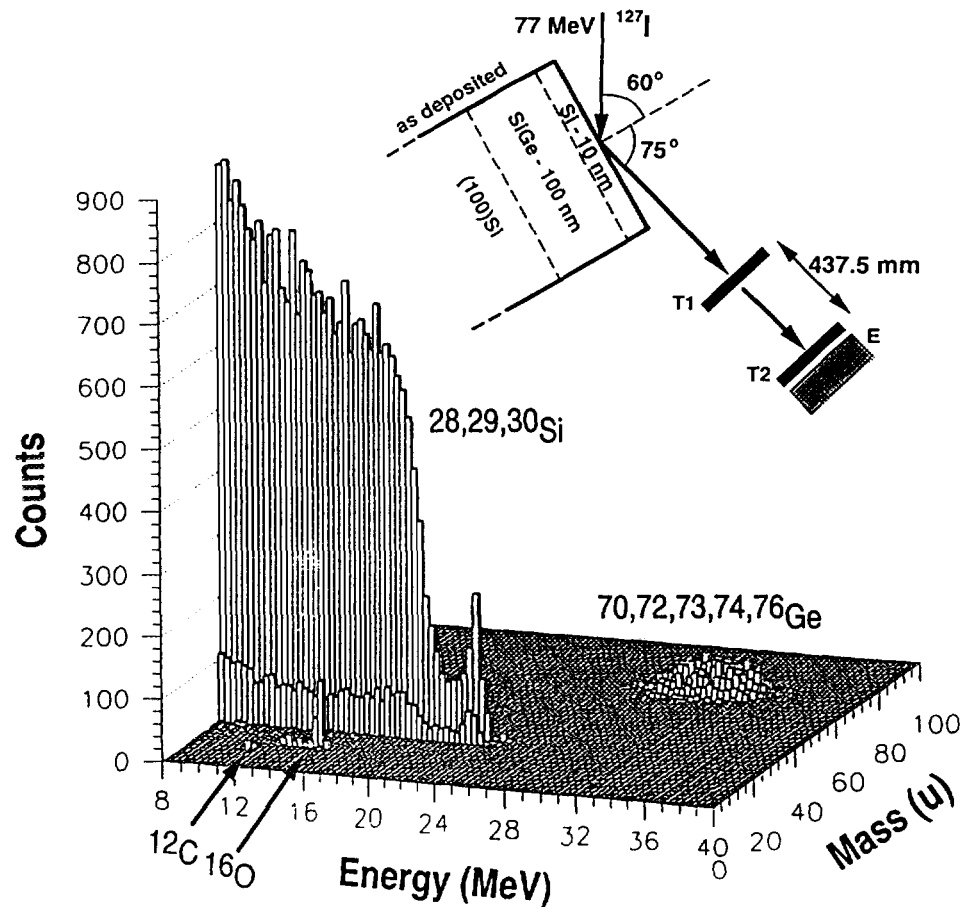


Figure 1. Recoil Spectrometry data for $\text{Si}_{0.2}\text{Ge}_{0.8}$ projected onto a histogram with axes E and M .

germanium signals and can provide individual energy spectra for Ge, Si and O in these structures, thus revealing the depth distribution of these elements.

EXPERIMENTAL

Seven samples of the structure 10 nm Si/100 nm Si_xGe_{1-x}/ (100) Si were analysed with x ranging from 0.2 to 0.9.

The Recoil Spectrometry experiments were performed at Lucas Heights using the ANTARES Tandem Accelerator. 77 MeV $^{127}\text{I}^{10+}$ ions impinged on the sample at an angle of 60° relative to the target surface normal and recoiling ions from the sample were detected, with a Time of Flight and Energy (TOF-E) detector subtending a solid angle of 0.10 msr, at 45° to the incident beam (Fig. 1). The spectrometer consisted of two time pickoff detectors separated by a flight length of 437.5 mm and a 100 mm² ion implanted Si detector [2-4]. The time detectors functioned by the detection of electron emission from the passage of recoil ions through a thin carbon foil ($\approx 3 \mu\text{g}/\text{cm}^2$) and employed a mirror electrode configuration to provide isochronous electron trajectories in order to minimise the electron path effect on time resolution [2,4]. The experiments used a conventional electronic instrumentation arrangement, as used in previous experiments [3,4], however the instrumentation included a second Time-to-Amplitude Converter (TAC), to examine the time resolution of the energy detector.

DATA ANALYSIS

The data from the experiment were examined and manipulated using the CERN data analysis package, PAW (Physics Analysis Workstation) [5].

For non-relativistic particles of mass m ,

$m = \frac{2E}{L^2} t^2$ where t is the time taken to travel the flight length, L , and the kinetic energy of the detected ion, T , can be related to the pulse height from the Si detector, E .

Experimentally the signals from recoiling ions of differing mass are separated using the transformation:

$$M = CE(t - t_0)^2$$

Where t is the output from the first TAC and t_0 represents the delay imposed on the time pickoff nearest the target [6]. Data for one measurement projected onto a histogram in the (E, M) plane is shown in Fig. 1.

M is not linearly related to m due to inevitable small electronic offsets and variations in the Si detector response with recoil mass. Simulations with TRIM 91 [8] using full damage cascades can be used to predict the fraction of the incident ion energy converted into ionisation (Fig. 2). It is the ionisation created in the Si detector that determines the pulse height.

The data for each separate element can be selected according to mass and projected onto the E axis. The data were quantitatively analysed using a variant of the RMIT software for Nuclear Reactions Analysis (NRA) [9]. Recoil Spectrometry can be considered to be a special case of NRA where the reaction is $X(^{127}\text{I}, X)^{127}\text{I}$ and the Q -value is 0. The spectrum is simulated for each isotope and fitted to the raw data using a non-linear least squares routine. Fig. 3 shows an energy spectrum and corresponding simulation for oxygen.

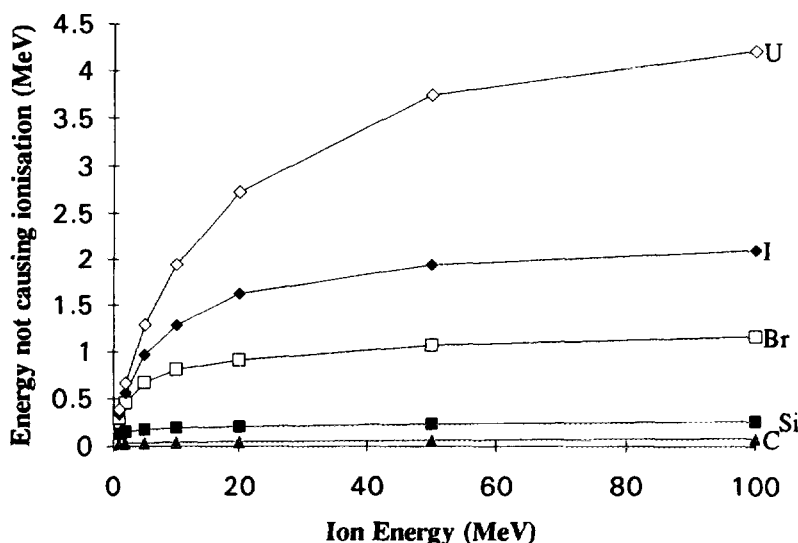


Figure 2. Energy not causing ionisation versus Ion energy for ^{238}U , ^{127}I , ^{81}Br , ^{28}Si and ^{12}C

RESULTS

The Mass versus Energy spectrum (Fig. 1) displayed features consistent with the known structure of the sample investigated. The Si signal contains a surface peak associated with the 10 nm Si layer, the decrease associated with the $\text{Si}_{0.2}\text{Ge}_{0.8}$ layer and the signal from the substrate. The Ge signal displays a broad peak from the 100 nm buried $\text{Si}_{0.2}\text{Ge}_{0.8}$ layer. The spectrum also displays a peak associated with surface carbon. The O spectrum (Fig. 3) exhibits two main features, a definite peak due to contamination at the surface and the bulk impurity signal from O contained in the $\text{Si}_x\text{Ge}_{1-x}$ layer.

The analysis software was used to fit simulations to the elemental energy spectra and quantify the atomic fractions. The seven $\text{Si}_x\text{Ge}_{1-x}$ samples analysed ranged in x from 0.2 to 0.9. The bulk oxygen content of the $\text{Si}_x\text{Ge}_{1-x}$ layers ranged from 2.6 to 5.0 at. %. O content increased with increasing x (decreasing Ge content).

CONCLUSIONS

Recoil Spectrometry is a technique with significant potential in the study of light elements incorporated in heavier element compounds. Recoil spectrometry has demonstrated that O is the contaminant in the $\text{Si}_x\text{Ge}_{1-x}$ layers studied in this work and has allowed the quantification of O levels. Recoil Spectrometry allows the determination of not only bulk concentration levels but provides significant depth information, with good discrimination of surface contamination. It enables the determination of separate elemental depth distributions in multi element materials.

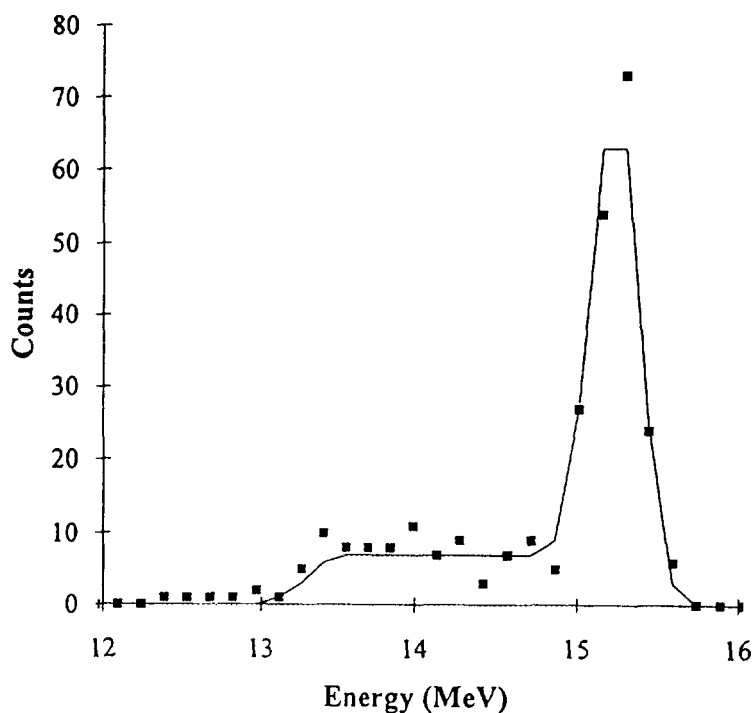


Figure 3. Simulation fit for oxygen spectra in $\text{Si}_{0.2}\text{Ge}_{0.8}$ sample from quantitative analysis

ACKNOWLEDGMENTS

The authors wish to acknowledge the support of the Australian Institute of Nuclear Science and Engineering (AINSE), the Australian Department of Industry, Technology and Commerce (DITAC), the Swedish Institute and the Craaford Foundation. SRW also acknowledges the support of an Australian Postgraduate Research Award and an AINSE Postgraduate Research Award. The $\text{Si}_x\text{Ge}_{1-x}$ was produced at the Australian National University Department of Electronic Materials Engineering.

REFERENCES

- [1] M. Hult, H.J. Whitlow and M. Östling, *Appl.Phys.Lett.* 60 (1992) 219.
- [2] H.J. Whitlow, in: *Proc. High Energy and Heavy Ion Beams in Materials Analysis*, Albuquerque, 1989, eds. J.R. Tesmer, C.J. Maggiore, M. Nastasi, J.C. Barbour and J.W. Mayer (Materials Research, Society, Pittsburgh, PA, U.S.A.) p.73 (1990).
- [3] H.J. Whitlow, B. Jakobsson and L. Westerberg. *Nucl.Instr.Meth.* A310 (1991) 636.
- [4] H.J. Whitlow, G. Possnert and C.S. Petersson, *Nucl.Instr.Meth.* B27 (1987) 448.
- [5] Application Software Group Computing and Networks Division at CERN, the PAW Manual Version 1.14 (July 1992), CERN, Geneva, Switzerland.
- [6] R. Ghetti, B. Jakobsson and H.J. Whitlow, *Nucl.Instr.Meth.* A317 (1992) 235.
- [8] P.N. Johnston, *Nucl.Instr.Meth.* B79 (1993) 506.
- [9] J.F. Ziegler, J.P. Biersack and U. Littmark, "The Stopping and Ranges of Ions in Solids 1, The Stopping and Ranges of Ions in Matter", ed. J.F. Ziegler, Pergamon Press, 1985.



STRAIN RELAXATION DURING SOLID-PHASE EPITAXIAL CRYSTALLISATION OF $\text{Ge}_x\text{Si}_{1-x}$ ALLOY LAYERS WITH DEPTH DEPENDENT Ge COMPOSITIONS

Wah-chung Wong, R.G. Elliman and P. Kringhoj

*Electronic Materials Engineering, Research School of Physical Sciences and Engineering,
Australian National University, Canberra, ACT 0200, AUSTRALIA.*

ABSTRACT

The solid-phase epitaxial crystallisation of depth dependent $\text{Ge}_x\text{Si}_{1-x}$ alloy layers produced by implanting Ge into Si substrates was studied. In-situ monitoring was done using time-resolved reflectivity (TRR), whilst post-anneal defect structures were characterised by Rutherford backscattering and channelling spectrometry (RBS-C) and transmission electron microscopy (TEM). Particular attention was directed at Ge concentrations above the critical concentration for the growth of fully strained layers. Strain relief is shown to be correlated with a sudden reduction in crystallisation velocity caused by roughening of the crystalline/amorphous interface.

INTRODUCTION

For certain simple device structures [1,2], the synthesis of Si/SiGe heterostructures by ion-implantation and thermal annealing should be an attractive alternative to growth by molecular beam epitaxy (MBE) or chemical vapour deposition (CVD). However, this presupposes that device structures of sufficient crystalline quality can be fabricated by such means. It is important therefore to examine the nature, concentration and distribution of strain relieving defects in such systems and to determine the conditions under which fully strained layers can be fabricated. Strained-layer heterostructures are also of fundamental interest [3,4] since they offer important model systems for comparison with theory and provide useful information about the properties and structure of strain relieving defects. In this regard, graded alloy structures, such as those produced by ion implantation, offer further challenges [2]. In the present study, strain relief is examined during solid-phase epitaxial crystallisation of ion-beam synthesised GeSi/Si heterostructures.

EXPERIMENTAL

Si wafers of (100) orientation were implanted at room temperature with 800 keV Ge ions to fluences in the range from $8.4 \times 10^{16} \text{cm}^{-2}$ to $3.8 \times 10^{17} \text{cm}^{-2}$, and subsequently at -196°C with either 750 or 800 keV Si ions to a fluence of $5 \times 10^{15} \text{cm}^{-2}$. The Si implants produced amorphous layers either 1060 nm or 1150 nm thick respectively, extending at least 200 nm beyond the end of Ge distribution. Thermal annealing was performed at 600°C either in air by contacting the sample to a pre-heated metal block, during which the crystallisation velocity was monitored by time resolved reflectivity (TRR) [5] at a wavelength of 1150 nm, or in a quartz tube furnace with a N_2 ambient. Rutherford backscattering and channelling analysis (RBS-C) was performed with 2 MeV He ions, with channelling along the [001] axis normal to the sample surface, and a scattering angle of 165° . Transmission electron microscopy (TEM) was performed on plan view and cross-section samples using a JEOL 2000X microscope operating at 200 kV.

RESULTS AND DISCUSSION

Like strained Si/GeSi heterostructures of uniform composition, gaussian distributed GeSi structures synthesised by ion implantation and thermal annealing have a critical thickness/composition beyond which strain relaxation occurs during crystallisation [6,7]. The prediction of this critical point is complicated for implanted structures since there is no well defined interface between the substrate and alloy layer but rather a continuously graded interface. A model developed by Paine et al [6] attempts to overcome this problem by defining an effective interface depth given by the equilibrium penetration depth of particular strain relieving defects. In the present study, the critical fluence for

800 keV Ge implants was determined to be $\sim 1.1 \times 10^{17} \text{cm}^{-2}$, or a peak concentration of 6.6 at.%, in excellent agreement with the predictions of this model under the assumption that pure edge dislocations are the dominant strain relieving defect [6,10]. Layers implanted with fluences below this critical value crystallise as fully strained layers whereas those implanted with fluences above this value contain strain relieving defects. The depth at which the defects are first generated can also be predicted theoretically [6] and clearly depends on the Ge distribution. Figure 1 shows RBS-C spectra of samples implanted with $1.2 \times 10^{17} \text{Ge.cm}^{-2}$ and $3.8 \times 10^{17} \text{Ge.cm}^{-2}$, before and after annealing at 600°C . Epitaxial crystallisation proceeded to completion in both cases but the high fluence sample clearly contains high concentrations of strain relieving defects, as evidenced by the high rate of dechannelling in the Si portion of the spectrum. Note that the lower fluence sample also marginally exceeds the critical fluence and contains a significant concentration of strain relieving defects which are not immediately evident in the RBS-C spectrum.

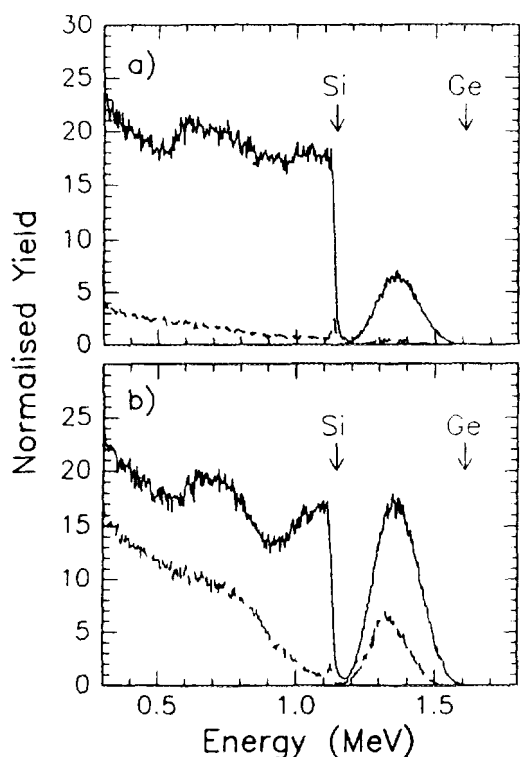


Figure 1: RBS-C spectra of samples implanted with a) $1.2 \times 10^{17} \text{Ge.cm}^{-2}$ and b) $3.8 \times 10^{17} \text{Ge.cm}^{-2}$, before (solid lines) and after (broken lines) annealing.

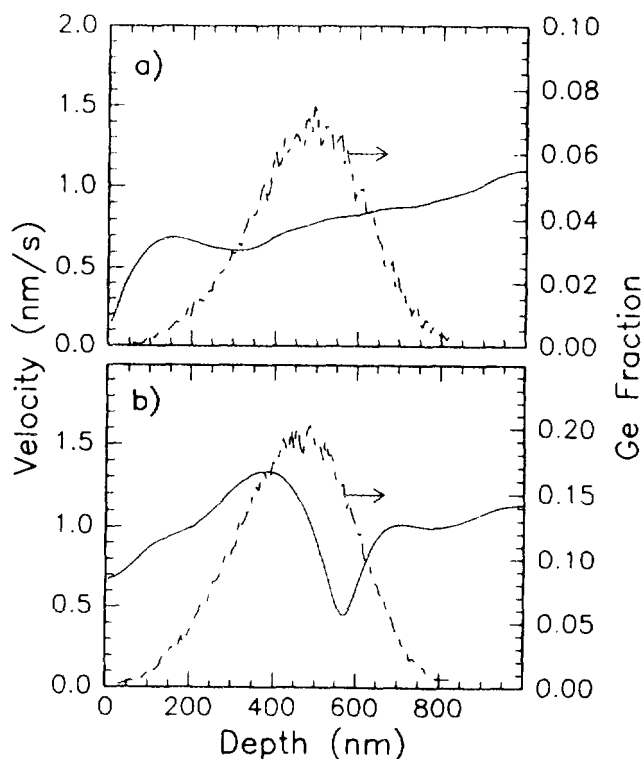


Figure 2: Crystallisation velocity as a function of depth from TRR analysis and Ge distribution from RBS-C analysis for samples implanted with a) $1.2 \times 10^{17} \text{Ge.cm}^{-2}$ and b) $3.8 \times 10^{17} \text{Ge.cm}^{-2}$.

Previous studies have shown [6,8,9] that strain relief during solid-phase epitaxial crystallisation of GeSi alloy layers is preceded by a roughening of the crystalline/amorphous interface. This roughening appears to be accompanied by (111) faceting of the interface which leads to the generation of strain relieving stacking faults and dislocations. Figure 2 compares the crystallisation velocity as a function of depth, extracted from TRR measurements, with the Ge distribution, extracted from RBS-C analysis, for the two samples described with reference to Fig. 1. The most evident feature in the velocity-depth curves is the sudden decrease in velocity at a depth of ~ 570 nm for the high-fluence sample, Fig. 2b. This feature is also present, although far less evident, at a depth of ~ 310 nm in Fig. 2a, for the low-fluence sample. It has recently been shown [11] that this velocity decrease is correlated with a reduction in TRR contrast and as such is believed to result from interface roughening and strain relief. Of particular interest in this regard is the observation that both

the crystallisation velocity (Fig. 2b) and TRR contrast increase again as crystallisation proceeds in the strain-relaxed material. This suggests that the interface roughness is somehow reduced by continued growth in strain-relaxed material. For the $1.2 \times 10^{17} \text{cm}^{-2}$ sample, cross-sectional TEM results showed dislocations extending from a depth of ~ 420 nm to the sample surface. The depth from which the dislocations originate is in excellent agreement with the onset of the velocity decrease reported in Fig. 2a. This is even more evident for the high $3.8 \times 10^{17} \text{cm}^{-2}$ sample in which a dense band of dislocations originating at a depth of ~ 615 nm, in agreement with the onset of velocity decrease shown in Fig. 2b. A reduction in the crystallisation velocity appears to be typical behaviour for all samples implanted to fluences above the critical fluence of $1.1 \times 10^{17} \text{cm}^{-2}$. Table 1 summarises the results for a range of implant fluences and compares them with the depth for relaxation, y_c , determined theoretically [6].

Fluence (cm^{-2})	Peak Conc. (at. %)	R_p (nm)	ΔR_p (nm)	y_c (TEM) (nm)	y_c (Theory) (nm)	v_{onset} (nm)	v_{min} (nm)
8.4×10^{16}	4.8	475	141	n/a	n/a	n/a	n/a
1.2×10^{17}	7.1	473	141	420	417	400	310
2.3×10^{17}	12.6	466	141	555	561	618	508
3.8×10^{17}	19.6	458	144	616	627	663	569

Table 1: Summary of experimental results and theoretical predictions as a function of Ge fluence. R_p and ΔR_p are the projected Ge range and standard deviation of the projected Ge range, respectively; $y_c(\text{TEM})$ is the depth to which dislocation bands extend, measured from TEM micrographs; $y_c(\text{Theory})$ is the depth at which strain relief is predicted to occur, using the experimentally measured Ge distributions [6]; v_{onset} is the depth at which the velocity begins to decrease; and v_{min} is the depth at which the the crystallisation velocity reaches a local minimum.

CONCLUSIONS

The ion-beam synthesis of GeSi/Si strained-layer heterostructures was achieved for Ge fluences below a critical value. For fluences above this critical value strain relief was observed during solid-phase epitaxial crystallisation at a well defined depth dependent on the Ge fluence. The generation of strain relieving defects was accompanied or preceded by a roughening of the crystalline amorphous interface which also caused a sudden reduction in the rate of epitaxial crystallisation.

REFERENCES

- [1] J.C. Bean, Proceedings of the IEEE **80** (1992) 571.
- [2] E.A. Fitzgerald, Y.H. Xie, D. Monroe, P.J. Silverman, J.M. Kuo, A.R. Kortan, F.A. Thiel and B.E. Weir, J. Vac. Sci. Technol. **B10** (1992) 1807.
- [3] S.C. Jain, J.R. Willis and R. Bullough, Advances in Physics **39** (1990) 127.
- [4] E.A. Fitzgerald, Mat. Sci. Rep. **7** (1991) 87.
- [5] G.L. Olson and J.A. Roth, Mat. Res. Rep. **3** (1988) 1.
- [6] D.C. Paine, D.J. Howard and N.G. Stoffel, J. Electronic Materials **20** (1991) 735.
- [7] R.G. Elliman and W.C. Wong, Proceedings of the 8th Ion Beam Modification of Materials Conference, Nucl. Instr. Meth. **B80/81** (1993) 768.
- [8] D.C. Paine, N.D. Evans and N.G. Stoffel, J. Appl. Phys. **70** (1991) 4278.
- [9] D.C. Paine, D.J. Howard, N.G. Stoffel and J.A. Horton, J. Mater. Res. **5** (1990) 1023.
- [10] U. Jain, S.C. Jain, J. Nijs, J.R. Willis, R. Bullough, R.P. Mertens and R. Van Overstraeten, Solid-State Electronics **36** (1993) 331.
- [11] R.G. Elliman and W.C. Wong, Proceedings of the 11th Ion Beam Analysis Conference, Nucl. Instr. Meth. (In Press).



Depth profile of In and As in Si measured by RBS with He and C ions

Q. Yang¹⁾, Z. Fang¹⁾ and T.R. Ophel²⁾

1) Department of Physics, University of Newcastle, NSW 2308, Australia

2) Department of Nuclear Physics, Australia National University, Canberra, Australia

ABSTRACT

The depth profile of As and In implanted into Si have been measured by RBS (Rutherford Backscattering Spectrometry) with 2 MeV He ions and 6 MeV C ions. Advantages of enhanced depth and mass resolution with C ions have been demonstrated over the conventional He RBS. More reliable information for the depth profile of In and As in Si has been obtained.

INTRODUCTION

Ion implantation is a powerful technique in material science and engineering. The distribution of the implanted dopants in crystalline Si has been an active area of research. The redistribution and segregation of the dopants during and after annealing for Si crystallisation are very important for both scientific and technological interest [1,2]. The segregation of In during solid-phase-epitaxial crystallisation of Si has been studied recently with high depth resolution He RBS and channelling techniques. It was found that the segregation properties of In could be influenced significantly by the presence of an As dopant. With high depth resolution He RBS, the In and As signals overlapped and could not be resolved. In order to profile the In dopant in Si in the presence of an As dopant, it was necessary to assume that the As profile was not influenced either by the presence of In dopant or the annealing process [2]. Although He ion RBS has been a powerful technique in material analysis, heavy ion RBS (HIRBS) has revealed many advantages over the conventional He RBS [3-7]. The specific advantages of the combined high mass/depth resolution and larger resolvable depth, which have been reported in more detail recently [7], should enable profiling of In and As in Si simultaneously.

In this work we are reporting on the profiling of In and As in Si measured by HIRBS with 6 MeV C ions. For comparison, 2 MeV He RBS measurements were also performed.

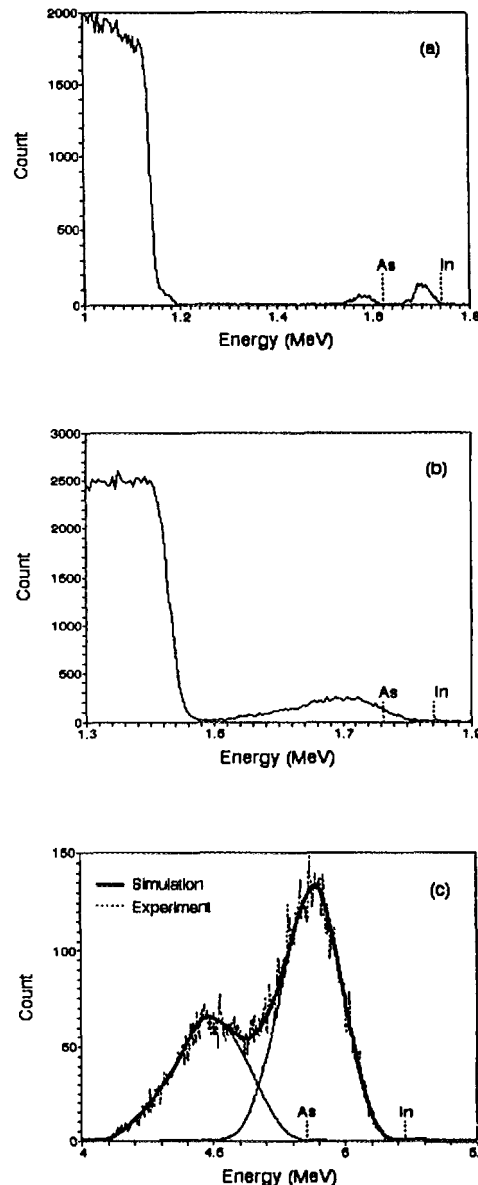


Fig. 1. RBS spectra (random) of 2 MeV He ions for a) 165°, b) 100° scattering at normal incidence, and c) 6 MeV C ions 70° scattering at 35° incidence to the surface of In and As implanted Si.

EXPERIMENT

Commercially prepared Si wafers of (100) orientation were implanted with In and As at room temperature. The implantation conditions were 140 keV As to a fluence of 3×10^{15} atom/cm² and then 190 keV In to a fluence of 2×10^{15} atom/cm² (In : As = 2 : 3) with an fluence uncertainty of 10%.

A beam of 6 MeV C ions was produced by the 14UD accelerator [8] and detected by a Enge magnetic spectrometer with a focal-plane position-sensitive detector [9]. The experimental setup has described in more detail elsewhere [7]. The C ion beam current was typically 30 nA and the total C ion fluence was below 10^{15} atom/cm². No beam induced diffusion and mixing were expected in the depth range of In and As distribution. The RBS measurement was performed with a beam of 2 MeV He ions incident normal to the target surface. The spectra were collected with two solid surface barrier detectors (SSBD) at scattering angles of 165° and 100° respectively.

RESULTS AND DISCUSSION

A comparison of the RBS spectra taken at 165° and 100° scattering to that of the HIRBS with 6 MeV C ions at 70° scattering and 35° incidence to surface is shown in Fig. 1. The depth resolution for In and As in Si were calculated using the simulation model [7] including multiple scattering, lateral spread, geometrical effects, detector resolution and a new formula for heavy ion energy straggling [10]. The surface barrier detectors for He ions had resolution of 17 keV (FWHM), and the Enge spectrometer/detector system was calibrated as $\delta E(\text{FWHM}) = 50 - 80/E$ (keV) for C ions, where E is the detected C ion energy in MeV [7]. The depth resolution versus depth for In and As in each case is shown in fig. 2. It is clear from fig. 1 and fig. 2 that the depth and mass resolution could not be satisfied simultaneously in one He RBS spectrum. High mass resolution can be obtained with poor depth resolution (fig. 1a) while better depth resolution can be achieved with poor mass resolution (fig. 1b). On the other hand, high mass resolution has been achieved together with much better depth resolution using C ions (fig. 1c and fig. 2). Although the depth resolution at the surface for He and C ions is nearly the same (100 nm), the resolution for C ions is relatively constant for depth down to 200 nm. With a realistic simulation program (GRACES) for

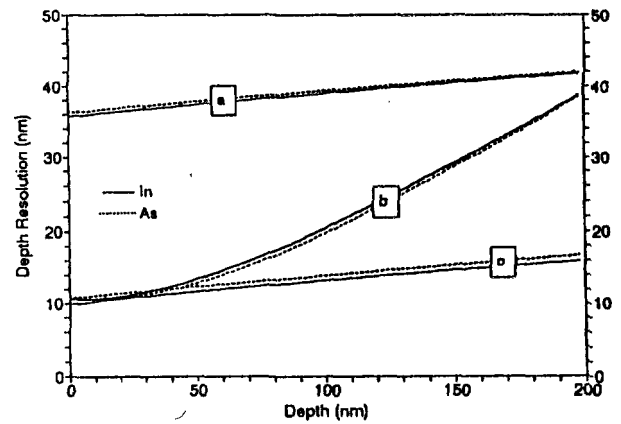


Fig. 2. Depth resolution of In and As dopants in Si versus depth in the cases of fig. 1a, 1b and 1c.

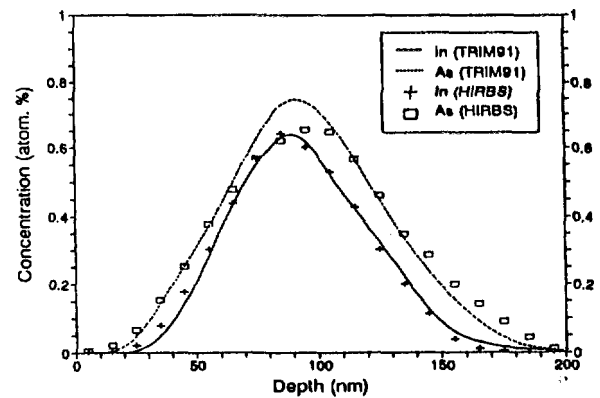


Fig. 3. Profiles of In and As in Si obtained by fitting the simulated spectrum to the experimental result. Profiles from TRIM simulation are also shown for comparison.

the HIRBS spectrum [11], the In and As signals could be resolved clearly and the depth profile of In and As were determined simultaneously by fitting the simulation to the experimental spectrum.

The fitted spectrum is shown in fig. 1c together with the separate component signals of In and As. The fitted depth profile of In and As are shown in figure 3 for a In fluence 2.2×10^{15} atom/cm² assuming the As fluence of 3×10^{15} atom/cm² remained a constant (fitted ratio 2.2 : 3 instead of 2 : 3 determined from implantation condition with 10% uncertainty). The results from TRIM simulation [12] (version 91.00) have been smoothed and shown in fig. 3 for comparison. It is seen that the In profile agrees well with the TRIM prediction. However, there is a discrepancy for the As profile around the distribution peak. The measured As profile has a flatter peak and a deeper tail than the TRIM prediction, which may be due to redistribution of As in Si caused by post ion implantation of In.

CONCLUSION

The advantages of high mass and depth resolution of HIRBS have been demonstrated and applied to the depth profiling of In and As in Si. The depth profile of In and As in Si have been obtained by 6 MeV C scattering with higher depth resolution for the whole distribution depth (down to 200 nm). The study of segregation of In during solid-phase-epitaxial crystallisation of Si will be studied in further HIRBS measurements.

ACKNOWLEDGMENT

The authors are indebted to Professor Dezhang Zhu for his help and assistance in the 2 MeV He ion RBS measurements. We would like to thank Professor R.J. MacDonald and D.J. O'Connor for helpful discussion.

REFERENCES

- [1] J.M. Poate, G. Foti and D.C. Jacobson, *Surface Modification and Alloying by Laser, Ion and Electron Beams* (Plenum Press, New York 1983).
- [2] R.G. Elliman and Z. Fang, *J. Appl. Phys.*, to be published, and references therein.
- [3] W.K. Chu, J.W. Mayer and M.A. Nicolet, *Backscattering Spectrometry* (Academic Press, New York, 1978).
- [4] M.R. Weller, M.H. Mendenhall, P.C. Haubert, M. Döbeli and T.A. Tombrello, *Conference Proceedings, Heavy Ion Beams*, Materials Research Society, (1990) 139.
- [5] J. Weidhaas and W. Lang, *Surface and Interface Analysis*, 17 (1991) 357.
- [6] E. Rauhala, J. Saarihahti and N. Nath, *Nucl. Instr. and Meth.* B61 (1991) 83.
- [7] D.J. O'Connor and TAN Chunyu, *Nucl. Instr. and Meth.* B36 (1989) 178; Q. Yang, D.J. O'Connor, Z. Fang, T.R. Ophel, H.J. Hay and T.E. Jackman, *Nucl. Instr. and Meth.* B74 (1993) 431.
- [8] T.R. Ophel, J.S. Harrison, J.O. Newton, R.H. Spear, E.W. Titterton and D.C. Weisser, *Nucl. Instr. and Meth.* 122 (1974) 227.
- [9] T.R. Ophel and A. Johnston, *Nucl. Instr. and Meth.* 157 (1978) 461.
- [10] Q. Yang, D.J. O'Connor and Zhonglie Wang, *Nucl. Instr. and Meth.* 61 (1991) 149.
- [11] Q. Yang, *Nucl. Instr. and Meth.* B, submitted.
- [12] J.F. Ziegler, J.P. Biersack and U. Littmark, *The Stopping and Range of Ions in Solids* (Pergamon, New York, 1985).



STOICHIOMETRY, THICKNESS AND CRYSTALLINITY OF MOCVD GROWN $\text{Hg}_{1-x-y}\text{Cd}_x\text{Mn}_y\text{Te}$ DETERMINED BY NUCLEAR TECHNIQUES OF ANALYSIS.

Warren B. Studd¹, Peter N. Johnston¹, Ian F. Bubb¹ and Patrick W. Leech²

1) Department of Applied Physics, Royal Melbourne Institute of Technology.

G.P.O. Box 2476V, Melbourne 3001 Australia

2) Applied Research and Development, Telecom Australia

770 Blackburn Road. Clayton 3168 Australia

ABSTRACT

The quaternary semi-conductor $\text{Hg}_{1-x-y}\text{Cd}_x\text{Mn}_y\text{Te}$ has been grown by Metal Organic Chemical Vapour Deposition using the Interdiffused Multi-layer Process. The layers have been analysed by Ion beam (PIXE, RBS, channelling) and related analytical techniques (EDXRF, XRD, RHEED) to obtain stoichiometric and structural information. The analysis shows that all four elements are present throughout the layer and that the elemental concentrations and thickness of the layer vary considerably over the film. Channelling, XRD and RHEED have been combined to show that the layer is polycrystalline.

INTRODUCTION

II-VI based dilute magnetic semi-conductors (DMS) which exhibit both semi-conducting and semi-magnetic behaviour are attracting considerable interest and research activity. These materials contain a fraction (x) of magnetic ions substituted on the Group II sites. The semi-magnetic properties arise from the exchange interaction between the localised magnetic moments associated with Mn^{2+} ions and the conduction band electrons [1]. These characteristics have resulted in the application of CdMnTe in optical isolators [2] and in magnetic field sensors [3]. In addition the alloys $\text{Hg}_{1-x}\text{Mn}_x\text{Te}$ and $\text{Hg}_{1-x-y}\text{Mn}_x\text{Cd}_y\text{Te}$ have been used in the fabrication of photo diodes [4-6], LED and laser diodes [7] at 5-12 μm and 1-2.5 μm wavelength ranges respectively. The ability to magnetically tune the energy gap and the additional stabilising of the Hg-Te bond by Mn are advantages of these devices.

Metal Organic Chemical Vapour Deposition (MOCVD) offers the capability of epitaxial growth on various substrates with high wafer throughput. Composition and layer thickness are critical factors in the performance of these devices. Several analysis techniques have been used to determine these properties, each with limitations. Particle induced X-ray emission (PIXE) analysis has been successfully applied to the elemental analysis of $\text{Hg}_{1-x}\text{Cd}_x\text{Te}$ over a wafer [8]. The epitaxial layers of interest are typically 1 to 10 μm thick and consist of elements well suited for the application of PIXE [9]. In addition, energy dispersive X-ray fluorescence analysis (EDXRF) has been successfully used for determining the Cd/Te ratio and the epitaxial layer thickness for HgCdTe and similar materials [10].

In this investigation the composition and thickness of MOCVD grown $\text{Hg}_{1-x-y}\text{Cd}_x\text{Mn}_y\text{Te}$ thin films was examined using PIXE and EDXRF. Also RBS channelling techniques have been combined with X-Ray Diffraction (XRD) and Reflection High Energy Electron Diffraction (RHEED) to determine the extent of epitaxy in the grown layer.

EXPERIMENTAL

$\text{Hg}_{1-x-y}\text{Mn}_x\text{Cd}_y\text{Te}$ films were grown in a M.R. Semicon Quantax 226 MOCVD atmospheric reactor at Telecom Australia using an interdiffused multilayer process (IMP). Alternate layers of CdMnTe and HgTe were deposited at a temperature of $\approx 280^\circ\text{C}$ on a substrate of semi-insulating GaAs misoriented 2° off $\langle 100 \rangle$. Initially a buffer layer of CdTe of $\approx 1.0 \mu\text{m}$ was deposited on the wafer. The multi-layers were subsequently interdiffused by annealing in-situ at 360°C .

PIXE analysis was performed using a beam of 3.0 MeV He^{2+} ions on the RMIT 1 MV Tandem accelerator. Emitted X-rays were detected using a HNU Systems SiLi detector with an energy resolution of 158 eV for the MnK_α line (5.90 keV) and located at an angle of 135° with respect to the incident beam direction. A 10 μm copper filter was placed in front of the SiLi detector to attenuate GaK and AsK x-rays from the substrate and secondary electron bremsstrahlung and lower energy HgM, CdL and TeL X-rays while having minimal effect on the MnK X-rays. The average composition of the epilayer at a particular point was determined by peak fitting to the MnK_α line (5.90 keV), HgL_γ (13.83 keV), CdK_α (23.17 keV) and TeK_α (27.47 keV) x-rays. Peak fitting and X-ray yield calculations were performed with a PIXE analysis package, PIXAN, developed by Clayton [11] and modified at RMIT.

EDXRF analysis was performed by the method outlined by Johnston et al. [10] using the 59.5 keV γ -ray from a ^{241}Am source and a PGT SiLi detector having a resolution of 150 eV at 5.9 keV. As EDXRF data included a signal from the CdTe "buffer" layer as well as the HgCdMnTe layer, a sample was obtained having only the CdTe "buffer" layer on the GaAs substrate. Information obtained from this sample was then used to determine the net thickness and Cd/Te ratio of the HgCdMnTe layer.

Crystal structure of the HgMnCdTe layer was investigated by RBS Channelling, XRD and RHEED. One end of a sample was etched by the method outlined by Leech et al. [12] so that only the bare GaAs substrate was present. The GaAs substrate was channelled along the $\langle 100 \rangle$ axis in the exposed region. Then, while maintaining crystallographic alignment, the sample was translated until the beam was incident on the HgCdMnTe. No channelling was observed in the HgCdMnTe layer.

An electron diffraction pattern was obtained by RHEED using a Jeol 100CX 100 kV electron microscope. A Laue XRD pattern was obtained using a copper tube operating at 40 kV.

RESULTS AND DISCUSSION

The EDXRF results were analysed using the software program BATTY [11] to obtain the peak areas. The Cd/Te ratio and thickness were then determined and corrected for secondary fluorescence as outlined by Johnston et al. [10]. Figure 1 shows the total layer thickness and the thickness of the buffer layer in the direction of gas flow as obtained by EDXRF analysis. Figure 2 shows the variation in calculated Cd/Te ratio (by atoms) in the HgCdMnTe layer along the wafer.

Figure 3 shows the variation in Mn and Hg concentrations along the sample as determined by PIXE analysis. Composition was calculated using the peak area and x-ray yield results determined by PIXAN [11]. These results are consistent with EDX cross-sections using Transmission Electron Microscopy (TEM) as obtained by Rossouw [13] on the same samples.

Channelling indicated that the layer was not epitaxial. The Laue pattern has suggested the presence of some poor quality crystallinity by blurred spots apparently due to the layer. RHEED has revealed rings with some intense spots which differed from point to point on the samples. This data indicates polycrystallinity with some crystallites of significant size.

While indicating the feasibility of growth of $\text{Hg}_{1-x-y}\text{Mn}_x\text{Cd}_y\text{Te}$ by IMP, these results also demonstrate the large variation in thickness and stoichiometry of the layer across the wafer. The higher levels of Mn near the leading edge of the wafer may be attributed to the temperature of deposition ($\approx 160^\circ\text{C}$) of the organometallic $\text{MeMn}(\text{CO})_5$. More uniform distribution of Mn requires optimisation of the H_2 flow rate and further reduction in growth temperature. The increase in thickness of the quaternary layer with flow occurred despite reduction in the Mn content. This trend corresponds to the increasing deposition rate of both CdTe [14] and HgTe along the flow direction. This non-uniformity in the deposition profile has, in turn, been attributed to a variation in the supply rate of metal vapour.

ACKNOWLEDGMENTS

The permission to publish this work by the Director, Applied Research and Development, Telecom Australia is acknowledged. The work has been supported by the Australian Research Council and the Australian Telecommunications and Electronics Research Board.

REFERENCES

- [1] J.K. Furdyna, *J. Vac. Sci. Technol.* A4 (1986) 2002.
- [2] A.E. Turner, R.L. Gunshor and S. Datta, *Appl. Optics* 22 (1983) 3152.
- [3] N. Kullendorf and B. Hok, *Appl. Phys. Letts.* 46 (1985) 1016.
- [4] P. Becla, *J. Vac. Sci. Technol.* A4, (1986) 2014.
- [5] S.H. Shin, J.G. Pasko, D.S. Lo, W.E. Tennent, M. Gorska, M. Fotouhi and C.R. Lu, *Mat. Res. Soc. Symp. Proc.* 89 (1987) 267.
- [6] A. Rogalski, *Infrared Physics* 31 (1991) 117.
- [7] P. Becla, *J. Vac. Sci. Technol.*, A6, (1988), 2725
- [8] S.P. Russo, P.N. Johnston, R.G. Elliman and G.N. Pain. *Mat. Res. Soc. Symp. Proc.* 216 (1991) 23.
- [9] J.P. Willis, *Nucl. Instr. and Meth.* B35 (1988) 378.
- [10] P.N. Johnston, S.P. Russo, R.C. Short, S.R. Walker and G.N. Pain, *Nucl. Instr. Meth.* B69 (1992) 361.
- [11] E. Clayton, AAEC/M113(1986), *Nucl. Instr. and Meth.* B22(1987) 64.
- [12] P.W. Leech, P.J. Gwynn and M.H. Kibel, *Applied Surface Science* 37 (1989) 291.
- [13] C. Rossouw, private communication (1993).
- [14] T.J. Davis, T. McAllister, V. Maslem, S.W. Wilkins, M. Faith and P. Leech, *J. Cryst. Growth* (1993) in press.

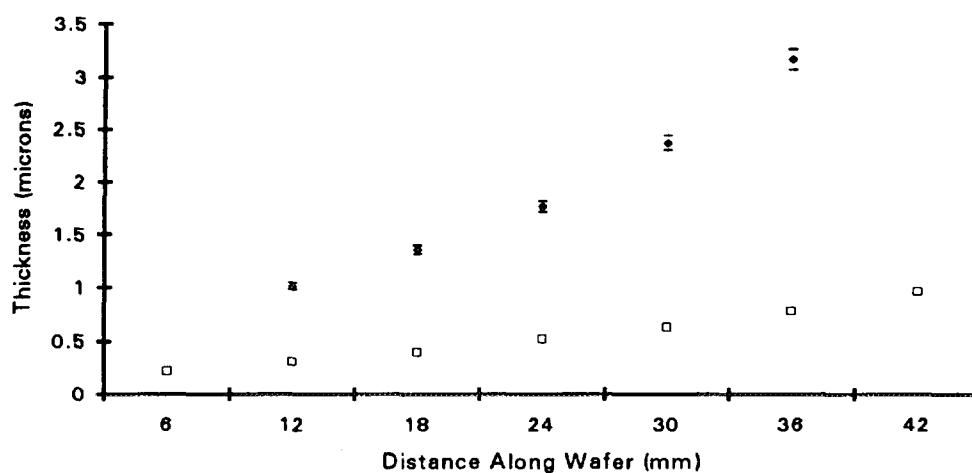


Figure 1 The thickness of the total layer (◆) and CdTe buffer layer (□) versus distance along the wafer in the direction of gas flow in the MOCVD reactor as determined from EDXRF analysis.

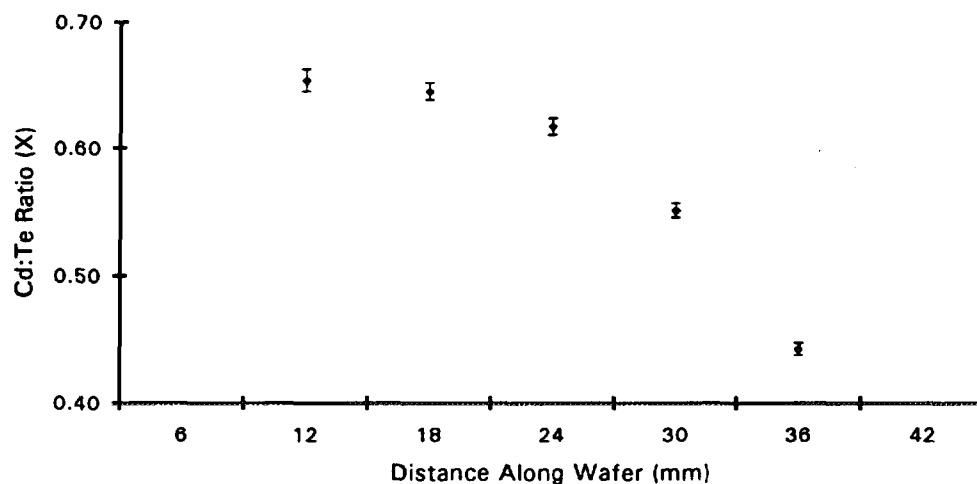


Figure 2 The calculated Cd/Te ratio (by atoms) as a function of distance along the wafer in the direction of gas flow in the MOCVD reactor as determined from EDXRF analysis.

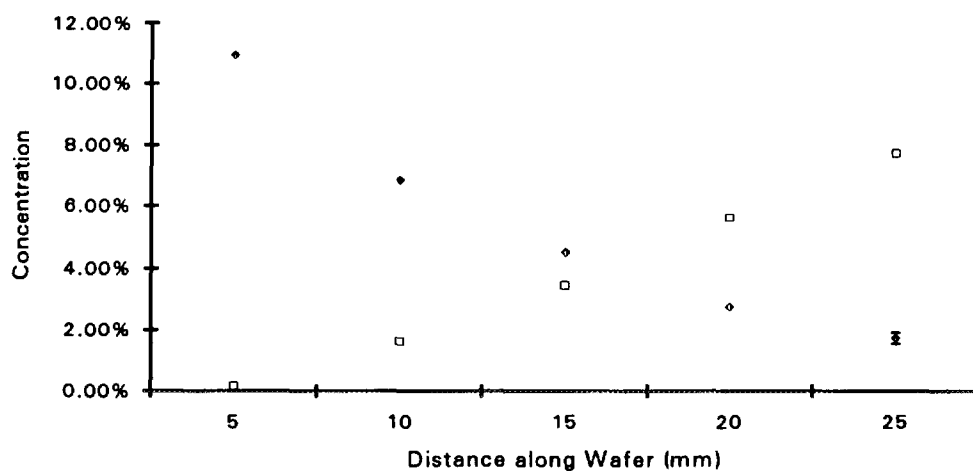


Figure 3. Variation of Mn (□) and Hg (◆) concentrations in the sample as a function of distance along the wafer in the direction of gas flow in the MOCVD reactor as determined from PIXE analysis.

Error bars (± 1 std. dev.) are shown when greater than the size of the symbol denoting the estimate.

**ENHANCED RELAXATION OF STRAINED $\text{Ge}_x\text{Si}_{1-x}$ LAYERS
INDUCED BY $\text{Co}/\text{Ge}_x\text{Si}_{1-x}$ THERMAL REACTION**

M.C. Ridgway*, R.G. Elliman*, M.R. Rao* and J.-M. Baribeau**,
 *Department of Electronic Materials Engineering, Australian
 National University, Canberra, Australia,
 **Institute for Microstructural Sciences, National Research
 Council of Canada, Ottawa, Canada.

Enhanced relaxation of strained $\text{Ge}_x\text{Si}_{1-x}$ layers during the formation of CoSi_2 by $\text{Co}/\text{Ge}_x\text{Si}_{1-x}$ thermal reaction has been observed. Raman spectroscopy and transmission electron microscopy were used to monitor the extent of relaxation. Possible mechanisms responsible for the enhanced relaxation, including metal-induced dislocation nucleation, chemical and/or structural inhomogeneities at the reacted layer/ $\text{Ge}_x\text{Si}_{1-x}$ interface and point defect injection due to silicide formation will be discussed. Also, methodologies for inhibiting relaxation will be presented.

Metal/ $\text{Ge}_x\text{Si}_{1-x}$ contacts have possible application in the fabrication of $\text{Ge}_x\text{Si}_{1-x}$ -based heterojunction bipolar transistors (HBTs). With the widespread usage of Co metallization in Si devices, the potential extension of this technology to $\text{Ge}_x\text{Si}_{1-x}$ devices is thus of technological interest. As a consequence, the thermally-induced $\text{Co}/\text{Ge}_{.17}\text{Si}_{.83}$ reaction has been investigated in previous studies [1,2] with a variety of analytical techniques including electrical measurements, Rutherford backscattering spectrometry, Auger electron spectroscopy and electron microscopy. Following 240 min annealing, the reacted surface layer was composed of CoSi , CoSi_2 and $\text{Ge}_x\text{Si}_{1-x}$ precipitates (the latter probably rich in Ge). Lateral phase non-uniformity was evident with both transmission and scanning electron microscopy. For samples annealed with and without an evaporated Co film, enhanced relaxation of the underlying $\text{Ge}_{.17}\text{Si}_{.83}$ layer was apparent in the former. In an HBT, such processing-induced relaxation of a $\text{Ge}_x\text{Si}_{1-x}$ base would degrade device performance due to the concomitant reduction in Si/ $\text{Ge}_x\text{Si}_{1-x}$ band edge discontinuity with the loss of tetragonal strain. For the present report, Raman spectroscopy results are presented and correlated with electron microscopy to examine the extent of relaxation of the underlying $\text{Ge}_{.17}\text{Si}_{.83}$ layer induced by $\text{Co}/\text{Ge}_{.17}\text{Si}_{.83}$ thermal reaction.

Strained $\text{Ge}_{.17}\text{Si}_{.83}$ layers of thickness 110 nm were grown on (100) Si substrates by molecular beam epitaxy as described elsewhere [3]. Co layers of thickness 15 nm were then deposited by electron-beam evaporation at a pressure of 1×10^{-6} torr. Samples were subsequently annealed for 0-240 min under vacuum at a pressure of 1×10^{-5} torr and at a temperature of 600°C.

Relaxation of the underlying $\text{Ge}_{.17}\text{Si}_{.83}$ layer was monitored with Raman spectroscopy using a backscattered

geometry and a 200 mW Ar laser operating at 514.5 nm with a beam diameter of ~ 1 μm . Results were correlated with transmission electron microscopy (TEM) measurements using 200 keV electrons.

Raman spectra for samples annealed for 120 min with and without an evaporated Co film are shown in Figure 1. The intense peak at ~ 520 cm^{-1} in both spectra is due to the Si-Si mode of the Si substrate. The Si-Si mode of the $\text{Ge}_{.17}\text{Si}_{.83}$ layer is anticipated at ~ 514 and ~ 509 cm^{-1} for strained and unstrained layers, respectively [4]. Note the distinct shoulder apparent at ~ 510 cm^{-1} for the sample annealed with an evaporated Co film, indicative of partial relaxation of the $\text{Ge}_{.17}\text{Si}_{.83}$ layer and consistent with previous TEM observations of the presence of misfit dislocations at the $\text{Ge}_{.17}\text{Si}_{.83}/\text{Si}$ interface [1,2]. No shoulder is evident in the Raman spectrum of the sample annealed without an evaporated Co film and furthermore, the peak at ~ 402 cm^{-1} is consistent with the Si-Ge mode of a strained $\text{Ge}_{.17}\text{Si}_{.83}$ layer [4]. (The Si-Ge mode of a relaxed $\text{Ge}_{.17}\text{Si}_{.83}$ layer is anticipated at ~ 398 cm^{-1} [4].) The thermally-induced $\text{Co}/\text{Ge}_{.17}\text{Si}_{.83}$ reaction thus results in enhanced relaxation of the $\text{Ge}_{.17}\text{Si}_{.83}$ layer. Metal-induced dislocation nucleation [5], point defect injection due to silicide formation [2] and/or the presence of dislocation nucleation sources (chemical inhomogeneities, stacking faults, microtwins, etc.) at the reacted layer/ $\text{Ge}_{.17}\text{Si}_{.83}$ interface [6] may be responsible for this phenomenon. For the samples annealed with an evaporated Co film, peaks at ~ 472 , ~ 402 and ~ 291 cm^{-1} are consistent with Si-Si, Si-Ge and Ge-Ge modes [4,7], respectively, of the $\text{Ge}_x\text{Si}_{1-x}$ precipitates first identified with TEM [1,2]. The Raman shift indicates the precipitates are Ge-rich, with an approximate stoichiometry of $\text{Ge}_{.75}\text{Si}_{.25}$ (assuming the precipitates are fully relaxed). However, note that the precipitate composition may vary either from precipitate to precipitate or within a given precipitate. The latter may contribute to the relative broadening, apparent in Figure 1, of the precipitate peaks in comparison to that of the Si substrate.

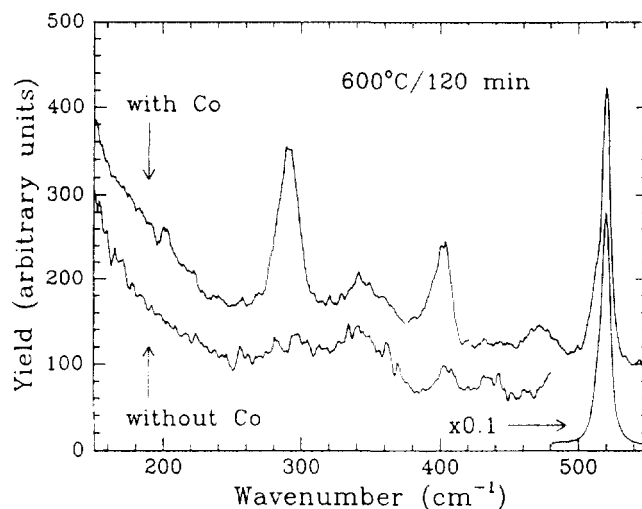


Figure 1: Raman spectra for samples annealed for 120 min with and without an evaporated Co film.

The peak at $\sim 202 \text{ cm}^{-1}$ is attributable to CoSi based on the observations of Shergill et al [8]. A peak at 515 cm^{-1} , attributed to CoSi_2 , has been reported in some [8] but not all [9] Raman studies of CoSi_2 formation. In the present report, such a peak would potentially not be discernable due to superposition with that of the Si substrate. The possibility that such a peak could contribute to the shoulder apparent at $\sim 510 \text{ cm}^{-1}$ for samples annealed with an evaporated Co film was not considered significant based on the given difference in wavenumber.

The potential technological application of the $\text{Co}/\text{Ge}_x\text{Si}_{1-x}$ reaction for contact metallization is diminished given the observed enhanced relaxation of the underlying $\text{Ge}_{.17}\text{Si}_{.83}$ layer. Co metallization of $\text{Ge}_x\text{Si}_{1-x}$ layers may be better achieved with either co-deposition of Si and Co or sequential Si and Co deposition, the latter with the film thicknesses appropriate for consumption of both layers to form homogeneous CoSi_2 . Alternatively, lower annealing temperatures are potentially possible if Co is deposited on an amorphized $\text{Ge}_x\text{Si}_{1-x}$ layer. (Reduced CoSi_2 formation temperatures have been observed for $\text{Co}/(\text{amorphous Si})$ structures in comparison to $\text{Co}/(\text{crystalline Si})$ structures [10].) Preamorphization may thus reduce the extent of thermally-induced relaxation. Such measurements are now in progress [11].

- [1] M.C. Ridgway, R.G. Elliman, N. Hauser, J.-M. Baribeau and T.E. Jackman, in Advanced Metallization and Processing for Semiconductor Devices and Circuits - II, eds. A. Katz, S.P. Murarka, Y.I. Nissim and J.M.E. Harper (Mat.Res.Soc., Pittsburgh, 1992) p. 857.
- [2] M.C. Ridgway, R.G. Elliman, R. Pascual, J.L. Whitton and J.-M. Baribeau, in Phase Transformations in Thin Films - Thermodynamics and Kinetics, eds. M. Atzmon, A.L. Greer, J.M.E. Harper and M.R. Libera (Mat.Res.Soc., Pittsburgh, 1993) in press.
- [3] J.-M. Baribeau, T.E. Jackman, D.C. Houghton, P. Maigne and M.W. Denhoff, J.Appl.Phys. 63, 5738 (1988).
- [4] S.M. Prokes, O.J. Glembocki, M.E. Twigg and K.L. Wang, J.Elec.Mat. 20, 389 (1991).
- [5] V. Higgs, P. Kightley, J. Goodhew and P.D. Augustus, Appl.Phys.Lett. 59, 829 (1991).
- [6] A. Buxbaum, E. Zolotoyabko, M. Eizenberg and F. Schaffler, Thin Solid Films 222, 157 (1992).
- [7] M.I. Alonso and K. Winer, Phys.Rev. B39, 10056 (1989).
- [8] G.S. Shergill, C.-S. Wei, J.N. Cox, D.B. Fraser and J.J. Murray, Int.Anal. (1988).
- [9] L. Weaver, M. Simard-Normandin, A. Naem and A.J. Clark, in Advanced Metallization and Processing for Semiconductor Devices and Circuits - II, eds. A. Katz, S.P. Murarka, Y.I. Nissim and J.M.E. Harper (Mat.Res.Soc., Pittsburgh, 1992).
- [10] C.-D. Lien, M.-A. Nicolet and S.S. Lau, Appl.Phys. A34, 249 (1984).
- [11] M.R. Rao, M.C. Ridgway, R.G. Elliman and J.-M. Baribeau, to be published.



Heavy Ion Elastic Recoil Detection Analysis of Optoelectronic and Semiconductor Devices

N. Dytlewski and D.D. Cohen, Australian Nuclear Science and Technology Organisation

P. Johnston and S. Walker, Royal Melbourne Institute of Technology

H. Whitlow and M. Hult, University of Lund, Sweden

M. Ostling and C. Zaring, Royal Institute of Technology, Stockholm, Sweden

Introduction

In recent years, the use of heavy ion time-of-flight elastic recoil spectrometry (HIERDA) has been applied to analyse multi-phase, thin layer devices used in optoelectronics, semiconductors and solar power generation. HIERDA gives simultaneously, mass resolved elemental concentration vs depth profiles of the matrix constituents, and is particularly suited to the determination of light elements in a heavy matrix. The beam/target interaction process is similar to RBS, but has the difference that the recoiling target atoms are detected instead of the scattered projectile. High energy, heavy ions beams bombard the sample, ejecting recoil atoms which are detected at a forward angle of 45° . A time-of-flight and total energy detection system enables the ejected particle's mass to be identified, and allows energy spectra to be obtained and interpreted in an analogous way to RBS, but with the important difference that the elemental spectra are separated, and not superimposed on a background as in RBS. We will describe some of the measurements made with a HIERDA system on the ANTARES Tandem Accelerator at ANSTO.

Experimental

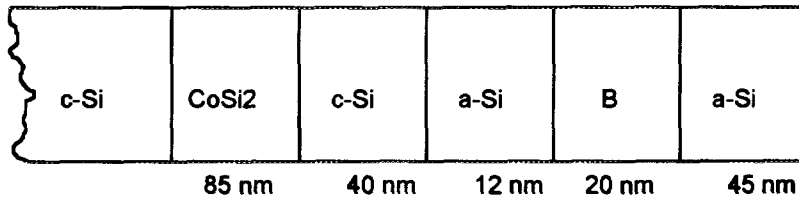
A heavy ion beam of ^{127}I was injected into the Tandem Accelerator with terminal voltage set at 7MV, with the emergent 77 MeV 10+ charge state directed into the experimental target chamber. Beam stripping was with a $3 \mu\text{g}/\text{cm}^2$ carbon foil. Iodine is chosen as the projectile species as the ERDA cross-section varies as Z^2 , and as the ToF detector is positioned at 45° , it is kinematically not possible for iodine to scatter off elements with mass < 90 , and enter the detector. After the iodine beam is energy analysed by a 90° analyser magnet, it enters a switching magnet, where it is deflected into the IBA beamline and target chamber. The vacuum system of the Tandem Accelerator and target chamber is maintained at approx. 10^{-5} Pa by cryopumps. The ToF detector was brought to Australia from Sweden by Harry Whitlow and Mikael Hult, and installed on the Australian target chamber. This detector is the electrostatic mirror type, as developed by Busch [1].

Measurements

The focus of the measurements made to date have been metallisation studies on substrate materials from columns III and V in the periodic table, investigating the formation of various ohmic contacts to AlGaAs, GaAs, InP and related materials for use in two-dimensional electron devices. The contact resistance and device performance depends strongly on the interaction of the contact material with the active device layers, and it is of interest to follow certain aspects of the manufacturing technology. Rather than presenting a detailed interpretation of the data obtained, a qualitative overview will be given, with reference to two structures, which outline some of the capabilities of the HIERDA technique.

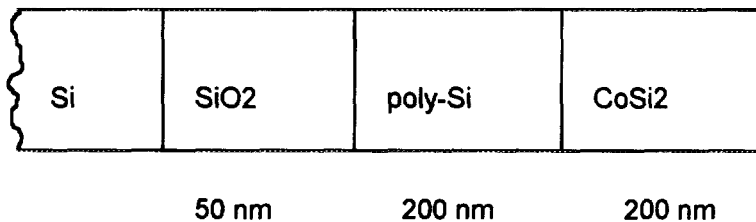
Sample #1 Si/CoSi₂/Si/a-Si/B/a-Si

A contact layer of interest is CoSi₂. Of interest, is the diffusion of some ion implant species, in this case boron, into the contact layer. The following structure was analysed:



The objective is to study the boron distribution, and subsequent solubility of boron in CoSi₂ upon heat treatment. The CoSi₂ was formed by ion implantation of Co into Si, and heat treated to form epitaxial silicide. Boron and silicon was then electron beam evaporated on top to form the layered structure, then heat treated at 900° C for 24hrs. Fig. 1 shows the HIERDA spectra of this sample. In the mass vs energy diagram, the strong continuous silicon mass-energy and weaker boron curves are seen. There is also the presence of oxygen and titanium, which results from stray iodine beam hitting part of a titanium backing plate on which the samples were mounted. In the ADC1 vs ADC2 diagram, the short curve corresponding to cobalt recoils is seen, as is another short track corresponding to multiply scattered iodine beam entering the detector. In fig.2, a two-dimensional surface plot is presented which more graphically illustrates the boron and oxygen yields as a function of depth. It remains to transform the measured yield information into a quantitative concentration-depth distribution.

Sample #2 Si/SiO₂/poly-Si/CoSi₂ implanted with BF₂⁺ (75 keV, dose 10¹⁵/cm²)



Four samples were implanted and measured; as implanted, and annealing temperatures of 650° C, 850° C and 1050° C for 1 hr. In fig.3, a surface view of the silicon yield is shown, and in the "as implanted" view, it can be seen that near the surface, the silicon yield is low (CoSi layer), then increases sharply (poly-Si layer), decreases again (SiO₂ layer), then rises again (Si substrate). Heating to 650° C shows no change, but at 850° C, there is an increase in silicon yield for this surface layer, with a corresponding decreased yield from the second layer. This is due to cobalt diffusing from the first layer into the second. The buried oxygen layer and boron implant is easily seen in fig. 4, which is an expanded view of the un-annealed sample. Also evident, is some surface oxygen contamination.

Summary

The data presented in this paper represents some of the results of a joint project in HIERDA between Sweden and Australia; the time-of-flight detector provided by Sweden, and the Tandem Accelerator and multi-parameter data acquisition facilities provided by Australia. From the described measurements, it is apparent that HIERDA offers the capability to investigate complex structures and processes in today's high technology areas. The good mass resolution for the light elements, and the ability to do depth profile studies in the presence of a heavy matrix, will, with RBS and hydrogen specific ERDA, will open the way for complex R&D projects.

References

- [1] F. Busch, W. Pfeffer, B. Kohlmeyer, D. Schull and F. Puhlhofer, Nucl. Inst. Meth. 171 (1980) 71.

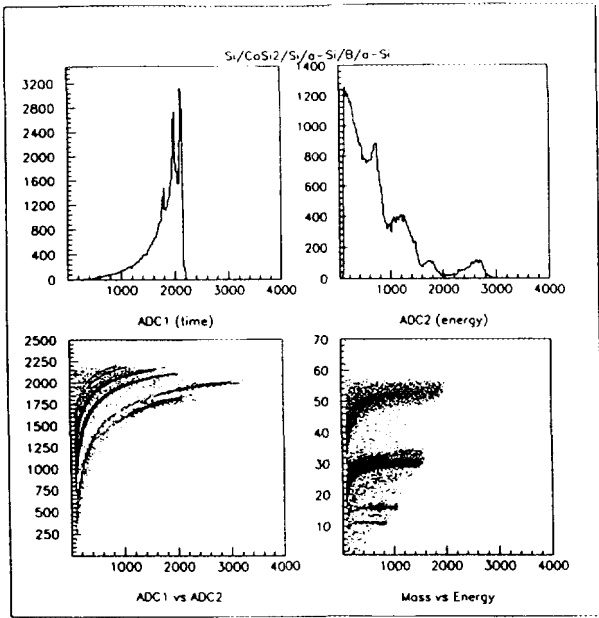


Fig. 1 Energy and flight time spectra for sample #1, and the 2-dimensional mass-energy transformations.

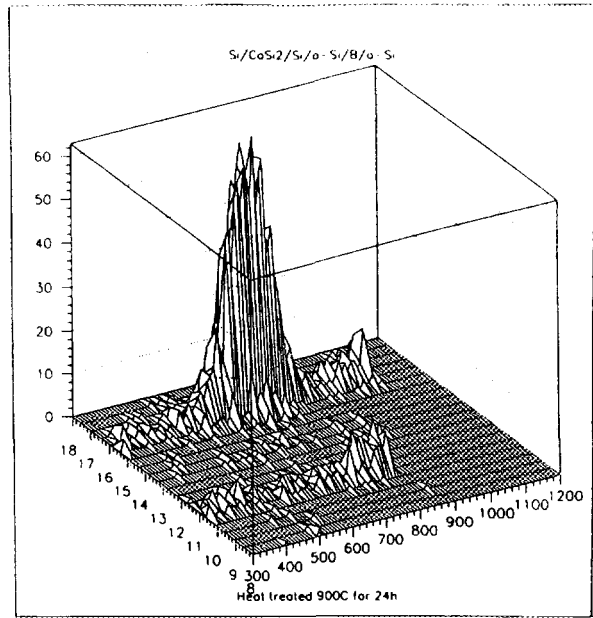


Fig. 2 Surface contour plot of the oxygen and boron yields for sample #1.

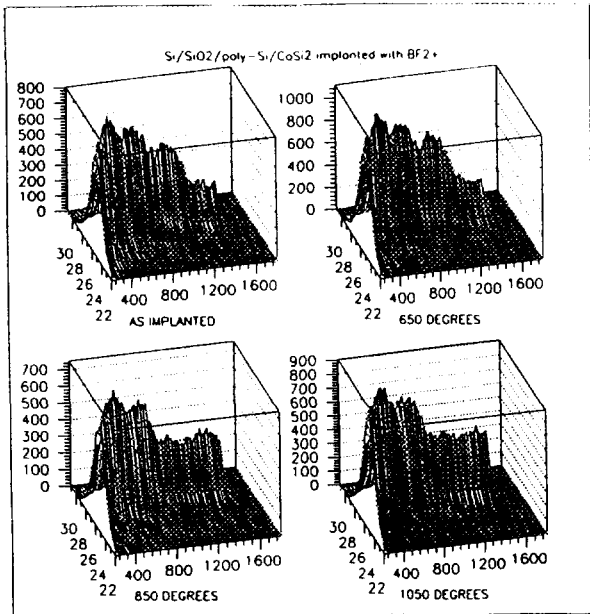


Fig. 3 Surface contour plots of the silicon yields at different temperatures, for sample #2.

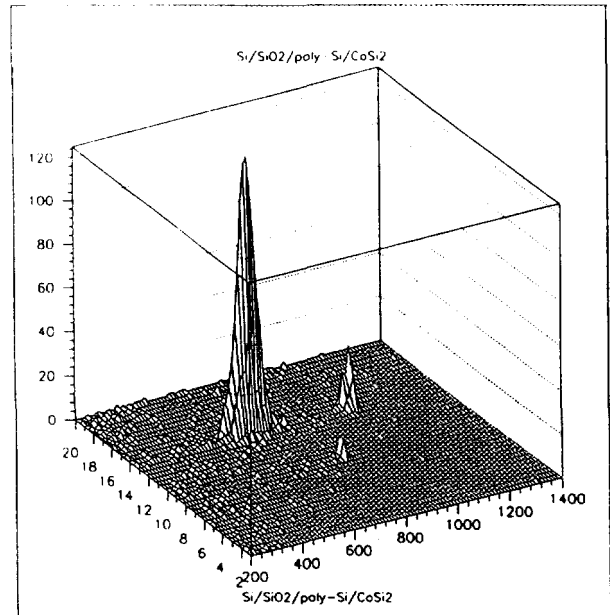


Fig. 4 Magnified surface yield plots for sample #2, showing a large oxygen yield from the buried oxide layer, surface oxygen contamination, and a small peak due to the implanted boron.



ABSOLUTE CALIBRATION IN PIXE-PIGME ANALYSIS

G. Bailey, R. Bird, P. Johnson

**Australian Nuclear Science & Technology Organisation
Private Mail Bag 1, Menai, NSW 2234, Australia**

PIXE-PIGME measurements can be made with a precision of 1 per cent or better but standards are seldom available with compositions known to this accuracy. Repeated measurements on a variety of standard reference materials have been compared with calculated yields to establish the accuracy that can be achieved in extended measurement programs.

First Measurements with the ANU PAC facility

A.P.Byrne

Department of Nuclear Physics, RSPHySE
and Department of Physics and Theoretical Physics,
The Australian National University, ACT 0200, Australia

A four detector BaF₂ array has been established to investigate semiconductor materials using the Perturbed Angular Correlation (PAC) technique. These methods use the sensitivity of the emitted nuclear radiation pattern to hyperfine fields to provide a probe of local internal magnetic fields and electric field gradients. In these measurements a $\gamma\gamma$ -time coincidence spectrum must be measured, with the hyperfine interaction producing a time varying disturbance in the normal decay spectrum.

The use of probe nuclei such as ¹¹¹In, with relatively simple decay schemes permits the use of scintillation detectors rather than the high resolution Ge detectors. While the majority of existing facilities use NaI(Tl) detectors improvement in the time response can be achieved by using faster scintillators, such as BaF₂, albeit at some cost in energy resolution.

In contrast to most such arrays used for PAC studies a modular system has been developed, with data being recorded in an event-by-event mode. The modularity of the system allows the easy inclusion of additional detectors, whilst maintaining the ability to record all possible combinations of coincidence pairs. The use of event-by-event recording followed by the use of software gating gives the ability to more closely control sources of background and monitor, and correct for, gain and time shifts in the system.

The principle characteristics of the system will be described in relation to existing systems.



A Study of Aluminium-Exposed Fish using a Scanning Proton Microprobe

M. Cholewa, G.J.F. Legge

*Micro Analytical Research Centre, School of Physics, The University of Melbourne, Parkville,
Vic. 3052, Australia*

S. Eeckhaoudt, R. Van Grieken

Department of Chemistry, University of Antwerp (U.I.A.), Universiteitsplein 1, B-2610 Wilrijk-Antwerp, Belgium

ABSTRACT

A major problem has arisen in Europe with the depopulation of fresh water fish in lakes and streams collecting acid rain. The sensitivity to acidification is species specific and appears to be associated with metal levels.

The Scanning Proton Microprobe (SPMP) at the Micro Analytical Research Centre of the University of Melbourne was used to study the subcellular distribution of aluminium and other elements in the gills of fish exposed to acidified water with elevated Al-levels. Experiments were performed on thin sections taken from fish exposed to media with different pH and aluminium concentration.

Aluminium was found on the surface of the gill lamellae, but also inside the tissue. Bulk analysis of the gills showed much higher concentrations in the aluminium-exposed fish, compared to the control ones, but no information regarding the actual accumulation sites can be inferred.

Extensive study of damage done to the sample by intense proton beams during elemental analysis was performed with scanning transmission ion microscopy (STIM).

INTRODUCTION

One of the consequences of the acidification of our environment is a higher mobility of metals in soils. They are washed out into the ground water and transported to rivers and lakes. Especially aluminium has been put forward as being toxic for fish. By using bulk analysis one obtains an idea about the amount of aluminium accumulated in or on the gills, but not about the accumulation sites. Information about the actual localization of insoluble aluminium deposits on or in the gill tissue is becoming accessible due to the availability of micro-analytical techniques. Laser microprobe mass analysis (LAMMA) and energy dispersive X-ray analysis in a scanning transmission electron microscope (STEM-EDX) and in a scanning proton microprobe (SPMP-EDX), often known as micro-PIXE, were used to study the (sub-) cellular distribution of aluminium at the gill level of different aluminium-exposed fish species. The morphological information obtained by LAMMA and micro-PIXE is inferior to that from electron microscopy, but these techniques offer a greater sensitivity as compared to X-ray micro-analysis in an electron microscope. In this paper, we report the findings obtained with a scanning particle microprobe.

MATERIALS and METHODS

The fish used in this study are Bullhead (*Ictalurus nebulosus*), Pumpkinseed (*Lepomis gibbosus*) and Rainbow trout (*Salmo gairdneri*). The first two species are known to be "acid-resistant", the latter is an "acid-sensitive" type of fish. Bullhead and Pumpkinseed were exposed to acidified water (pH 4.2) containing 1.4 mg Al/l for 10 and 21

days. Rainbow trout, being much more sensitive, were exposed to lower levels of acidity and aluminium (pH 5.00, 200 ug Al/l, for 16 and 24 hours). Control fish were only exposed to acidified water.

At the end of the exposure periods, the fish were killed with a blow on the head. The gills were cut into small pieces of approximately 1 mm³, fixed in a buffered 2.5 ethanol series, passed through propylene oxide and embedded in epoxy resin (LX-112). Sections of approximately 2 um were cut and mounted on formvar- covered sample holders. No staining was applied for the micro-analytical measurements.

EXPERIMENTS and RESULTS

Individual control and Al-exposed fish gill samples, were scanned with a microprobe beam of 3 MeV protons at the Micro Analytical Research Centre in Melbourne, Australia. A continuously moving 2 micron diameter beam spot was scanned over the sample for approximately 2 hours and all PIXE data were collected by TQSA [1]. The spectra and all the elemental maps could be observed during data collection, so that errors in identifying and centring the specimen or any movements could be detected. Fig. 1 shows the energy spectrum from a sample and Fig. 2 shows the distribution of sodium (Na), aluminium (Al), phosphorus (P) and chlorine (Cl).

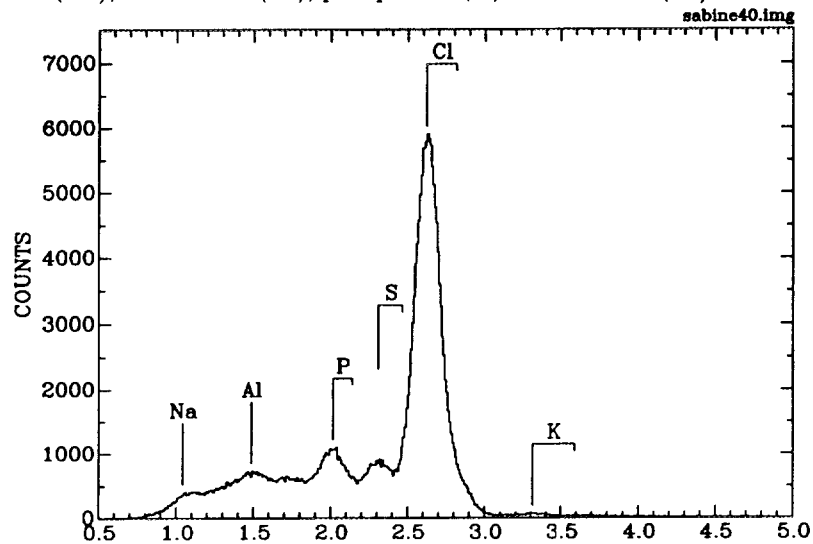


Fig.1 X-ray energy spectrum collected from the sample.

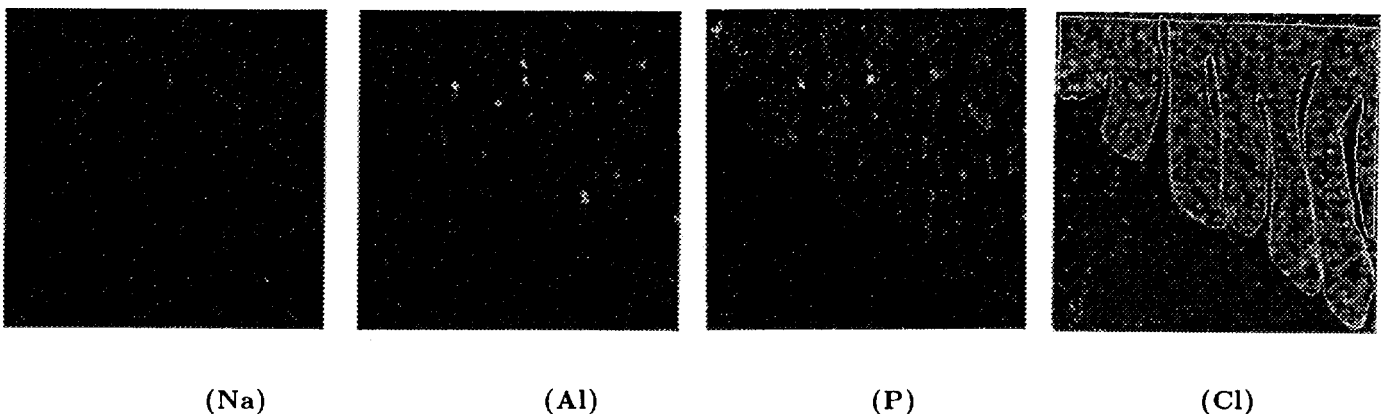


Fig.2 X-ray intensity maps from a scanned area for sodium (Na), aluminium (Al), phosphorus (P) and chlorine (Cl).

Knowing that these samples were sensitive to irradiation, we examined them with scanning transmission ion microscopy (STIM) [2,3]. A 2 MeV beam of alpha particles was used in order to maximise the density sensitivity.

This beam was focussed to less than 500 nm and scanned over a sample region. The bright field median image in Fig. 3a shows the specimen before PIXE data were collected. Fig. 3b shows a second STIM image of this sample,

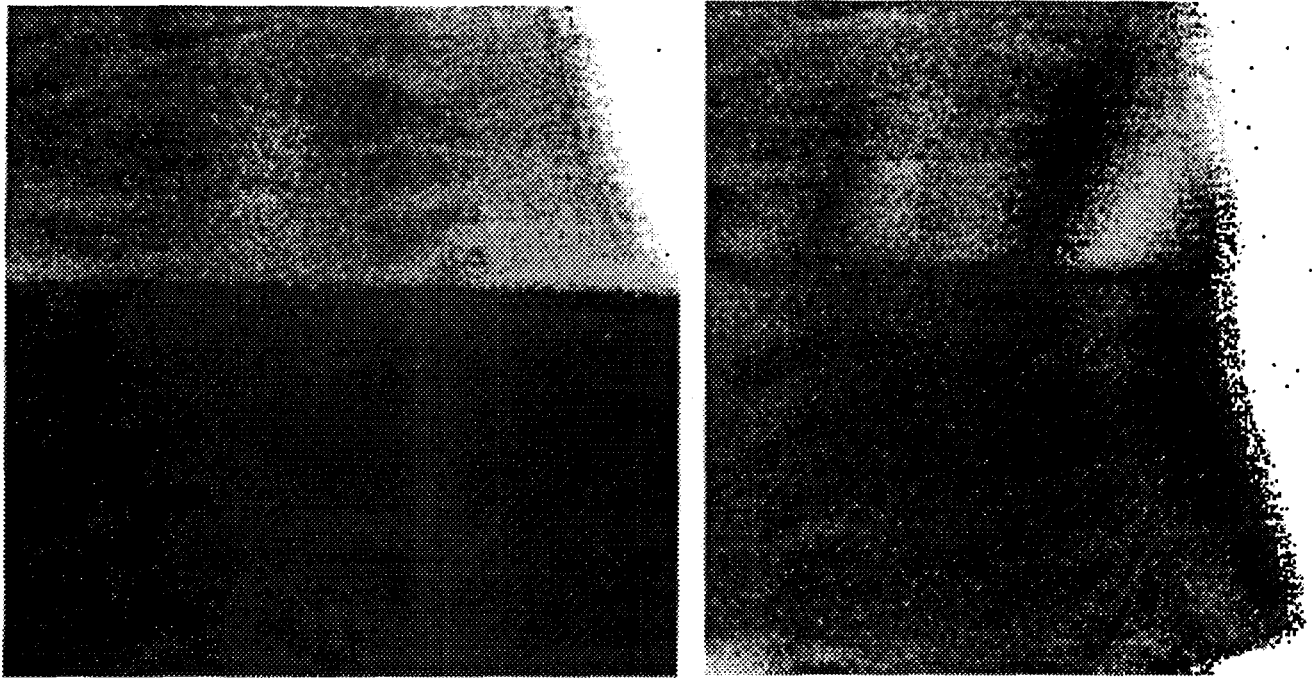


Fig.3 Bright field STIM image of median energy loss from the specimen before (a) and after (b) PIXE analysis.

collected after PIXE irradiation. As can be seen from these two data sets, the sample experienced severe movements and changes in thickness.

CONCLUSIONS

When a 3 MeV proton beam was used to collect PIXE data, damage was almost invisible. When a 2 MeV alpha beam was used, damage however was of great concern. The distribution of aluminium proved to be very localized. Some aluminium was found on the lamellae edges but also inside the tissue it could be detected. Especially in the pumpkinseeds, large deposits with an enhanced aluminium concentration were situated inside the secondary lamellae.

This work was supported by grants from the Australian Research Council. S. Eeckhaoudt is indebted to the Institute for the Encouragement of Scientific Research in Industry and Agriculture (IWONL) for financial support.

REFERENCES

- [1] G.J.F. Legge and I. Hammond
J. Microsc., 117 (1979) 201.
- [2] J.C. Overley, R.C. Overley, R.C. Connolly, G.E. Sieger, J.D. MacDonald and H.W. Lefevre
Nucl. Instrum. & Method., 218 (1983) 43.
- [3] R.M. Sealock, A.P. Mazzolini and G.J.F. Legge
Nucl. Instrum. & Meth., 218 (1983)214.



AUSTRALIS: AMS for Ultra Sensitive TRAce eLement and Isotopic Studies.

S.H. Sie and G.F. Suter
Heavy Ion Analytical Facility
CSIRO Division of Exploration and Mining
P.O. Box 136, North Ryde, NSW 2113, Australia

ABSTRACT

The AMS at the CSIRO HIAF laboratory is being upgraded to enable in-situ measurements of ultra-traces and isotopic-ratios in mineralogical applications. The upgraded system will include a microbeam Cs ion source which is designed to produce better than 50 micrometre diameter Cs beam to enable analyses of monomineralic grains. The Cs primary beam will be mass analysed in order to minimize contamination of the sample. The detection system will be upgraded to enable analyses of elements up to U, at 2 MV terminal voltage for charge states 4 and 5. The system will be known as AUSTRALIS: A.M.S. for Ultra Sensitive TRAce eLement and Isotopic Studies. An overview of the system and the anticipated applications in minerals exploration and mining research are presented.

1. INTRODUCTION

Mass spectrometry in its many forms represents an important cornerstone of the geosciences by producing chemical and isotopic data that provide insight into geological and mineralogical structure and processes. One of the fundamental limitations of any system, particularly for isotopic analysis, is the presence of mass interferences due mainly to oxides, hydrides and a few other complexes. For conventional thermionic sources, chemical separations are usually the prerequisite in order to circumvent or reduce the problem.

Probe techniques (i.e. in situ microanalysis, as opposed to bulk analysis) in mass spectrometry, such as SIMS (Secondary Ion Mass Spectrometry) or ion microprobes, and more recently laser-ablation microprobes, enable analysis of microscopic samples or features, which add another dimension to the information obtained. With these probes, data can be obtained from monomineralic grains, inclusions or microstructures (e.g. zoning) in minerals which are relics of physico-chemical processes of their formation and evolution. In addition these methods obviate the usually laborious mineral separation and chemical extraction. However the problem of interferences has to be addressed.

Very high mass resolution, usually at the expense of efficiency, can be used to solve this problem. Increased efficiency can be obtained by invoking higher order corrections to the beam transport system, enabling large acceptance angle for the mass spectrometers. In ion microprobes, this approach is particularly successful when applied to cases where additional information is available to correct for molecular and isobaric interferences, e.g. for U/Pb and S isotopes. Such information however is not always available for a number of potentially useful chronographs. SIMS has also been applied successfully to determination of trace elements, particularly light elements, many of which are of geochemical interest. For heavy elements, REE represent one such example but their determination is hampered by molecular interference problems.

AMS presents significant progress in the resolution of this problem. Most interference is eliminated by virtue of complete destruction of molecular ions through acceleration to high energies and charge exchange collisions, and isobaric discrimination is achieved through particle identification techniques available at MeV energies. The use of negative ions from the source, and availability of variety of molecular ions themselves can also be exploited to reduce or eliminate interference.

2. AUSTRALIS

The AUSTRALIS system being developed at CSIRO is an AMS system with a microprobing source, and thus fulfils the requirements for in-situ microanalysis at high efficiencies and sensitivities. This

system represents a continuing development of the existing conventional AMS system, based on the 3 MV Tandatron in the HIAF laboratory at North Ryde. Figure 1 shows the schematic of the laboratory, showing the existing system and the AUSTRALIS system. The modified HICONEX 834 source in the present system (used for C14 and Be10 measurements), will be replaced by a new source, and a new high energy analysing system will be constructed.

2.1. The Ion Source

The new source features a microbeam of Cs, which is mass analysed in order to minimise contamination of the sample, essential for example when Rb/Sr, K/Ar chronology are contemplated. It is envisaged that the Cs beam will be of the order of 30-50 microns in diameter, with intensities of the order of 1 micro ampere for an acceptable yield of the secondary ions. In this respect the source will be similar to that being developed at North Texas University [1].

To facilitate the production of the microbeam, the magnetic analyzer for the Cs system should have low aberrations coefficients, and for high intensities should have as large an acceptance angle as possible. The Cs beam will have no more than 10-15 keV energy when analyzed, and thus a magnet with beam product of 2 MeV.amu. is sufficient.

The image of the analyzing magnet for the Cs beam serves as the object of a microbeam lens system that will focus it onto the sample. The extraction geometry for the secondary ions is critical since it is intertwined with the primary beam lens system. The first order effect is the deflection of the primary beam by the secondary ions extraction fields because of the off-normal (45°) entry, compounded with higher order effects that will defocus the primary beam.

The secondary ions are extracted at normal angle and first focussed at some distance from the sample using an einzel lens, to form the object for a spherical ESA. This can be used as a simple double focusing analyser, as well as an energy filter to minimise injection of molecular ions. The image of the ESA in turn is the object for a 90 degree analyzing magnet. This magnet is already emplaced as part of the present AMS system. The various isotopes will be selected for injection into the accelerator by modulating the ion energy to give the same magnetic rigidity, i.e. the standard "bouncing" method.

Other features of the source include a sample viewing system with high ($> \times 100$) magnification, a microstage for sample manipulation with precision of 1 micron. In addition, a provision is made for an electron flood gun to prevent charge build up on the sample, and for a second Cs gun to improve the negative secondary ion yield from insulating samples, e.g. silicates

2.2. Analysing system

The high energy side features a high energy mass spectrometer system suitable for analysis of ions up to the actinides at 2.5 MV terminal voltage.

At the accelerator exit, the beam is focussed by an electrostatic quadrupole doublet to form the object for the analyzing magnet. In the present setup, the focus is at 1.2 m from the doublet. The present 90 degree analyzing magnet has a beam product of only 16, radius 50 cm and 2.5cm gap, and is set to give unity magnification. For the new system, a 90 degree magnet with beam product ~ 120 will be acquired, to enable analysis of mass 240 with 17.5 MeV and 6+ charge state, which is expected to be one of the more abundant charge states. In the new system, in order to maintain a reasonable gap size, the high energy quadrupole will have to be focussed further downstream, but physical constraints imposed by the present analysing magnet limits this point to at most 2.2 m from the quadrupole. According to the beam optical calculation, if the quadrupole is focussed in the x (in plane) direction as required for maximum resolving power, the beam will diverge to as much as 50 mm in the x direction but only ~ 6 mm in the vertical (y axis) at the magnet and thus a 25 mm gap may be sufficient. It is assumed that the beam can be focussed to $\sim 1-2$ mm wide at the object point of the magnet.

To detect the various isotopes, it is planned to use a technique whereby the magnet setting is kept constant, and the different isotopes are deflected into the magnet using an electrostatic deflector, such that the exit orbit is on axis. This will require special shaping of the entry pole face to maintain low aberrations. This technique requires the magnet to have a quasi-broad range transmission (± 10 a.m.u. for a central trajectory of mass 240).

The beam is further deflected electrostatically after magnetic analysis. Here the ESA acts only as a deflector rather than a focussing element, since the required distances are impractical otherwise. A quadrupole is used to focus the beam into the detector system. This ESA serves to clean up the background further. The detector system will be the usual proportional counter system, or a non-dispersive ion counting system, depending on the beam intensity.

3. Applications

The AUSTRALIS system will be applied to minerals exploration and mining research, through measurements of ultra traces (concentrations in the sub parts-per-billion range), various stable isotopes and potential chronographs on microscopic samples.

A number of applications will be developed as an extension of current studies of trace element geochemistry by means of the proton microprobe. Whereas the proton microprobe typically has detection limits in the 1-100 ppm, AMS has been shown [3] to be capable of detecting trace elements (demonstrated mainly for the platinum group elements, Au) at sub-ppb level. Such sensitivity is warranted in exploration problems, where it is for example desirable to understand the distribution of trace elements in coexisting phases in the deposit, both for ore genesis studies and deposit delineation in mining operations.

In most geological samples, the micro-PIXE detection limits for trace elements lighter than Fe are generally poor, because of the ubiquitous presence of Fe and the limitations imposed by the use of energy dispersive spectrometers (Si(Li) detectors). Many light elements are important geochemical markers, and in-situ detection of these at sub-ppm levels will become possible. Similarly, for heavy elements there is a gap in sensitivity for the REE in micro-PIXE, and the new system will be able to remedy this situation.

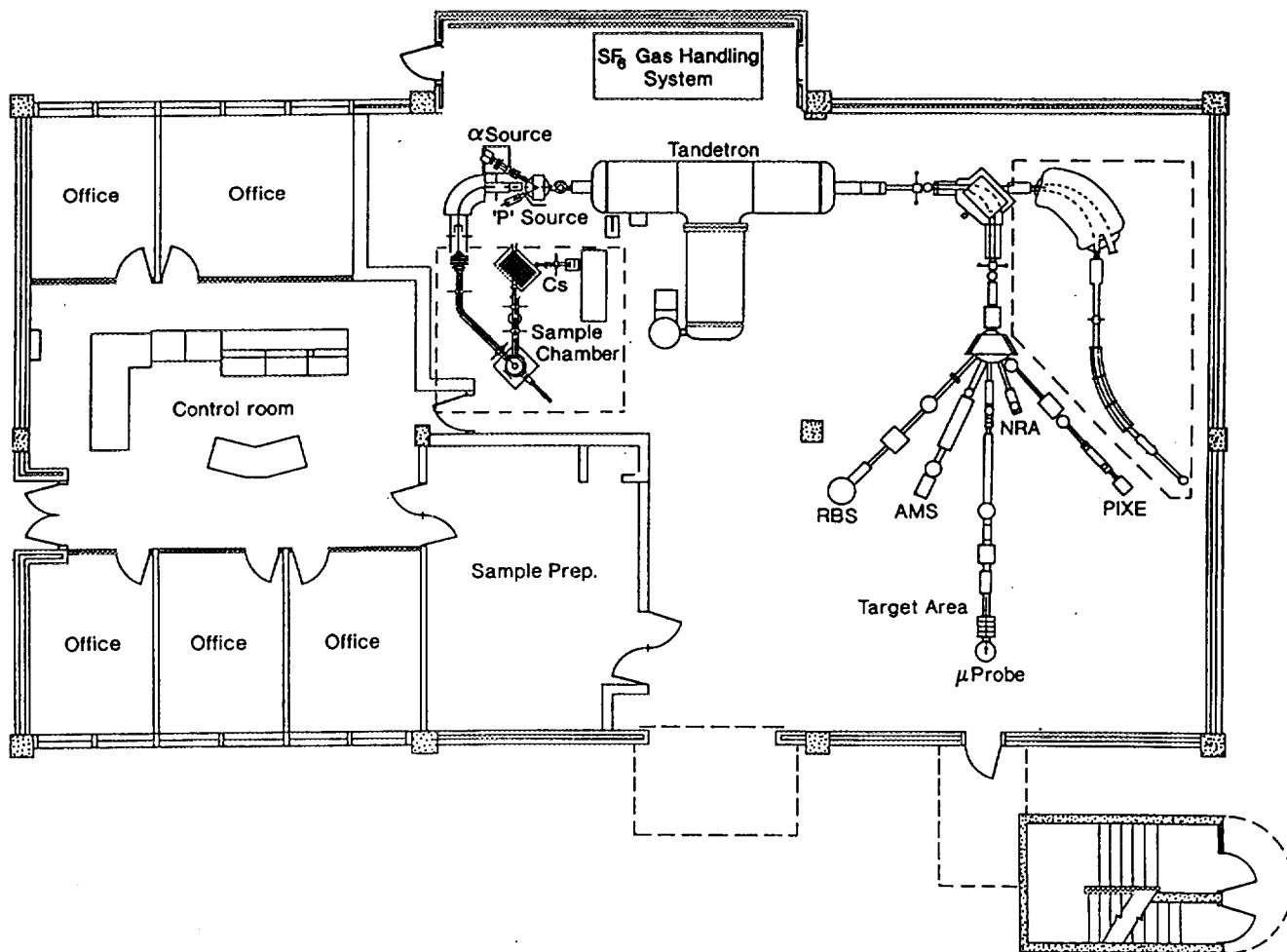
In isotopic studies, AUSTRALIS will enable applications of a few chronographs or tracers previously either tedious and limited to bulk applications, or completely inaccessible. Potentially useful applications include the common Pb, U/Pb (Pb^{207}/Pb^{206}), Rb⁸⁷/Sr⁸⁷, Re¹⁸⁷/Os¹⁸⁷ systems. The particular advantage of the AMS principle can be exploited: in the Rb/Sr case, the interfering isobar (the parent Rb⁸⁷) can be suppressed by selecting the hydride beam from the source. In the Re/Os system, the negative elemental ions of Re is highly suppressed [4].

To balance these optimistic expectations, it should be noted that AMS has not been applied to determination of isotopic ratios to very good precisions (permil range) on a routine basis except for C isotopes measurements. Fractionation effects due to the source, the accelerator and beam transport system, and physical processes involved (e.g. Coulomb explosion, charge changing multiple collisions) can affect and perhaps obscure the effects sought. For this reason some system, e.g. the Sm¹⁴⁷/Nd¹⁴³, where the required precision is in the 0.05 permil range, is unlikely to be feasible. In contrast, fractionation of Re/Os during partial meltings in the mantle, resulting in high ratios in the crust makes it an attractive candidate for a chronometer or tracer. The development of AUSTRALIS presents an exciting challenge to expand the capabilities of AMS.

References.

- [1] S. Matteson et al., Nucl. Instr. Meth. **B52** (1990) 327.
- [2] W.E Kieser et al., "The ISOTRACE/HVEE high capacity ion source for AMS", Nucl. Instr. Meth. (1993) in press, and priv. communication.
- [3] J.R. Rucklidge et al., Nucl. Instr. Meth. **B52** (1990) 507.
- [4] R. Middleton, "A Negative Ion Cookbook", 1989. unpublished.

Fig. 1. A schematic diagram showing the plan view of the HIAF laboratory. The present conventional AMS system is based on a modified HICONEX 834 source, and the detector system is installed in the 22.5° left beam line after the switching magnet. The "AUSTRALIS" system being developed is shown enclosed in the dashed line. The microprobing ion source will replace the existing HICONEX source. The analysing system will bypass the present high energy analysing magnet.



OBSIDIAN SOURCING STUDIES IN PAPUA NEW GUINEA USING PIXE-PIGME ANALYSIS

Glenn R Summerhayes (1), Roger Bird (2), Mike Hotchkiss(2), Chris Gosden (1), Jim Specht (3), Robin Torrence (3) and Richard Fullagar (3)

(1) Department of Archaeology, La Trobe University, Bundoora, Vic 3083

(2) Australian Nuclear Science and Technology Organisation, Private Mail Bag 1, Menai, NSW 2234

(3) Division of Anthropology, Australian Museum, P.O. Box A285, Sydney South, NSW 2000.

Introduction

The extraction and use of West New Britain obsidian has a twenty thousand year history in the western Pacific. It is found in prehistoric contexts from Malaysia in the west to Fiji in the east. Of significance is its spread out into the Pacific beginning at c.3500 B.P. It is found associated with the archaeological signature of this spread, Lapita pottery, in New Ireland, Mussau Island, South east Solomons, New Caledonia, Vanuatu, and Fiji.

Yet the number of places where obsidian occurs naturally is few in number, making the study of obsidian found in archaeological contexts away from their sources a profitable area of research. The chemical characterisation of obsidian from the source area where it was extracted and the archaeological site where it was deposited provides important information on obsidian production, distribution and use patterns. The objective of this project is to study these patterns over a 20,00 year time span and identify changing distribution configurations in order to assess the significance of models of exchange patterns or social links in Pacific prehistory.

To achieve this objective over 1100 pieces of obsidian from archaeological contexts and over 100 obsidian pieces from sources were analysed using PIXE-PIGME from 1990 to 1993. Our aims were twofold. First, to discriminate between individual source areas in West New Britain, in particular sources in the Talasea area. The second objective is to map out the distribution of West New Britain obsidian from where it was found back to its source area, and compare the changing configurations over time. A third aim associated with the above objective was to test the formation of unascribed sources. Previous sourcing studies undertaken in the 1980's by Dr Roger Bird had shown that some archaeological samples although clustering near known Talasea obsidian sources, formed separate groups. He named these clusters TT, UU and ZZ. To test whether they were unidentified obsidian subgroups or the result of the effects of surface alteration on the chemical makeup of these pieces a reanalysis was undertaken.

Machine Conditions

PIXE-PIGME measurements were made using a 2.5 MeV proton beam from the ANSTO 3 MV Van de Graaf accelerator. In order to

obtain a better discrimination between sources, a beam current of 300 nA was obtained by increasing the beam defining aperture to 2#mm diameter. Using the ten minute measuring time, the dose for each sample was increased by a factor of 3. Other parameters were the same as in previous studies. Wekok obsidian from the Admiralty Islands (AD2000), the standard used in all previous analyses, were used to check the efficiency of the measurement system.

Discrimination of Source Areas

Over 100 obsidian samples were analysed using PIXE-PIGME in 1990. These samples were collected during intensive surveys of the source areas around Talasea, Garua Island, and the Mopir area in 1988, 1989 and 1990.

A ratio combination of 9 elements were used to separate out groups as per previous studies: F/Na, Al/Na, K/Fe, Ca/Fe, Mn/Fe, Rb/Fe, Y/Zr, Sr/Fe and Zr/fe. Five groupings are distinguished:

1. Kutau/Bao
2. Pilu
3. Baki and Garala
4. Mt Hamilton
5. Mopir

Note that such a discrimination was possible only with extensive sampling of the source areas, and increasing the beam current to 300 nA.

Distribution of Obsidian

Over 1100 pieces of obsidian found in archaeological contexts covering a 20,000 year time span were analysed using PIXE-PIGME. The significance of the results can be summarised below:

First, the results extend our knowledge of obsidian exploitation and exchange well into the Pleistocene and show that differential exchange of obsidian existed between regions down into the mid Holocene. Results from the New Ireland late Pleistocene sites of Matenbek (dating from c.20,000 B.P.) and Matenkupkum (dating from c.16,000 B.P.) demonstrate an exchange of obsidian from the Mopir source, c.350km distant. Obsidian from the Mopir source account for roughly three quarters of that analysed, while the Talasea sources (Kutau/Bao, Hamilton and Gulu) accounted for the rest. Kutau/Bao provides up to 75% of the Talasea obsidian. Late Pleistocene and early to mid Holocene sites located on the south coast and interior of West New Britain, such as Misisil Cave (dating from ca.11,000 B.P.), Yombon (dating from c.4200 B.P.), Lolmo (dating from c.5700 B.P.) and Alanglong (dating to c.3500 B.P.), on the other hand, have more or less equal amounts of obsidian from Mopir and the Talasea sources, with Kutau/Bao again dominating the Talasea obsidian present. The distribution of obsidian can be due to two factors: geographic proximity and mobility patterns. If populations were semi sedentary and moving frequently around the landscape the dominance of Mopir in New Ireland would thus be explained by Mopir being closer to New Ireland than

Talasea. Misisil, Yombon, Lolmo and Alanglong on the other hand are closer to both sources.

Sites closer to the sources themselves have predictably obsidian from the nearest source. As such Bitokara Mission located next the Kutau/Bao source has Kutau/Bao obsidian, Walindi located 25km south of Kutau/Bao and the Garua Island sources has predominantly Kutau/Bao obsidian and one piece from Baki (on Garua Island), Buvussi located near the Mopir source has Mopir obsidian, and sites on Garua (FAO and FAQ) have Baki obsidian.

Secondly, at c.3,500 B.P. a different picture emerges which allows us to assess the impact of social, geographic, economic and environmental influences on obsidian exchange. The sourcing results demonstrate that at 3500 B.P. obsidian from Kutau/Bao dominated the distribution patterns. Mopir obsidian ceases to be found in archaeological deposits in West New Britain at this time (eg. sites in the Arawe Islands - Lolmo, Adwe, Apalo, Paligmete; and Misisil, and Yombon). Such an absence could be connected with the eruption of Mt Witori, a volcano near the Mopir source, making this source inaccessible. Such inaccessibility would not have lasted long as Mopir obsidian is found at c.2,600 B.P. in north east New Britain at the site of Watom. Yet such inaccessibility is not the case with sites on Garua Island where the use of Baki obsidian virtually drops off and is replaced by obsidian from Kutau/Bao. Ash from the Witori eruption would have had a devastating effect on the population of this area, either killing the local population or driving them out with the destruction of flora and fauna, however it would not have blocked the access of obsidian as is evident by the continued use of Kutau/Bao obsidian.

The archaeological evidence suggests that settlements were more permanent than before, and the control of production and distribution of obsidian has more to do with social factors. This is in contrast to what when on before. Although mobility patterns are still important, (ie. a change from mobile semi-sedentary to sedentary), geographical proximity is no longer crucial.

The timing of this shift in production and distribution is important as it occurs at the same time that Lapita ceramics appeared in these areas. Lapita ceramics are the archaeological signature of people entering Remote Oceania for the first time. They are found from New Britain to Samoa, in contexts dated to between c.3500 to 2000 B.P. and have a distinctive set of designs suggestive of a complex exchange system or communication network.

ZZ, UU and TT.

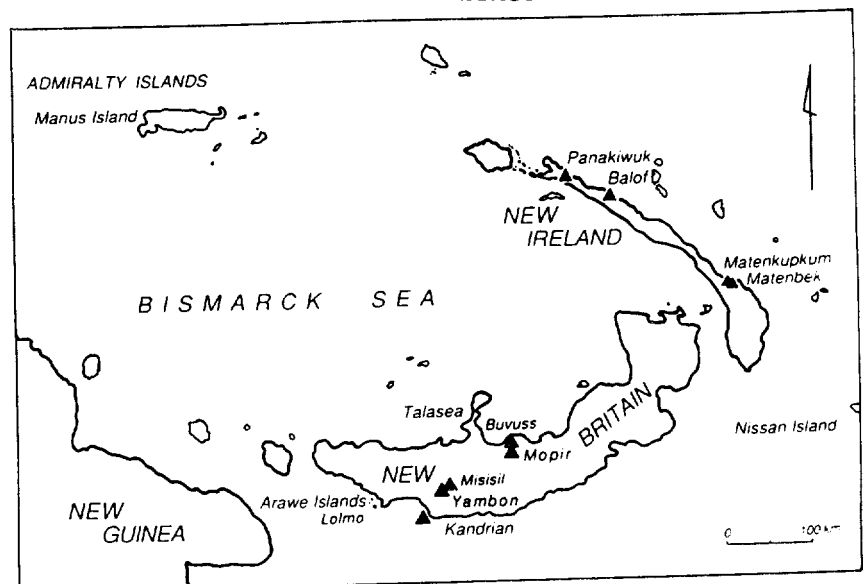
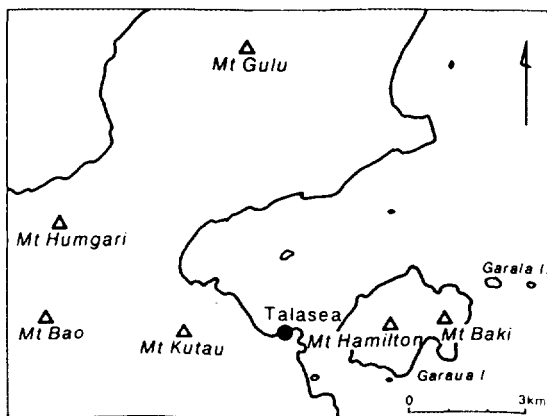
To test whether these groups are distinct obsidian subgroups or the results of surface modification on the elemental makeup caused by weathering or post depositional effects, such as abrasion, leaching or hydration, a series of tests were performed.

Thirty obsidian pieces assigned to these groups in previous PIXE-PIGME analyses performed in the 1980's were re-analysed with the same machine conditions as set out above. Some were broken, and repeat measurements made on both the abraded exterior and fresh interior edges. Samples were also carefully mounted as low energy X-rays from elements such as Si, S, Cl, K and Ca suffer varying degrees of attenuation as they leave the surface layer - depending on the angle of the surface relative to the beam and detector directions. Results showed that that these subgroupings were from the Kutau/Bao source and their elemental separation was due to the effects of surface weathering. The results showed a considerable excess of Ca in the badly abraded portion, a slight excess of Ca in non abraded parts of the surface and the correct level of Ca in the interior of the artefacts compared to the nearest known material. Other artefacts showed reduced Na concentrations which are often associated with increased K concentrations. Clearly major elements are not well suited to artefact characterisation although they do give valuable information on the type of material submitted and factors which have affected it during handling and burial.

In spite of variations in major elements, the close agreement between results for minor and trace element concentrations in artefacts and known source material indicates that the provenance of each artefact can be reliably determined. This conclusion provides important validation of the use of ion beam analysis in obsidian artefact characterisation. Other methods of bulk analysis such as neutron activation analysis also use trace elements but require more sample and are more time consuming and destructive.

THE BISMARCK ARCHIPELAGO

VOLCANOES IN THE TALASEA AREA





**ELECTRON PARAMAGNETIC RESONANCE (EPR) SPECTROSCOPY
SUPPORTED BY PARTICLE-INDUCED X-RAY EMISSION (PIXE) AND
PARTICLE-INDUCED GAMMA RAY EMISSION (PIGME)
SPECTROSCOPY IN MINERAL EXPLORATION.**

van Moort, JC¹ and Hotchkis, M²

¹ Geology Department, University of Tasmania

² Australian Nuclear Science and Technology Organisation

Abstract

Van Moort and Russell (1987) observed that microcrystalline vein quartz associated with gold mineralisation shows in general stronger room temperature electron paramagnetic resonance than barren vein quartz. Because powder EPR spectra are so difficult to interpret the quartz was later chemically analysed by proton probe analysis (van Moort et al. 1990)

As the types of orebodies investigated increased it became apparent that several types of quartz can be characterised by their EPR spectra and by their trace element content. more importantly the intensity of the EPR spectra increases when the quartz contains or is close to ore and the associated trace element patterns change accordingly (Pwa and van Moort, 1992). Siliceous rocks may be used as an alternative to quartz in the delineation of ore.

The spectra of quartz associated with gold, zinc, copper and gold mineralisation shown in figure 1 may serve as examples of some types of spectra encountered. Table 1 presents some of the trace elements in the respective samples

At present 3800 EPR spectra and 900 multi element PIXE/PIGME proton probe analyses have been performed.



PIXE-PIGME ANALYSIS OF ARABIAN BRONZE AND SILVER COINS

R.Bird, P.Grave, D.Potts
Australian Nuclear Science and Technology Organisation
Private Mail Bag 1, Menai, NSW 2234, Australia

A number of coins minted in Arabia and dating from the first century BC to the third century AD were analysed by PIXE-PIGME techniques. Fifteen major, minor and trace elements were detected showing the presence of at least three different compositional types. The results also show the effects of debasement with elements such as iron, nickel and lead.



A back-arc setting for mafic rocks of the Honeysuckle Beds, southeastern N.S.W.: the use of trace and rare earth element abundances determined by INAA.

K.A. Dadd

Department of Applied Geology, University of Technology, Sydney,
P.O. Box 123, Broadway, N.S.W. 2007.

The tectonic setting in which the Honeysuckle Beds erupted is a key to reconstructions of the Lachlan Fold Belt in N.S.W. during the Silurian. The Honeysuckle Beds, located in southeastern N.S.W. (Fig. 1) within the Tumut Synclinal Zone, comprise pillow basalt, massive basalt, basalt breccia and fine-grained sedimentary rocks metamorphosed to the lower greenschist facies. They form part of the fill of a palaeogeographic feature known as the Tumut Trough or Basin. The Honeysuckle Bed rocks occur to the east of and stratigraphically above the dacitic volcanoclastic rocks of the Blowering Formation with which they have both conformable and faulted contacts, and to the west of the fault-bounded Coolac Serpentinite.

A sequence including the Honeysuckle Beds, Coolac Serpentinite and mafic and ultramafic intrusives of the North Mooney Complex, was interpreted by Ashley et al. (1979) as representing the upper part of layer 2 and layer 1 of oceanic crust. The presence of an oceanic basin implied in their model and used in many reconstructions of the Silurian Lachlan Fold Belt (e.g. Crook, 1980; Cas, 1983), has been disputed, for example by and Wyborn (1992), who considered that the Fold Belt had a continuous continental basement at this time.

The mafic rocks of the Honeysuckle Beds range in composition from tholeiitic basalt to andesite (SiO₂ 47.0-64.2%) (Table 1). The primary mineralogy of the suite probably consisted of plagioclase, augite and opaque minerals set in a glassy groundmass. Plagioclase is now altered to albite, epidote and clay, and clinopyroxene largely to actinolite.

Table 1. Representative analyses from Groups 1H, 2H and 3H of the Honeysuckle Beds. Analyses for SiO₂-Zr determined by XRF at Macquarie University; La-Ta by INAA at Lucas Heights.

Sample No.	K90-44	K91-323	K90-136
Group	1H	2H	3H
Grid Ref.*	26908144	14152321	17571429
SiO ₂ #	49.28	53.07	52.4
TiO ₂	0.74	0.99	1.11
Al ₂ O ₃	17.63	17.39	16.85
FeOT	6.42	7.96	7.95
MnO	0.22	0.13	0.16
MgO	9.26	7.01	7.22
CaO	14.48	8.7	9.6
Na ₂ O	0.84	3.96	4.27
K ₂ O	1.05	0.42	0.23
P ₂ O ₅	0.08	0.13	0.21
Ba	167	90	44
Cr	558	346	202
Rb	74	19	6
Sr	419	250	195
Th	1	2	4
V	232	198	215
Y	20	27	33
Zr	44	107	200
La	4.1	9.5	14.6
Ce	8.9	20.8	32
Nd		9	19
Sm		3.11	4.7
Eu	2.05	0.95	1.19
Tb	0.71	0.75	0.9
Dy	4	4.5	
Yb	2.1	2.8	3
Lu	0.32	0.41	0.4
Sc	36	38	34
Hf	2.2	3.7	5
Ta			1

* Grid references refer to Tumut 1:100 000 sheet

Analyses recalculated to 100% on a volatile-free basis

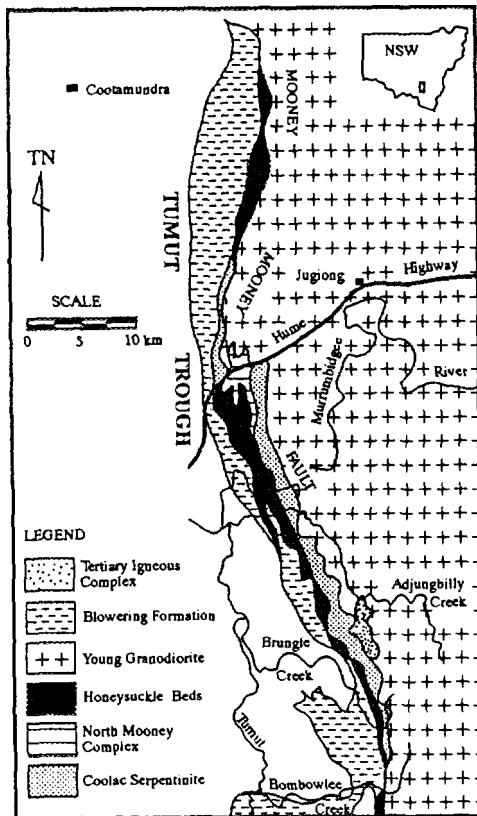


Figure 1. Location of the Honeysuckle Beds in southeastern N.S.W.

Other alteration minerals are chlorite, calcite, zoisite and quartz. No relict olivine or pseudomorphs after olivine have been observed. All samples have Nb/Y below 0.67 and therefore are classified as subalkalic (Winchester and Floyd, 1977). The wide range of MgO (3.7-11.5%) and Mg # (32.2-54.9) suggests that the mafic rocks cover a spectrum from little fractionated to highly evolved but that none probably represent primary melts. Three main groups of samples are recognised within the unit (Fig. 2). Samples within each group are related by fractionation processes and the spread of data for most major and compatible trace elements can be explained by a combination of fractionation and varying degrees of partial melting.

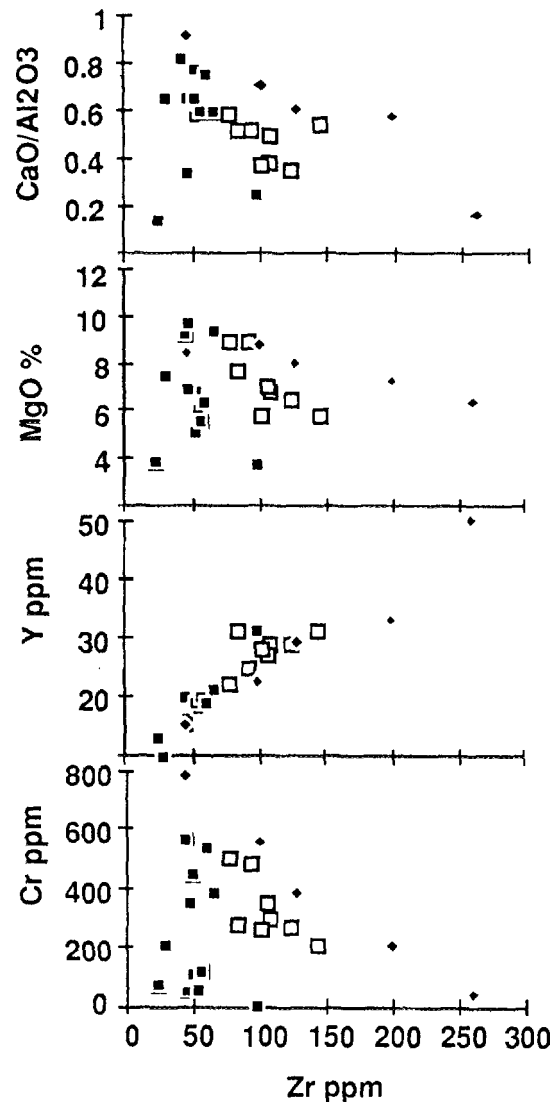


Figure 2. Major and trace element abundances in mafic rocks of the Honeysuckle Beds. Open squares = Group 1H; solid squares = Group 2H; solid diamonds = Group 3H.

The Honeysuckle mafic rocks span the mid-ocean ridge basalt (MORB) to island arc basalt fields of most discrimination diagrams but are most similar to back-arc basin basalts. A comparison with typical MORB compositions reveals that compositions are enriched in light rare earth elements (Fig. 3), Ba, Rb and Th and depleted in Nb, Ta and Ti (Figs 4 and 5), consistent with modification of the source by subduction-related fluids. There is a large variation in incompatible element ratios within the suite and samples plot away from a typical MORB mixing curve (Fig. 6), indicating the

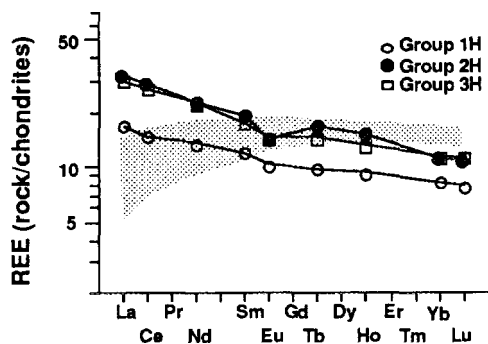


Figure 3. Representative REE profiles. The shaded area shows the field of typical N-MORB (Sun et al., 1979).

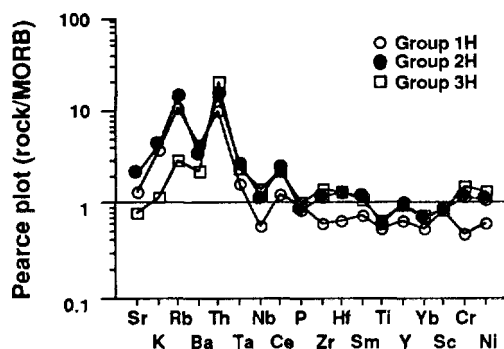


Figure 4. Pearce plot showing enrichment and depletion of elements relative to MORB (after Pearce, 1983).

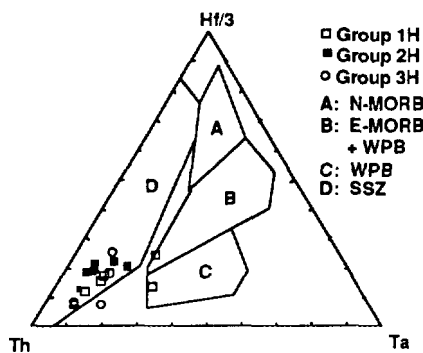


Figure 5. Samples plot in the supra-subduction zone field (SSZ). WPB = within-plate basalt. (after Elthon, 1991)

Honeysuckle Beds are derived from a contaminated source. The composition of the Honeysuckle Beds most resembles that of mafic rocks erupted in an incipient back-arc basin behind an arc floored by continental crust. The basin probably never developed a ensimatic substrate.

References

- Ashley, P.M., Brown, P.F., Franklin, B.J., Ray, A.S. and Scheibner, E., 1979. Field and geochemical characteristics of the Coolac Ophiolite suite and its

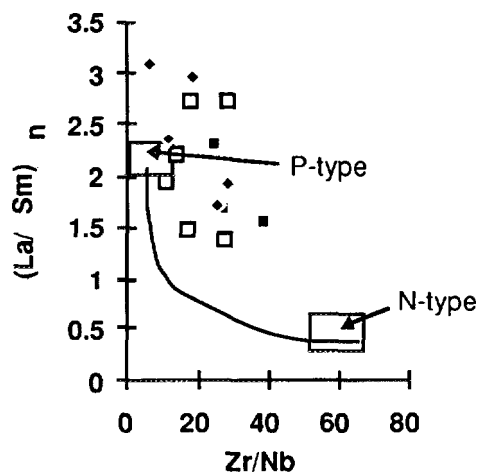


Figure 6. Honeysuckle samples plot to the right of a mixing trend for P and N-type MORB indicating contamination (after Wilson, 1989).

- possible origin in a marginal sea. *J. Geol. Soc. Aust.*, 26, 45-60.
- Cas, R.A.F., 1983. A review of the palaeogeographic and tectonic development of the Palaeozoic Lachlan Fold Belt of southeastern Australia. *Geol. Soc. Aust. Spec. Pap.*, 10.
- Crook, K.A.W., 1980. Fore-arc evolution in the Tasman Geosyncline: the origin of the southeast Australian continental crust. *J. Geol. Soc. Aust.*, 27, 215-232.
- Elthon, D., 1991. Geochemical evidence for the formation of the Bay of Islands ophiolite above a subduction zone. *Nature*, 354, 140-143.
- Pearce, J.A., 1983. Role of sub-continental lithosphere in magma genesis at active continental margins. In: *Continental Basalts and Mantle Xenoliths*. C.J. Hawkesworth and M.J. Norry eds, Shiva Publ., Cheshire, 230-249.
- Sun, S.-S., Nesbitt, R.W. and Sharaskin, A.Y., 1979. Geochemical characteristics of mid-ocean ridge basalts. *Earth Planet. Sci. Lett.*, 44, 119-138.
- Wilson, M., 1989. *Igneous Petrogenesis*. Unwin Hyman Inc., London, 466p.
- Winchester, J.A and Floyd, P.A., 1977. Geochemical discrimination of different magma series and their differentiation products using immobile elements. *Chem. Geol.*, 20, 325-345.
- Wyborn, D., 1992. The tectonic significance of Ordovician magmatism in the eastern Lachlan Fold Belt. *Tectonophysics*, 214, 177-192.



Immiscible Silicate Liquids at High Pressure: the influence of melt structure on elemental partitioning.

E. Vicenzi (Princeton Materials Laboratory, Princeton, N.J., U.S.A.),

T.H. Green (Macquarie University, North Ryde, NSW) and

S.H. Sie (HIAF, CSIRO Exploration and Mining, North Ryde, NSW)

ABSTRACT

Micro-PIXE analyses have been applied to study partitioning of trace elements between immiscible silicate melts stabilised at 0.5 and 1.0 GPa over a temperature range of 1160-1240 °C in the system $\text{SiO}_2\text{-FeO-Al}_2\text{O}_3\text{-K}_2\text{O (+P}_2\text{O}_5)$. The system was doped with a suite of trace elements of geochemical interest: Rb, Ba, Pb, Sr, La, Ce, Sm, Ho, Y, Lu, Th, U, Zr, Hf, Nb and Ta at approximately 200 ppm level for all elements except for the REE's, Ba and Ta (600-1200 ppm). Trace element partitioning was found to be a complex function of cation field strength (charge/radius²). Although field strength is important in determining the nature and degree of partitioning, it is clearly only one component of the underlying mechanism for the way in which elements distribute themselves between two silicate liquids.

1. Introduction

Knowledge of trace element partitioning between crystals and silicate melts has allowed geologists to model the geochemistry and evolution of magmatic systems, to deduce genetic relationships of associated rocks, and to perform mass balance computations to test particular physical mechanisms for separation of crystals and melt. In the present investigation, we studied the partitioning of trace elements between two immiscible silicate melts that differ greatly in composition at 0.5 and 1.0 GPa, and 1160-1240 °C temperature. Pioneering work in the field of trace element partitioning between immiscible silicate liquids was conducted by Watson [1] and Ryerson [2], while more recent work has been completed by Ellison [3]. The present study is a direct outgrowth of Watson's earlier work in the system $\text{SiO}_2\text{-FeO-Al}_2\text{O}_3\text{-K}_2\text{O}$ and is most different in three regards:

- 1.) the experiments have been performed at elevated pressures, and
- 2.) most of the runs contain P_2O_5 , an oxide known to enhance liquid unmixing [4] [5] [6]
- 3.) a cross-section of the periodic table, including 16 elements of geochemical interest, has been incorporated into a single starting mixture at the trace element level.

The application of quantitative microbeam PIXE has enabled one to study many cations in a single run without altering the major element chemistry of a starting material.

2. Experimental Method

The samples were prepared from a mixture of major element oxides (SiO_2 , FeO, Al_2O_3 , and K_2O) doped at approximately the following levels: Rb, Sr, Pb, Y, Zr, Nb, Th, and U at 200 ppm, Ta at 400 ppm, Hf and Ba at 650 ppm, La, Ce, Sm, Ho, at 700 ppm, and Lu at 1100 ppm. 5.5 wt % P_2O_5 was also added to an aliquot of the mixture as $(\text{NH}_4)\text{H}_2\text{PO}_4$. The mixture was homogenised by repeated (three times) fusion at 1425 °C in an Ar atmosphere at room pressure and grinding. Samples were sealed and welded in 2 mm diameter Pt capsules and pressure was applied to the sample using a conventional 12.7 mm piston cylinder apparatus and laboratory grade NaCl cells as the medium. High temperatures were generated by a graphite resistance furnace. Spec pure Fe wire was added to the glass powder prior to welding to offset the loss of Fe from the sample as a result of PtFe alloy formation along the capsule walls. Experiments were initially held at 1280°C for 4 hours to dissolve the Fe-wire, and were then lowered to the run temperature for between 30 and 90 hours. Quenching at the termination of the runs took place on the order of several hundreds of degrees per second, and resulted in the formation two distinct amorphous silicate phases. PIXE analyses of the polished samples were conducted with 3 MeV proton beam focused to between 30-50 microns. A 300 micron Al filter was used to suppress most of the Fe lines, and thus limits the elements that can be analysed

to those with $Z > 26$ (Figure 1). Each glass was analysed in 8-11 locations with an accumulated charge of 9μ Coulombs. Major elements were determined using a CAMEBAX electron microprobe.

3. Results

Liquid unmixing in the system $\text{SiO}_2\text{-FeO-Al}_2\text{O}_3\text{-K}_2\text{O (-P}_2\text{O}_5)$ produces one melt rich in SiO_2 and another rich in FeO plus crystals of beta quartz. Al_2O_3 is preferentially incorporated into the Si-rich melt where it has been suggested that AlO_4 substitutes for SiO_4 tetrahedral units [8]. Apart from FeO , P_2O_5 is the only major oxide that partitions into the Si-poor melt. Ryerson [6] concluded that $\text{P}_2\text{O}_5\text{-M}_x\text{O}_y$ (where M represents a metal e.g. Fe) complexes form bonds that are generally stronger than those formed by corresponding $\text{SiO}_2\text{-M}_x\text{O}_y$ groups. The strong partitioning of Fe resulted in a substantial density contrast between the immiscible melts. Densities for the Si-poor (Fe-rich) melt range from 3.4 to 3.8 gm/cm^3 , and for the Si-rich the range is more restricted at 2.4 to 2.5 gm/cm^3 . Although spheres of either glass were observed within a matrix of the other, the negative buoyancy of the Si-poor liquid caused a large pool to form at the base of the capsules. Multiple PIXE spot analyses of the same glass and in Si-poor blebs of variable apparent diameter produced a narrow distribution of trace element concentrations for most elements, indicative of a close approach to chemical equilibrium. All elements except Rb (and Hf in one instance) have 2-liquid partition coefficients greater than 1, indicating that they are concentrated in the less structured Si-poor melt. The higher concentration of Rb^{1+} in the Si-rich glass is probably related to the local charge balance required by the substitution of Al^{3+} for Si^{4+} [8]. The pattern formed in a plot of 2-liquid partition coefficient K_d (defined as the ratio of the element concentrations in the phases) as a function of cation field strength is a complex one (Figure 2a and b). Among the low field strength cations, the trend is broadly positive from Rb to alkali earth cations (Ba and Sr) and Pb. The K_d 's increase further and reach a peak in the light rare earth elements which are moderate in terms of field strength. Partition coefficients decrease from the light to heavy rare (and Y), although Ho and Lu determinations have the greatest associated uncertainties. The values for the actinides (Th and U) are smaller than those for the REE and suggests the negative correlation between K_d and field strength extends from the LREE to Zr and Hf. The latter elements have the lowest K_d s. Nb and Ta are the highest field strength elements and have moderate K_d s that are similar to those of Sr. Decreasing temperatures for a given pressure yields increasingly greater K_d s (Figure 2a). This merely reflects the increase in the width of the solvus with falling temperature and the divergence of major element compositions of the liquid pairs. The effect of pressure is difficult to isolate because of shifts in the position and symmetry of the solvus. It is therefore not possible to stabilise two melts of identical composition under isothermal conditions at two different pressures. As for the case of major elements, the addition of phosphorus affects the trace element partitioning. Figure 2b shows that a P-bearing system at $0.5\text{GPa-}1200^\circ\text{C}$ produces a far wider range of K_d s than a P-free system at $0.5\text{GPa-}1160^\circ\text{C}$, the opposite of what would be expected for a decrease in temperature in two isochemical runs.

4. Discussion and Conclusions

Hess and Rutherford [8] suggested that high field strength cations are energetically unsuitable for a highly structured silicate melt, and hence they predicted those cations would partition into the less structured (Si-poor) member of a 2-melt system. Watson [1] explained that this theory is oversimplified in that it assumes bonding between metals and oxygen is entirely ionic, while a more realistic model would account for some degree of covalent and directional bonding. The data presented in figure 2 do not show a direct correlation between 2-liquid partitioning and field strength, and instead show the negative correlation from the LREE - actinides - Zr/Hf, which rules out the possibility of two groups of different cation-oxygen bonding character. Moreover, elements that are virtually identical in terms of their field strength, for example, Nb and Ta, do not have the same partition coefficient. Thus a model to describe partitioning in immiscible systems, will include field strength only as one component of a multi-term equation. Outside of the complexity mentioned by Watson [1], information concerning the type and distribution of cation coordination number, in addition to the effect of complexes with metals other than Si (i.e. P) are among the factors needed to fully describe partitioning between silicate liquids. Of the 16 trace elements studied, a high field strength cation, Hf, partitions most evenly (K_d close to 1) between the Si-poor and Si-rich melts. This behaviour suggests that Hf partitioning is nearly independent of melt composition. We therefore propose that Hf is best suited to model natural rock data where suitable crystals (those that incorporate Hf in measurable concentrations) are in equilibrium with a range of melt compositions.

Acknowledgements

This work was supported by the Australian Research Council. We would like to express sincere thanks to E. Bruce Watson for donating the starting mixture for the experiments.

References

- [1] Watson, E.B. *Contrib. Mineral. Petrol.* **56** (1976) 119-134.
- [2] Ryerson, F.J. & Hess, P.C. *Geochim. Cosmochim. Acta* **42** (1978) 921-932.
- [3] Ellison, A.G. & Hess, P.C. *Geochim. Cosmochim. Acta* **53** (1989) 1965-1974.
- [4] Visser, W. & Groos, A.F.K.v. *Amer. J. Sci.* **279** (1979) 1160-1175.
- [5] Visser, W. & Groos, A.F.K.v. *Amer. J. Sci.* **279** (1979) 970-989.
- [6] Ryerson, F.J. & Hess, P.C. *Geochim. Cosmochim. Acta* **44** (1980) 611-624.
- [7] Watson, E.B. *Carn. Inst. Wash. Yrbk.* **74** (1975) 500-504.
- [8] Hess, P.H. & Rutherford, M.J. *Proc. Lunar Planet. Sci. Conf. V* (1974) 328-329.

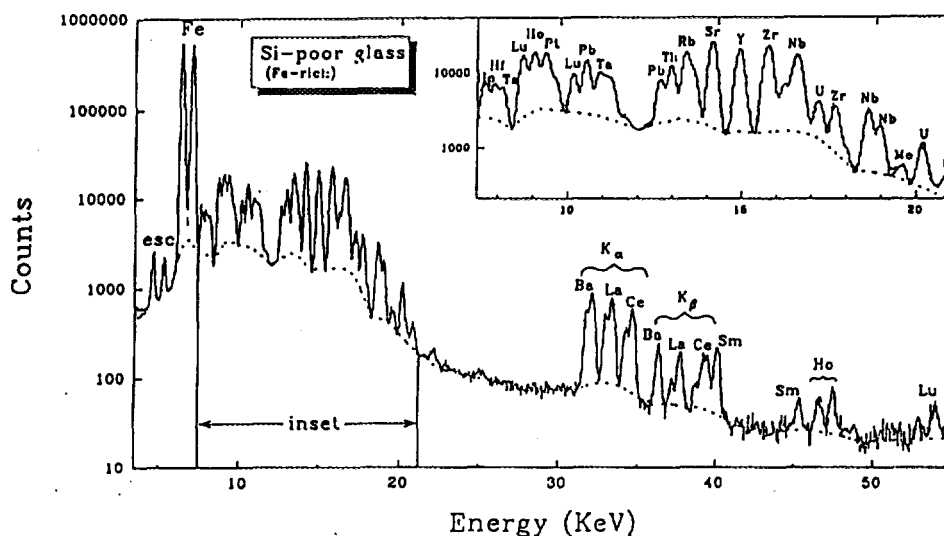


Figure 1. PIXE spectrum of the Si-poor glass obtained using a 300 micron Al filter. The high energy portion of the spectrum is dominated by the K lines of the rare earths.

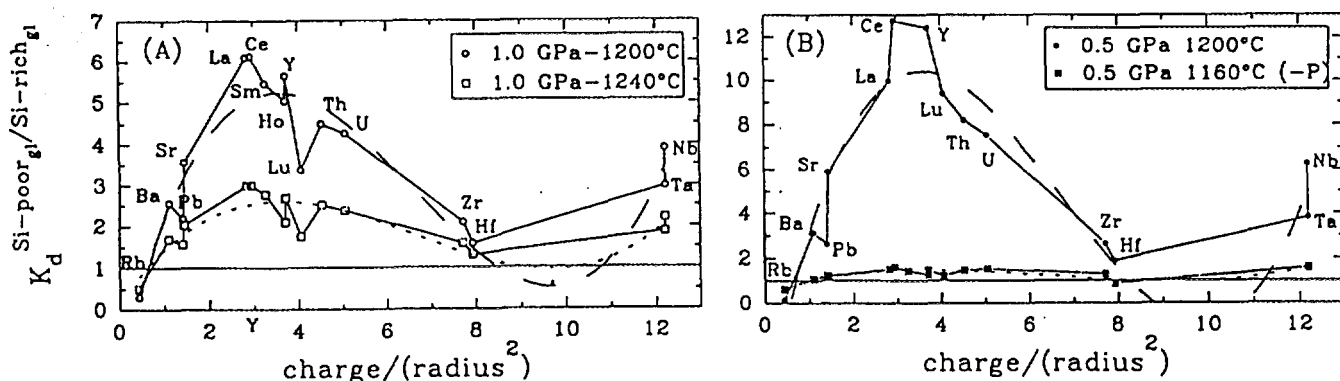


Figure 2. 2-liquid partition coefficient (K_d) as a function of cation field strength. (a) Results for 1.0 GPa experiments. Lower temperature runs produce larger K_d s as the width of the solvus increases and the major element compositions diverge. (b) Results for 0.5 GPa experiments. The effect of phosphorus addition causes a pronounced increase in partition coefficients, as shown by the P-bearing run (1200°C) and a P-free (1160°C) runs (see text). Note: Values for Sr and Ba are reversed in both (a) and (b).



S/Se ratio of pyrite from Eastern Australian VHMS deposits: implication of magmatic input into Volcanogenic hydrothermal systems

D.L. Huston (Geological Survey of Canada, Ottawa, Canada)
S.H. Sie and G.F. Suter (HIAF, CSIRO Exploration and Mining, North Ryde, NSW) and
D.R. Cooke (CODES, University of Tasmania, Hobart, Tas.)

1. Introduction

The proton microprobe was used to determine the concentrations of over twenty trace elements in pyrite grains from four volcanic-hosted massive sulphide (VHMS) deposits in eastern Australia. Of the elements determined, Se has the most potential in resolving important problems in the genesis of this class of ore deposits.

This paper summarises analytical conditions, describes the distribution of Se in pyrite in VHMS deposits as determined in this and other studies, discusses the speciation of Se in hydrothermal fluids, and presents a genetic model on the relative contribution of magmatic versus sea water Se (and S) in VHMS systems.

2. Experimental Conditions and Results

The samples consist of thin sections prepared from drill cores from VHMS deposits Rosebery, Agincourt, Mt. Chalmers and Dry River South. Analyses were carried out on 40 μm polished thin sections using 3 MeV proton microbeam at HIAF. Although the range of 3 MeV protons in pyrite is 50-60 μm , drop-offs in X-ray production and self-absorption with depth result in effective analytical depth of 30-40 μm . As the proton beam was typically focused to 20 μm , inclusion-free grains over 50 μm were selected for analysis. Beam currents (to 10 nA) were limited by the detector count rate. Data were collected for a 6 μC charge with 200 μm or 300 μm Al filters to absorb most Fe K-lines. Figure 1 shows the distribution of concentrations of selected trace elements as a function of depth. The minimum detection limit (at 98% confidence level) for Se for these conditions is typically 5 ppm.

For the purpose of this study, we have also included data from Kidd Creek, a Canadian deposit [1,2]. Se levels in pyrite from VHMS deposits vary spatially through the deposit and associated alteration zones. In Cu-poor deposits (Cu<1%; Rosebery and Agincourt), Se levels are low (mainly below detection limit) throughout. In Cu-rich deposits (Cu>1%; Mt. Chalmers, Dry River South and Kidd Creek), Se levels are highest (10-200 ppm) in stringer zones and in the lower parts of the massive sulphide lens, but decrease toward the top of the massive sulphide lens and into the peripheral parts of the alteration zone.

3. Discussion

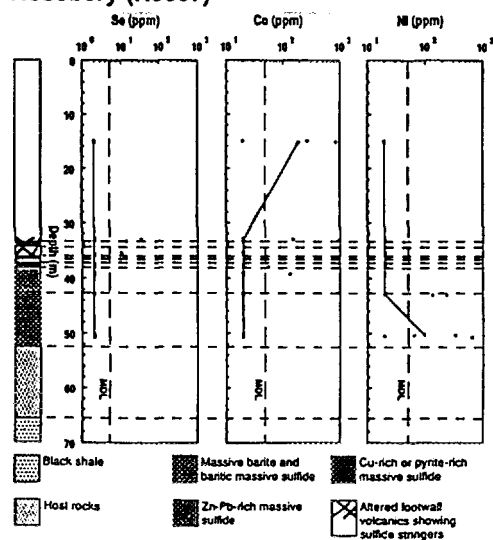
In high temperature (>200°C), reduced (H_2S > SO_4^{2-}), and moderately acid (pH between 4.0 and 5.5) conditions typical of volcanogenic fluids, the dominant aqueous Se and S species are H_2Se and H_2S , respectively. Consequently the concentration of Se in pyrite is controlled by the reaction $\text{FeS}_2 + 2\text{H}_2\text{Se} = \text{FeSe}_2 + 2\text{H}_2\text{S}$. Using available thermodynamic data the level of Se in pyrite was modelled as a function of temperature and $m_{\text{H}_2\text{Se}}/m_{\text{H}_2\text{S}}$ ($\sim m_{\text{Se}}/m_{\text{S}}$ above 200°C). For a $m_{\text{H}_2\text{Se}}/m_{\text{H}_2\text{S}}$ value of 10^{-7} (\sim sea water $m_{\text{Se}}/m_{\text{S}}$ value), the modelled Se concentration decreases from 9 ppm at 50°C to 0.2 ppm at 300°C. For magmatic $m_{\text{Se}}/m_{\text{S}}$ value of 10^{-4} , Se levels in pyrite decrease from 9000 ppm at 50°C to 200 ppm at 300°C. The above temperature dependence of Se levels in pyrite indicates that temperature variations in the hydrothermal system cannot account for the observed variations in Se levels in pyrite. Higher temperature (i.e. Cu-rich) portions of the deposits have higher Se levels, not lower levels as might be expected if temperature alone controlled the distribution. Rather, depletion of Se in the fluid passing through the hydrothermal system and precipitating seleniferous pyrite accounts for variations within the mound. Differences in Se levels between Cu-rich and Cu-poor deposits also can not be interpreted as the result of temperature differences. Rather, they are more likely due to differences in the $m_{\text{H}_2\text{Se}}/m_{\text{H}_2\text{S}}$ ratio of the hydrothermal fluids. At temperatures of 200°C and

250°C, the most likely temperatures for the deposition of Zn-rich, Cu-poor massive sulphide; pyrite containing 5 ppm Se is in equilibrium with fluids with $m_{\text{H}_2\text{Se}}/m_{\text{H}_2\text{S}}$ ratios of 7×10^{-7} and 10^{-6} , respectively. Conversely, at a temperature of 300°C, the minimum temperature required for the deposition of Cu-rich massive sulphide, pyrite containing 10-200 ppm Se is in equilibrium with a fluid with $m_{\text{H}_2\text{Se}}/m_{\text{H}_2\text{S}}$ ratio of $0.5-10 \times 10^{-5}$. Volcanogenic fluids are most likely mixtures between sea water and magmatic fluids which have dissolved a portion of their metals and sulphur from rocks through which they have passed. Sea water has a distinctive $m_{\text{H}_2\text{Se}}/m_{\text{H}_2\text{S}}$ ratios of about 10^{-4} . Using these two ratios as end-members, the relative contributions of sea water and magmatic Se and S can be estimated. For Zn-rich, Cu-poor deposits, the maximum component of magmatic Se and S is 1%, whereas for Cu-rich deposits, a magmatic component of 5-100% is indicated. Hence, the variations of pyrite Se contents between Cu-rich and Cu-poor deposits relate to the relative contribution of magmatic Se and S into volcanogenic fluids. Low temperature Cu-poor deposits formed from evolved sea water with virtually no magmatic component. As VHMS systems evolved and heated up, more magmatic Se and S (possibly to 100%) were added to the fluids. This magmatic component was either leached from volcanic rocks through which the volcanogenic fluids passed or from direct injections of magmatic volatiles.

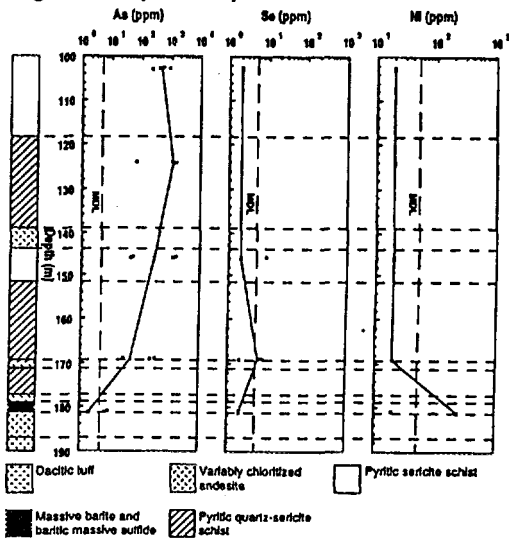
References

- [1] G. Auclair, Y. Fouquet, M. Bohn et al. *Can. Mineral.* 25 (1987) 577.
 [2] L.J. Cabri et al., *Can. Mineral.* 23 (1985) 133.

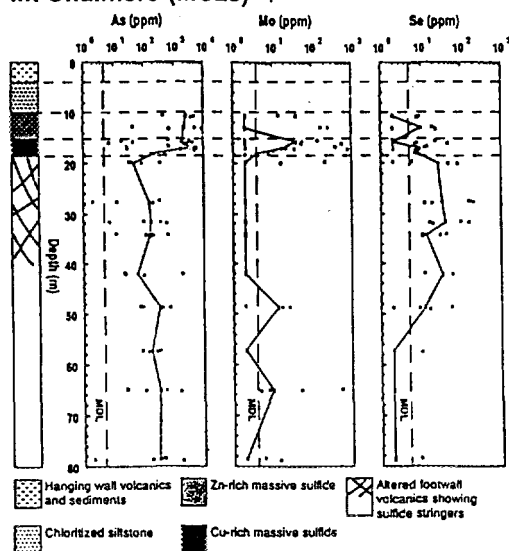
Rosebery (R3397)



Agincourt (AGDD1)



Mt Chalmers (MC25)



Dry River South (DRS22)

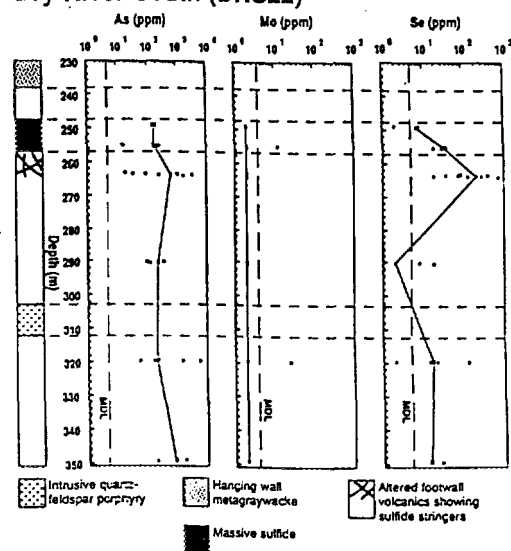


Fig 1. Variations in concentrations of selected elements in pyrite with depth in drill hole R3397 Rosebery, AGDD1 Agincourt, MC25 Mt Chalmers, DRS22 Dry River South



The analysis of thallium in geological materials by radiochemical neutron activation and X-ray fluorescence spectrometry: a comparison

P. J. McGoldrick and P. Robinson
CODES/Geology Department
University of Tasmania

Thallium is a trace element not routinely determined in geological materials, however, it may be of great interest because of its unusual geochemical properties. In magmatic systems univalent Tl is a lithophile trace element that behaves like Rb (de Albuquerque and Shaw, 1974; McGoldrick et al., 1979). In contrast, in sulphur-rich environments Tl behaviour is chalcophile, and it occurs as a minor element in sulphide minerals in many types of mineral deposits (de Albuquerque and Shaw, 1974). Furthermore, Tl is known to form large primary enrichment halos about many hydrothermal mineral deposits and these may extend into low sulphide, essentially barren, host rocks (Ikramuddin et al., 1983). Potassium silicate minerals are the Tl host in sulphide-poor parts of these halos (McGoldrick, 1986).

Carrier-based radiochemical neutron activation (RNAA) is a precise and accurate technique for the analysis of Tl in geological materials. For about a decade, until the mid-80s, a procedure modified from Keays et al. (1974) was used at the University of Melbourne to analyse for Tl in a wide variety of geological materials. Samples of powdered rock weighing several hundred milligrams each were irradiated in HIFAR for between 12 hours and 1 week, and subsequently fused with a sodium hydroxide - sodium peroxide mixture and several milligrams of inactive Tl carrier. Following acid digestion of the fusion mixture anion exchange resin was used to separate Tl from the major radioactive rock constituents. The Tl was then stripped from the resin and purified as thallium iodide and a yield measured gravimetrically. Activity from ^{204}Tl (a β -emitter with a 3.8 year half-life) was measured and Tl determined by reference to pure chemical standards irradiated and processed along with the unknowns. Detection limits for the longer irradiations were about one part per billion. Precision was monitored by repeat analyses of 'internal standard' rocks and was estimated to be about five to ten percent (one standard deviation). Accuracy was more difficult to assess because of a paucity of Tl determinations on international reference rocks. Keays et al. (1974) reported a value of 295 ± 30 ppb for twenty-seven determinations of BCR-1 which compares favourably with a recommended value of 0.3 ppm (Govindaraju, 1989). Three determinations of BCR-1 at Melbourne were 0.2, 0.3, and 0.3 ppm.

For a major study of the geochemistry of the host rocks of sedimentary base metal deposits currently being undertaken at the University of Tasmania, X-ray fluorescence

spectrometry (XRF) was seen as a potentially cost-effective technique for determining Tl at ppm levels. Furthermore, although XRF is subject to interelement and matrix effects, sample preparation is non-destructive. Hence, low analyses caused by Tl loss during acid digestion, or incomplete sample dissolution cannot occur. Pressed pellets of powdered rock are quick to prepare and quick to analyse using modern automated XRF units.

Optimum sensitivity for the XRF determination of Tl would be achieved with the Tl $L\alpha$ line (1.207 angstroms) using a Molybdenum X-ray tube at 100 Kv, a LiF 200 crystal, fine collimator and both the scintillation counter and the gas flow proportional counter as detectors. However, the Tl $L\alpha_1$ line suffers high interference from Ga $L\beta$ lines and generally cannot be used for accurate analysis.

In this work the Tl $L\beta_1$ line (wavelength 1.015 angstroms) was used. Minor interferences from Se, Ba, Pb, W and Hg occur but were minimised by using the scintillation counter with auxiliary collimator without the gas flow proportional counter. Careful choice of appropriate background angle positions is essential. Interference from Ba $K\beta_{1,2}$ (3rd order) lines was reduced with a narrow pulse height analyser window but could not be eliminated (>1000ppm Ba). Although loss in sensitivity does occur with the above conditions, a detection limit (3σ , 99% confidence) of 1ppm Tl in a quartz matrix is achievable with a background counting time of 400 seconds. Standards containing 2000 ppm Tl were prepared by mixing fresh high purity thallium oxide with pure quartz in a laboratory ring mill and pressed powder pellets were made containing PVA as a binder. Matrix corrections were applied using the standard Compton Scattering method with the Mo X-ray tube.

Blanks of fused Spectrosil™ along with spectroscopically pure silica powder pills were also run. Accuracy was checked by analysing twelve international standard rocks. Agreement was good with the limited amount of published data available (Table 1). Most international standard silicate rocks also have a low Tl content (< 4ppm).

Analyses of thirty sedimentary rock samples from Mount Isa, Queensland, allow a direct comparison of the XRF and RNAA techniques. Figure 1 displays these data and demonstrates excellent agreement between the two techniques. The correlation coefficient (for ranked data) between the two techniques is 0.895.

We conclude that because RNAA for Tl is sensitive, precise, accurate and subject to minimal interference from other elements it should be the 'method of choice' for Tl analysis. Unfortunately, the slow, labour intensive nature of the analysis means cost per analysis is high, and precludes using RNAA for routine Tl assays. On the other hand XRF provides an excellent, cost-effective alternative for Tl analysis in geological samples down to 1ppm.

References

- de Albuquerque, C.A.R. and Shaw, D.M., 1974. Thallium. Chapter 81 C-H. In Handbook of Geochemistry, K.H. Wedepohl (ed.), Springer-Verlag.
- Govindaraju, K, 1989, 1989 compilation of working values and sample descriptions for 272 geostandards. Geostandards Newsletter, 13, 1-113.
- Ikramuddin, M, Asmeron, y., Nordstrom, P.M., Kinart, K.P., Martin, W.M., Digby, S.J.M., Elder, D.E., Nijak, W.F., Afemari, A.A., 1983, Thallium: a potential guide to mineral deposits. Jour. Geochem. Explor., 19, 465-490.
- Keays, R.R., Ganapathy, R., Laul, J.C., Krahenbuhl, U. and Morgan, J.W., 1974. The simultaneous detection of 20 trace elements in terrestrial, lunar and meteoritic material by radiochemical neutron activation analysis. Anal. Chim. Acta, 72, 1-29.
- McGoldrick, 1986 Volatile and precious metal geochemistry of the Mount Isa ores and their host rocks: Unpub. Ph.D. thesis, University of Melbourne, 330 p.
- McGoldrick, P.J., Keays, R.R. and Scott, R.B., 1979. Thallium :a sensitive indicator of rock/seawater interaction and of sulfur saturation of silicate melts. Geochemica Cosmo.Acta, 43, 1303-1311.

Table 1: Comparison of published values for Tl in international standard rocks with XRF determinations at University of Tasmania (*suggested value; **recommended value)

	STM1	GSP1	GH	RGMI	G2	GXR1	GXR2	GXR3	GXR4	SY-2	SY-3	MICAFE
Published value:	0.26*	1.43**	1.8*	0.93*	0.91*	0.39*	1.03*	3.6*	3.2*	1.5*	1.5*	16*
XRF determination:	<1	1.6	1.7	1.1	1.3	<1	1.1	5.4	3.4	1.8	0.9	15.4

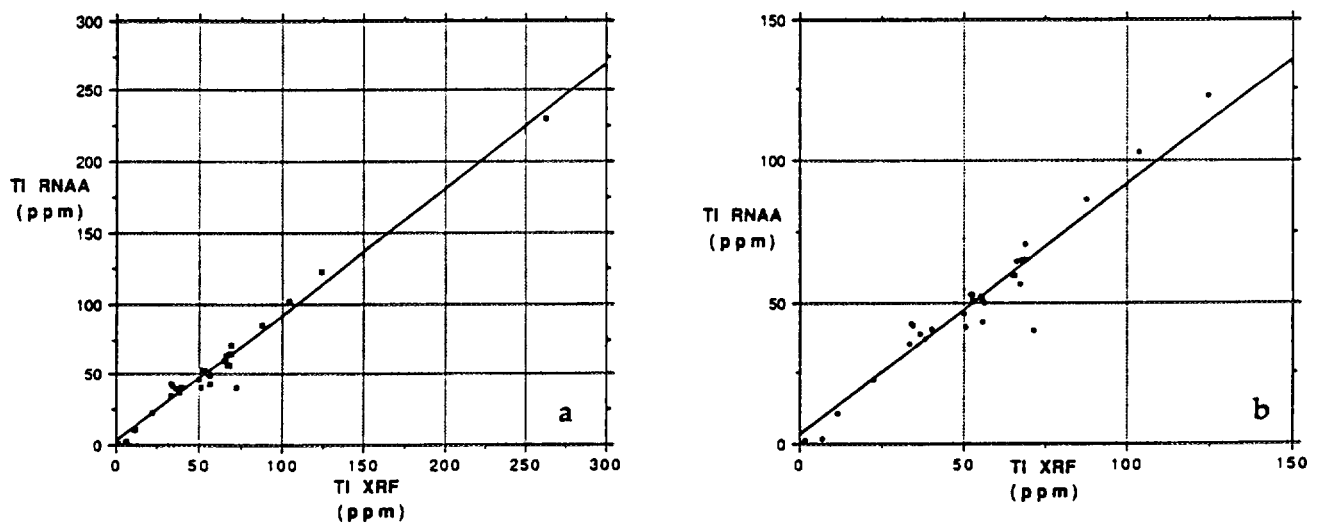


Figure 1. a) Comparison of Tl analyses by both XRF and RNAA for 34 siltstones and tuffaceous siltstones from Mount Isa, Qld. b) Enlargement of a).



IN-SITU BUILDUP OF COSMOGENIC ISOTOPES AT THE EARTH'S SURFACE: MEASUREMENT OF EROSION RATES AND EXPOSURE TIMES

*L.K. Fifield, G.L. Allan, J.O.H. Stone, J.M. Evans, R.G. Cresswell and T.R. Ophel
Australian National University, Canberra, ACT 0200, Australia*

Cosmic rays produce a number of nuclides in rocks that can be used to determine the geomorphic history of surfaces. The most useful are the radioactive isotopes ^{10}Be ($t_{1/2} = 1.5\text{Ma}$), ^{26}Al (0.7Ma) and ^{36}Cl (0.3Ma). Within the top 2m of the surface, these are produced principally by fast neutrons. At greater depths, production is dominated by the capture of negative muons. Measurements of a single nuclide produced *in situ* can be used to determine total exposure times or erosion rates. The use of multiple nuclides with different half-lives makes it possible to determine more complex histories such as exposures interrupted by periods of burial. At the ANU, all three of the isotopes above are being used to study a variety of problems in geomorphology and paleoclimatology, although to date, most of the work has concentrated on ^{36}Cl .

The accumulation of cosmogenic ^{36}Cl in calcite (CaCO_3) provides a means of measuring erosion rates on limestone surfaces. Sensitivity is achieved over a wide range of erosion rates due to the high production rate of ^{36}Cl in calcite (typically greater than 30 atoms/g/yr) and a detection limit of ca. 5000 atoms/g attainable with the ANU AMS system. The method is simplified by the predominance of Ca reactions (principally spallation) over other sources of ^{36}Cl in calcite, and the ease of sample preparation. The geological abundance of limestone ensures widespread applicability.

To provide a quantitative basis for the method, we have calibrated empirically the production rates of ^{36}Cl by Ca spallation, negative muon capture by ^{40}Ca and capture of muon-produced secondary neutrons. Samples were collected from glacial pavements in the Sierra Nevadas and to a depth of 20m from a marble quarry. Our estimate for the Ca spallation rate is in excellent agreement with the determination of Zreda *et al.* [1] and preliminary results for the $^{40}\text{Ca}(\mu^-, \alpha)^{36}\text{Cl}$ reaction rate suggest a value close to that measured by Dockhorn *et al.* [2]. These results imply that for shallow depths production decreases roughly exponentially, with Ca spallation dominating negative muon and thermal neutron capture production. At depths below 1 - 2m, the relative contributions of muon capture and mu-genic secondary neutron capture are comparable in magnitude (the latter varying with chlorine content) and total ^{36}Cl production follows the negative muon stopping rate.

For surfaces eroding at low rates (< 20 microns/yr), the effects of muon capture are subordinate to spallation and erosion rates can be calculated from measured ^{36}Cl concentrations using an exponential approximation for production with depth. At higher erosion rates, a greater proportion of ^{36}Cl at the surface is muon-produced, and the exact form of the production rate profile must be used to calculate rates accurately. Since near-surface and deep samples respond to erosion on different timescales (due to differing attenuation lengths for nucleon and muon fluxes) measurement of ^{36}Cl profiles can be used to detect changes in erosion rates through time.

We have measured ^{36}Cl in calcite from limestone samples from Australia and Papua New Guinea. Erosion rates derived from these measurements range from 3 microns/yr on the Nullarbor Plain of Western Australia to > 200 microns/yr in the New Guinea highlands. Numerous measurements on samples from south-eastern Australia give values ranging from 10 - 40 microns/yr. These results, which reflect rates over the past 50,000 to 200,000 years, accord surprisingly well with rates of limestone surface ablation measured directly on similar outcrops over the past decade [3]. They are somewhat higher, however, than average rates of landscape denudation and valley incision (generally estimated at < 5 microns/yr) in eastern Australia over the past 20 - 40 million years.

A series of measurements have also been performed on samples from the Vestfold Hills area of East Antarctica. This area is presently unglaciated and the extent of its glaciation during the previous glacial maximum is an important open question bearing on the role of the Antarctic ice sheet in changes in sea level at that time. Both ^{36}Cl and ^{26}Al have been measured at a number of locations. The results are highly variable, with apparent exposure ages varying from 10 to 60 ka. Possible explanations will be discussed.

- [1] M.G. Zreda, F.M. Phillips, D. Elmore, P.W. Kubik, P. Sharma and R.I. Dorn, *Earth Planet. Sci. Lett.* 105, 94-109 (1991).
- [2] B. Dockhorn, S. Neumaier, F.J. Hartmann, C. Petitjean, H. Faestermann, G. Korschineck, H. Morinaga and E. Nolte, *Hadrons and Nuclei* 341, 117-119 (1991).
- [3] A. Spate, pers. comm.

**THE PARAMAGNETISM AND TRACE ELEMENT CONTENT OF
AURIFEROUS VEIN QUARTZ AT BEACONSFIELD, TASMANIA**

*DW. Russell, JC. Van Moort
University of Tasmania*

(Paper to be handed out at Conference)



Scanning Deep Level Transient Spectroscopy Using An MeV Ion Microprobe.

J.S.Laird,R.A.Bardos, A.Saint, G.M.Moloney and G.F.J.Legge

Abstract: Traditionally the Scanning Ion Microprobe has given little or no information regarding the electronic structure of materials in particular semiconductors. We present here a new imaging technique called Scanning Ion Deep Level Transient Spectroscopy (SIDLTS) which is able to spatially map alterations in the band gap structure of materials by lattice defects, impurities etc.

Introduction.

The existence of impurities and intrinsic defects in a semiconductor greatly alter the electrical characteristics of a device through their activation in the form of deep levels in the bandgap. In the case of indirect bandgap semiconductors deep levels act as efficient non radiative recombination centres greatly affecting carrier concentrations and their lifetimes. Techniques such as Deep Level Transient Spectroscopy (DLTS) developed by Lang et al offers a means of characterizing such levels [1].

In DLTS the traps in a sample region are populated by a forward bias filling pulse after which a reverse bias is applied to create a space-charge region. The capacitance of the region depends on its space-charge density which, as the traps thermally release their carriers results in a capacitance transient whose sign is carrier dependant. From the transient response as a function of temperature the depth of levels as well their capture cross sections and densities over the bulk of the sample can be measured .

However, to fully understand the role of deep traps on device performance it is often highly desirable to know their spatial location across the device. Several scanning techniques on the SEM have since been developed in which the keV electron beam itself is used to inject the carriers . The spatial resolution of these techniques and their ability to probe regions deep in a sample are severely limited by both a large degree of lateral straggling and a short range of a several microns. For an ion beam however the relative straggling is minimal and the range is controllable to a greater extent allowing regions deeper in the sample to be imaged with little degradation in the beam spot resolution [2].

Using an MeV ion beam also provides an increase by several orders of magnitude in the amount of injected carriers increasing its sensitivity per ion compared to the electron case though the high relative brightness and low damage rates of the SEM means beam pulsing can easily overcome this disadvantage. With the ion case the relatively high amount of Ion Beam Induced Damage (IBID) means that care must be taken to ensure that one is only examining native defects and not those created by the beam. i.e the beam induced defect levels must be lower than the techniques sensitivity or be resolvable.

Theoretical Background

Defect energy levels in semiconductors arise from structural perturbations in the lattice potential by either the introduction of lattice defects or the existence of impurity atoms. Deep levels in particular are those existing near the middle of the bandgap and hence act as efficient centres for processes such as carrier recombination involving both the capture and emission of carriers. The capture rates $C_{n,p}$ and the emission rates $e_{n,p}$ are given respectively by:

$$C_{n,p} = \sigma_{n,p} \langle v_{th} \rangle [n,p]$$

$$e_{n,p} = \left(\frac{1}{g}\right) \sigma_{n,p} \langle v_{n,p} \rangle N_{c,v} e^{-\frac{E_a}{k_B T}}$$

where $\sigma_{n,p}$ are the capture cross sections (cm^{-2}) for the electrons and holes assumed to be temperature independent, $\langle v_{n,p} \rangle$ are the mean electron thermal velocities (proportional to $T^{1/2}$), n and p are the free electron and hole densities, g is the trap degeneracy, N_c and N_v are the density of states of the conduction and valence band (proportional to $T^{3/2}$), E_a is the activation energy defined as $E_c - E_T$ for electrons and $E_T - E_v$ for holes, k_B is Boltzmann's constant and T is the sample temperature in Kelvin [3].

The rate of emission from a trap is a strong function of both the sample temperature and the trap level. The lower the temperature or the deeper the trap the slower the rate of emission. Upon scanning with an ion microbeam a fraction of the Ion Beam Induced Charge within a depletion region will be trapped. The amount trapped depends heavily on the trap density $N_T (\text{cm}^{-3})$, the generation or plasma density, temperature and the electric field dependant carrier capture cross section.

The charge swept out by field assisted drift is collected as a prompt component in the external circuit. The entire process described here is analogous to the filling pulse used to populate trap levels in DLTS. The main difference between the DLTS means of filling traps and that of SIDLTS using an ion beam is the ability of the filling pulse used in DLTS to inject a particular carriers type and hence differentiate between hole and electron traps.

Having populated the trap levels and removed the free carriers from the depletion region, the occupied traps are no longer in thermal equilibrium since $p \approx 0$ and $pn < n_i^2$. Hence $C_p \approx 0$ and it can be shown that:

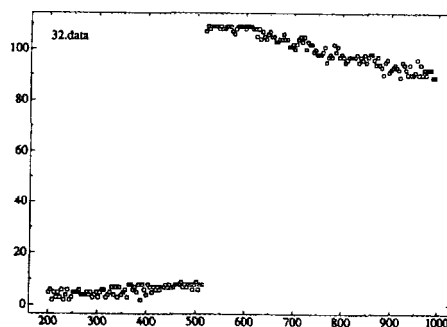
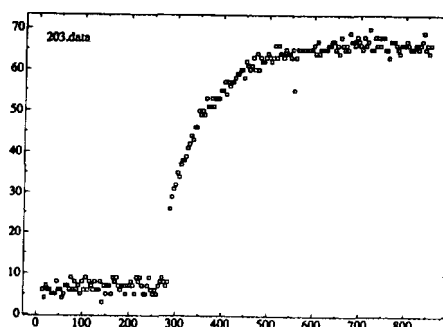
$$Q_p = \left(\frac{1}{e}\right) N_{p0} (1 - e^{-e_p t})$$

where N_{p0} is the initial trapped population and e is the electronic charge. Following similar arguments an equation can also be derived for the charge emitted by the trapped elec-

tron population. A sampling system comprising a Digital CRO can then be used to capture the charge transient, from which the value of e_p or e_n can be extracted. By acquiring the emission rates as a function of sample temperature and beam position one is able to derive the trap level spatially across the scanned region of the sample.

Preliminary Results:

A 2MeV He⁺ beam was used to irradiate a p-i-n diode over a 30x30 μ m area. As a function of sample temperature transients were collected within the damaged area as well as the virgin region. Shown below are 2 transients collected at 296K for a region inside(a) and outside(b) the damage scan:



References:

- [1] Deep Level Transient Spectroscopy: A new method to characterize traps, D.V.Lang
- [2] Trim 88
- [3] Semiconductor Devices: Physics and Technology, S.M.Sze Wiley.

**DEPLETION WIDTH IMAGING AND INTERPAD
CHARGE COLLECTION STUDIES OF A
SEGMENTED p^+n SILICON DETECTOR USING
SCANNING ION BEAM INDUCED CHARGE**

R.A. Bardos, G.F. Moorhead and G.N. Taylor
Research Centre for High Energy Physics, University of
Melbourne, Parkville 3052.

J.S. Laird and A. Saint
Micro Analytical Research Centre, University of Melbourne,
Parkville 3052.

20 August 1993

ABSTRACT

A method for determining the depletion width (W) v.s. reverse bias voltage (V_b) characteristics of a p-n diode from the V_b dependance of the charge collected from MeV protons incident on the junction side of the device has been tested experimentally using a Scanning Ion Microprobe. The position dependence of the depletion width obtained in this way cannot be obtained using purely electrical methods, such as capacitance - voltage (CV) or reverse bias leakage current - voltage measurements. In addition, the difficulties associated with the interpretation of electrical measurements, such as the frequency dependence of the diode capacitance in the presence of traps (following radiation damage for example) and the existence of currents other than the depletion region generation current, are avoided. A comparison with CV data shows however that the proton beam technique significantly overestimates W . This is probably due to charge carrier diffusion, occurring in a time interval comparable to the electronics shaping time following the proton event. A further contribution may arise from the funneling phenomena previously observed in the case of alpha particles and heavier ions. An alternative experimental method designed to minimize the effects of diffusion is proposed along with a variation of the technique, involving protons incident on the ohmic side of the diode, which should be immune from both diffusion and funneling. Images of the charge sharing region between pads (segments) were collected by means of coincident measurements on adjacent pads. The effect of an unbiased pad on the size of the charge collection regions of neighbouring pads as a function of V_b was studied.



SEEDING OF SILICON BY COPPER ION IMPLANTATION FOR SELECTIVE ELECTROLESS COPPER PLATING

S. Bhansali, D.K. Sood and R.B. Zmood*

Microelectronic and Materials Technology Centre, Royal Melbourne Institute of Technology,
PO. Box 2476V, Melbourne 3001.

We report on the successful use of copper(self) ion implantation into silicon to seed the electroless plating of copper on silicon (100) surfaces. Copper ions have been implanted to doses of $5E14$ - $6.4E16$ ions/cm² using a MEEVA ion implanter at extraction voltage of 40kV. Dose was varied in fine steps to determine the threshold dose of $2E15$ Cu ions/cm² for "seed" formation of copper films on silicon using a commercial electroless plating solution. Plated films were studied with Rutherford Backscattering Spectrometry, Scanning electron Microscopy, EDX and Profilometry. The adhesion of films was measured by "scotch tape test". The adhesion was found to improve with increasing dose. However thicker films exhibited rather poor adhesion and high internal stress. SEM results show that the films grow first as isolated islands which become larger and eventually impinge into a continuous film as the plating time is increased.

INTRODUCTION

In recent years there has been considerable and rapidly growing interest in the use of copper as an interconnect material for the microelectronics industry. It is also of interest to researchers at RMIT engaged in fabrication of micro-machines. One of the major problems faced by researchers has been their ability in patterning copper. Recently, ion implantation [1] has been employed to solve some of the difficulties associated with patterning and selective electroless plating. Most of the research has been carried out using SiO₂ as substrate and various elements as seed materials [1,2]. We report on successful selective electroless plating on Si using Cu ions.

EXPERIMENTAL METHOD

<100> silicon wafers were used for experiments. The wafers were cleaned, cut into strips and partially masked along their length. They were then implanted using the metal vapour vacuum arc (MEVVA) ion implanter. The samples were implanted by Cu⁺ ions. The fluence of ions was varied from $5E14$ ions/cm² to $6.4E16$ ions/cm² at an extraction voltage of 40 kV. Implantation was carried out at room temperature. For electroless plating, the implanted samples were treated with 10% HF for 5 minutes to remove any SiO₂ that may have formed on the surface. They were next immersed in a commercial electroless copper plating solution. The solution was maintained at 46.5C using a constant temperature bath and the plating time was varied from 4 to 30 minutes. The

films were studied and characterised using a profilometer, Rutherford Backscattering Spectroscopy, optical microscopy and Scanning Electron Microscopy. The adhesion of the films was qualitatively measured using the scotch tape test.

RESULTS AND DISCUSSION

The sample was deemed to have plated when a continuous layer of copper deposited on the implanted region in 30 minutes. The threshold dose for electroless plating of copper on silicon was found to be $2E15$ Cu⁺ ions/cm². The rate of growth of the film and its adhesion to the substrate increased with increasing dose. The texture and uniformity of the film also improved with increasing dose. However adhesion of the film to the substrate reduced with increasing thickness.

The process of film formation can be understood by examining the SEM micrographs taken at different plating times. Fig 1 is the SEM micrograph of a film which grew on the substrate implanted with $3.2E16$ Cu⁺ ions/cm². The plating time was 16 minutes. The bright granules are grains of copper in the film deposited by electroless plating. The grains of copper have an average diameter of about 0.8μ. The dark region is the silicon substrate. The deposition of the film (bright granules) has taken place only in the implanted region of the substrate and there is no deposit on the unimplanted (dark) region. Absence of copper on the unimplanted region was confirmed with EDX and Rutherford

* Department of Electrical Engineering, Royal Melbourne Institute of Technology, Melbourne.

Backscattering Spectroscopy. The sharp interface between the implanted/plated and unimplanted/unplated region shows that ion implantation can be used for patterning and selectively growing films chemically.

Fig 2 is the micrograph of a sample implanted with $2E15 \text{ Cu}^+$ ions/cm². The plating time for the sample was 8 minutes. The circular white grains are grains of copper as established by spot EDX. The darker region under the grains is silicon. The grains of copper for a film such a film have an average diameter of 1.4μ . They show the nucleation stage of the film. The copper ions in silicon act as sites for nucleation of copper grains. As the grains of copper continue to grow they start impinging on the adjoining grains and coalesce into a film. Fig 2 also shows regions of impingement of the film. As the dose is increased a greater number of nucleation sites are available for copper and the average grain size is reduced (compare figs 1 & 2). This ensures that the surface layer of copper is formed faster and hence the film grows at a higher rate. Table 1 shows the thickness of the films grown for different time on substrates implanted with $3.2E16 \text{ Cu}^+$ ions/cm².

Fig 3 is a micrograph of a film grown on a substrate implanted with $6.4E16 \text{ Cu}^+$ ions/cm² showing a peeled off and curled region. From this edge-on view a film thickness of $\approx 3\mu$ is measured directly from the micrograph. Peel off/delamination of the film is indicative of poor adhesion while its curling indicates a high level of internal stresses. Both adhesion and delamination of the film (for similar plating conditions) depends largely on internal stresses [4]. The region on the left (Fig 3) is a section of the film/substrate interface that has curled up. The micrograph of this region shows the texture of the film which nucleated at the interface. This is slightly different from texture of the surface of the film (region on the right in the micrograph). Also the film's sectional view (region on the right) indicates two distinct regions within the film. Both these microstructural variations may be a result of different grain growth conditions that exist between the nucleation stage and the final stage [5]. As the copper grains nucleate, they grow epitaxially to large grain sizes. As they grow bigger, they impinge on adjacent grains and stop growing. This results in nucleation of smaller grains and a refinement of grain size towards the surface.

Voids in the film also have a pronounced effect on the microstructure of the film[5]. Our results show that films deposited in a well aerated bath exhibit

poor adhesion to the substrate and delaminate, while films deposited without aeration have a high amount of blisters. Scotch tape test results showed that films with greater thickness exhibited poor adhesion due to greater internal stress. Table 1 also gives the results of Scotch Tape tests performed on the samples.

CONCLUSION

Copper Ion implantation offers a viable alternative for selective electroless plating of silicon for thicknesses up to 2 microns. At higher thicknesses adhesion of the film deteriorates as the stresses in the film rise.

REFERENCES

- [1] Qian, X.Y., Kiang, M.H. et al., Nucl. Instrum. and Meth. in Phys. Res. B55 (1991) 893-897.
- [2] Kiang, M.H., Pico, C.A. et al. MRS Proc 223 (1991) 377-383.
- [3] Echigoya, J. Materials Forum 17 (1993) 15-26.
- [4] Raub, E. and Muller, K., "Fundamentals of Metal Deposition". Elsevier, Amsterdam (1967) 150-164.
- [5] Nakahara, S., Mak, C. Y. and Okinaka, Y., J. Electrochem. Soc., 140 (1993) 533-538.

ACKNOWLEDGMENTS

A part of this work was performed under the management of the Micromachine Center as a part of ISTF project of AIST/MITI "Micromachine Technology", by NEDO (New Energy and Industrial Technology Development Organisation). Ion implantation was made possible at ANSTO by an AINSE grant. We thank J.W. Chu and P.J. Evans for their kind assistance for implantation.

Table 1
Sample implanted with $3.2E16 \text{ Cu/cm}^2$ and plated for times as shown.

Plating Time	Thickness	STT*
4 Min	448 A	Passed
8 Min	933 A	Passed
16 Min	2627 A	Failed
32 Min	5349 A	Failed

*STT: Scotch Tape Test

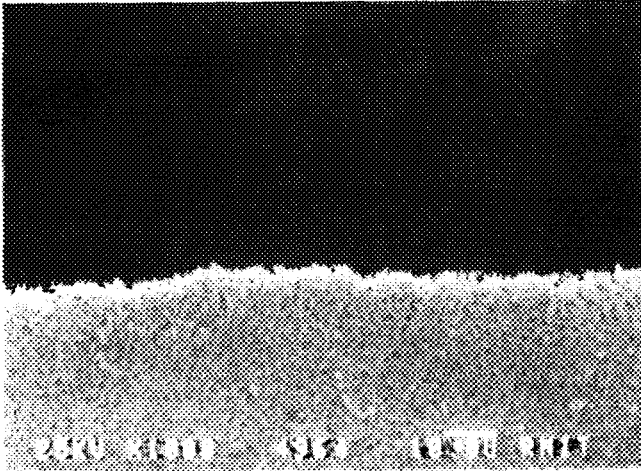


Fig 1: SEM micrograph of the film, grown on a substrate implanted with $3.2E16 \text{ Cu}^+$ ions/cm² for 16 mins. Dark region is the unimplanted substrate and the grains are of electroless copper.

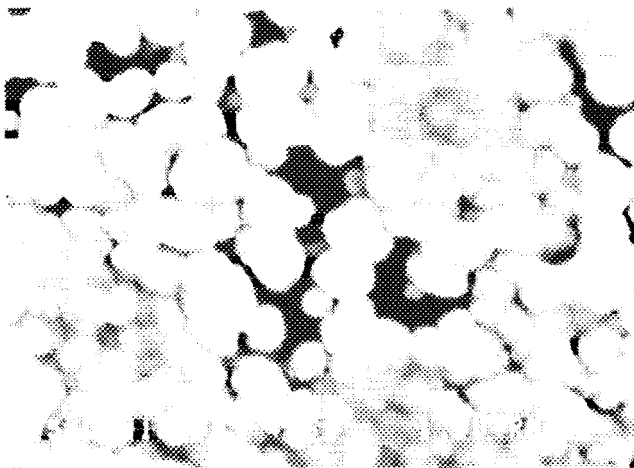


Fig 2: SEM micrograph of the film, grown on a substrate implanted with $2E15 \text{ Cu}^+$ ions/cm² for 8 minutes. Dark region is the unimplanted substrate and the white "spheres" are grains of copper.

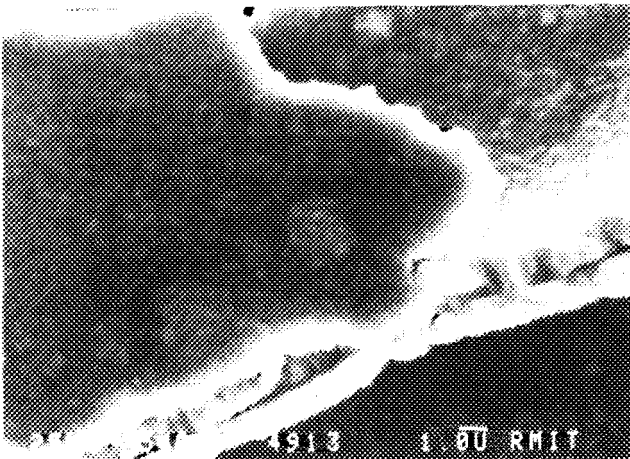


Fig 3: SEM micrograph of the film, grown on a substrate implanted with $6.4E16 \text{ Cu}^+$ ions/cm². Film peeled off and curled because of high internal stress.



The Effectiveness of Ti implants as barriers to Carbon Diffusion in Ti implanted Steel under CVD diamond deposition conditions.

Paul S. Weiser¹, Steven Prawer¹, Alon Hoffman², Peter J. Evans³ and Peter J. K. Paterson⁴,

¹ School of Physics, University of Melbourne, Parkville, Victoria, 3052.

² Chemistry Department, Technion, Haifa, 32000, Israel.

³ Australian Nuclear Science and Technology Organisation, PMB 1, Menai, NSW 2234.

⁴ Department of Applied Physics, RMIT, GPO Box 2476V, Melbourne, Victoria 3001.

Introduction

The growth of chemical vapour deposited (CVD) diamond onto iron based substrates is complicated by preferential soot formation and carbon diffusion into the substrate [1], leading to poor quality films and poor adhesion. In the initial stages of exposure to a microwave plasma, a layer of graphite is rapidly formed on an untreated Fe based substrate. Once this graphite layer reaches a certain thickness, reasonable quality diamond nucleates and grows upon it. However, the diamond film easily delaminates from the substrate, the weak link being the graphitic layer. Following our initial success in using a TiN barrier layer to inhibit the formation of such a graphitic layer [2], we now report on attempts to use an implanted Ti layer for the same purpose. This work was prompted by the observation that, although the TiN proved to be an extremely effective diffusion barrier, adhesion may be further enhanced by the formation of a TiC interface layer between the diamond film and the Fe substrate.

Experimental

In our experiments, the substrates used were 10x10x1mm³ plates of Enamel Steel which were polished down to a ¼µm diamond paste finish and then ultrasonically rinsed in organic solvents. Half of the substrates were then masked and the exposed half implanted with 60 keV Ti ions to a retained dose of 3.0x10¹⁶ ions/cm² using a vacuum arc technique. Figure 1 shows an Auger Electron Spectroscopy (AES) depth profile for the as-implanted substrate. This shows a Ti implant layer of 15-18 at. % of Ti for the first 500Å decreasing to less than 3 at. % at a depth of 1000Å. This result compares favourably to the profile predicted by TRIM90 [3]. The depth profile also shows that significant amounts of C have been co-implanted with the Ti and that some O has diffused deep into the substrate during the ion implantation. The C(KLL) line shape of the co-implanted C shows evidence of graphitic and carbidic bonding. The small amount of C (<2 at. %) in the steel prior to implantation displays a graphitic line shape. Hence, it is clear that at least some of the co-implanted C is present either as a carbide of Ti or Fe or a mixture of both.

The implanted substrates were again ultrasonically rinsed in organic solvents prior to insertion in the CVD diamond deposition system, consisting of a waveguide plasma applicator encasing a 1" quartz tube containing the reactant gases (CH₄/H₂ mix), which are excited using a frequency of 2.45 GHz. The substrate was orientated so that the incoming gases were perpendicular to the abraded substrate surface. An optical pyrometer was employed to measure the substrate temperature. The CVD deposition parameters used were: pressure 20 Torr; total flow rate 100 sccm; and CH₄/H₂ ratio 1:99. Depositions of 5 min. and 6 h. duration were performed at temperatures of 900 and 1000°C. The samples were then analysed using AES, Rutherford Backscattering Spectroscopy (RBS), micro-Raman Spectroscopy and Optical microscopy. The AES measurements were performed using a Varian Cylindrical Mirror Analyser (CMA) with a coaxial electron gun. A primary current of 5µA and primary electron energy of 5 keV were used. The RBS was performed using 1.5 MeV protons (H⁺) and a beam diameter of ~20µm, employing a detector scattering angle geometry of 170°.

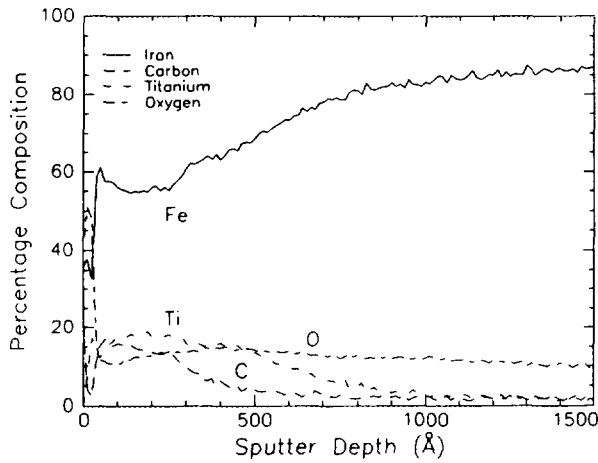


Figure 1 - The AES Depth Profile of the Ti implanted Fe prior to exposure to the CVD diamond deposition conditions.

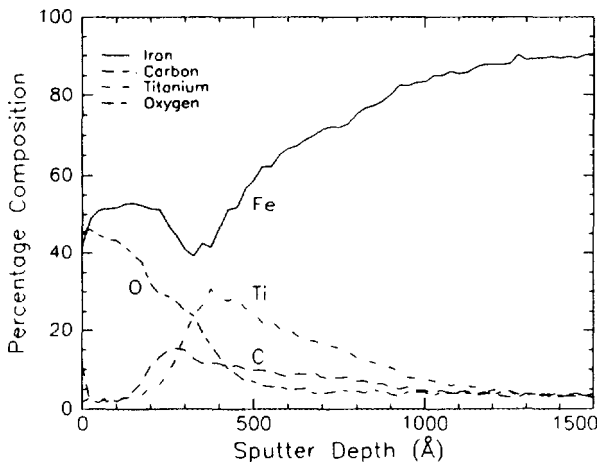


Figure 2 - The AES Depth Profile of the Ti implanted region of the sample after exposure to the 900°C CVD diamond deposition conditions for 6 hours.

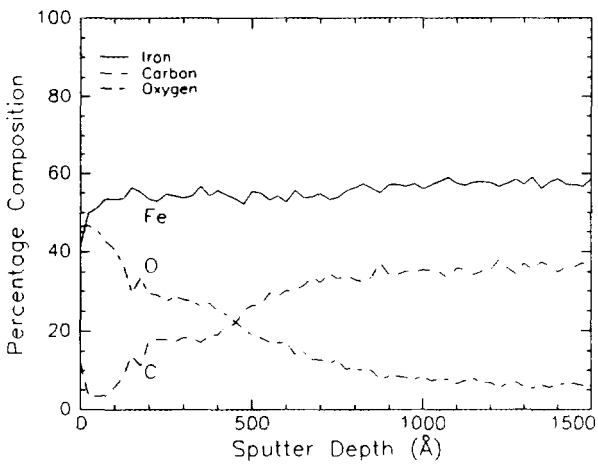


Figure 3 - The AES Depth Profile of the Unimplanted Fe region of the sample after exposure to the 900°C CVD diamond deposition conditions for 6 h.

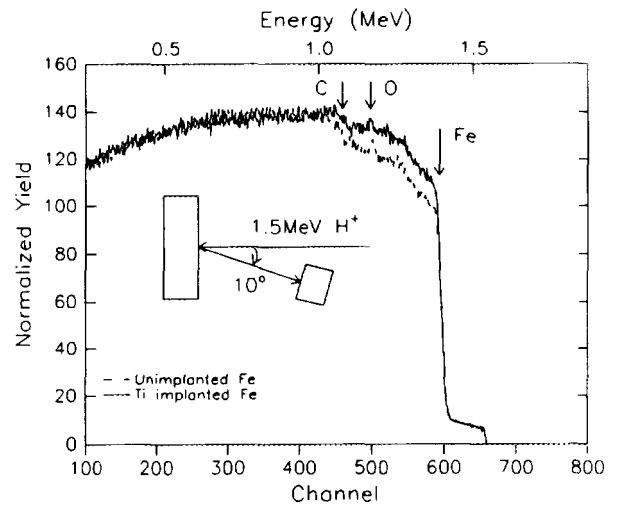


Figure 4 - The RBS spectra of the Ti implanted and unimplanted regions of the sample prior to exposure to the CVD diamond deposition conditions. The inset shows the detector scattering angle geometry of 170°.

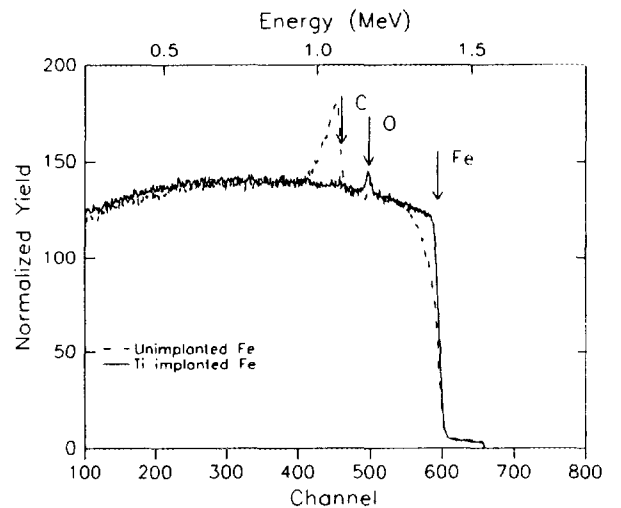


Figure 5 - The RBS spectra of the Ti implanted and unimplanted regions of the sample after exposure to the 1000°C CVD diamond deposition conditions for 5 min.

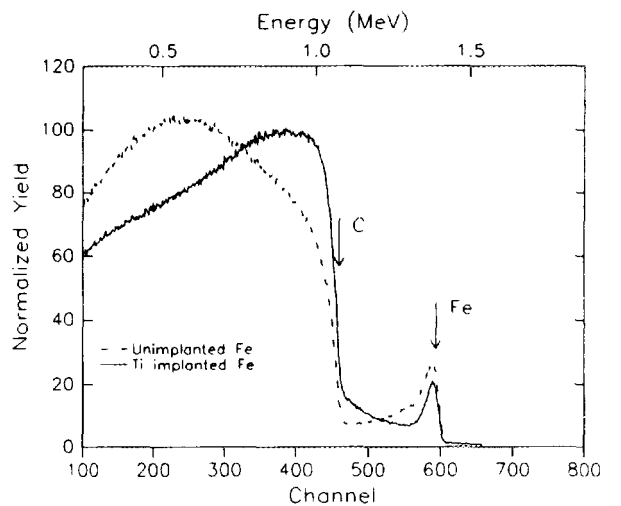


Figure 6 - The RBS spectra of the Ti implanted and unimplanted regions of the sample after exposure to the 1000°C CVD diamond deposition conditions for 6 h.

Results and Discussion

Growth at 900°C: After exposure to the CVD plasma for 6 h. at 900°C, the AES depth profile (fig. 2) of the Ti implanted sample shows a sharpening of the Ti profile, but without any evidence of the implanted Ti diffusing into the Fe substrate. In the near surface region a layer of iron oxide appears to have formed rather than a C layer. Hence, at this deposition temperature (900°C) no diamond (or graphite layer) has formed on the Ti implanted surface. Also, the retention of the Ti peak at 400Å below the surface suggests that little or no sputtering of the Fe surface has occurred during the 6 h. exposure to the plasma. By contrast, the AES profile of the unimplanted Fe (fig. 3) shows massive C diffusion into the Fe with 35 at. % C at a depth of 1000Å below the surface. Once again there is evidence for the formation of an iron oxide layer on the surface.

Growth at 1000°C: After 6 h. of CVD at 1000°C small diamond particles (as identified by Raman spectroscopy) were observed to have formed upon a thick graphitic layer which was deposited on both the Ti implanted and unimplanted portions of the Fe sample. The similarity of the growth on both the implanted and unimplanted Fe suggests that the Ti may have diffused into the sample, thus removing the barrier and allowing the type of growth expected on unimplanted Fe. The AES depth profiling of these diamond particles, grown on the thick graphite layer, was not practical due to the long sputtering times required to remove many microns of C. Hence, RBS was performed on these 1000°C CVD deposition samples.

The RBS spectra (1.5 MeV H⁺) from the implanted and unimplanted portions of the sample prior to exposure to the CVD plasma are shown in fig. 4. The Ti implant cannot be observed as it is not resolved from the Fe. The differences in the RBS spectra are probably due to the different phases and surface topographies of the implanted and unimplanted portions of the sample. The RBS spectra from the implanted and unimplanted portions of the specimen after 5 min. and 6 h. exposures to the CVD plasma are shown in figs. 5 and 6. For the 5 min. exposure (fig. 5) the unimplanted sample shows the formation of a 1µm thick C layer. The presence of O is also clearly visible. For the Ti implanted portion of the sample no such C layer forms after 5 min. exposure to the CVD plasma (fig. 5). However, after 6 h. exposure, both the implanted and unimplanted Fe return essentially the same RBS spectra, showing the formation of a thick (>10µm) C layer in which a small amount of Fe is present (<0.5%), with some evidence for a segregation of Fe to the surface. The differences in the shape of the RBS spectra is once again attributed to the differences in surface roughness. Thus, we see that after 5 min. exposure to CVD diamond growth conditions, Ti inhibits C diffusion and the formation of soot, both of which occurred on the unimplanted portion of the substrate. However, after 6 h. CVD soot does form even on the Ti implanted portion of the substrate, which probably indicates that the Ti has diffused into the Fe, leaving it unprotected and susceptible to soot formation and C diffusion.

Conclusions

The use of a Ti implanted (3×10^{16} ions/cm²) barrier layer, in the CVD diamond deposition on Fe, is successful in halting the C diffusion into the substrate at 900°C for up to 6 h. However, there is no significant C growth under these conditions. When conditions more favourable for the synthesis of CVD diamond are employed (6 h. at 1000°C), the Ti barrier layer appears to diffuse into the substrate. The removal of the Ti barrier layer allows the C to diffuse into the Fe and form a layer of graphitic soot upon the Fe. The present results do not bode well for the use of Ti implants as C diffusion barriers for CVD diamond growth on Fe, unless the deposition temperature can be lowered, possibly by the addition of O to the growth mixture.

References

- [1] L.F. Albright and T.C. Tasi, in *Pyrolysis: Theory and Industrial Practice*, edited by L.F. Albright, B.L. Crynes, and W.H. Corcoran, (Academic, New York, 1983).
- [2] P.S. Weiser, S. Prawer, A. Hoffman, R.R. Manory, P.J.K. Paterson and S-A. Stuart. *J. Appl. Phys.*, **72**(10), 15 Nov. 1992.
- [3] J.F. Ziegler and J.P. Biersack, *The Stopping and Ranges of Ions in Solids*, (Pergamon, New York, 1988).



Raman Microprobe Measurements of Stress in Ion Implanted Materials

K. W. Nugent, S. Praver, P. S. Weiser and S. P. Dooley
School of Physics, University of Melbourne

Raman microprobe measurements of ion implanted diamond and silicon have shown significant shifts in the Raman line due to stresses in the materials. The Raman line shifts to higher energy if the stress is compressive and to lower energy for tensile stress¹.

The silicon sample was implanted in a 60 μm square with 2.56×10^{17} ions per square centimetre of 2 MeV Helium. This led to the formation of raised squares with the top 370 nm above the original surface. In Raman studies of silicon using visible light, the depth of penetration of the laser beam into the sample is much less than one micron. Thus, the Raman line is due to the silicon overlying the damage region.

A series of spectra were recorded at 5 μm intervals across the raised square. The 520 cm^{-1} Raman line showed no broadening as would be expected if there were significant damage at the surface. The peak position shifted around 2.3 cm^{-1} to lower energy across most of the implanted region, relative to the unimplanted silicon, as shown in Figure 1. On the edges of the implanted region, the Raman line is shifted to higher energy by around 1.5 cm^{-1} . This indicates that the top of the raised area is under tensile stress, while the sides of the raised region are under compressive stress.

The diamond results are complicated by the transparency of the sample. The minimum depth resolution of the Raman microprobe is 2 μm , and thus the Raman signal comes both from the diamond lying above the damage region, and the damage region itself, at about 1.7 μm under the surface.

The diamond sample was a (110) diamond window which had been implanted with 2×10^{15} ions per square centimetre of 2.8 MeV carbon. One corner had been masked. Inspection of the edge between the implanted and unimplanted region showed the "notch" shown in Figure 2(a). Raman spectra were recorded at one micron intervals covering unimplanted-implanted-unimplanted-implanted. Both parallel and perpendicular polarisation components were collected.

The Raman spectrum of the bulk unimplanted sample showed a single sharp 1332 cm^{-1} line. All other spectra showed a similar sharp component, assigned to diamond above and below the damage region, and also a broad component, assigned to diamond at the depth of the damage region. The sharp component both in the bulk implanted material and in the region of the interface was shifted by around 1 cm^{-1} to lower energy, indicating a tensile stress.

The broad component varied widely in position, as shown in Figure 2(b). In particular, there was a very large shift to lower energy (around 6 cm^{-1}) for the spectrum from the centre of the enclosed "tongue" of implanted material. The graph shows that the implanted region close to the interface is under tensile stress, while the unimplanted region close to the interface is under compressive stress.

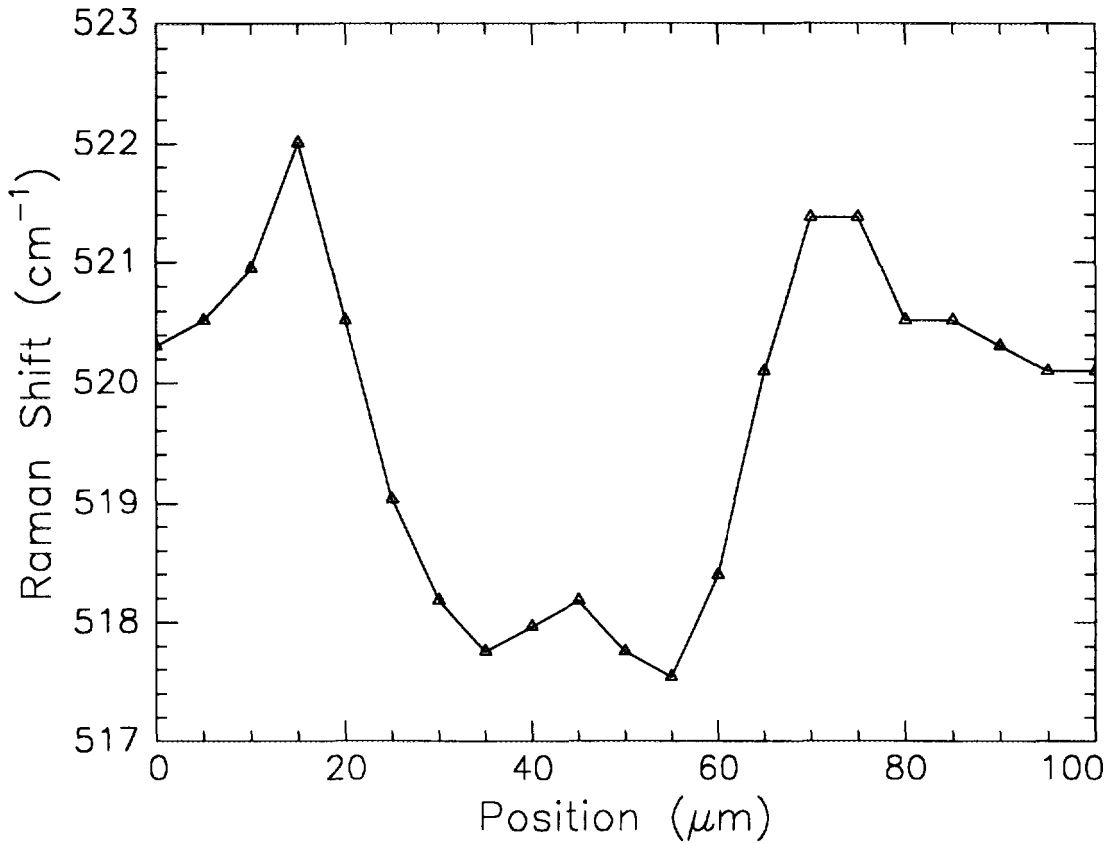


Figure 1. Variation of 520 cm^{-1} Raman line position across the raised implanted region of the silicon sample.

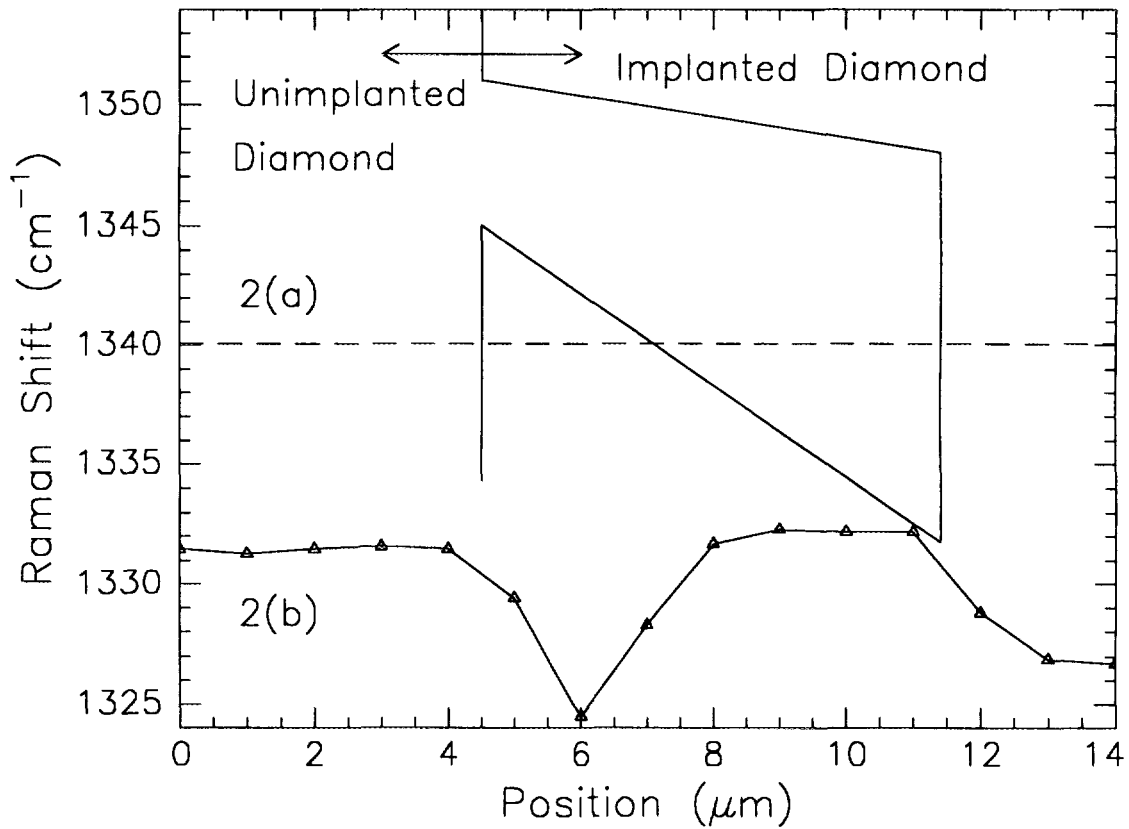


Figure 2. (a) The geometry of the "notch" between implanted and unimplanted regions of diamond. **(b)** The variation of the broad component of the 1332 cm^{-1} Raman spectrum of the diamond sample with position along the dotted line shown in (a).

Further interesting results come from the polarisation measurements. In the sample orientation used, the intensity of the bulk diamond line shows little polarisation dependence. In all cases, the polarisation behaviour of the sharp component is similar. Also, the broad component shows little polarisation dependence except on the enclosed tongues of implanted and unimplanted diamond. The large polarisation dependence in these cases indicates that the stress direction is not parallel to the direction of propagation of the laser beam.

In summary, the measurement of the Raman spectrum can give information concerning both the magnitude and the direction of stress in an ion implanted sample. It is possible, in some cases, to determine whether the stress direction is parallel or perpendicular to the sample surface.

References

1. D. S. Knight and W. B. White, *J. Mater. Res.* **4**, 385 (1989)



ION BEAM INDUCED LUMINESCENCE FROM DIAMOND USING AN MeV ION MICROPROBE.

A.A. Bettiol, D.N. Jamieson, S. Praver and M.G. Allen.
MARC, School of Physics, University of Melbourne
Parkville, 3052, Victoria, AUSTRALIA.

ABSTRACT

Analysis of the luminescence induced by a MeV ion beam offers the potential to provide useful information about the chemical properties of atoms in crystals to complement the information provided by more traditional Ion Beam Analysis (IBA) such as Rutherford Backscattering Spectrometry (RBS), ion channeling and Particle Induced X-ray Emission (PIXE). Furthermore, the large penetration depth of the MeV ion beam offers several advantages over the relatively shallow penetration of keV electrons typically employed in cathodoluminescence. We have developed an Ion Beam Induced Luminescence (IBIL) detection system for the Melbourne microprobe that allows the spatial mapping of the luminescence signal along with the signals from RBS and PIXE. Homoepitaxial diamond growth has been studied and remarkable shifts in the characteristic blue luminescence of diamond towards the green were observed in the overgrowth. This has been tentatively identified as being due to transition metal inclusions in the epitaxial layers.

1. INTRODUCTION

Although very successful in determining elemental composition and depth information, traditional MeV Ion analytical techniques such as PIXE and RBS cannot directly probe the band structure of a material. For this information one must look at the characteristic luminescence emitted by the sample during some form of excitation. Since emission spectra are independent of the excitation source, the wealth of information obtained from work done with laser (Photoluminescence) and electron beam (Cathodoluminescence) excited luminescence can be applied to an Ion Beam Induced Luminescence (IBIL) system [1,2].

A system to detect IBIL which allows for spectroscopic and micrographic studies of materials has been developed for the Melbourne Microprobe [3]. The data acquisition system at Melbourne which employs Total Quantitative Scanning Analysis (TQSA) has the capabilities of producing IBIL images simultaneously with PIXE and RBS maps [4].

2. DETECTION SYSTEM

The detection system which is currently in operation at the Melbourne Microprobe can be easily adapted to either a front or rear viewing microscope. Light is extracted from the sample by the microscope objective lens and diverted from the eye piece lenses to a grating monochromator. The band width of the instrument is about 3 nm for 1/2 mm slits, a resolution appropriate for uncooled samples. A photomultiplier tube (EMI 9656 KB) configured to do single photon counting is used for detection. IBIL spectra can be

obtained by scanning the monochromator with a stepper motor while simultaneously collecting data on a Multichannel Analyser in Multichannel Scaling mode. Monochromatic maps are obtained by dialing up the desired wavelength and scanning the micro beam over the sample. (See Figure 1a)

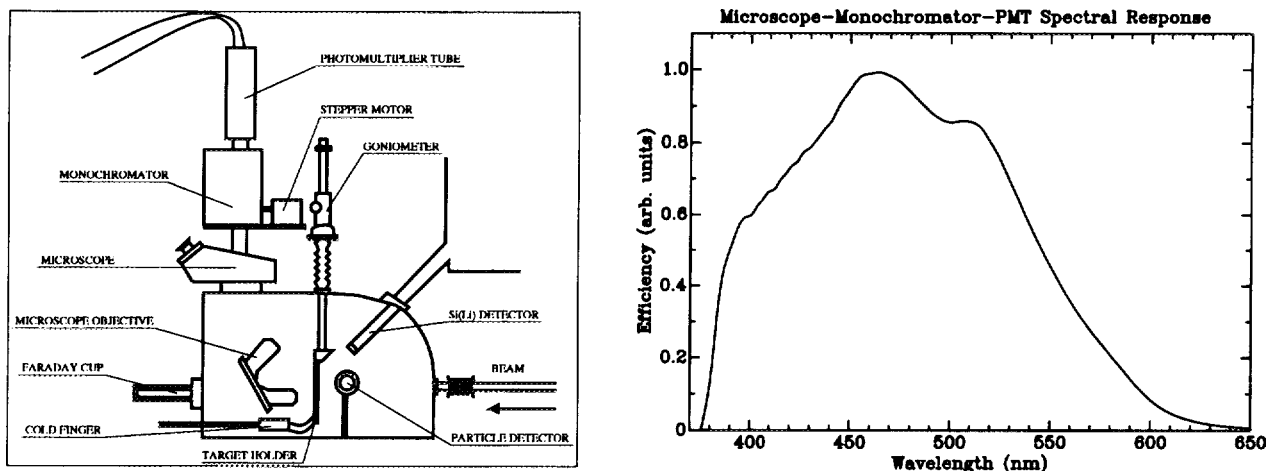


Figure 1 : (a)IBIL Detection System and (b)Efficiency Curve

Dyer and Matthews [5] found in fluorescence experiments carried out on diamond samples that the intensity of the 415 nm emission system increased by 34 % for type I samples and 170 % for type IIa samples by cooling from 290 K down to 80 K. A second consequence of sample cooling is the sharpening of line width. These two effects make it desirable to introduce a target cold stage into the detection system. This was achieved with a copper cold finger which was pumped with liquid nitrogen and attached to the target via a copper braid. Sample cooling down to about 100K was achieved and with improved thermal contacts lower temperatures may be possible.

Wavelength calibration of the detection system was achieved by using the atomic spectral lines off a cadmium lamp. A spectrum obtained from a hot tungsten filament was normalised to the appropriate Black body curve allowing us to obtain a spectral response curve for the system. Colour temperature measurements were made with an optical pyrometer. A similar method was proposed by Steyn et al [6] in 1976 as a way of calibrating a Scanning Electron Microscope (SEM) Cathodoluminescence detection system. Figure 1b shows the spectral response curve of our current system.

3. RESULTS

The optical properties of natural and synthetic diamonds have been extensively studied by previous workers and reviewed by Walker [7]. There however still exists much speculation on the mechanisms behind much of observed structure in absorption and emission spectra. A homoepitaxial diamond sample provided by the Solid State Institute, Technion Israel was analysed with the newly developed IBIL detection system. The much studied A-Band luminescence system, which is attributed to the recombination of electron-hole pairs at donor-acceptor levels, was observed in the homoepitaxial sample [8]. The epitaxial layers were produced by a hot tungsten filament Chemical

Vapour Deposition (CVD) technique. Approximately three quarters of the sample was masked by Mo during the growth process which consisted of a gas mixture of about 99 % hydrogen and 1% methane at a filament temperature of 2100-2300 K. Characteristic blue luminescence was observed from the substrate diamond. An extra band shifted to longer wavelengths was measured coming from the epitaxial layers. PIXE data from the two regions clearly show the presence of impurities in the overgrowth (Figure 2b).

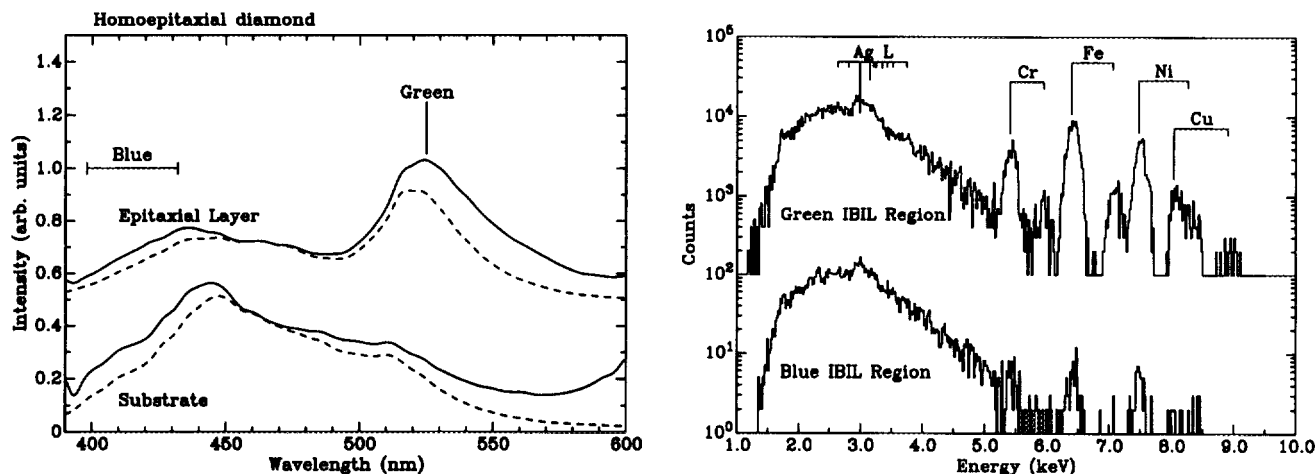


Figure 2 : (a)IBIL Spectra and (b)PIXE Spectra from Homoepitaxial Diamond Sample.

4. CONCLUSION

The continued development and improvement of the IBIL detection system will allow for samples to be analysed by multiple ion beam analytical techniques. Improvements in light collection efficiency with the addition of an optical fibre feed through, and the reduction of detector dark noise levels with the introduction of a new cooled photomultiplier tube, will expand the range of samples that are able to be analysed with the technique. Light dispersive detectors such as CCD array spectrographs are also being considered as alternative detection systems.

REFERENCES

- [1] C.A. Klein, J. Appl. Phys 39 4 (1968) 2029
- [2] B.G. Yacobi and D.B. Holt, Cathodoluminescence Microscopy of Inorganic Solids, Plenum Press, New York (1990) 56
- [3] G.J.F. Legge, P.M. O'Brien, R.M. Sealock, G.C. Allan, G. Bench, G. Moloney, D.N. Jamieson, A.P. Mazzolini and J. Zhu, Nucl. Inst. Meth. B30 (1988) 252
- [4] P.M. O'Brien, G. Moloney, A. O'Connor and G.J.F. Legge, Nucl. Inst. Meth B77 (1993) 52
- [5] H.B. Dyer and I.G. Matthews, Proc. R. Soc. A 243 (1957) 320
- [6] J.B. Steyn, P. Giles and D.B. Holt, J. Micro. 107 (1976) 107
- [7] J. Walker, Rep. Prog. Phys. 42 (1979) 108
- [8] P. Dean, J. Phys. Rev. 139 2A (1965) 588



FORMATION OF OXIDES AND SEGREGATION OF MOBILE ATOMS DURING SIMS PROFILING OF Si WITH OXYGEN IONS

M.Petravić, J.S.Williams, B.G.Svensson and M.Conway

Department of Electronic Materials Engineering, Research School of
Physical Sciences and Engineering, Australian National University
Canberra, ACT 0200

INTRODUCTION

An oxygen beam is commonly used in SIMS analysis to enhance the ionization probability for positive secondary ions. It has been observed, however, that this technique produces in some cases a great degradation of depth resolution [1]. The most pronounced effects have been found for impurities in silicon under oxygen bombardment at angles of incidence smaller than $\sim 30^\circ$ from the surface normal [2]. In this paper we report on broadening of SIMS profiles for some mobile atoms, such as Cu, Ni and Au, implanted into Si. The anomalously large broadening is explained in terms of segregation at a SiO_2/Si interface formed during bombardment with oxygen at impact angles $< 30^\circ$.

RESULTS AND DISCUSSION

The ion-implanted silicon samples used for this study are listed in Table 1. All SIMS measurements were performed in a quadrupole-type ion microprobe (Riber MIQ 256) using typically 8keV O_2^+ beam. In this instrument the primary beam energy and the angle of incidence can be changed independently.

Table 1: List of elements implanted into Si, together with the implantation conditions.

Element	Mass [amu]	Implantation energy [keV]	Dose density [cm^{-2}]
Au	197	97	5e14-8e15
Ni	58	60	8e15
Cu	63	60	5e14-8e15

As an example, Fig.1 shows several SIMS profiles of Ni implanted into Si, obtained by 8keV O_2^+ bombardment at different angles of incidence. The profiles obtained at 45° - 75° show no unusual perturbation and the difference in broadening observed for these angles is dominated by the angular dependence of ion beam mixing. On the other hand, the 30° -profile shows an anomalously large broadening. The same effect is found for all

angles $<30^\circ$ and also for profiles of Au and Cu implanted into Si.

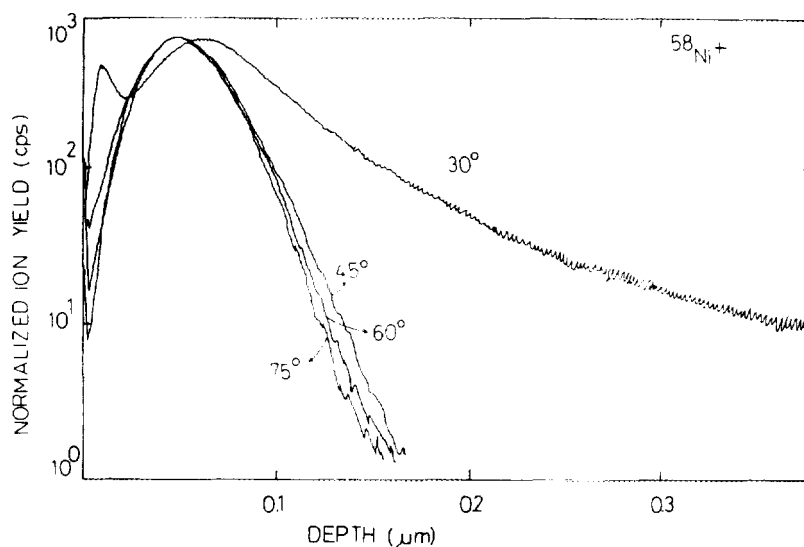


Fig.1: Dependence of SIMS profiles of Ni implanted into Si on 8keV O_2^+ beam angle of incidence.

Such a strong effect can be attributed to beam induced segregation of implanted atoms towards the interface between the SiO_2 film, formed during oxygen bombardment, and Si substrate. In order to reveal the oxygen build-up during O_2^+ -SIMS, we employed the RBS-C technique to analyse the SIMS craters. Fig.2 shows an RBS spectrum taken from the bottom of a SIMS crater obtained by 8keV O_2^+ bombardment at 20° to the surface normal. The RBS-C spectrum shows a stoichiometric SiO_2 surface layer of $\sim 200\text{\AA}$ in thickness and an underlying heavily damaged layer of $\sim 115\text{\AA}$ in thickness. Fig.3 shows an RBS spectrum taken after the SIMS profiling of Ni by 8keV O_2^+ bombardment at 0° . It shows the pile-up of Ni at the SiO_2/Si boundary.

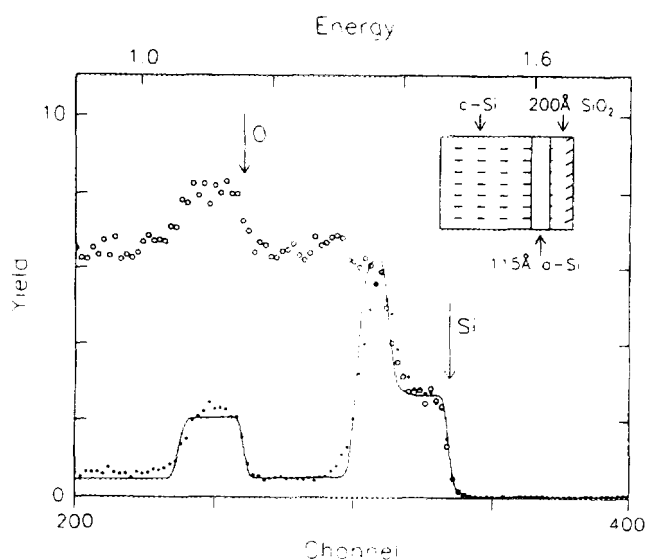


Fig.2: RBS spectra (obtained by 2 MeV He^+ at a grazing exit angle of 4° to the surface) taken from the bottom of a SIMS crater produced by 8 keV O_2^+ bombardment at 20° . Inset shows the structure used for the RUMP simulation (solid line).

The angular dependence of the retained oxygen content obtained

from the high resolution RBS measurements is shown in Fig.4. As the bombardment angle to the surface normal is increased, the sputtering yield increases until the sputter rate precludes the build-up of stoichiometric SiO_2 .

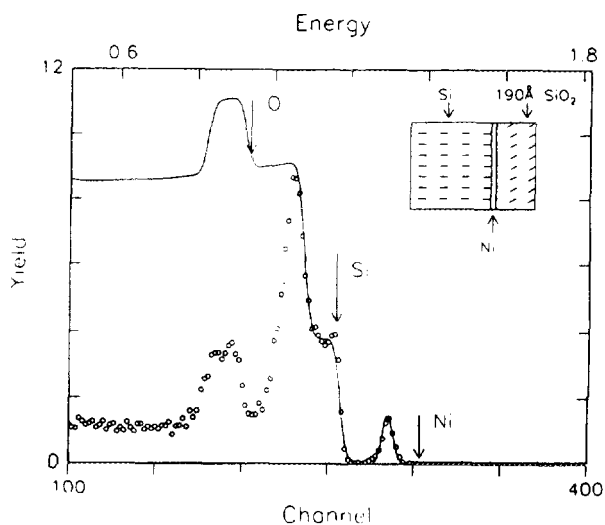


Fig.3: RBS spectra taken after SIMS profiling of a Ni implanted into Si. Solid line represents the RUMP simulation of the structure shown in inset.

In conclusion, we have shown that the strong degradation of SIMS profiles in Si under O_2^+ bombardment at impact angles $< 30^\circ$ is dominated by the segregation at a SiO_2/Si boundary: a stable SiO_2 layer forms during O_2^+ impact and the impurities are driven out of the oxide into underlying damaged Si. From a practical point of view, one should avoid the impact angles $< 30^\circ$ during SIMS analysis of impurities which tend to segregate out of the oxide.

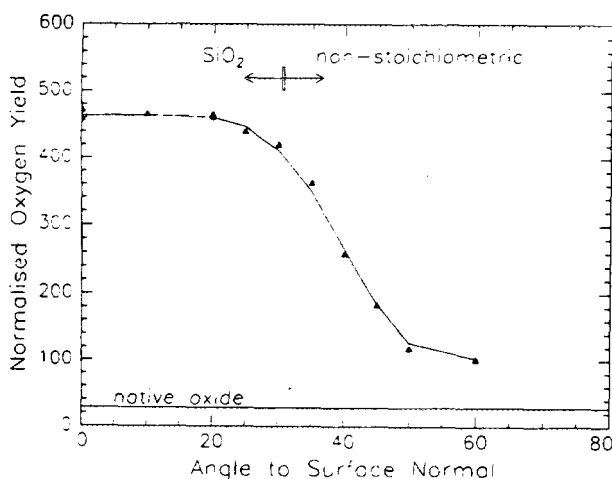


Fig.4: The angular dependence of the retained oxygen content, determined by RBS, for the 8 keV O_2^+ bombardment of Si.

REFERENCES

- [1] P.Williams and J.E.Baker, *Nucl.Instrum.Meth.* **182/183**, 15 (1981).
- [2] V.R.Deline, W.Reuter and R.Kelly, in "*Secondary Ion Mass Spectrometry, SIMS V*", edited by A.Benninghoven et al (Springer Verlag, Berlin, 1986) p.299.



THE EFFECT OF METAL ION IMPLANTATION ON THE SURFACE MECHANICAL PROPERTIES OF MYLAR (PET)

W. Zhou, D.K. Sood, X. Yao* and I.G. Brown*

Microelectronics and Materials Technology Centre, Royal Melbourne Institute of Technology, 124 La Trobe Street, Melbourne 3000, Australia

* Accelerator and Fusion Research Division, Lawrence Berkeley Laboratory, University of California, Berkeley, CA 94720, USA

INTRODUCTION

Ion implantation of polymers leads to the formation of new carbonaceous materials, the evolution during implantation of various species consists of (1) ion beam induced damage: chain scission, crosslinking, molecular emission of volatile elements & compounds, stoichiometric change in the surface layer of pristine polymers; and (2) chemical effect between ion and target materials: microalloying and precipitation [1, 2]. Literature regarding ion implanted polymers shows that the reorganisation of the carbon network after implantation can dramatically modify several properties of pristine polymers --- solubility, molecular weight, and electrical, optical [1] and mechanical [3] properties. However, ion implantation of polymers is actually a very complex interaction which depends on not only ion species, implantation condition, but also polymer type and specific structure. Therefore more experimental and theoretical studies are required.

We have started systematic work to modify the surface mechanical properties of several polymers (PET, PP & PVC) which have not been studied in detailed. Identical implantation conditions are employed in order to facilitate a clear comparison on the polymers with different type and structure. In this paper the effect of Ag or Ti ions implantation on surface mechanical properties of PET polymer is reported, as an initial presentation.

EXPERIMENTAL

The polymer samples, Mylar (PET, polyethylene terephthalate), used here are in the form of sheets, approximately 20 μm thick. Molecular structure of the PET polymer is illustrated in Fig.1. Ion implantation was carried out, using a metal vapour vacuum arc (MEVVA) high current ion implanter at Lawrence Berkeley Lab., with Ag or Ti ions at 100 keV energy and at doses ranging from 1×10^{15} to 5×10^{16} ions/cm². The beam current was kept low enough to prevent significant temperature rise of the samples during implantation at room temperature. 2 MeV He ions Rutherford Backscattering Spectrometry is employed to determine depth distributions of implanted ions. A pin-on-disc tribometer was used to measure friction and produce wear at a constant sliding speed of 0.38 m/s. A 3 mm diameter SAE 52100 high carbon chrome steel ball was slidden, under a load from 1 N to 5 N, on a disc with a flat polymer film which was rotated to 10,000 cycles. Tests were conducted in air ambient at room temperature. The wear grooves were analysed by optical microscopy and by a profilometer instrument (Tencor Alpha Step 250).

RESULTS AND DISCUSSION

After implantation of both Ag and Ti ions, the white transparent films of pristine PET polymer were changed to light yellowish-brown which deepened to a graphite-like black colour with increasing ion dose. The colour from the samples of Ti ion implantation is deeper than that from Ag ion implantation with the same dose. The colour change is similar to previous studies on other implanted polymers [1]. A typical friction trace from pin-on-disc measurements is shown in Fig.2 for an unimplanted PET sample. Three typical parameters may be noted: (1) maximum value of friction coefficient, μ_o , at the initial stage for running-in, (2) the number of cycles at breaking-through the surface of polymer film, B.T., and (3) average value of friction coefficient, μ_{ave} , stabilising to a nearly constant value after breaking-through. All implanted samples showed similar features and the results are summarised in Table 1. Fig.3 shows typical profilometer traces across wear tracks under 1 N load. The wear data in table 1 are average values corresponding to four orthogonal measurements along each wear track. Under 1 N load, μ_o is clearly increased after implantation, B.T. is greatly reduced. These trends correlate well with wear data which indicate the deterioration of wear up to 4.5 times after ion implantation with Ti. The μ_{ave} prior to and after ion implantations dose not change much, this can be accepted as accounting with the fact that the implanted layer of PET was almost worn off. Under 1 N load, it is also found that the wear after Ti ion implantation is much more, about 2 times, than that after Ag ion implantation. It could result from different chemical effect of implanted species. We speculate that a carbide phase could be formed after implantation. The higher wear for Ti implantation could therefore arise from more abrasive and hard TiC particles. The dependence of friction and wear on load listed in Table 1 is difficult to explain because of an early break-through the implanted layer under higher load conditions. Thus only the lowest load of 1 N gives us true dependence on implantation effects. This deterioration in wear on implantation is rather extraordinary. Our preliminary results on other implanted polymers (PP and PVC) are quite different and show large improvements.

CONCLUSION

1. Ion implantations into PET polymers produce extraordinary deterioration in wear resistance at both specieses of Ag and Ti
2. The increment of wear after implantation may result from not only ion damage but also chemical effect between ion and target material.

REFERENCES

- [1] T. Venkatesan, L. Calcagno, B.S. Elman and G. Foti, Ion Beam Modification of Insulators, eds. P. Mazzoldi and G. Arnold (Elsevier, Amsterdam, 1987) P.301 & ref. therein.
- [2] E.H. Lee, M.B.Lewis, P.J. Blau, and L.K. Mansur, J. Mater. Res. Vol.6,No.3 (1991) 610.
- [3] J.D. Carlson, J.E. Bares, A.M. Guzman and P.P. Pronko, Nucl. Instr. and Meth. B7/8 (1985) 507.

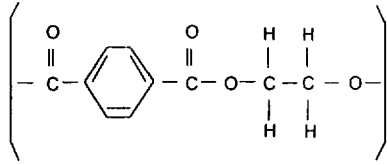


Fig.1 chemical structure of the PET polymer used in the present study.

Fig. 3 Wear track profiles for PET films (a) unimplanted, and after implantations at a dose of 5×10^{16} ion/cm² with (b) Ag ions & (c) Ti ions.

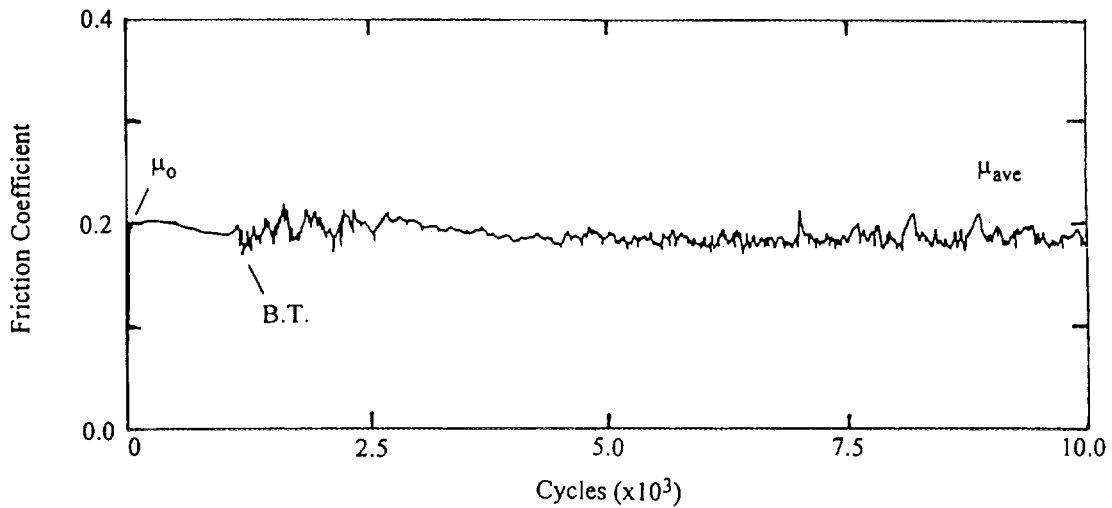
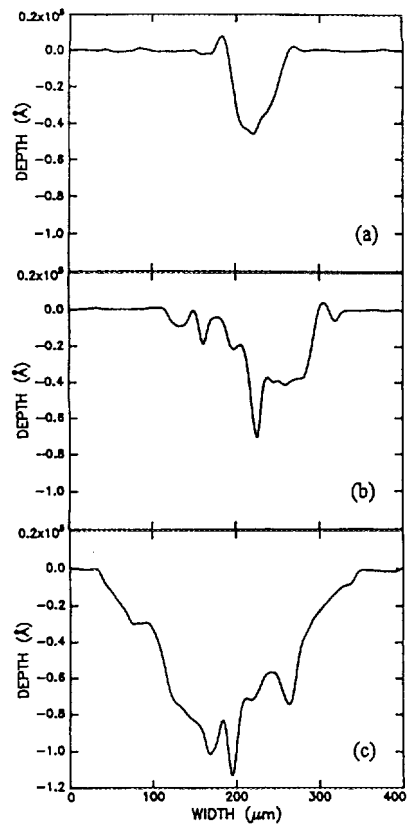


Fig.2 Friction coefficient of high carbon chrome steel ball sliding, under 1 N load, on unimplanted PET film.

Table 1. Experimental results on friction and wear for different ion implantations

MATERIALS		IMPLANTATION			LOAD	FRICTION			WEAR		
Disc	Pin	Ion	E(keV)	D(ions/cm ²)	(N)	μ_0	B.T.(c)	μ_{ave}	Depth(Å)	Width(μm)	Area(μm ²)
Pet	SAE52100				1	0.2	1130	0.18	39	69	179
Pet	SAE52100	Ag	100	5×10^{16}	1	0.29	174	0.18	71	199	462
Pet	SAE52100	Ti	100	5×10^{16}	1	0.35	348	0.23	80	231	804
Pet	SAE52100				2	0.13	821	0.13	104	255	1487
Pet	SAE52100	Ag	100	5×10^{16}	2	0.22	96	0.13	67	363	1213
Pet	SAE52100	Ti	100	5×10^{16}	2	0.23	169	0.13	137	380	2035
Pet	SAE52100				5	0.12	292	0.12	136	505	4579
Pet	SAE52100	Ag	100	5×10^{16}	5	0.22	17	0.13	142	510	4828
Pet	SAE52100	Ti	100	5×10^{16}	5	0.21	17	0.12	145	425	4108



THE EFFECT OF ION IMPLANTATION ON THE TRIBOMECHANICAL PROPERTIES OF CARBON FIBRE REINFORCED POLYMERS

Romano Mistica, D.K. Sood, and M.N. Janardhana[@],
Microelectronic and Materials Technology Centre, Royal
Melbourne Institute of Technology, Melbourne 3000
[@]School of Engineering and Technology, Deakin University

INTRODUCTION

Graphite fibre reinforced epoxy composite material (GFRP) is used extensively in the aerospace and other industries for structural application. The trend is to address the 20 to 30 year life endurance of this material in service. Mechanical joints in aircrafts are exposed to dynamic loads during service and wear may be experienced by the composite material joint. Generally it has been shown that graphite fibre reinforced polymers have superior wear and friction properties as compared with the unfilled polymers. To take the research one step further we have used ion implantation as a novel surface treatment. Wear and friction of a polymer composite material (GFRP) is studied and ion implantation is used in order to observe the effect on the tribomechanical properties of the material. Ion implantation on polymers has been observed previously to improve the wear property[1].

EXPERIMENTAL

Material used: GFRP - 40% Epoxy resin (TGDDM) + 60% Graphite fibre. Unidirectional continuous fibre.
Titanium (Ti6Al4V)

A pin and disc machine (CSEM) is used to study the friction and wear behaviour before and after ion implantation. Rectangular GFRP pins were used, cut 3mm x 3mm x 1cm to produce an apparent contact area of 10mm². The pins are cut to produce three different fibre orientation to the direction of sliding and counterface. Titanium discs are used as a counterface. Ti discs are hand polished using SiC paper to a finish of 600 Angstrom. The Ti disc is rotated to produce a constant speed of 300mm/s. The load used is 5N. A total of 20 kms distance is run measuring the weight at intervals of 5 kms. The GFRP pins are ion implanted with C ions using doses 1E14, 1E15 and 1E16 ions/cm² at 35 keV.

RESULTS and DISCUSSION

Friction and wear data for the unimplanted (virgin) and ion implanted with C ions (1E14 ions/cm²) are shown in figures 1 & 2 respectively. The results are for the fibres running parallel in the direction of sliding. It has been well documented that fibre direction of sliding can influence the friction and wear behaviour of continuous fibre reinforced polymers.

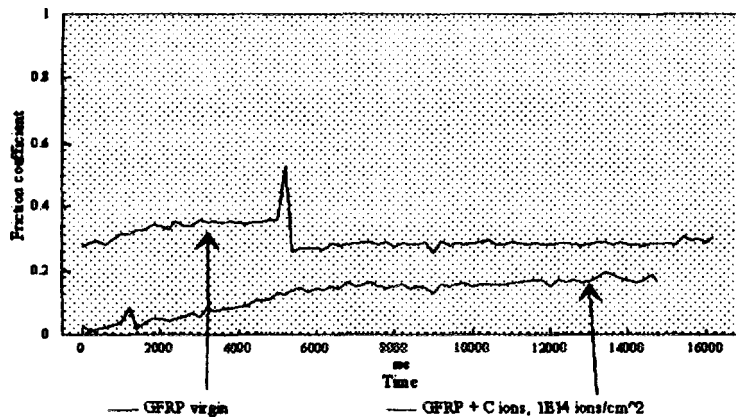


Fig 1. Friction data for unimplanted and implanted pins

During the initial stages of sliding for the virgin sample, no tracks were observed. It was seen that tracks formed fully for the GFRP virgin sample 1.5 hours after running which is indicated by the peak in figure 1 and thereafter steady state condition prevailed. The peak in friction for the ion

implanted GFRP was not as significant. This pre steady state condition may be due to the change in surface topography [2]. Carbonaceous film as well as a wear track for the ion implanted GFRP became visible not long after the start of the run. No significant transfer film formed for the virgin sample, a similar result was obtained by Giltrow[3] using a similar counterface. It is clear from figure 1 that the coefficient of friction is reduced from 0.3 to .15 by ion implanting the GFRP with C. Giltrow [3] and Lancaster[4] showed that the coefficient of friction for carbon fibre reinforced polymers against steel lie within the range of 0.25-0.35 and appear to be almost independent of the matrix materials. The friction coefficient for our unimplanted data is very similar, which implies that the graphite fibre could be the influential characteristic in the case of GFRP sliding against Ti. This also suggests that the graphite fibre may not be the influencing characteristic that generates the coefficient of friction results obtained for the ion implanted GFRP composite.

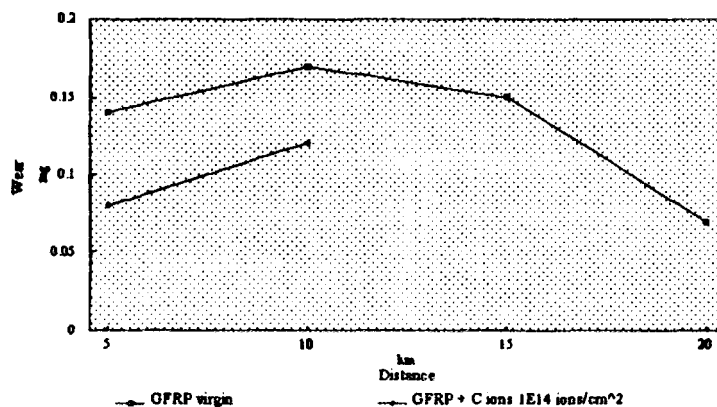


Fig 2. Wear data for unimplanted and implanted pins

Initial wear results show (Fig.2) there is a decrease in cumulative wear for the ion implanted GFRP. It was observed that wear debris appeared to be more significant for the virgin sample in comparison with the implanted

sample. As mentioned above the carbonaceous film was prominent for the implanted sample suggesting that the carbon film characteristic influenced the wear result. Giltrow[3] observed that transfer film formed for most counterfaces used except for Ti and Gold and explains why no film transfer occurred. The presence of the carbonaceous film on the Ti counterface for the ion implanted GFRP indicate that the carbon rich surface (produced by ion implantation) of the pin changed the wear property of the tribological system.

CONCLUSION

The results reported herein lead to the following conclusion.

1. Ion implantation of GFRP changes the tribological property of the system, significantly.
2. Ion implantation of C on GFRP sliding against Ti decreased the coefficient of friction and wear.
3. Further investigation is required to form an understanding of the effects of ion implantation on GFRP and their beneficial effects on the tribological properties.

ACKNOWLEDGMENTS

Ion implantation was made possible at ANSTO by an AINSE grant. Thanks to J.W. Chu and P.J. Evans for their kind assistance for implantation.

REFERENCES

1. E.H. Lee, et al. J.Mater. Res., Vol, No.3, Mar 1991
2. J.Bijwe, U.S Tewari and P. Vasudevan, Wear, Vol 132 (1989) 247.
3. J.P. Giltrow and J.K. Lancaster, Wear, Vol 16, (1970), 359-374.
The role of the counterface in the friction and wear of carbon fibre reinforced thermosetting resin.
4. J.K. Lancaster. Brit. J. Appl. Phys, Vol 1, Ser. 2, 1968, 149.
The effect of carbon fibre reinforcement on friction and wear of polymers.

Annealing Behaviour of MeV Erbium Implanted Lithium Niobate

P. Gortmaker and J.C. McCallum^a *

^aMicroelectronics and Materials Technology Centre, Royal Melbourne Institute of Technology,
P.O. Box 2476V, Melbourne, 3001, Australia

Lithium Niobate (LiNbO_3) is a crystalline ceramic commonly used in the fabrication of optoelectronic devices. Recently, rare earth doping of LiNbO_3 has become a topic of particular interest. The electronic configuration of rare earth elements such as Erbium (Er) and Neodymium (Nd) allows them to lase in nearly any host matrix making fabrication of a whole range of new optoelectronic devices possible. At present, the doping techniques for LiNbO_3 are centred upon diffusion technology, but the diffusion profiles for the rare earths are not generally well-matched to the optical modes of the device. The aim of this research is to develop MeV implantation and annealing conditions of rare earth doped LiNbO_3 that would be compatible with optoelectronic device fabrication. To determine the characteristics of the rare earth elements in the LiNbO_3 host material over the depth range of interest in optoelectronic device applications, high energy Rutherford Backscattering Spectrometry and Ion Channeling (RBS-C) must be used. Presented here are the Er depth profile and lattice damage results obtained from 5 MeV RBS-C measurements on samples of LiNbO_3 implanted with various doses of MeV Erbium and subsequently thermally annealed at a temperature of 1000°C .

1. INTRODUCTION

The electronic configuration of rare earth elements such as Erbium (Er) and Neodymium (Nd) allows them to lase in nearly any host matrix. This is due to the fact that the electrons involved in the bonding do not have a significant effect on those involved in the lasing action. At present, the doping techniques for LiNbO_3 are centred upon diffusion technology, however, ion implantation may allow the impurity profile to be tailored to obtain a better match to the optical modes of the device. Previous implantation research has been performed with ion energies less than 500 keV[1], but these implants suffered similar problems to the diffusion studies, such as long annealing times and impurity profiles which were peaked at the sample surface. By using MeV implantation, one can place the rare earth dopants at the depths required by optical device technology.

When Rutherford backscattering spectrometry (RBS) is used to profile Er in LiNbO_3 , the Er signal merges with the Nb signal except in the near surface region. This limited depth profiling capability can be extended by increasing the incident

He beam energy, but one must then be concerned with non-Rutherford scattering cross sections, and nuclear reactions. The maximum approximate accessible depth for profiling Er in LiNbO_3 is only about 1100\AA with standard 2 MeV RBS. By using 3 MeV RBS, this can be extended to approximately 2500\AA , and with 5 MeV, it can be pushed beyond 5000\AA .

2. EXPERIMENTAL

All samples were taken from a z-cut LiNbO_3 wafer supplied by Crystal Technologies. The samples were approximately $10\text{mm} \times 10\text{mm}$, and were secured against a copper block for implantation. The implants were performed at room temperature. The Er was implanted with energies ranging from 1 to 3 MeV, and with doses ranging from 1 to 4×10^{16} Er/cm². The results presented here focus mainly on those samples implanted at 2 MeV. A range of Er isotopes were implanted since the mass resolution of the ion implanter was not fine enough to select a single isotope. The as-implanted Er profile was then measured via 3 and 5 MeV Rutherford Backscattering and ion channeling. The samples were then thermally annealed to recrystallise the implanted region. This was performed in a wet O_2 environment to prevent the enhanced Li out-diffusion that occurs in

*This research is sponsored in part by The Australian Research Council Special Research Centre for Advanced Surface Processing of Materials

the damaged region[3]. Thermal cycling to and from the annealing temperature took place over a period of 15 minutes to avoid thermal stresses, however others have had success with rapid cycling.[2]

Rutherford backscattering spectrometry and ion channeling were used to determine the regrowth behaviour, Er concentration profiles, and residual defect structures. The experimental configuration for the 5 MeV RBS-C results shown here had an energy conversion of 10.0 keV/channel, and were taken at a scattering angle of 165°. The depth scales shown were derived by using the above configuration together with the known value of the density of crystalline LiNbO₃, which is 4.644 g/cm³.

3. RESULTS AND DISCUSSION

Fig. 1 shows RBS-C spectra obtained with 5 MeV He⁺⁺ ions from Er-implanted and annealed LiNbO₃ samples. The energies associated with surface scattering from Er, Nb and O are indicated. The as-implanted, random spectrum for the 1 × 10¹⁶ Er/cm² (triangles) shows the typical data obtained from LiNbO₃ at this energy. The small signal just in front of the Nb scattering edge is that of the implanted Er, with the larger of the two Gaussian profiles being that of a 4 × 10¹⁶ Er/cm² implant. The region in the channelled as-implanted spectrum (squares) where the backscatter yield reaches the random level indicates that an amorphous layer has been generated under these implantation conditions. The depth range over which the yield reaches the random level corresponds to an amorphous layer thickness of 7200 Å. The channelled spectrum of the 1 × 10¹⁶ Er/cm² annealed sample was equivalent to the RBS-C spectrum obtained from a virgin piece of LiNbO₃ (not shown). This indicates that the annealing conditions are sufficient to recrystallise the implanted region.

Details of the Er profiles for as-implanted (2 MeV Er, 1 × 10¹⁶ cm⁻²) and annealed samples are shown in Fig. 2. The as-implanted spectrum (squares) shows the approximately Gaussian Er implant profile centred at a depth of ~ 3400 Å. This is in reasonable agreement with the pro-

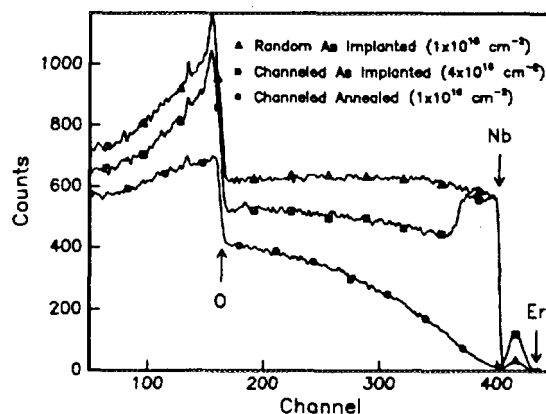


Figure 1. 5 MeV RBS-C spectra for z-cut LiNbO₃ samples implanted with 2 MeV Er at room temperature.

jected range of 3240 Å for the Er ions predicted by the TRIM code [4]. The random spectrum from the annealed sample (triangles) shows that during the anneal, the Er redistributes to form a constant concentration profile at 0.1 atomic percent extending from the surface to depths in excess of the 5000 Å resolved by 5.0 MeV He⁺⁺ backscattering. In the channeling spectrum for the annealed sample (not shown), the yield from the Er is very low suggesting that the Er is sitting on substitutional lattice sites in the recrystallised material.

At implantation doses of 2 × 10¹⁶ Er/cm² and above the Er fails to go substitutional and the lattice recovery is drastically degraded. The Er concentration profiles for the as-implanted and the post-anneal 4 × 10¹⁶ Er/cm² case are shown in Fig. 3. For optical device fabrication, one would like to maximise the Er concentration while still recovering the original crystal quality by thermal annealing, as any introduced defects can act as scattering sites, and degrade performance. In Fig. 3 the behaviour of the Er during the annealing process is shown for the highest dose studied. In this case, the post-anneal Er profile (tri-

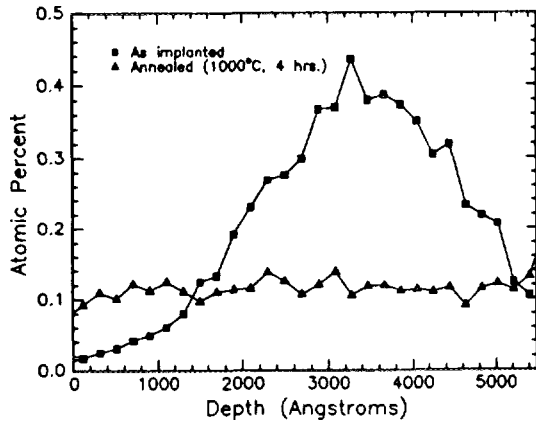


Figure 2. As implanted ($2 \text{ MeV Er}, 1 \times 10^{16} \text{ cm}^{-2}$) and post-anneal ($1000^\circ\text{C}, 4 \text{ hrs.}$) Er concentration profiles in z-cut LiNbO_3 , obtained from RBS with random incidence of the analysis beam.

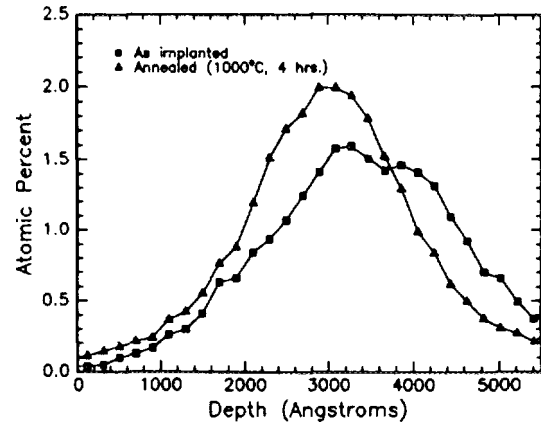


Figure 3. As implanted ($2 \text{ MeV Er}, 4 \times 10^{16} \text{ cm}^{-2}$) and post-anneal ($1000^\circ\text{C}, 4 \text{ hrs.}$) Er concentration profiles in z-cut LiNbO_3 , obtained from RBS with random incidence of the analysis beam.

angles) shows some redistribution from that of the as-implanted profile (squares). The RBS-C results indicated that the region extending to 3500 \AA below the surface was still heavily damaged, and hence unfit for optical device substrate material. This behaviour is similar to that observed when one has a low solubility impurity being partially zone-refined in front of a mobile crystalline-amorphous interface during regrowth.

4. CONCLUSIONS

Various concentrations of Er have been introduced into z-cut LiNbO_3 by MeV ion implantation. There exists a peak implant concentration for which the Er no longer goes substitutional in the lattice, and the implantation damage is not fully removed by annealing. For optical device fabrication, the lattice must fully recover from the implantation damage. This observed limit corresponded to a solubility limit of 0.1 at. % of Er in LiNbO_3 for a four hour anneal at 1000°C . However, samples having an implant dose below this limit are feasible for optical device use. Fluorescence and wave-guiding measurements are cur-

rently underway on such samples.

REFERENCES

1. Ch. Buchal and S.Mohr, *J. Mater. Res.*, **6** (1991) 134.
2. T. Bremer and W. Heiland, *J. Appl. Phys.* **67** (1990) 1183.
3. G.W. Arnold, *Nucl. Instr. and Meth.* **B39** (1989) 708.
4. J.F. Zeigler, *Transport and Range of Ions in Matter*, computer code.
5. A. Polman, D.C. Jacobson, D.J. Eaglesham, R.C. Kistler and J.M. Poate, *J. Mater. Res.*, **70** (1991) 3778.
6. P. Becker, R. Brinkmann, M. Dinand, W. Sohler, and H. Suche, *Appl. Phys. Lett.* **61** (1992) 1257.
7. D.M. Gill, A. Judy, L. McCaughan and J.C. Wright, *Appl. Phys. Lett.*, **60**, (1992) 1067.
8. Ch. Buchal, *Nucl. Instr. and Meth.* **B68** (1992) 355.



Ion Beam Analysis Techniques Applied to Large Scale Air Pollution Studies

David D. Cohen, G. Bailey, J. Martin, D. Garton, H. Noorman, E. Stelcer,
P. Johnson,

Australian Nuclear Science and Technology Organisation,
PMB1 Menai, NSW, 2234, Australia.

Ion Beam Analysis (IBA) techniques are ideally suited to analyse the thousands of filter papers a year that may originate from a large scale aerosol sampling network. They are fast multi-elemental and, for the most part, non-destructive so other analytical methods such as neutron activation and ion chromatography can be performed afterwards.

ANSTO in collaboration with the NSW EPA, Pacific Power and the Universities of NSW and Macquarie has established a large area fine aerosol sampling network covering nearly 80,000 square kilometres of NSW with 25 fine particle samplers see Fig. 1. This network known as ASP was funded by the Energy Research and Development Corporation (ERDC) and commenced sampling on 1 July 1991. The cyclone sampler at each site has a 2.5 μm particle diameter cut off and runs for 24 hours every Sunday and Wednesday using one Gillman 25mm diameter stretched Teflon filter for each day. These filters are ideal targets for ion beam analysis work. Currently ANSTO receives 300 filters/ month from this network for analysis using its accelerator based ion beam techniques on the 3 MV Van de Graaff accelerator. One week a month of accelerator time is dedicated to this analysis. Four simultaneous accelerator based IBA techniques are used at ANSTO, to analyse for the following 24 elements H, C, N, O, F, Na, Al, Si, P, S, Cl, K, Ca, Ti, V, Cr, Mn, Fe, Cu, Ni, Co, Zn, Br and Pb. The four techniques are:-

Particle Induced X-ray Emission (PIXE)

PIXE provides most of the elemental information, it is used for elements from aluminium to uranium. The X-ray spectra are especially free from background emission and this allows lower detection limits typically less than 10 ngm^{-3} of air sampled (130 ng/cm^2 of filter) for input proton energies of between 2 and 3 MeV. Typical proton beam currents are less than 1 nA/mm^2 for beam diameters of around 8 mm. Thin standard Micromatter foils of Al, Si, Cl, Ca, Fe and Sr are used to calibrate the PIXE detection system from 1.4 keV to 20 keV. Over the past 18 months the calibration has been reproducible to better than $\pm 3\%$.

Particle Induced Gamma Ray Emission (PIGME)

We use PIGME to measure sodium and fluorine only. It has higher minimum detectable limits than PIXE being typical around 150 ngm^{-3} of air ($2 \mu\text{g/cm}^2$ of filter) for sodium and 60 ngm^{-3} ($0.8 \mu\text{g/cm}^2$ of filter) for fluorine for a few minutes of beam time using 2.6 MeV protons. The PIGME technique is run simultaneously with the PIXE technique on the same sample although count rates into the PIGME spectra a somewhat lower than into the PIXE spectrum since PIGME is a nuclear reaction while PIXE is an atomic one.

Particle Elastic Scattering (PESA)

Hydrogen is a difficult species to measure accurately, in our system we acquire total hydrogen measurements on the filter using the proton elastic scattering (PESA) or forward scattering technique at 30 degs. We obtain minimum detection limits around 15 ngm^{-3} (200 ng/cm^2 of filter) for a typical $3 \mu\text{C}$ run. The PESA technique can clearly only be used with a thin filter target where the ion only loses a small fraction of its total input energy, for 2.6 MeV protons we typically lose only 15 keV.

Rutherford Backscattering (RBS)

Rutherford Backscattering is similar in nature to PESA except the detection is in the backward direction. In our case we use a reaction angle of 169 degs to detect total carbon nitrogen and oxygen on the filter. Standard thin Mylar and Kapton foils are used to calibrate the detection yields since the reaction cross sections for these light elements are non - Rutherford. Detection limits for carbon, nitrogen and oxygen are around 200 to 500 ngm^{-3} (2 to $7 \mu\text{g/cm}^2$ of filter) for typical $3 \mu\text{C}$ run.

Each of the 24 elements detected on the filters can act as a fingerprint or tracer for fine particle sources, for example Al and Si from windblown soil, S from fossil fuel burning, K from wood burning, V from oil combustion, Cr, Mn, Fe, Zn from industrial processes and Br and Pb from motor vehicles. These IBA techniques have allowed us to determine the average fine aerosol composition over the network for 1992. The average fine particle total mass was $7.7 \mu\text{g/m}^3$ of air and this was composed of 23% organics (C, H, and O), 23% ammonium sulphate (H and S), 7% salt (Na and Cl), 6% soil (Al, Si, Ca, Ti and Fe), 22% elemental carbon or soot and 1% lead, the remainder was made up of other trace elements, nitrates and water.

The placing of our samplers around the major population areas and industrial centres of NSW (see Fig. 1) enables us to measure spatial and seasonal variations of these elements. In Fig. 2 we show the variation of sulphur with distance up to 200 km from the centre of Sydney and for the industrial centres of Wollongong and Sydney. Sulphur occurs mainly as ammonium sulphate in the aerosol and originates from coal burning and smelting operations in industrial centres. Fig. 3 is a similar plot for lead which mainly originates from motor vehicles, smelting operations and possibly domestic wood burning in the winter time. The sulphur levels drop by only about 30% from the inner city out to 200 km whereas the lead levels fall by a factor of 20 over the same distance. This demonstrates that the lead sources are strongly associated with the city centre and motor vehicle density whereas the sulphur sources are more diverse being well distributed between industrial centres at Newcastle, Wollongong, the Sydney centre and the coal burning power stations in the north and to the west of Sydney.

Clearly the IBA techniques described here are capable of producing similar information on many other elemental concentrations besides sulphur and lead. They are proving invaluable in identifying sources of fine particles and their spatial and seasonal variations across the large area sampled by the ASP network.

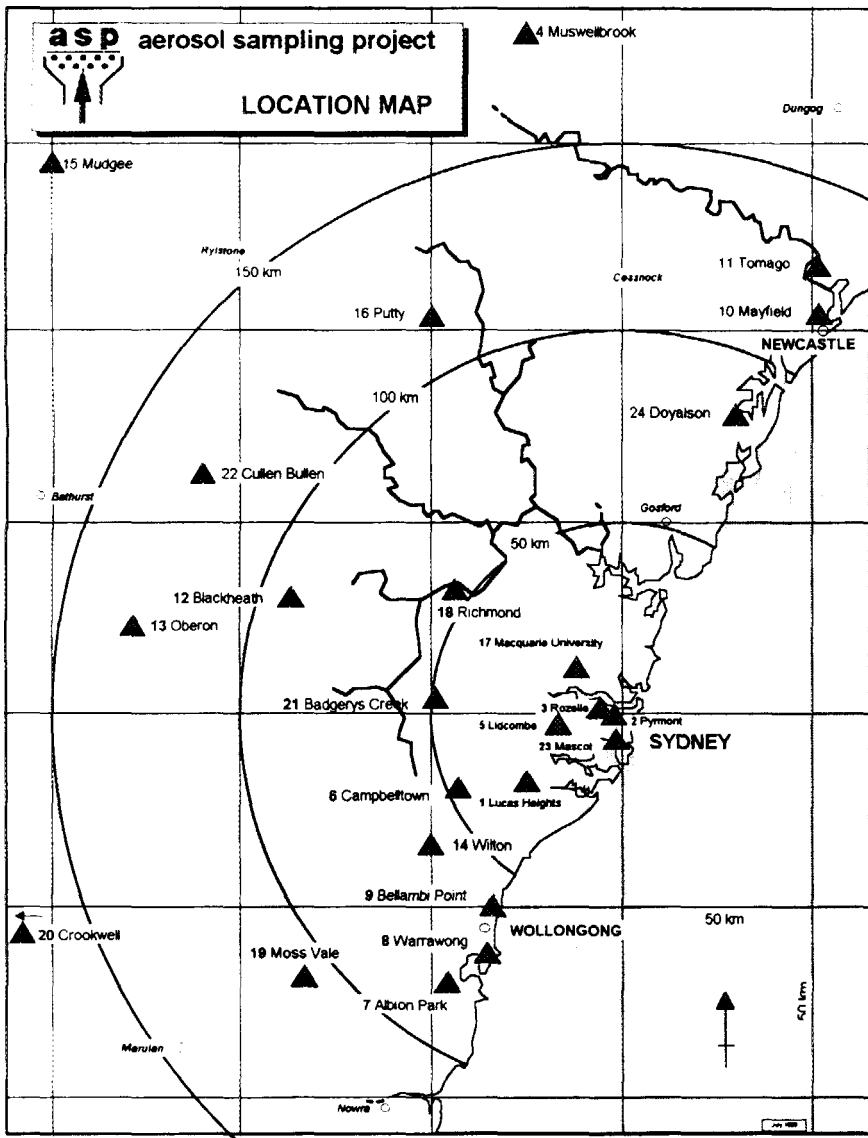


Fig. 1. ASP sampler locations

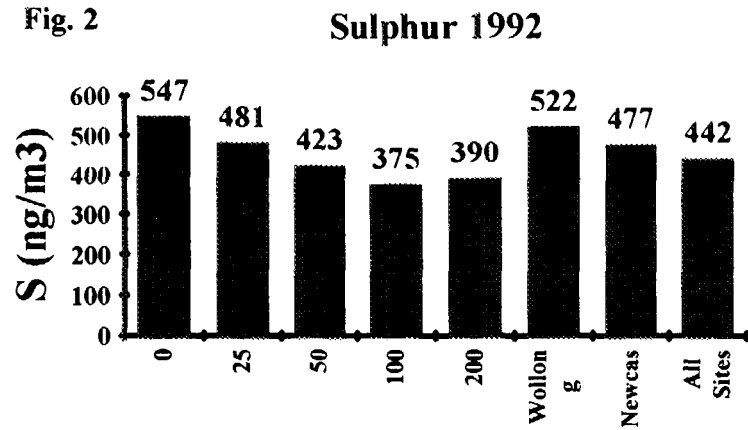


Fig. 2. Sulphur concentrations for various distance from Sydney

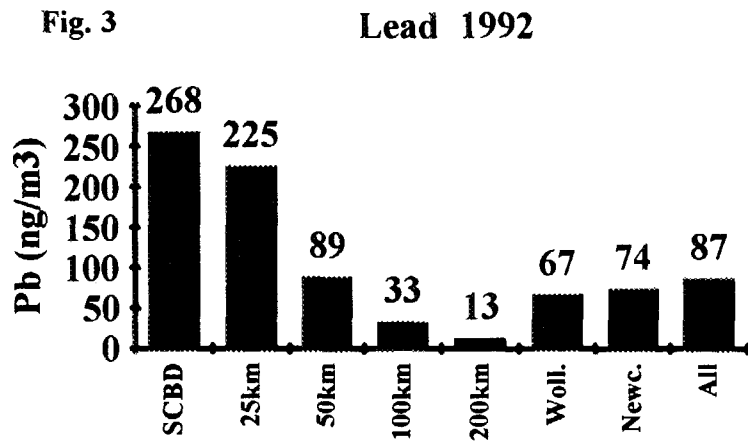


Fig. 3. Lead concentrations for various distance from Sydney



SODIUM , POTASSIUM AND CHLORIDE STATUS IN AUSTRALIAN FOODS AND DIETS USING NEUTRON ACTIVATION ANALYSIS

J.J. FARDY, G.D. McORIST, Y.J. FARRAR, C.J. BOWLES

Radioanalytical Applications, Ansto Environmental Science Program
Lucas Heights Research Laboratories, Private Mail Bag 1 MENAI, NSW, 2234

ABSTRACT

A study of the status of essential, toxic and trace elements in the foods and diets of Australian has been in progress for six years. Results for sodium, potassium and chloride levels are reported here. The average daily dietary intake of sodium and chloride exceeded the range of values recommended by the National Health & Medical Research Council (NH & MRC) for most population groups with grain and dairy products the main contributor to these high intakes. In contrast, the average daily intakes of potassium fell well within the recommended values for all age groups with intakes for adult females close to the recommended minimum figure.

INTRODUCTION

Sodium, potassium and chloride are essential elements required in the daily diets of humans¹. However, there is some evidence that both an excess of sodium and a marked alteration of the sodium:potassium ratio are related to high blood pressure and heart diseases that occur in some individuals²⁻⁴. While sodium is the principal cation of extracellular fluid involved in the maintenance of osmotic equilibrium and extracellular fluid volume, potassium is the principal cation in the intracellular fluid where it controls the activity of the heart, muscles, nervous system and most of the living cells in the body⁵. Chlorine, which is present in the body almost exclusively as chloride, is an important anion in the maintenance of fluid and electrolyte balance and is a necessary component of gastric juices. In general, the build up and losses of this electrolyte in the body closely parallels that for sodium.

During recent research investigations of reasons for the low selenium content of the plasma of Australians⁶, the concentration of selenium and a wide range of other essential, toxic and trace elements were measured in the foodstuffs commonly consumed by Australians. The resulting status of selenium⁷ and manganese⁸ in the foodstuffs and diets of Australians have been published. This paper reports the results for sodium, potassium and chloride.

EXPERIMENTAL

Australian-wide samples of representative foods from the diets of Australians were used in this study. Full details of the sampling program were described earlier⁷. Fifty representative foods from each of the seven State capitals were prepared according to strict guidelines at the East Sydney Technical College. Foods normally washed before use were washed. Those normally cooked were cooked without salt and then blended. Samples were placed in cleaned, screw-top, polystyrene containers, frozen and shipped to the laboratory.

All samples were stored frozen until ready for analysis. They were either dried in an air oven at 105°C or by vacuum desiccation, or lyophilized according to the nature of the material. Samples were blended further using the brittle fracture technique⁹.

Instrumental neutron activation analysis techniques for measuring sodium, potassium and chloride were similar to those described earlier for manganese⁸. Analyses were performed via the ³⁸Cl, ²⁴Na and ⁴²K radionuclides using the respective photopeaks at 1642, 1368 and 1525 keV after cool periods of 1 and 24 hours.

RESULTS AND DISCUSSIONS

Three hundred and fifty food samples were analysed for chlorine, sodium and potassium. All results were calculated as g.g^{-1} on a wet basis of the food prepared for consumption. The range of concentrations found in each class of food for each element are listed in Table 1.

The total intake of each element present in each food item listed in a number of hypothetical human diets was calculated. These diets were compiled by the Nutrition Section of the Federal Department of Health for nine-month old infant (9M), a two-year-old child (2Y), a twelve and a half-year old male (YM), a similarly aged female (YF) and an adult male (AM) and an adult female (FM) based on the eating habits of Australians and food consumption statistics. Daily intake figures for all these electrolytes were then compared with the Australian NH&MRC recommendations for sodium and potassium and US Food and Nutrition Board (US-FNB) recommendations for chloride (Fig 1)

The average daily dietary intake of sodium for all population groups exceeded the range of values recommended by the NH&MRC with the sole exception of adult females. The major food contributing to these high intakes were dairy and grain (Fig 2). Similar results were obtained for chloride intakes for three of the six age groups higher than the recommended ranges of the US-FNB. However, intake data for YM, AM and AF fell within the recommended ranges. Again, grain and dairy products were the main contributors. In contrast, the average daily intake of potassium fell within the recommended values for all age groups with intakes for adult females of 2060 mg close to the recommended minimum figure of 1875 mg. While dairy products were the main contributor of potassium for the younger age groups, adults obtained their potassium requirement from a much wider range of food types.

References

1. Food and Nutrition Board: Recommended Dietary Allowances, 9th Ed., National Academy of Science, Washington, DC, 1980, p. 166-178.
2. Meenely, G.R., Ball, C.O.T., Am. J. Med., 25 (1958) 713.
3. Gros, G., Weller, J.M., Hoobler, S.W., Am. J. Clin. Nutr., 24 (1971) 605.
4. MacGregor, G.A., Hypertension, 5 (1983) 79.
5. Passwater, R.A., Cranton, E.M., Eds., Trace Elements, Hair Analysis and Nutrition, Keats Publishing Inc, New Canaan, CT, 1983, p. 80.
6. McOrist, G.D., Fardy, J.J., Farrar, Y.J., J. Radioanal. Nucl. Chem., 134 (1989) 65.
7. Fardy, J.J., McOrist, G.D., Farrar, Y.J., J. Radioanal. Nucl. Chem., 133 (1989) 397.
8. Fardy, J.J., McOrist, G.D., Farrar, Y.J., J. Radioanal. Nucl. Chem., 163 (1992) 195.
9. Iyengar, G.V., Kasperek, K., J. Radioanal. Chem., 39 (1977) 301.

Table 1
Sodium, chloride and potassium concentration in Australian foods
(mg/g, wet basis)

Food Class	Sodium		Chloride		Potassium	
	Min	Max	Min	Max	Min	Max
Grain Products	0.01	11.05	0.04	18.1	0.1	4.16
Meat/Poultry	0.37	1.18	0.43	1.18	1.85	4.14
Fish	0.92	5.53	1.05	7.92	2.12	3.47
Eggs/offal	0.67	1.26	1.03	1.97	1.02	3.63
Dairy products	0.31	15.53	0.71	13.61	0.56	13.92
Oils/Fats	4.22	7.21	2.42	12.33	0.53	6.04
Vegetables	0.01	4.02	0.08	1.06	0.79	3.05
Fruit	0.01	0.04	<0.01	1.09	0.49	3.14
Miscellaneous	0.55	3.81	<0.01	7.44	0.53	6.02

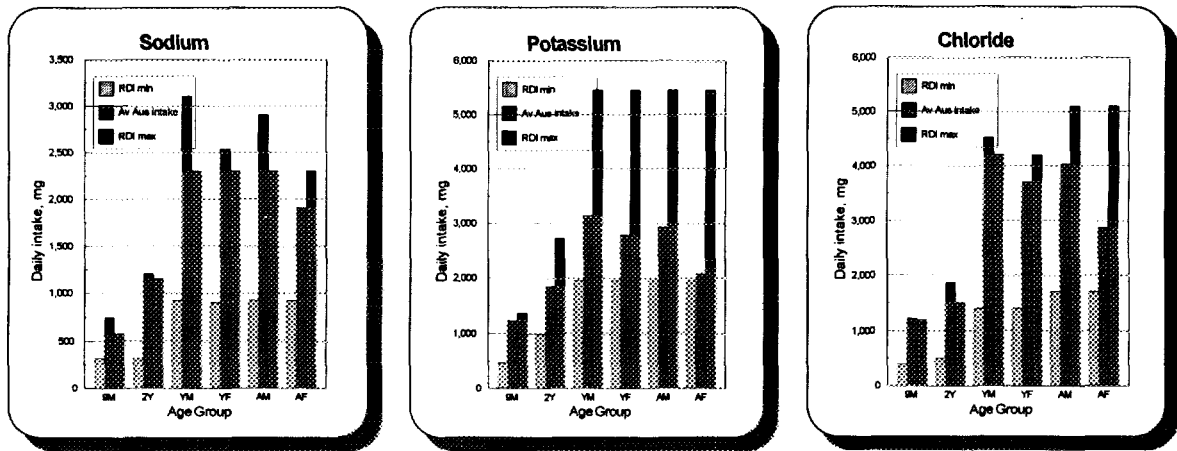


Fig 1 Average Na, K and Cl intake compared with recommended figures.

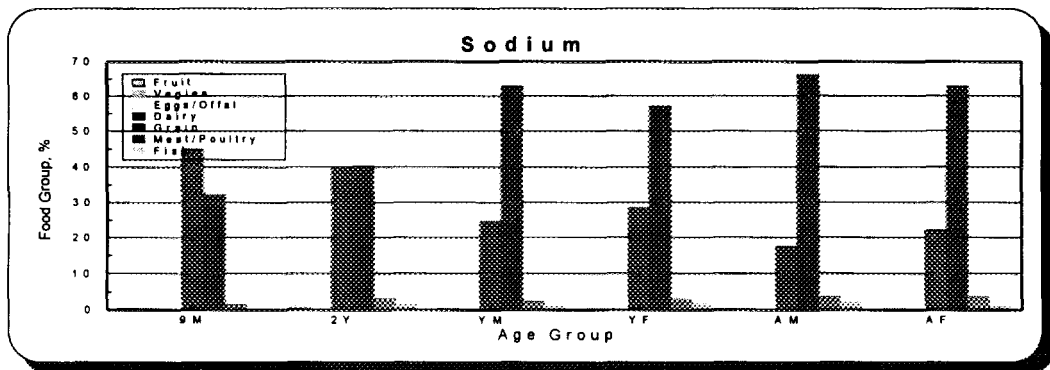


Fig 2 Percentage food contribution for different age groups

DETECTION OF SUBMONOLAYER OXYGEN-18 ON A GOLD SURFACE BY NUCLEAR REACTION ANALYSIS.

L.S.Wielunski¹, M.J.Kenny¹ and L. Wiczorek²

(1) CSIRO, Division of Applied Physics, P.O.Box 218 Lindfield, NSW 2070, Australia.

(2) Cooperative Research Centre for Molecular Engineering and Technology, CSIRO Division of Applied Physics, PO Box 218, Lindfield, NSW 2070, Australia

A gold substrate is the preferred solid surface for formation of an organic self-assembled monolayer (SAM). Device fabrication process may require the gold film to be exposed to photolithographic processing and plasma treatment prior to molecular assembly. It has been observed that oxygen plasma treatment prevents the formation of SAMs; however, subsequent treatment with an argon plasma allows assembly of the organic monolayers. To understand the mechanisms involved, a plasma containing 98% ¹⁸O was used and the film surface was analysed using the ¹⁸O(p,α)¹⁵N nuclear reaction.

Semiconductor quality silicon wafers were coated with a 200 nm thick gold layer using DC magnetron sputtering. These samples together with reference samples of clean silicon and silicon covered with aluminium were exposed to an oxygen RF plasma for 3 or 7 minutes with an RF power of 0.1 W cm⁻².

A 2.7 MV tandem accelerator was used as a source of H⁺ and He⁺⁺ ions for sample analysis. The thickness of the gold layer was measured by 2 MeV He⁺⁺ RBS. The ¹⁸O content was measured by detecting 3.42 MeV α-particles produced by 830 keV H⁺ ions. The shape of broad (30keV) resonance was measured and the energy of 830 keV with cross-section about 50 mb sr⁻¹ was chosen to optimise detection sensitivity [1]. The reaction cross-section for the energy chosen does not vary very rapidly with energy and allows a simple experiment without accurate energy calibration in contrast to the case of a narrow resonance [2]. In order to reduce the backscattered proton yield and to minimise pileup effects a thin gold layer, about 200 nm on a silicon substrate was used. This structure allowed use a proton beam current, of about 100 nA without any detectable pileup in the energy region where the oxygen signal was detected. Emitted particles were detected by a solid state surface barrier detector with a detection solid angle of 1.1 msr, positioned at 160° to the incident beam direction. Typical analysis time was about 20 min for 100 μC beam charge. A nuclear reaction spectrum for ¹⁸O plasma treated silicon sample is shown in Fig. 1. The oxygen signal is in the form of a high energy peak centred in channel 373. The data were collected using a Hypra automatic data collection system [3].

Oxygen can be detected using a deuterium beam and the ¹⁶O(d,p)¹⁷O nuclear reaction. However, high energy background is present from deuterium induced reactions in silicon substrate [4]. The relatively low proton energy used in this experiment leads to very little or no high energy background counts in the spectrum and at the same time the source of detected surface oxygen can be identified.

A typical RBS spectrum of an ¹⁸O plasma treated gold layer on a silicon substrate is shown in Fig. 2. The Hypra program [3] was also used to analyse RBS data and determine the gold layer thickness and uniformity and the presence of other heavy elements in the sample. The gold layer thickness is 204±5 nm. There is an interface adhesion layer about 20 nm thick between the gold and the silicon. The NRA spectrum from the same sample is shown in Fig. 3. The ¹⁸O signal is in

the form of a small peak in about channel 373. This peak contains only 25 counts and corresponds to about $0.73 \times 10^{15} \text{cm}^{-2}$ ^{18}O atoms, the equivalent of about 50% of a monolayer and is 20 times less than the ^{18}O detected in a clean silicon sample treated with the same ^{18}O plasma at the same time, see Fig. 1.

Table 1 compares the amounts of ^{18}O detected in the different samples. The last column in table 1 shows the total amount of oxygen on sample surface after correction for the cross contamination factor.

The observed surface oxygen concentration on gold after oxygen plasma treatment is about 50% of the theoretical surface density of gold: $1.39 \times 10^{15} \text{at cm}^{-2}$ in the $\langle 111 \rangle$ direction and can be interpreted as one oxygen atom bonded with two gold surface atoms. This bond is strong as there was no any reduction of the ^{18}O signal after storing the sample for a month and measuring again. When the oxygen plasma treatment time was reduced from 7 to 3 minutes there was minimal reduction in the oxygen signal, suggesting a saturation effect after two or three minutes of treatment.

The presence of the oxygen submonolayer significantly changes the chemical property of the gold surface preventing further sulfur chemistry and formation of a SAM. Ellipsometry used to observe the growth of SAMs on gold surfaces treated with oxygen and argon plasma [5] reveals that when the oxygen plasma treatment was followed with argon plasma treatment, the formation of SAMs was restored. The NRA shows no ^{18}O in sample treated with ^{18}O and argon plasma. This suggests that the presence of an oxygen submonolayer on the gold surface plays an inhibiting role in SAM formation.

Table 1 Detection Results for Different Samples

Sample Type	Plasma Treatment	NRA Peak Counts	Oxygen-18 $10^{15} \text{ atoms cm}^{-2}$	Total Oxygen $10^{15} \text{ atoms cm}^{-2}$
	Isotope Time (min)			
Si	18 7	503	14.65	15.46
Si	18 7	534	15.56	16.41
Si+Al	18 7	296	8.62	9.10
Si+Au	18 7	25	0.73	0.77
Si+Au	18 7	30	0.87	0.92
Si+Au	18 3	21	0.61	0.65
Si	16 7	19	0.55	16.15
Si+Al	16 7	10	0.29	8.50

References

- [1] Ion Beams for Materials Analysis, editors J.R. Bird and J.S. Williams, Academic Press 1989.
- [2] A. Barcz, A. Bienkowski, A. Turos, L. Wielunski and L.Zemlo, Nucl. Instr. and Meth. 113 (1973) 413.
- [3] Hypra RBS data collection and analysis program, Charles Evans and Associates, Redwood City, California, USA.
- [4] A. Turos, L. Wielunski and A. Barcz, Nucl. Instr. and Meth. 111 (1973) 605.
- [5] R. Netterfield, L. Wiczorek and L.S. Wielunski, to be published.

Fig 1. NRA spectrum from a pure silicon sample exposed to ^{18}O plasma treatment for 7 minutes. The ^{18}O signal is seen as a high energy peak well above the region of backscattered protons.

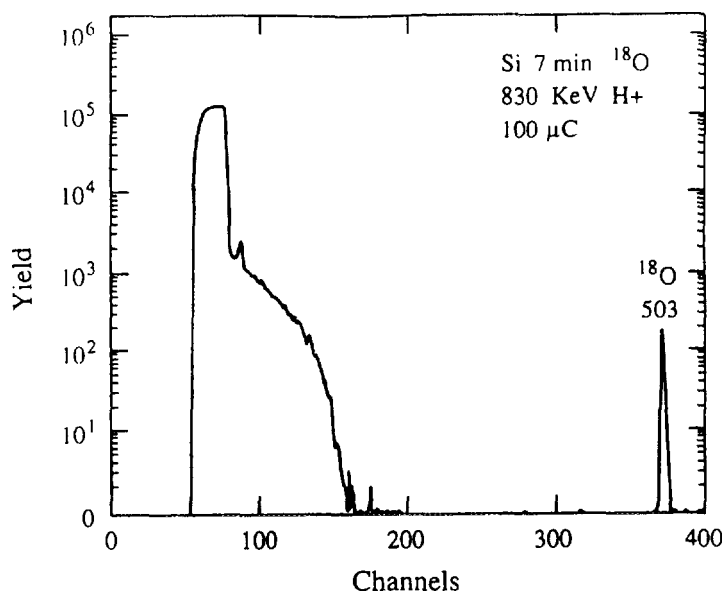


Fig 2. A 2 MeV He RBS spectrum from a 204 nm thick gold layer on silicon exposed to ^{18}O plasma treatment for 7 minutes. The small peak between gold and silicon signals corresponds to an interface adhesion layer about 20 nm thick. The theoretical spectrum generated by Hypra [3] program is also shown.

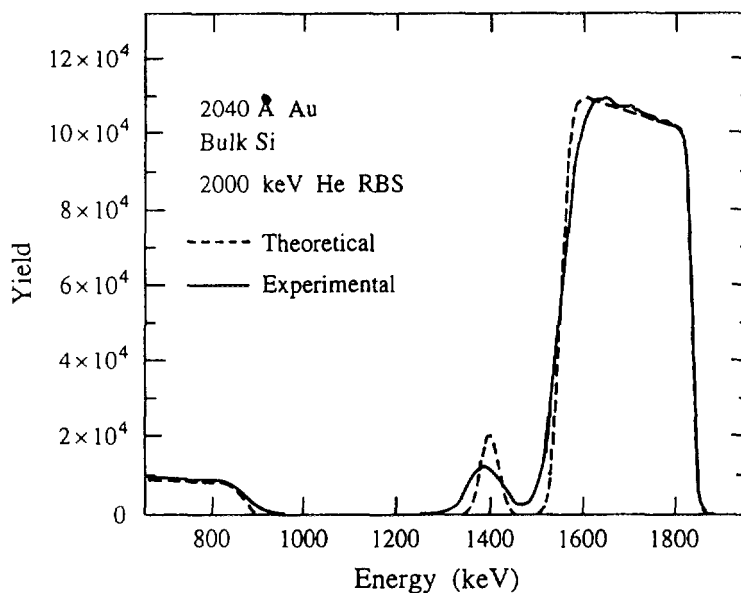
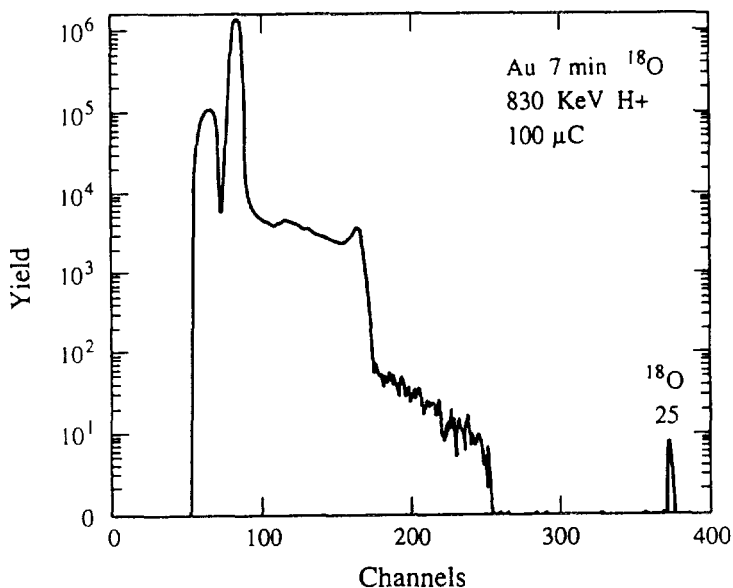


Fig 3. The NRA spectrum from the sample shown on Fig. 2. The ^{18}O signal from the oxygen submonolayer is the small peak at the high energy end of the spectrum. The backscattered protons from gold and silicon are in the low energy part of the spectrum. The two middle energy steps are backscattered proton pileups.



SOLID PHASE EPITAXY IN CERAMIC OXIDES

Dr JC McCallum
Royal Melbourne Institute of Technology

(Paper to be handed out at Conference)



RBS ANALYSIS OF ELECTROCHROMIC LAYERS

by

D.C. Green¹, M.J. Kenny², L.S. Wielunski² and J.M. Bell¹

¹ Department of Applied Physics,
University of Technology, Sydney, P.O. Box 123, Broadway, 2007

² Division of Applied Physics,
CSIRO, P.O. Box 218, Lindfield, NSW, 2070

Tungsten oxide thin films produced by dip-coating from tungsten alkoxide solutions are of interest for their application in large area switchable windows. The application consists of a layer of electrochromic tungsten oxide (WO_3) on indium tin oxide (ITO) coated glass in contact with a complementary structure. Electrochromic devices are switchable between states of high and low transparency by the application of a small voltage. The mechanism relies on the dual injection of ions and electrons into the WO_3 layer from adjacent layers in the device.

Electrochromic tungsten oxide can be deposited using standard techniques (eg. sputtering and evaporation) but also using sol-gel deposition. Sol-gel processing has an advantage over conventional preparation techniques because of the simplicity of the equipment. The scaling up to large area coatings is also feasible.

Sol-gel processing involves dipping a substrate in a precursor solution and withdrawing it again at a constant rate. The film then forms on the substrate as the solvent evaporates and hydrolysis and polymerisation of the tungsten alkoxide occurs. The sample is usually fired at 200-300°C to assist the formation of a tungsten oxide network. There is the possibility with sol-gel processing of hydrocarbon by-products remaining trapped within the film. Such hydrocarbon does not appear to seriously affect the electrochromic performance of the films¹. The optical properties of the coatings will depend on the tungsten:oxygen stoichiometry. Moisture affects the depth of coloration and the stability of the films under repeated cycling.

Ion beam analysis is ideal for determining elemental composition and depth profiles in these film structures. Rutherford Backscattering Spectroscopy (RBS) of 2MeV helium ions has been used on samples produced under a range of sol-gel processing conditions. By using standard analysis software, profiles for individual elements in the structures have been obtained. It is possible to profile heavy elements (tungsten, indium and tin). Reasonable estimates for light elements such as carbon and oxygen can also be deduced.

There are two features of the RBS spectra which have been observed. The first is the apparent weakness of the tungsten peaks relative to that expected for the stoichiometric oxide. (see figure 1). This suggests that sol-gel samples contain a substantial level of a lighter element, such as carbon. Auger electron spectroscopy supports the presence of carbon in the films. In previous work² a composition of $\text{C}_{0.11}\text{W}_{0.22}\text{O}_{0.67}$ gave good agreement with the measured spectrum. The residual carbon can be burnt out by firing at higher than usual temperatures (ie. $\geq 300^\circ\text{C}$). The decreased carbon content can be seen in the increased strength of the tungsten feature in

the RBS spectra. Figure 2(a) compares the measured spectra for films fired at 250°C and 550°C. A densification of the film is also evidenced in the width of the tungsten feature.

Hydrogen present in the samples has been probed using forward recoil induced by the 2MeV helium ions. The hydrogen has two potential origins, adsorbed atmospheric water and hydrocarbon by-products. Film surface morphology will greatly affect both. The measured spectra for low and high temperature firing samples are shown in Figure 2(b). The decrease in yield in the high temperature film can be attributed to hydrocarbon burnoff with the remainder due to surface water. The hydrogen content has been reduced by a factor of 3.6.

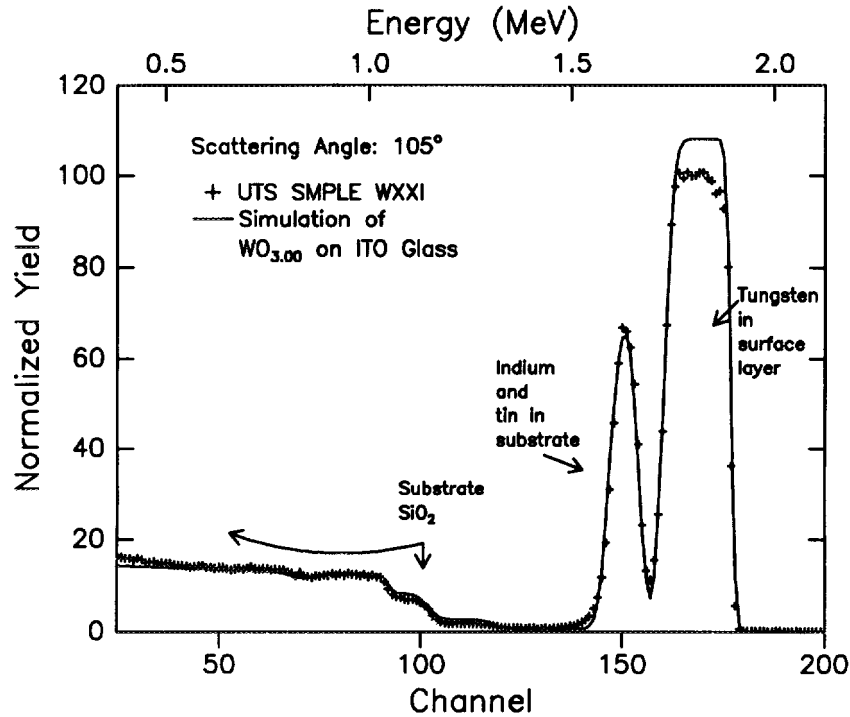


Figure 1: Comparison of a simulated spectrum for tungsten oxide ($\text{WO}_{3.00}$) on indium tin oxide coated glass³ with the RBS spectrum for sol-gel deposited tungsten oxide.

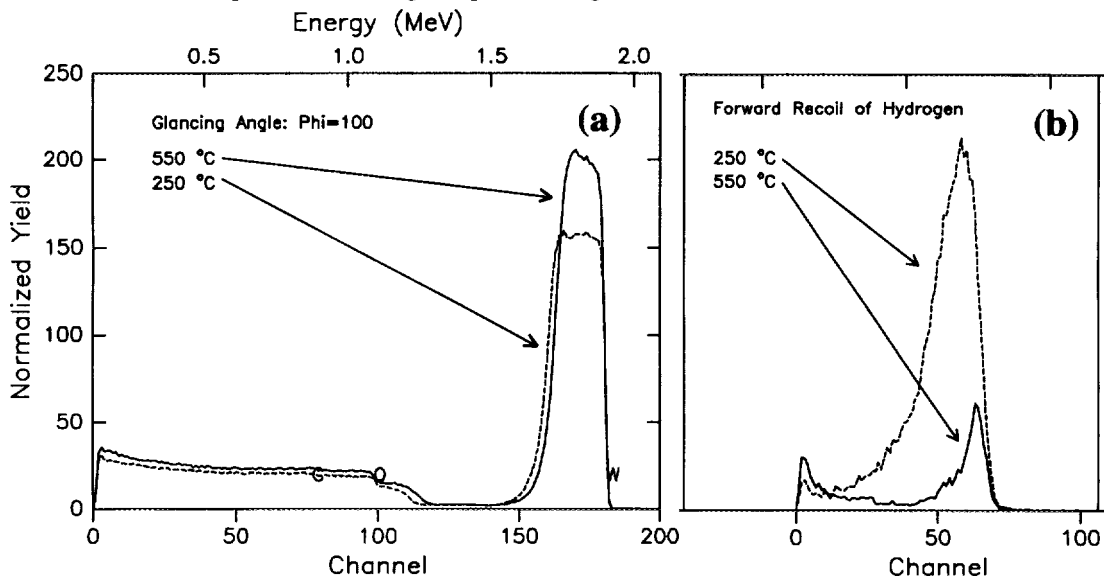


Figure 2: (a) RBS spectra for sol-gel coatings on quartz substrates showing the affect of firing treatment. (b) Hydrogen forward recoil spectra for the same samples as appear in (a).

The second feature of some of the RBS spectra has been a considerable variation in the apparent tungsten stoichiometry with depth. To acquire adequate thickness, the substrates are dipped a total of five times and fired after the second, fourth and fifth coats. Figure 3 shows a depth dependent feature for tungsten which mirrors this 2 coats, 2 coats, 1 coat structure.

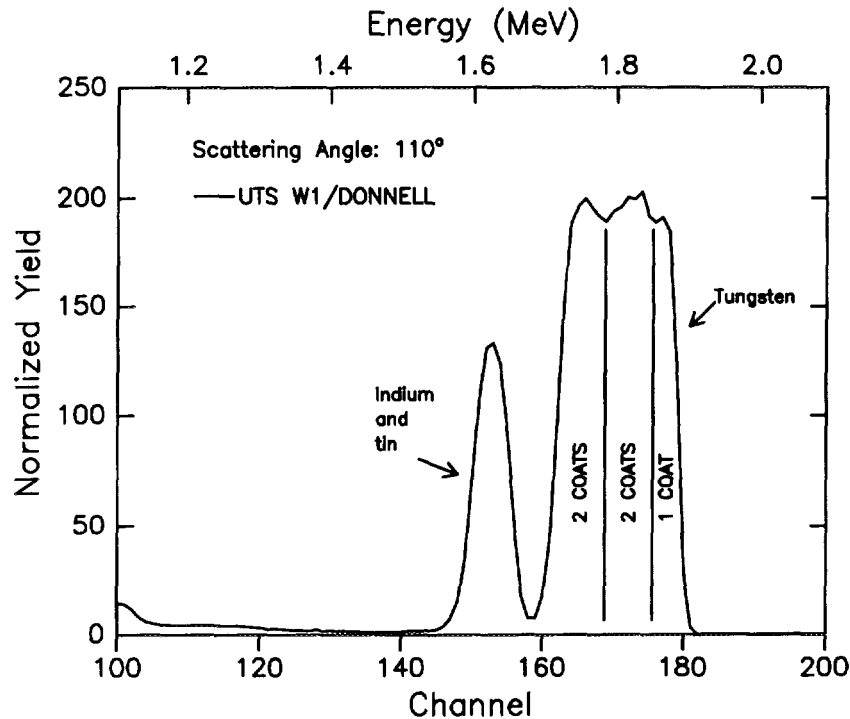


Figure 3: A typical nonuniform tungsten feature in the RBS spectrum of a sol-gel deposited film on ITO.

A structural interpretation of this effect can be made that is consistent with the location of the local minima of tungsten counts. The film surface which is presented to the precursor solution after firing is very porous. This surface absorbs and traps a quantity of the alkoxide from the solution. With a double unfired layer on top, the diffusion of this hydrocarbon is impaired to the point where some remains in the region around the top of the last fired layer.

RBS and forward recoil provide convenient methods of analysing the structure of electrochromic films. The techniques are useful adjuncts to routine analyses. The carbon residue present in sol-gel films fired to low temperatures is confirmed. Sublayer structures within the sol-gel tungsten oxide layers are observed under certain firing conditions.

- 1 J.M. Bell, G.B. Smith, D.C. Green, J. Barczynska, L. Evans, K.A. MacDonald, G. Voekl, B.O. West & L. Spiccia "Assessment of electrochromic devices based on sol-gel deposited films", S.P.I.E. Conference Proc. 2017, to appear, (1993)
- 2 D.C. Green, M.J. Kenny, C.J. Fell, J.M. Bell & L.S. Wielunski, "RBS Analysis Of Electrochromic WO₃/ITO Layers", presented at the AINSE 7th NTA Conference, Melbourne, November 1991, page 52
- 3 Donnelly Corp., Holland, Michigan, USA, PD5005, Resistivity of 75Ω/□.



Selective Rutherford Backscattering Techniques in the Study of Transition-Metal Implanted $\text{YBa}_2\text{Cu}_3\text{O}_{7-\delta}$

Jarrod W. Martin and Greame J. Russell.

School of Physics, University of New South Wales, Kensington, Sydney.

David D. Cohen and Peter J. Evans.

Australian Nuclear Science and Technology Organisation, Lucas Heights, Sydney.

The implantation of ions into solids has been long recognised as a method by which the chemical and structural properties of a sample can be altered in a controlled fashion. Studies of such alterations can contribute significantly to possible applications of these modified solids as well as provide a better understanding of their properties. The application to the field of high T_c superconductors has been present ever since the discovery of the new oxides.

Using a metal-vapour vacuum arc (MEVVA) ion source, several as-grown, large, high quality, single crystal $\text{YBa}_2\text{Cu}_3\text{O}_{7-\delta}$ ($\delta > 0.7$) were implanted with a dose of $\sim 1 \times 10^{17}$ ions. The species implanted included zinc, nickel and iron with those reported here being the latter two. After implantation the crystal was subjected to two anneal cycles, one of 60 hours duration and another for a further 48 hours, with both at 550°C in a flowing oxygen atmosphere. The two separate anneal cycles allowed us to examine crystal structure, superconducting transitions and composition, through X-ray diffraction (XRD), Rutherford Backscattering Spectroscopy (RBS) and A.C. susceptibility measurements respectively.

The application of RBS using a 3 MV Van de Graaff particle accelerator for the non-destructive depth profiling of high Z elements is ideally suited to the determination of cation stoichiometry for the samples studied here. Figure 1 shows the RBS spectra for 2.0 MeV normally incident $^4\text{He}^+$ on the nickel implanted crystal at several stages throughout the crystal modification. The nickel is clearly visible immediately after implantation, with the depth of maximum concentration being found at $300 \pm 100\text{\AA}$. Following the initial 60 hour anneal cycle the nickel had diffused some what through the surface of the crystal, with a calculated depth of $500 \pm 150\text{\AA}$. After a further 48 hours at 550°C RBS is not sensitive enough to detect a nickel edge.

The advantages of 2.0 MeV RBS are clearly evident when examining the cation concentrations for Y, Ba and Cu in the surface and near surface region. For the Ba, Y, and to some extent, the Cu edge, show changes after implantation and the subsequent annealing cycles. These changes represent structural modifications in the surface and near surface region of the crystal. In each case the cation stoichiometry in this region was well below the 1:2:3 ratio expected for a superconducting sample of this nature, but was unchanged for the crystal bulk. The addition of nickel through a sintered power growth method

has been reported to be deleterious to the 92°K transition temperature. This is contrary to the results we have found where a 83°K transition temperature after the 60 hour anneal cycle and 92°K after 108 hours, though this transition temperature is for the surface region, and we add that the crystal bulk was still not fully oxygenated.

In the case of the iron implant the RBS spectra, shown in figure 2, have similar features. The notable difference being the existence of an iron peak after a total of 108 hours at 550°C. The lack of diffusion of the iron throughout the surface suggests that the iron is bonding within the lattice. This was confirmed with X-ray photoelectron spectroscopy (XPS) which showed the existence of iron oxide to a depth of 1200Å. Whereas the nickel implant improved the rate of oxygenation of the crystal, at least in the surface and near surface region, the iron implant was deleterious to the 92°K transition, with a transition temperature of only 76°K obtained after the same anneal times.

The oxygen content of YBCO, and indeed many other superconductors plays an important role in the superconducting transition temperatures obtainable. For YBCO, a difference in the oxygen content of 0.7 can mean the difference between a 92°K transition and a non-superconductor. Although RBS discriminates strongly against light elements in a heavy substrate, such as oxygen in the YBCO lattice, the use of the resonant reaction $^{16}\text{O}(\alpha, \alpha)^{16}\text{O}$ at 3.04 MeV is very beneficial, as its cross section is nearly 23 times that of the rutherford cross section. Other advantages of using higher energies are the better mass resolution obtained, though the trade off is poorer depth resolution.

For a fully oxygenated crystal and the iron implanted crystal after the two anneal cycles, the $^{16}\text{O}(\alpha, \alpha)^{16}\text{O}$ resonant reaction was performed with the resulting spectra shown in figures 3 and 4 respectively. The resonance has a width of 10 keV, which constitutes a depth sensitive technique. Both the spectra were obtained at an energy of 3.07 MeV to ensure that the resonance was below the surface, and energy calibration using aluminium oxide standards. For greater depth information of the oxygen content of these crystals, higher energy helium beams are required which are above the operating voltage of the accelerator used.

By using different variations of the RBS technique, it is possible to obtain a range of information from the one sample. The use of RBS has the added advantage of being a non-destructive depth profiling technique and is ideally suited the the analysis of high T_c superconductors. Moreover, the use strategically selected resonant reactions overcome the lack of signal from light elements in a heavy substrates, as shown in this paper.

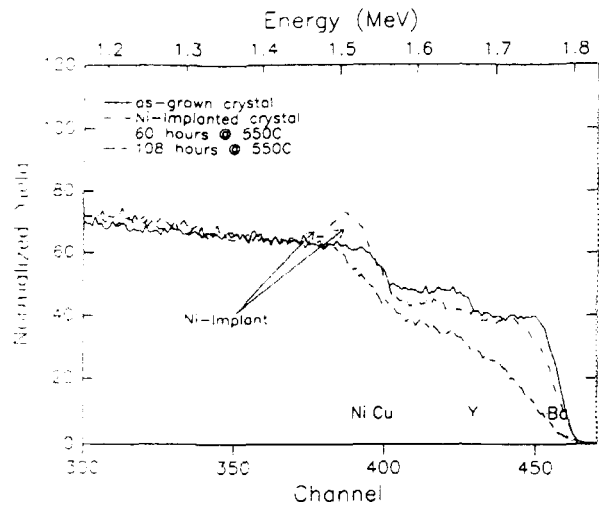


Fig. 1 2.0 MeV RBS spectra for a Ni-Implanted YBCO single crystal.

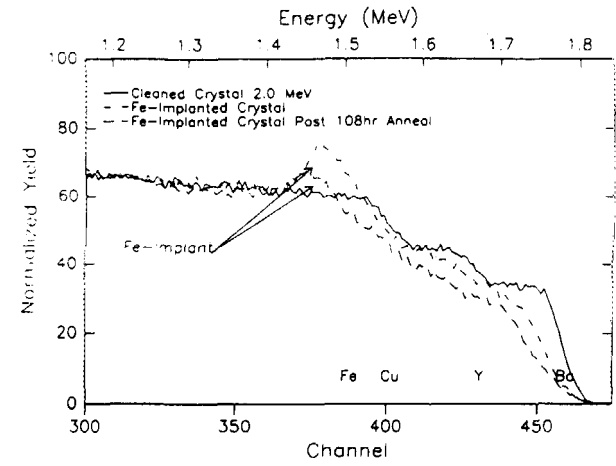


Fig. 2 2.0 MeV RBS spectra for an Fe-Implanted YBCO single crystal.

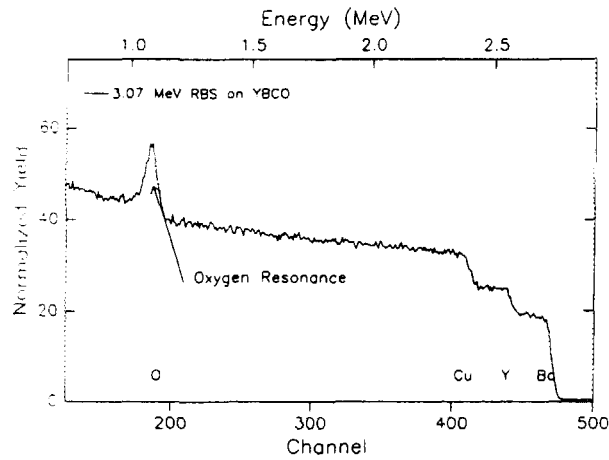


Fig. 3 3.07 MeV RBS Spectrum showing the oxygen resonance.

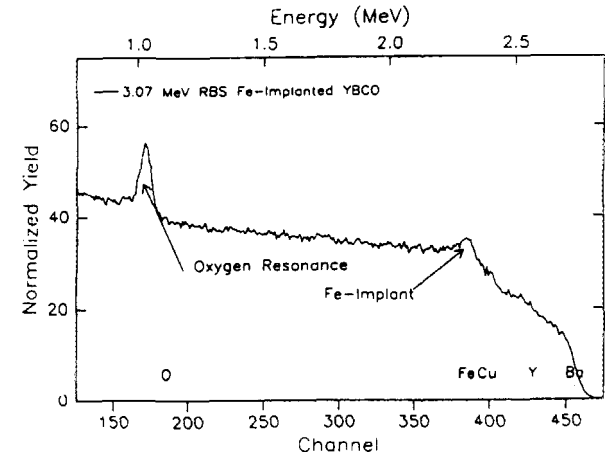


Fig. 4 3.07 MeV RBS spectrum of an Fe-Implanted YBCO single crystal.



ION BEAM MODIFICATION OF THERMAL SHOCK RESISTANCE CHARACTERISTICS OF BRITTLE MATERIALS

V. N. Gurarie, *School of Physics, University of Melbourne, Parkville, VIC, 3052, Australia. Fax. (61 3) 3474783.*

J. S. Williams, *Microelectronics and Materials Technology Centre, RMIT, Melbourne 3001, and Department of Electronic Materials, Engineering Research School of Physical Sciences, ANU, Canberra, 2600, Australia. Fax. (61 062) 490511.*

Monocrystals of sapphire, magnesia and lithium fluoride, together with glass samples have been subjected to ion implantation with Ar^+ and Si^+ ions at variable doses, prior to exposure to thermal shock testing in a plasma. Measurements of the depth of plastic flow penetration have been used to estimate the surface temperature [1]. Fracture and deformation characteristics of the surface layer are measured in ion implanted and unimplanted samples subjected to a wide range of thermal shock intensity.

Ion implantation is shown to substantially alter the response of the material to thermal shock loading. The comparison of fracture patterns, produced by thermal shock in both ion implanted and unimplanted crystals, generally indicates the appearance of much higher crack density in the surface layers of ion implanted crystals. Ion implantation is also shown to shift the fracture threshold temperature and the maximum crack density towards a lower temperature range. The observed effects are considered to be due to lattice damage, an increase in the density of crack initiating flaws and lowering of the fracture stress and the brittle-ductile transition temperature. Compressive stresses, caused by ion implantation in near-surface layer, also appear to play a role in changing the thermal stress resistance of ceramic materials.

The degree of damage following thermal shock, characterised by the average depth of crack propagation, is shown to be lower in the ion implanted areas. This effect obviously results from an increased density of microcracks, which is known to lead to major improvements in thermal shock resistance of brittle materials [2,3]. The thermal stress damage resistance parameter is investigated experimentally over a wide range of heat flux. These results suggest that the stress resistance parameters and fracture characteristics of ceramic materials exposed to thermal shock loading can be effectively controlled by ion implantation.

1. V.N. Gurarie and J.S. Williams, "Thermal Shock -Induced Fracture of Ion Implanted LiF Crystals". *J. of Mater. Res.*, v.5, No.6, pp. 1257-1265, 1990.
2. D.P.H. Hasselman, "Thermal Stress Resistance of Engineering Ceramics". *Materials Science and Engineering*, v.71, pp.251-264, 1985.
3. D.P.H. Hasselman and J.P. Singh, "Analysis of Thermal Stress Resistance of Microcracked Brittle Materials". *Am. Cer. Soc. Bull.*, v.58, No.9, pp. 856-860, 1979.



DETERMINATION OF FLOW RATES OF OIL, WATER AND GAS IN PIPELINES

G.J. Roach, J.S. Watt and H.W. Zastawny
CSIRO Division of Mineral and Process Engineering, Lucas Heights

INTRODUCTION

The extraction of fluid hydrocarbons from their geological reservoirs involves the piping of multiphase mixtures of crude oil, (salt) water and gas from each well. Knowledge of the flow rates of each component, in each well pipeline feeding to the production platform, is required to control production. Current practice is to feed sequentially the outputs from each well to a common test separator, and to measure the flow rates of each (single phase) component after separation. The time to determine the flow rates for each well is many hours, and the determination can also be unrepresentative because the flow rate is sampled for only a small part of the production time of a well.

The oil industry requires a multiphase flow meter (MFM) which is compact, measures the flow rates continuously, and can be mounted directly onto each well pipeline. Use of such a meter should lead to

- a) the replacement of the need for test separators, initially in non-critical applications and later, after the MFM technology has been proved to be dependable, in most new offshore platforms,
- b) the reduction in the cost of subsea piping because the outputs of two or more wells can be commingled and flow through a single flowline from satellite platform to central facility,
- c) the reduction in capital costs of new platforms because the heavy test separator can be replaced by the light MFM,
- d) better reservoir management, production allocation, and optimisation of total oil production over the field lifetime.

This paper describes a multiphase flow meter developed by CSIRO for determining of the flow rates of oil, water and gas in high pressure pipelines, and the results of a trial of this flow meter on an offshore oil platform.

DETERMINATION OF FLOW RATES

Two gamma-ray transmission gauges are mounted about a pipeline carrying the full flow of oil, water and gas (Fig. 1). The flow rates are determined by combining

- * single energy gamma-ray transmission measurements which determine the mass per unit area of fluids in the gamma-ray beam as a function of time,
- * dual energy gamma-ray transmission (DUET) which determine the approximate mass fraction of oil in the liquids,
- * cross-correlation of gamma-ray transmission measurements, with one gauge upstream of the other, which determines flow velocity,
- * pressure and temperature measurements, and
- * knowledge of the specific gravities of oil and (salt) water, and solubility of the gas in the liquids, all as a function of pressure and temperature.

The measurements are first used to identify the flow regime. They are then combined in models of the identified flow regime to give the flow rates of each component. Computer programs process the measurements to give the flow rates of oil, water and gas.

PLATFORM TRIAL

A full scale trial of the MFM was undertaken on the Vicksburg platform during February and March, 1992. This platform, on the Northwest Shelf offshore from Onslow, West Australia, is an oil production platform operated by Western Mining Corporation. The wells drain a thin layer of oil about 1500 metres below the sea bed.

The gauges were mounted on both vertical and horizontal sections of a 74 mm bore test pipeline carrying the oil/water/gas mixtures from the test manifold to the test separator. The flows from each of the nine separate wells feeding the platform, and combinations of these well flows, were sequentially routed through this pipeline, thus achieving a wide range of flow conditions. The flow rates determined by the MFM were compared with the flow rates determined by the single phase flow meters which monitor the outputs of the separator.

Fig. 2 shows the time variation of the mass per unit area of fluids in the gamma-ray beam in the vertical section of the test pipeline, taken from the measurement records of two separate wells. The fairly regular slugging behaviour (left) is typical of flows from wells close to the platform. The frequency and length of the slugs vary from well to well, and also depend on the pipeline pressure. The plot (right) shows the highly irregular record caused by terrain slugs which develop in the subsea flowline between the well head and the platform for wells distant from the platform.

The velocities of the liquid flows were determined every 17 seconds by cross-correlation of the outputs of the two gauges. The velocities corresponding to different individual, and combined, wells covered the range of 3.5 to 13 m s⁻¹. For wells close to the platform, the velocities varied little with time over the total measurement period of 40 minutes, the standard deviation being about 5 to 10% relative. For wells far from the platform, the variations in velocity were much greater, the standard deviation being in the range of about 20 to 40% relative. This wider range of velocities is a true measure of the large variations of flow which occur over the 40 minute period, due to the terrain slugging.

The results of determinations of the flow rates of oil and gas in the vertical pipe are shown in Fig. 3. Each point corresponds to the flow rate averaged over a forty minute period. Each flow rate was measured twice, in consecutive forty minute periods, and results for both periods are shown as separate points on the graphs.

R.m.s. differences were calculated by least squares regression of flow rates of oil, water and gas as determined by the gamma-ray transmission gauges and by the relevant separator output meter. The ratios of r.m.s. difference and mean flow rate, expressed in per cent, were 8.9% for oil, 5.6% for water, 8.2% for gas, and 5.2% for total liquids for measurements on the vertical pipe, and somewhat larger for measurements on the horizontal pipe.

The accuracies of determination of the flow rates of oil, water and gas on the Vicksburg platform are sufficient for many potential applications of the MFM on offshore platforms. CSIRO is currently undertaking a further field trial to prove the gamma-ray transmission MFM at WAPET's oil production facilities on Thevenard Island, North West Shelf. A MFM based on microwave phase shift and gamma-ray transmission will also be trialled. CSIRO has licensed Mineral Control Instrumentation Ltd. to manufacture the commercial MFM. CSIRO and MCI plan to prove jointly the commercial prototype in a long term trial in 1994.

Acknowledgments: The authors wish to thank our sponsors ERDC, The Shell Company of Australia Ltd., West Australian Petroleum Pty. Ltd. (WAPET) and Western Mining Corporation for financial support in part for this project.

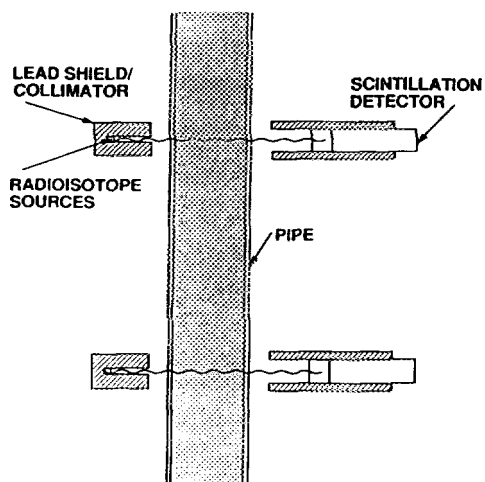


Fig. 1 (left). Gamma-ray transmission gauges mounted about pipeline.

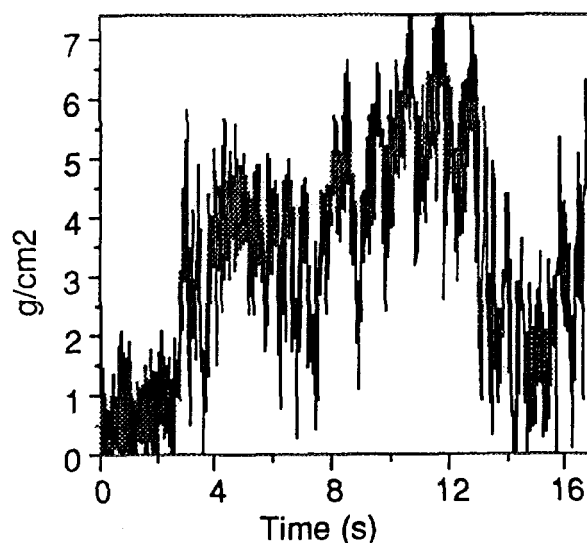
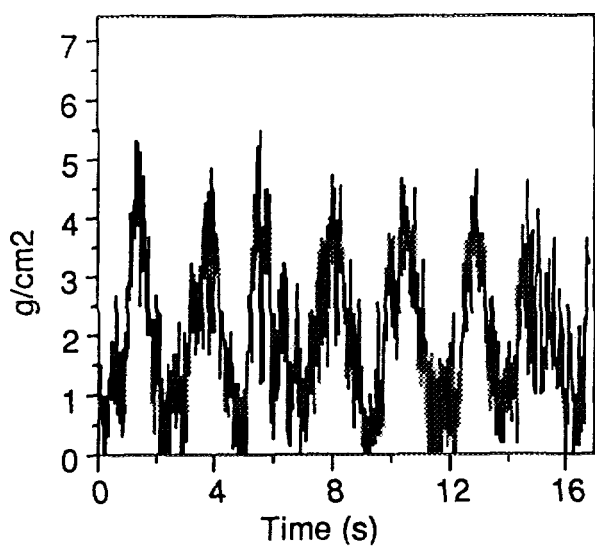


Fig. 2. Variations in mass per unit area of liquids with time.

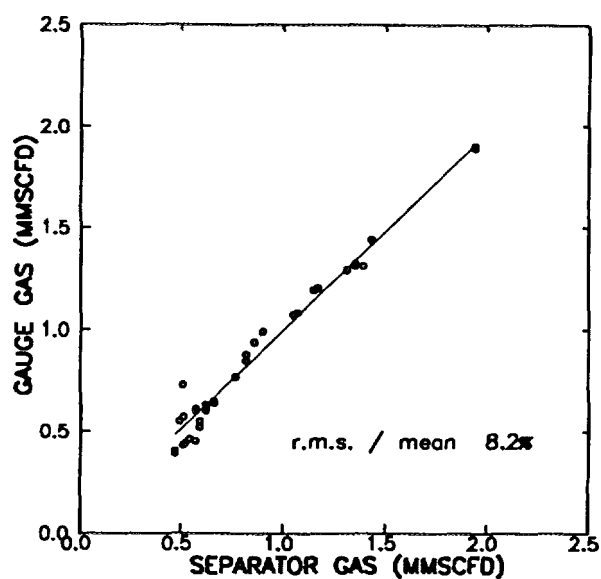
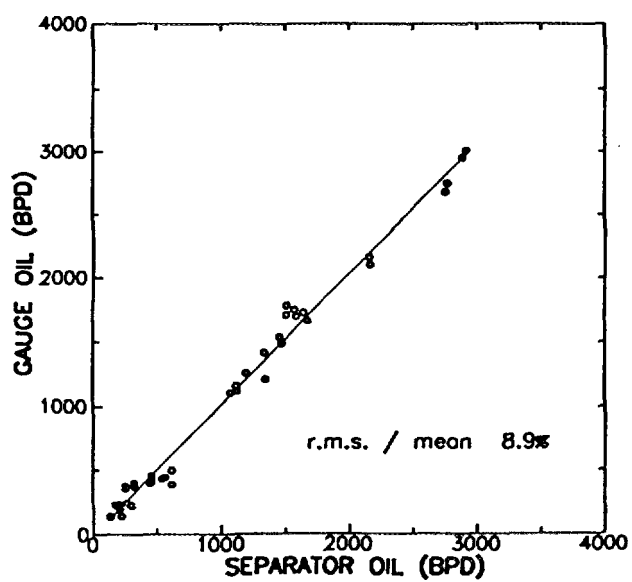


Fig. 3. Gauge and separator output determinations of the flow rates of oil and gas.

Advances of the IBIC technique

M B H Breese, J S Laird and D N Jamieson

Physics Department, University of Melbourne, Parkville, Victoria 3052, Australia

Abstract

The ion beam induced charge (IBIC) technique has been used for a wide variety of analytical applications in the study of semiconductor materials. This paper briefly reviews these uses and identifies those areas which require further development in order to facilitate the more widespread use of the IBIC method. Progress towards implementing these improvements is discussed.

Ionising radiation such as MeV light ions, keV electrons or laser light can create mobile carriers in semiconductor material by transferring enough energy to the sample to move valence electrons to the conduction band, leaving behind a positively charged hole. The average energy needed to create this electron-hole pair does not depend on the type of ionising radiation and is constant for a given material. The IBIC method measures the number of carriers created by a focused MeV light ion beam as a function of beam position on the sample surface, and it has recently been developed to image the depletion regions of microelectronic devices (1-3), and as a method of identifying the irradiated device area in conjunction with the single event upset (SEU) imaging technique (4-6) and interpreting the observed SEU image contrast. It has also been used to image variations in the charge collection efficiency of semiconductor pad detectors (7), to image buried dislocation networks in semiconductor material (8), and as a method of imaging the beam halo around a focused MeV ion beam spot (9). The main advantages of IBIC over other beam induced current techniques such as EBIC, which uses a keV electron beam, and OBIC which uses a laser beam are its larger analytical depth and lower scattering through the surface layers, enabling a higher spatial resolution in buried layers. Another degree of flexibility which arises using IBIC is the choice of different ions, as discussed below.

Two current problems with IBIC are the small measured charge pulses which give a low signal to noise ratio, and ion induced damage which limits the maximum ion dose which can be used to form an IBIC image. This results in statistically 'noisy' IBIC images. A method of partially compensating for the effects of ion induced damage such that a larger ion dose could be used to generate an IBIC image is described in (12). Recent theoretical work (13) has quantified the measured charge pulse height so that the measured charge pulse height can be interpreted, and the signal to noise level optimised. The charge pulse height has been calculated as a function of diffusion length, proton and α particle energy, surface and depletion layer thickness, ion channeling and ion induced damage. It was shown that a larger charge pulse is measured for an incident α particle than with protons, which results in a higher signal to noise level, allowing smaller contrast variations to be resolved from the noise level. It was also calculated that the measured charge pulse height decreases more rapidly for incident α particles than with protons because they introduce more defects close to the surface which decrease the diffusion length of the substrate. It was calculated that in a microcircuit device with a typical diffusion length of 1-10 μ m, the charge pulse height changes rapidly as

a function of surface and depletion layer thickness with α particles and only slowly for protons. It was predicted that for a microcircuit device structure where there is a lot of topographical variation, the IBIC image contrast will be sensitive to topography with α particles but not with protons.

It was experimentally verified that the problem of the low measured signal to noise level can be solved by the use of α particles instead of protons (14), and also that the measured charge pulse height decreased more slowly with α particles than with protons, which was contrary to the predicted variation (13). The postulated explanation for this was that the 1.8 MeV α particles were stopped within the depletion region of the device and so charge diffusion did not significantly contribute to the measured charge pulse height, whereas for incident 2 MeV protons, the major component of the measured charge pulse height is from diffusion of charge carriers from beneath the depletion region. Carriers generated in the depletion region are less affected by ion induced damage than carriers diffusing to it from the substrate because the electric field in the depletion region decreases the probability of carrier recombination there.

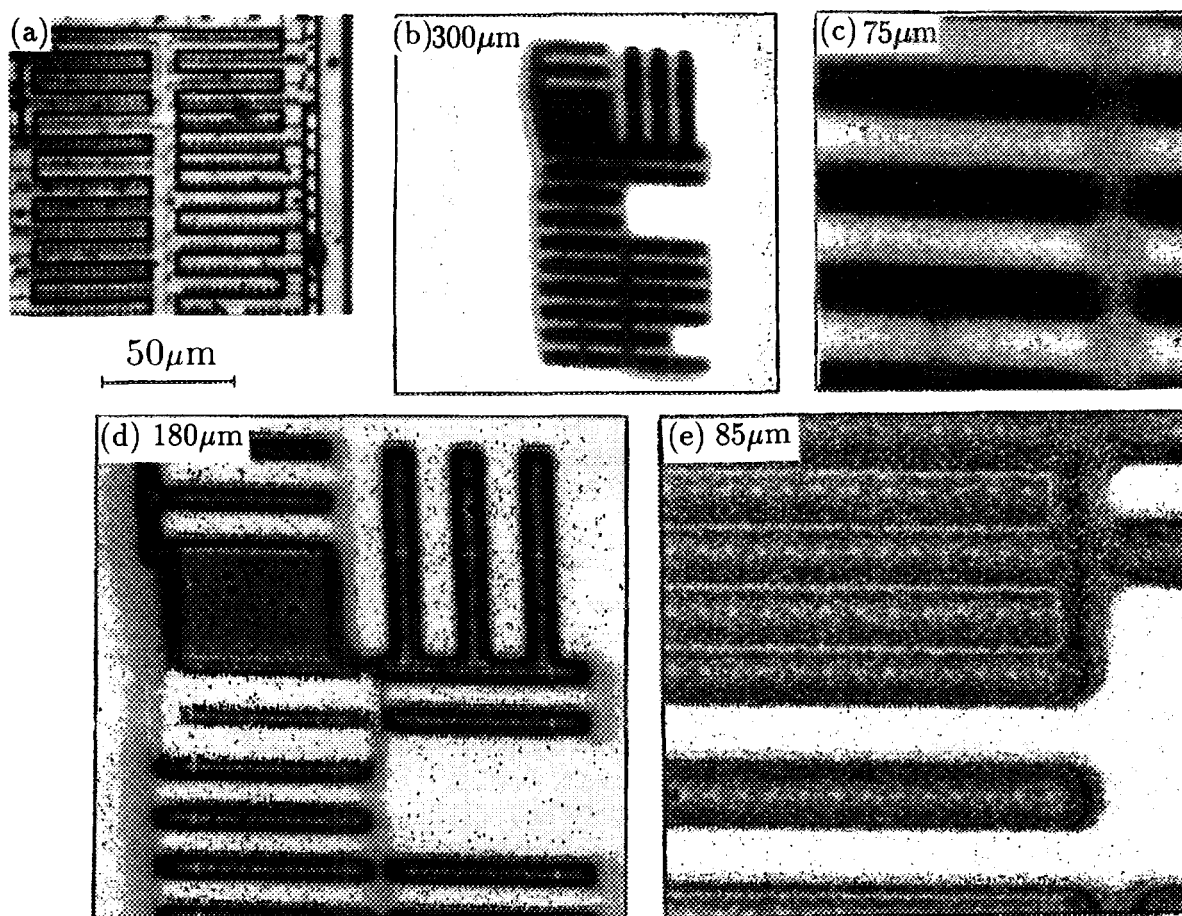


Figure 1. (a) optical micrograph. (b,c) proton induced IBIC images, (d,e) α particle induced IBIC images of similar areas.

The advantages of using α particles over protons is now further discussed. Figure 1a shows an optical image of the device studied here and also four IBIC images of

similar areas. The optical image shows the topography of the device surface layers and the small holes along the length of the interdigitated 'fingers' are contacts from the overlying aluminium metallisation to the device substrate, and these represent regions of thinner surface layer coverage. Figure 1b,c show two IBIC images generated using 2 MeV protons with different scan sizes, and figure 1d,e show two IBIC images generated using 2.3 MeV α particles, with different scan sizes. In all these IBIC images, dark represents a large measured charge pulse height and light represents a low measured charge pulse height. The dark regions show the locations of the underlying pn junctions of the device and the lighter regions show the effects of charge diffusion into the pn junctions. The signal to noise level in the proton induced IBIC images was $\sim 5 : 1$ whereas in the α particle induced IBIC images it was $\sim 40 : 1$, which represents a significant improvement. The IBIC images generated using protons shows no topographical contrast, whereas the IBIC images generated using α particles shows strong contrast due to the device topography. In these images the resultant contrast is due to both topography and the distribution of the underlying depletion regions. In particular the small holes along the interdigitated fingers can be clearly seen using α particles, and closer examination shows that extremely small variations in the topography can be detected in this image, which are not detectable in the proton induced images.

This work demonstrates the features of using protons or α particles for IBIC analysis. With protons there is typically a low signal to noise level and the image contrast is independent of device topography, whereas with α particles there is a higher signal to noise level and the image contrast depends strongly on the topography. Compensation routines for the effects of proton and α particle induced damage on the IBIC image contrast are currently being developed in order to use a higher ion dose to generate IBIC images.

References

- (1). M B H Breese, G W Grime and F Watt, Oxford Nuclear Physics report OUNP-91-33 (1991)
M B H Breese, P J C King, G W Grime and F Watt, *J. Appl. Phys.* **72**(6) (1992) 2097
- (2). M B H Breese, G W Grime and F Watt, *Nucl. Instrum. and Meth.* **B77** (1993) 301
- (3). M B H Breese, G W Grime and F Watt and R J Blaikie, *Vacuum* **44** (1993) 175
- (4). K M Horn, B L Doyle, D S Walsh and F W Sexton, *Scanning Microscopy* **5** (1992) 969
- (5). K M Horn, B L Doyle, F W Sexton, J S Laird, A Saint, M Cholewa and G J F Legge, *Nucl. Instrum. and Meth.* **B77** (1993) 355
- (6). F W Sexton, K M Horn, B L Doyle, J S Laird, M Cholewa, A Saint and G J F Legge, *Nucl. Instrum. and Meth.* **B79** (1993) 436
- (7). R A Bardos, G F Moorhead, G N Taylor, J S Laird and A Saint, *submitted to Nucl. Instrum. and Meth. B* (1993)
- (8). M B H Breese, P J C King, G W Grime and P R Wilshaw, *Appl. Phys. Lett.* **62** (1993) 3309
- (9). M B H Breese, G W Grime and F Watt, *Nucl. Instrum. and Meth.* **B77** (1993) 243
- (10). H J Leamy, *J. Appl. Phys.* **53** (1982) R51
- (11). C J R Sheppard, *Scanning Microscopy* **3** (1989) 15
- (12). M B H Breese, G W Grime and M Dellith, *Nucl. Instrum. and Meth.* **B77** (1993) 332
- (13). M B H Breese, *J. Appl. Phys* **74**(6), 15th Sept (1993)
- (14). M B H Breese, C H Sow and D N Jamieson, *submitted to Nucl. Instrum. and Meth.* (1993)



A New Method for True Quantitative Elemental Imaging using PIXE and the Proton Microprobe

C.G. Ryan¹, D.N. Jamieson², C.L. Churms³ and J.V. Pilcher³

- ¹ CSIRO Division of Exploration and Mining, North Ryde.
- ² Microanalytical Research Centre, School of Physics, University of Melbourne.
- ³ National Accelerator Centre (NAC), Faure, South Africa.

Introduction

Traditional methods for X-ray imaging using PIXE and the Proton Microprobe have used a simple gate set on an X-ray peak in a spectrum from a Si(Li) detector to provide an image of the distribution of an element. This method can produce artefacts in images, due to overlapping X-ray lines from interfering elements, charge collection tails on peaks, background variation, Si escape peaks and pileup, all of which can render images misleading or qualitative at best. To address this problem, a matrix transform method has been developed at the CSIRO which not only eliminates most artefacts, but can be implemented on-line. The method has been applied to study trace gold distribution in a complex gold bearing ore from Fiji [1], and more recently has been installed for direct on-line elemental imaging at the NAC in South Africa [2].

The Dynamic Analysis Method

Decomposition of a PIXE spectrum into contributions from component elements commonly uses a non-linear least-squares fitting approach. If the non-linear parameters have been determined, for example by prior non-linear iterations, then the remaining linear parameters a_k , representing major-line peak-areas and background intensity, can be found by solving the matrix equation $\alpha a = \beta S$ where α and β are matrices in terms of the partial derivatives $\partial f_i / \partial a_k$ (f_i is the fitting function at channel i), and S is the spectrum vector (see ref. [1]). The peak-areas a_k are related to element concentration C_k by the equation $a_k = Q\Omega\epsilon_k T_k Y_k C_k$ in terms of the integrated charge Q , detector solid-angle and efficiency Ω and ϵ_k , X-ray absorber attenuation T_k and generic X-ray yield Y_k [3]. Hence, the solution of the linear least-squares problem can be cast as a matrix equation which transforms directly from spectrum vector S to concentration vector C [1]

$$C = Q^{-1} \Gamma S \quad (1)$$

in terms of the matrix Γ (where $\Gamma_{ki} = (Q\Omega\epsilon_k T_k Y_k)^{-1} [\alpha^{-1}\beta]_{ki}$), which is independent of C and can therefore be precalculated. In the GeoPIXE analysis software package the Γ matrix can be calculated using the least-squares fit program PIXE_FIT, which includes a complete set of X-ray lines for each element, detection artefacts (tails, pileup and Si escape peaks), and an iterative approximation to the background. Because of its origins in the least-squares fit, this transformation resolves complex element line-shape overlaps, and subtracts background, in the same way as the least-squares fit to a PIXE spectrum.

While equation (1) permits rapid spectrum analysis [4], the most exciting application of equation (1) is its use for elemental imaging. Note that if the spectrum vector is replaced by a vector with just a single count in channel e , then the resultant concentration vector represents the set of increments to make to all element concentrations for one count at that channel. Therefore, if the beam is positioned at point x,y in a raster scan, this concentration vector is the set of increments to make to all elemental images at pixel x,y [1]. Hence, equation (1) provides a very simple method of generating elemental distribution images with three very important properties: (i) The images are quantitative; each pixel contains a value representing concentration times integrated charge. (ii) The images are inherently element overlap-resolved and background-subtracted. (iii) The images are formed directly on-line as the data accumulate.

Worked Example

Consider the overlap of Cr, Mn and Fe K lines in a very simple spectrum of only 6

ghosts. Only the Dynamic Analysis images portray realistic distributions of all elements.

Discussion and Conclusions

The Ca-Sc overlap problem observed in the example shown above is analogous to many situations encountered in Proton Microprobe applications in geology. In biological and medical applications it is common to observe K-Ca overlap. In this case Ca images can display marked features due entirely to K if a simple gate is set on Ca K_{α} . If the Ca K_{β} line is used then the image suffers from the concomitant reduction in yield and background becomes more prominent. PIXE elemental imaging can only be considered quantitative if each elemental image faithfully portrays the distribution pattern of that element with minimal misleading artefacts from other elements. The Dynamic Analysis transform outlined here provides an effective method for producing true elemental images that are not only quantitative, but can be obtained on-line as the data accumulate, obviating the need for expensive data storage and time-consuming off-line analysis.

References

- [1] C.G. Ryan and D.N. Jamieson, Nucl. Instr. Meth. **B77** (1993) 203.
- [2] C.G. Ryan, C.L. Churms and J.V. Pilcher, NAC Annual Report (1993) 7.4.6.
- [3] C.G. Ryan, D.R. Cousens, S.H. Sie, W.L. Griffin, G.F. Suter and E. Clayton, Nucl. Instr. Meth. **B47** (1990) 55.
- [4] C.G. Ryan, Proceedings of 7th AINSE NTA Conference (1991) p. 132.

fig. 1 CSIRO Dynamic Analysis method

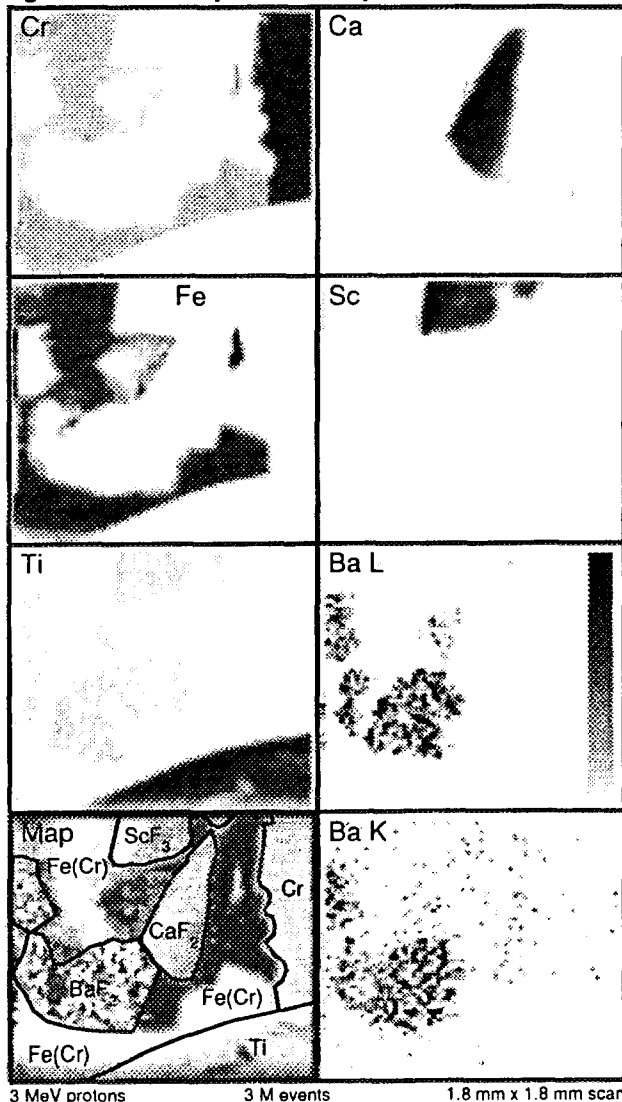
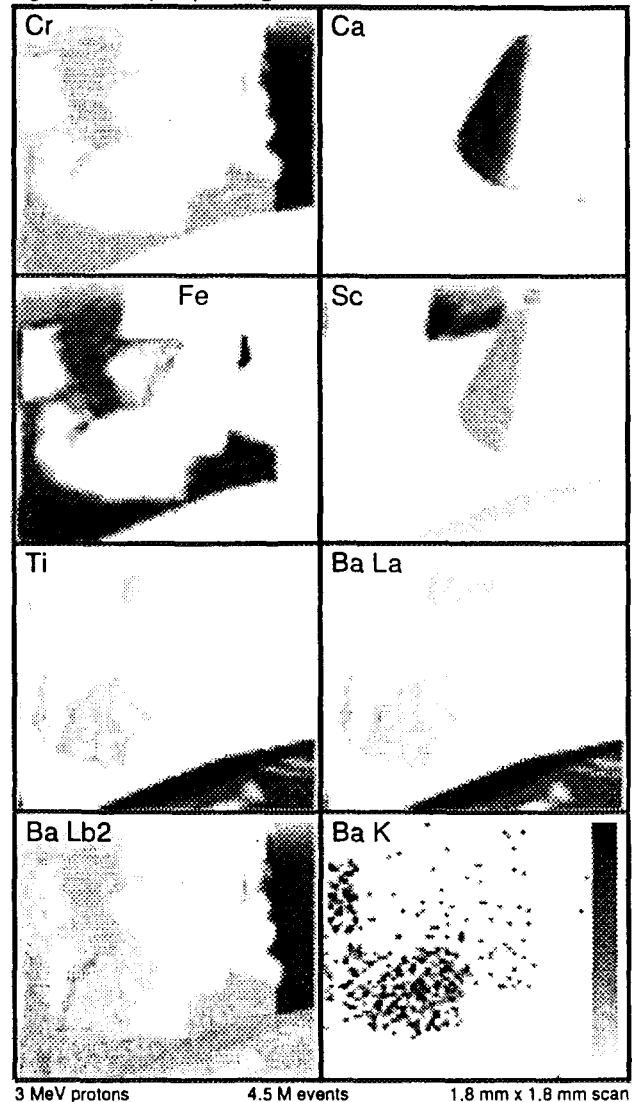


fig. 2 Simple peak gates method



channels and a flat background. With the channels centered on the X-ray lines, and considering only K_α and K_β lines with $K_\beta/K_\alpha=0.2$ and using unity statistical weights w_i , the β , α and $\alpha^{-1}\beta$ matrices become:

$\beta_{ji} = w_i (\delta f_i / \delta a_j)$	$i =$	<u>1</u>	<u>2</u>	<u>3</u>	<u>4</u>	<u>5</u>	<u>6</u>
	Cr	-	1.0	0.2	-	-	-
	$j =$ Mn	-	-	1.0	0.2	-	-
	Fe	-	-	-	1.0	0.2	-
	background	0.1667	0.1667	0.1667	0.1667	0.1667	0.1667

$\alpha_{jk} = \sum_i w_i^{-1} \beta_{ji} \beta_{ki}$	$k =$	<u>Cr</u>	<u>Mn</u>	<u>Fe</u>	<u>back</u>
	Cr	1.04	0.2	0.0	0.2
	$j =$ Mn	0.2	1.04	0.2	0.2
	Fe	0.0	0.2	1.04	0.2
	background	0.2	0.2	0.2	0.1667

$[\alpha^{-1}\beta]_{ki}$	$i =$	<u>1</u>	<u>2</u>	<u>3</u>	<u>4</u>	<u>5</u>	<u>6</u>
	Cr	-0.37770	1.0023	-0.01176	0.05880	-0.29400	-0.37770
	$k =$ Mn	-0.28777	-0.19784	0.98922	0.05396	-0.26979	-0.28777
	Fe	-0.37770	0.04081	-0.20407	1.0204	-0.10169	-0.37770
	background	2.2518	-0.01439	0.07194	-0.35972	1.7985	2.2518

If a given pixel records 100 counts of Cr K_α , 30 counts of Mn K_α and 10 counts of Fe K_α on a background of 20 counts, then the spectrum would have the following contributions:

Spectrum:	<u>channel i =</u>	<u>1</u>	<u>2</u>	<u>3</u>	<u>4</u>	<u>5</u>	<u>6</u>
	Cr	-	100	20	-	-	-
	Mn	-	-	30	6	-	-
	Fe	-	-	-	10	2	-
	background	20	20	20	20	20	20
spectrum S =	20	120	70	36	22	20	

Applying the matrix equation $(\alpha^{-1}\beta)S$ yields the vector {100, 30, 10, 120} which are the desired counts in the K_α peaks for the separate elements, free of overlap and background artefacts, and also the total background count of 120. This can be compared with the erroneous result if simple K_α gates are used of {120, 70, 36}. Even if a constant background of 20 is subtracted in off-line analysis, the result {100, 50, 16} is still seriously in error for Mn and Fe.

Tests of the Method

A number of tests have been carried out to simulate demanding mineralogical applications. In one, a sample consisted of small fragments of BaF_2 , CaF_2 and ScF_3 glued to an Fe foil (with minor Cr) and positioned between pieces of pure Ti and Cr metal (see map in Fig. 1). The test was to see if these distinct phases could be imaged accurately despite severe X-ray line overlaps. A comparison was made between images produced using simple gates set on the K_α of each element (or L_α , $L_{\beta 1}$, $L_{\beta 2}$ and $L_{\gamma 1}$ in the case of the Ba L-lines) (Fig. 2), and images produced at the NAC using a Dynamic Analysis Γ matrix built by simply fitting a PIXE spectrum from a preliminary scan with the GeoPIXE program PIXE_FIT (Fig. 1). Most images using the simple gates show inaccuracies or artefacts due to other elements except for Ba K. The Ba K lines are at high energy (32 keV) and free of interferences or significant underlying background. This image forms a useful point of reference for checking the Ba image based on the L-lines. In this case only the Dynamic Analysis Ba L image matches the Ba K image, despite the complete overlap of Ba L_α and Ti K_α . The images based on Ba L_α , $L_{\beta 1}$, $L_{\beta 2}$ and $L_{\gamma 1}$ gates show artefacts due primarily to the Ti K_α , Sc K_β , Ti K_β lines and the Cr and Fe K_α tails. The Ca and Sc images using Dynamic Analysis show clearly separated phases. Due to the overlap of the Ca K_β and the tail of the Ti K_α , the Sc image based on a simple gate on the Sc K_α contains significant Ca and Ti

APPLICATIONS OF FOCUSED MeV LIGHT ION BEAMS FOR HIGH RESOLUTION CHANNELING CONTRAST IMAGING.

D.N. Jamieson, M.B.H. Breese, S. Prawer, S.P. Dooley, M.G. Allen, A.A. Bettiol, A. Saint (MARC, School of Physics, University of Melbourne, Parkville, 3052) and C.G. Ryan (CSIRO Division of Exploration Geoscience, North Ryde, 2113).

INTRODUCTION.

The technique of Nuclear Microscopy, utilizing a focused ion probe of typically MeV H^+ or He^+ ions, can produce images where the contrast depends on typical Ion Beam Analysis (IBA) processes. The probe forming lens system usually utilizes strong focusing, precision magnetic quadrupole lenses and the probe is scanned over the target to produce images. Originally, this imaging technique was developed to utilize backscattered particles with incident beam currents typically of a few nA, and the technique became known as Channeling Contrast Microscopy (CCM). Recently, the technique has been developed further to utilize the forward scattering of ions incident along a major crystal axis in thin crystals. This technique is known as Channeling Scanning Transmission Ion Microscopy (CSTIM). Since nearly all incident ions are detected, CSTIM is highly efficient and very low beam currents are sufficient for imaging, typically as low as a few fA. This allows probes as small as 50 nm to be used. In this paper we briefly review the recent applications of these emerging techniques to a variety of single crystal materials. For a complete description of the nuclear microprobe technology, see the recent conference proceedings [1]. For a review of applications before 1990, see [2]. The parameters of the system in Melbourne, relevant to the channeling measurements described here, appear in the table.

	CCM	CCM	CSTIM
Target material	Si (100)	C (110)	various
Microprobe beam	2 MeV He^+	1.4 MeV H^+	various
Microprobe diameter	1 μm	1 μm	100 nm
Object diaphragm diameter	20 μm	20 μm	< 1 μm
Beam convergence angle, $2\theta_i$	2.2 mrad	2.8 mrad	0.041 mrad
Convergence compared to $\psi_{\frac{1}{2}}$, $\theta_i/\psi_{\frac{1}{2}}$	0.16	0.18	<0.002
Detector solid angle	35 msr	35 msr	n.a.
Beam current on target	100 pA	100 pA	1 fA (5kHz)
Matrix scattering height (counts/ $\mu C/keV/msr$)	17.1	820	-
Time for 3 % statistics	1.2 hours	1.5 min	-
Total dose in a $100 \times 100 \mu m^2$ scan	$3 \times 10^{16}/cm^2$	$4 \times 10^{14}/cm^2$	-

In CCM, the convergence angle of the beam can limit the quality of the channeling in the crystal if the convergence angle approaches or exceeds the critical angle of the crystal. However, for axial channeling with the Melbourne system, this is not usually a limitation as the channeling patterns shown in figure 1 demonstrate. Ample beam for axial channeling is available, however the convergence angle of the beam is generally too steep to allow planar channeling to be used analytically.



Figure 1: Convergent beam channeling/blocking pattern with 3 MeV H^+ .

Routine applications of CCM and CSTIM utilize a beam collimated so the convergence angle is well within the inner circle shown in figure 3(b). This ensures that the convergence

angle of the focused probe is less than the critical angle for axial channeling for typical crystals. This is also seen by the figures in the table for $\theta_i/\psi_{\frac{1}{2}}$. Hence χ_{min} measurements are not degraded.

Damage and Swelling.

Almost all applications of IBA techniques with a microprobe, except for CSTIM, require careful attention to the damage and swelling introduced by the intense irradiation which can be 100 times larger than with an unfocused beam [3]. Swelling induced dechanneling is shown in figure 2 for two very high dose irradiations in diamond. The diamond is otherwise undamaged. The critical dose at which swelling-induced dechanneling becomes significant, D_s , is not a strong function of beam, crystal composition or axis and is typically $1-4 \times 10^{17}$ ions/cm². Therefore swelling is an almost inevitable consequence of microprobe imaging if images with good statistics are to be obtained. The width of the swollen region seen in a CCM image is typically $\sim 10 \mu\text{m}$, so clearly any scan over a region of interest should be at least this much larger. However, GaAs and HgCdTe suffer severe lattice damage due to point defect creation by the microprobe. In these crystals, CCM analysis is more challenging. The damage is less severe at lower beam fluxes at the same dose, owing to room temperature annealing [4,5].

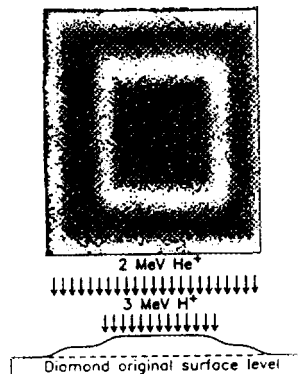


Figure 2: CCM image from swelling in diamond.

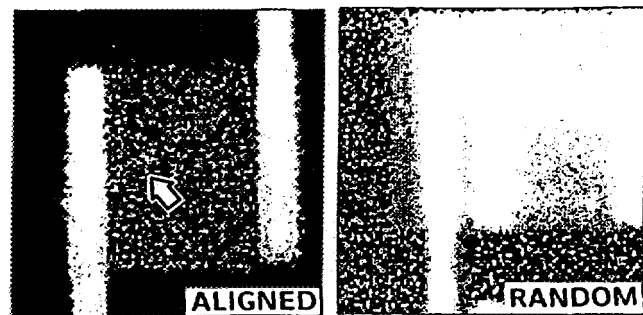


Figure 3: CCM image of an IR photodetector.

Photodetectors

the past two years in Melbourne, extensive studies have been performed on materials used to fabricate infrared detectors for optical fiber communication systems. These studies included investigations of the substrate material [6], novel etching techniques [7], and complete devices. Linear growth defects have been observed that bridge electrical contacts on 2 out of 3 photodetector devices in some production runs, as shown in figure 3. It is likely that these linear growth defects account for the erratic electrical properties from device to device on the same wafer.

Diamonds

A potentially excellent material for semiconductor devices is diamond. However, diamond-based semiconductor devices have proved to be an elusive goal, mainly because of the difficulties of producing n-type diamond. The Melbourne group has devised a method of deep, MeV ion implantation followed by focused laser annealing [8, 9], which has the potential to produce n-type diamond, but certainly regrows the damaged diamond, see figure 4. Nuclear elastic cross sections of C, O and Si have been measured and are used for quantitative analysis of diamonds when probed with non-Rutherford MeV H beams [10].

Pyrite

In addition to synthetic materials, CCM has been applied to study naturally occurring pyrite crystals [11]. A CCM image, shown in figure 5, reveals a large number of elongated

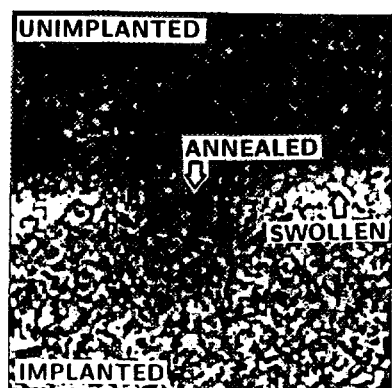


Figure 4: Implanted and annealed diamond.

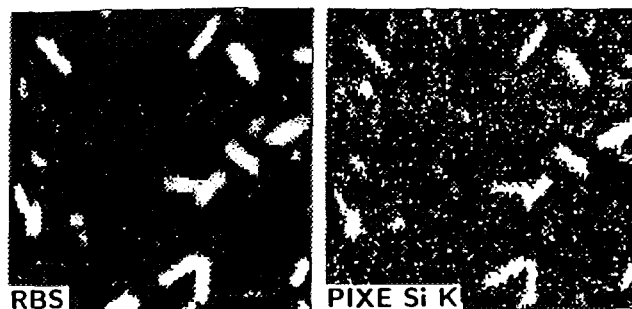


Figure 5: Pyrite crystal with FeSiO_4 inclusions.

inclusions, with an x-ray spectrum showing Ni substitutionality in some crystals. In other crystals, CCM revealed 50 % Au substitutionality.

Channeling Scanning Transmission Ion Microscopy.

The CSTIM technique has been found useful as a method of imaging dislocations in thick crystal samples in order to overcome the limitations of other dislocation imaging techniques. Dislocation networks in SiGe could be imaged to a resolution of 200 nm by contrast produced by dechanneled ions forward scattered through a sample thinned to 20 μm [12].

CONCLUSION.

New imaging techniques are now under development for single crystals, including use of Ion Beam Induced Charge (IBIC) and Ion Beam Induced Luminescence (IBIL) [13]. We look forward to further developments, particularly in the use of CSTIM for high resolution imaging with 100 nm probes and smaller.

The work done by the Melbourne group and described here has been supported by grants from the Australian Research Council, the Australian Telecommunications Research Board and a research contract with the Australian Overseas Telecommunications Corporation.

References.

- [1] U. Lindh, ed., Proceedings of the Third International Conference on Nuclear Microprobe Technology and Applications, Nucl. Instr. Meth., B77 (1993).
- [2] D.N. Jamieson, R.A. Brown, C.G. Ryan and J.S. Williams, Nucl. Instr. Meth., B54 (1991) 213.
- [3] S.P. Dooley and D.N. Jamieson, Nucl. Instr. Meth., B66 (1992) 369.
- [4] R.A. Brown, J.C. McCallum and J.S. Williams, Nucl. Instr. Meth., B54 (1991) 197.
- [5] S.P. Russo, P.N. Johnston, R.G. Elliman, S.P. Dooley, D.N. Jamieson and G.N. Pain, Nucl. Instr. Meth., B64 (1992) 251.
- [6] D.N. Jamieson, S.P. Dooley, G.N. Pain and S.P. Russo, Mat. Res. Soc. Symp. Proc. 235 (1992) 253.
- [7] A. Semu, L. Montelius, P. Leech, D.N. Jamieson and P. Silverberg, Appl. Phys. Lett. 59 (1991) 1752.
- [8] S. Prawer, D.N. Jamieson, S.P. Dooley and R. Kalish, Mat. Res. Soc. Symp. Proc. 235 (1992) 431.
- [9] M.G. Allen, S. Prawer, D.N. Jamieson and R. Kalish, submitted to Appl. Phys. Lett. (1993).
- [10] R. Amirikas, D.N. Jamieson and S.P. Dooley, Nucl. Instr. Meth. B77 (1993) 110.
- [11] D.N. Jamieson and C.G. Ryan, Nucl. Instr. Meth., B77 (1993) 415.
- [12] M.B.H. Breese, P.J.C. King, J. Whitehurst, G.R. Booker, G.W. Grime, F. Watt, L.T. Romano and E.H.C. Parker, J. Appl. Phys. 73(6) (1993) 2640.
- [13] A.A. Bettiol, D.N. Jamieson, S. Prawer and M.G. Allen, these proceedings.

**THE AUSTRALIAN/SWEDISH COLLABORATION
ON ION BEAM TIME-OF-FLIGHT**

*H. Whitlow
Lund Institute of Technology, Sweden*

(Paper to be handed out at Conference)



NONLINEAR DYNAMICS FOR CHARGED PARTICLE BEAMS WITH A CURVED AXIS IN THE MATRIX – RECURSIVE MODEL.

A.D. Dymnikov*, Institute of Computational Mathematics and Control Process, University of St Petersburg, RUSSIA.

INTRODUCTION.

A general relativistic theory of charged particle beam motion along a curved optical axis, s , is important for designers of optimal beam control systems. Some basic publications on this topic can be found in [1–4]. In these references the scalar and tensor methods are used and usually a nonrelativistic theory is developed. In this paper a new matrix approach is presented which is based on some previous papers [6,7]. This approach gives the possibility to develop a matrix relativistic theory of charged particle beam motion in the most general case of curved reference trajectory, including the gravitational force and space charge.

The term ‘beam control system’ is used throughout this paper for focusing, forming, deflecting and accelerating the beam. The beam control system is often a complicated nonlinear system whose optimal parameters can be found by optimization calculations. We consider the beam motion as a motion of the closed phase set. The representation of a real beam by the closed phase set is due to finite spreads of coordinates and time, momentum and energy of particles.

The Reference Particle.

We understand the motion of any material body as a motion relative to other material bodies. The motion of any particle Q of the beam is described in the form of a motion relative to a single particle M of the beam. The particle M is called the reference particle. This follows the ‘reference trajectory’ of the beam. We assume that the reference trajectory is known and the motion of the reference particle is described relative to any material body.

The Matrix - Recursive Approach.

The proposed matrix approach includes the following parts:

- Selection of the coordinate system, generally a curvilinear system in 4–dimensional space-time attached to a reference particle.
- Writing out of the matrix equations of motion and the matrix equations of electromagnetic field in the moving selected frame.
- Expansion of the equations of motion and of the electromagnetic field in a Taylor series in powers of the deviation from the reference particle.
- Solution of the nonlinear differential equations in phase space by reformulation of them as linear equations in phase moment space.
- Use of the new compact, conservative, recursive method of integration of the equations of motion. In this method the phase volume of the beam will be strictly conserved in each step of the numerical integration.
- Use of the method of the envelope matrix σ for calculation the beam envelopes in the

* Present address: MARC, School of Physics, University of Melbourne, Parkville, 3052, AUSTRALIA.

paraxial approximation.

- Use of the moments of the particle distribution function in phase space for calculation of the averaged characteristics of a beam.
- Solution of the paraxial nonlinear equations of motion of an elliptical 3-dimensional bunch of particles taking into account the effect of space change.
- Use of a special system of units in which all quantities in the equations of motion and in the field equations are either dimensionless or expressed in terms of units of length or inverse length.

The Moving System of Coordinates.

The position of an arbitrary particle in the moving reference frame is determined by the 4-vector $L = \hat{e}x$ where \hat{e} is the reference frame matrix, attached to the reference particle, x_1 and x_2 are the transverse coordinates, x_3 is the longitudinal coordinate, $x_4 = c\Delta t$, where Δt is the flight time.

The Observer Surface.

Let us assume that in the moving reference frame, there is a surface where all particles are detected. The equation of the observer surface is written as $f(x) = 0$. We use two kinds of this surface: $x_3 = 0$ and $x_4 = 0$. In the plane $x_3 = 0$ all particles are detected reaching this plane at different times. In the plane $x_4 = 0$ all particles are detected at the same time.

The Reference Frame Matrix.

The proposed matrix approach relies on three basic matrix functions: the reference frame matrix, the curvature matrix and the electromagnetic matrix. The Cartan method of the moving 3-vector is generalized as the method of the moving 4×4 reference matrix \hat{e} . The curvature matrix function consists of the normal curvature, the geodesic curvature and torsion and three components of the gravitational force acting on the reference particle.

The Method of Embedding in Phase Moment Space for Solving the Nonlinear Equations of Motion.

The analysis and calculation of the nonlinear systems of equations are considerably simplified by transforming from the nonlinear differential equations of motion in the phase space $\{q\} = \{x, x'\}$ to the system of linear equations in extended phase space – the phase moment space $\mu = \{q^1, q^2, \dots, q^m\}$, where q^r is the r -moment of the vector q . This is the essence of the method of embedding in phase moment space. For example, for n -vector x , where $n = 2$, we have $x^1 = x, x^2 = \{x_1^2, x_1 x_2, x_2^2\}; x^3 = \{x_1^3, x_1^2 x_2, x_1 x_2^2, x_2^3\}$. These terms are those involved in the most important second order and third order aberrations of a probe forming system.

The Equation for the Phase Moments.

Using the Taylor expansion, the linear equation for the phase moments can be written as

$$\frac{d\mu}{ds} = P(s)\mu$$

Here s is the path along the reference trajectory. We call the matrix $P(s)$ the coefficient matrix.

The Matrizant.

Writing a nonlinear equation in a linearized form makes it possible to construct the solution, using the matrizant, in the form:

$$\mu = R(P, s/s_0) \cdot \mu_0$$

The matrizant $R(P, s/s_0)$ is defined as the $n \times n$ matrix function which is the solution of the matrix linear differential equation

$$\frac{dR}{ds} = P(s)R.$$

The initial matrizant is the unit matrix, $R(P, s_0/s_0) = I_n$. This solution will be independent of the initial vector $\{q_0\}$ whereas the solution of the nonlinear equation is sought for each value of $\{q_0\}$. The use of matrices for solving nonlinear beam problems was first proposed by Brown [8].

The Method of Shuttle-Sums and Shuttle-Integrals.

A continuous, generalized analogue of the Gaussian Brackets or the method of shuttle-integrals [6,9], can be used to calculate the matrizant for an arbitrary coefficient matrix $P(s)$ with rigorous conservation of the phase volume of the beam at each stage of the calculation.

CONCLUSION.

In this paper a new matrix and recursive approach has been outlined for treating nonlinear optics of charged particle beams. This approach is a new analytical and computational tool for designers of optimal beam control systems.

This work has been supported at Melbourne University by a grant from the Australian Research Council.

References.

- [1] Cotte, M., Recherches sur l'optique électronique, Annales de Physique, 10 (1938), 333-405.
- [2] G.A. Grinberg, Selected Problems of Mathematical Theory of Electrical and Magnetic Phenomena, Press of Academy Sciences USSR, Moscow, Leningrad (1948), 507-535 (in Russian).
- [3] K.G. Steffen, High Energy Beam Optics, (Wiley 1965), 94-97.
- [4] Zhou Liwei, Ni Guoqiang and Qiu Baicang, Optic, 79, No.2 (1988) 53-66.
- [5] A.D. Dymnikov, Deposited Report B1-10427 (in Russian) JINR, Dubna (1977).
- [6] A.D. Dymnikov, Problems in Mechanics and Control Processes, No.2, Control of Dynamical Systems (in Russian), Leningrad State University, Leningrad, (1978), p64.
- [7] A.D. Dymnikov and G.M. Osetinskii, Sov.J. Part. Nucl. 20, No,3 (1989), 293-310.
- [8] K.L. Brown, R.Belbeoch and P.Bounis, Rev. Sci. Instr. 35, 481 (1964).
- [9] V.Yu Vasil'ev and A.D. Dymnikov, Sov. At. Energy (English translation), 374, 1091 (1974).



AU9715811

THE COMBINED APPLICATION OF ION AND RAMAN MICROPROBE TECHNIQUES

S. Prawer, K.W. Nugent, A. Orlov and L. Kostidis

Micro Analytical Research Centre (MARC), School of Physics,
University of Melbourne, Parkville, Vic 3052.

The recent establishment of a Raman Microprobe within MARC adjacent to the ion microprobe facility has provided new opportunities for materials analysis. The techniques are generally complementary, providing quantitative elemental, chemical and structural information at the micron level in a wide range of samples.



AMS AT THE ANU INCLUDING BIOMEDICAL APPLICATIONS

L.K. Fifield¹, S.J. King², J.P. Day², G.L. Allan¹, R.G. Cresswell¹ and T.R. Ophel¹
¹Department of Nuclear Physics, Australian National University, Canberra, Australia
²Department of Chemistry, University of Manchester, UK

An extensive accelerator mass spectrometry program has been conducted on the 14UD accelerator at the Australian National University since 1986. In the two years since the previous conference, the research program has expanded significantly to include biomedical applications of ^{26}Al and studies of landform evolution using isotopes produced *in situ* in surface rocks by cosmic ray bombardment. The system is now used for the measurement of ^{10}Be , ^{14}C , ^{26}Al , ^{36}Cl , ^{59}Ni and ^{129}I , and research is being undertaken in hydrology, environmental geochemistry, archaeology and biomedicine. On the technical side, a new test system has permitted the successful off-line development of a high-intensity ion source. A new injection line to the 14UD has been established and the new source is now in position and providing beams to the accelerator.

The measurement technique remains as described previously [1], with slow isotope cycling and transmission of all beams to the beam-line Faraday cup/detector unit. Absolute measurements are performed for ^{36}Cl , ^{26}Al and ^{59}Ni , with the other isotopes being measured relative to a standard. Detail refinement of the system has resulted in a steady improvement in measurement precision and at the present time measurement reproducibility for ^{36}Cl is presently 2%.

The ^{36}Cl program on the accelerator continues to concentrate on hydrological applications, with the principal emphasis being placed on groundwater tracing in Australia's Murray-Darling Basin. The Australian groundwater studies are being complemented by a continent-wide rainwater sampling program, which is investigating major element and stable isotope concentrations in rainwater along with ^{36}Cl fallout.

An increasing number of samples are being measured as part of geomorphological studies. These studies make use of the *in situ* production of the isotopes ^{10}Be , ^{26}Al and ^{36}Cl . The work was initiated with exposure age and erosion rate measurements employing ^{36}Cl in limestone [2], and now is being applied to ^{10}Be and ^{26}Al in quartz extracted from various rock types. This work is described in detail in an associated poster.

A program in biomedical applications of AMS isotopes has begun recently in conjunction with the Chemistry Department at the University of Manchester [3]. Initial work has concentrated on the measurement of biomedical ^{26}Al , as a prelude to toxicological studies using this isotope as a tracer for aluminium. Considerations which are peculiar to biomedical samples will be discussed. A first project on the uptake of aluminium by the various components (DNA, RNA, cytoplasm and nucleus) of human neuro-blastoma (brain) cells grown in culture has been completed and the results will be presented.

The ^{59}Ni measurements are performed by operating the accelerator at 15MV and transmitting the 13^+ charge state around the analysing magnet. The beam is then post-stripped to the 22^+ charge state before transmission through a 45° switching magnet. A $^{59}\text{Ni}/\text{Ni}$ background of $\sim 10^{-13}$ has been obtained, and measurements have been made on the metal phase of two meteorites [4].

- [1] L.K. Fifield, T.R. Ophel, G.L. Allan, J.R. Bird and R.F. Davie, Nucl. Instr. and Meth. B52 (1990) 233.
- [2] J. Stone, G.L. Allan, L.K. Fifield, J.M. Evans and A.R. Chivas, Proc. 6th Inter. Conf. on AMS, 1993.
- [3] S.J. King, R.V. Miller, J.P. Day, L.K. Fifield, G.L. Allan and J. Stone, Proc. 6th Inter. Conf. on AMS, 1993.
- [4] M.Paul, L.K.Fifield *et al.*, Nucl. Instr. B, in press.



EXAFS AND MICROPROBE ANALYSIS AT THE AUSTRALIAN NATIONAL BEAMLINE FACILITY

R. F. Garrett, D. J. Cookson, G. Foran
Australian Nuclear Science and Technology Organisation,
PMB 1, Menai, NSW, 2234, Australia.

D. C. Creagh
Physics Dept., University College UNSW,
Campbell, ACT

D. Balaic and S.W. Wilkins
CSIRO-DMST
Locked Bag 33, Clayton, Vic, 3168

K. Nugent, Z. Barnea and M. ~~Chowela~~^{Cholewa}
School of Physics, Melbourne University,
Parkville, Vic, 3052.

The Australian National Beamline Facility is a co-operative project involving several Australian research organisations, Universities and government funding agencies. A multi-purpose X-ray beamline is being constructed at the Photon Factory, Tsukuba, Japan. The aim of the project is to provide Australian scientists with routine access to synchrotron radiation in the hard X-ray region.

A number of powerful analysis techniques will be available at the ANBF. Various crystallography techniques form the basis for the design of a large vacuum diffractometer to be installed at the beamline later this year. Experiments have already begun on two other analysis techniques: Extended X-ray Absorption Fine Structure (EXAFS) and X-ray microprobe analysis.

The EXAFS technique has the unique ability to provide close range structural information from disordered samples, for example solutions. It only became routinely available with the advent of synchrotron radiation, and EXAFS beamlines are amongst the most utilised at synchrotron facilities world-wide.

X-ray microprobe facilities are in operation at several synchrotron facilities. In contrast to electron and proton microprobes, the spatial resolution available is relatively coarse, however the sensitivity can be several orders of magnitude higher. New optics are being developed to increase the x-ray flux into a micron or sub-micron beam spot.

The status of the Australian beamline will be described, and facilities available for EXAFS and micro-beam experiments will be detailed. A number of preliminary experiments have been carried out, and results will be presented.



RESEARCH FACILITIES ON THE NEW RESEARCH REACTOR

*J.W. Boldeman, D. Cookson, R.L. Davis, M.M. Elcombe,
C.J. Howard, S.J. Kennedy, R. Knott and S. Town*

Australian Nuclear Science and Technology Organisation
Private Mail Bag 1, Menal, NSW 2234, Australia

The highest priority for the proposed New Research Reactor will be neutron beam research. This paper will briefly discuss the specifications for the reactor and the proposed experimental facilities.

INDEX OF AUTHORS

INDEX OF AUTHORS

<u>Author</u>	<u>Page</u>
ALLAN GL	124, 189
ALLEN MG	140
BAILEY G	98, 155
BALAIC D	191
BARDOS RA	21, 130
BARIBEAU JM	92
BARNEA Z	191
BAXTER GR	9
BELL JM	165
BETTIOL AA	140
BETZ G	43
BHANSALI S	131
BIRD JR	65, 98, 112
BOLDEMAN JW	65, 66, 192
BOWLES CJ	158
BRAZHNİK VA	18
BREESE MBH	175, 181
BROWN G	146
BROWN IG	52
BUBB IF	80, 89
BYRNE AP	99
CAO DX	52
CHEKHMIR A	12
CHOLEWA M	100, 191
CHU JW	62, 68
CHURMS CL	178
CLARKE M	43
COHEN DD	66, 80, 95, 155, 168
CONWAY M	143
COOKE DR	119
COOKSON DJ	191
CREAGH CD	191
DADD KA	113

<u>Author</u>	<u>Page</u>
DYMINKOV AD	18, 185
DYTTLEWSKI N	80, 95
EECKHAOUDT E	100
ELLIMAN RG	83,92
ELLINGBOE SL	30
ELLIS PJ	29, 66
EVANS JL	124
EVANS PJ	62, 68
FALLON J	29, 66
FANG Z	6, 86
FARAONE L	76
FARDY JJ	158
FARRAR YJ	158
FELL C	46
FIFIELD LK	124, 189
FINK D	28, 29, 65
FORAN G	191
FULLAGAR R	107
GARRETT F	191
GARTON D	155
GORTMAKER P	152
GOSDEN C	107
GRAVE P	112
GREEN DC	165
GREEN TH	12, 116
GURARIE VN	171
HINDE D	1
HOFFMAN A	134
HOTCHKIS MAC	28, 29, 65, 76, 107, 111
HOWARD J	3
HULT M	80, 95
HUSTON DL	119
JACOBSEN GE	28, 29, 65, 67
JAMIESON DN	140, 175, 178, 181

<u>Author</u>	<u>Page</u>
JANARDHANA MN	149
JOHNSON EP	68
JOHNSTON PN	80, 89, 95, 98, 155
KENNY MJ	15, 46, 161, 165
KIJEK M	25
KING BV	43, 55, 59
KING S	189
KOSTIDIS L	188
KRINGHOJ P	72, 83
LAI ST	76
LAIRD JS	21, 127, 130, 175
LAWSON EM	28, 29, 65, 67
LEBED SA	18
LEE G	25
LEECH PW	89
LEGGE GJF	3, 21, 24, 100, 127
LIU LJ	37
MACDONALD RJ	49
MANORY RR	37
MARTIN JW	155, 168
M ^C CALLUM JC	152, 164
M ^C GOLDRICK PJ	121
M ^C ORIST GD	158
MILLAR J	25
MISTICA R	149
MITROVIC B	55
MOLONEY G	24
MOORHEAD GF	130
NASSIBIAN AG	76
NENER BD	76
NOORMAN H	155
NOORMAN JT	68
NUGENT KW	137, 188, 191
O'CONNOR DJ	6, 40, 49, 59

<u>Author</u>	<u>Page</u>
O'BRIEN PM	24
OPHEL TR	86, 124, 189
ORLOW A	188
OSTLING M	80, 95
PATERSON PJK	2
PETRAVIC M	143
PILCHER JV	178
PONOMAREV AG	18
POTTS D	112
PRAWER S	3, 134, 137, 140, 188
RAO MR	92
RIDGWAY MC	30, 92
ROACH G	172
ROBINSON P	121
RUSSELL DW	126
RUSSELL GJ	168
RYAN CG	178
SAINT A	3, 21, 24, 130
SCOTT A	24
SHEN YG	49, 59
SHYING M	28, 29, 65, 67
SIE SH	9, 12, 103, 116, 119
SMITH AM	28, 29, 65, 67
SOOD DK	37, 52, 131, 146, 149
SPECHT J	107
SSVENSSON BG	143
STELCER E	155
STONE JOH	124
STORIZHKO VE	18
STUART SA	3
STUDD WB	89
SUMMERHAYES G	107
SUTER GF	9, 103, 119
TAYLOR GN	130

<u>Author</u>	<u>Page</u>
TORRENCE R	107
TROMPETTER B	33
TUNIZ C	28, 29, 65, 66, 67
VAN GRIEKEN R	100
VAN MOORT JC	111, 126
VAN ZEE H	49
VICENZI E	116
VICKERIDGE I	33
WALKER SR	80, 95
WANDELT K	49
WATT JS	172
WEISER PS	134
WHITLOW HJ	80, 95, 184
WIELUNSKI LS	9, 15, 161, 165
WILKINS SW	191
WILLIAMS JS	143, 171
WILLIAMS N	149
WONG W	83
YANG Q	86
YAO J	59
YAO X	146
ZAHRING C	80
ZARING C	95
ZASTAWNY HW	172
ZHANG FM	59
ZHOU W	146
ZHU L	40
ZMOOD RB	131
ZUR MUHLEN E	40

LIST OF PARTICIPANTS

LIST OF PARTICIPANTS
(as at time of printing)

AUSTRALIAN NATIONAL UNIVERSITY

(Nuclear Physics)

Dr R Cresswell

Dr A Bryne

Prof T Ophel

Dr K Fifield

(Electronic Materials Engineering)

Mr M Petravic

Mr K Belay

Mr R Elliman

Mr M Ridgway

Mr R Rao

Mr H Tan

Dr P Kringhoj

Mr T Watt

Prof JS Williams

Ms S Ellingboe

Mr J Glasko

Mr B Mohadjeri

Ms J Wong-Leung

Mr WC Wong

AUSTRALIAN NUCLEAR SCIENCE & TECHNOLOGY ORGANISATION

Mr D Cohen

Mr E Stelcer

Dr P Evans

Dr N Dytlewski

Mr D Garton

Dr G Bailey

Mr R Bird

DR J Bolderman

Dr E Lawson

Mr H Linklater

Mr T Wall

Dr J Fardy

Dr C Tuniz

Mr A Smith

Mr J Fallon

LIST OF PARTICIPANTS

(as at time of printing)

CRA ADVANCED TECHNICAL DEVELOPMENT

Ms A Pidcock

CSIRO

(Mineral & Process Engineering)

Mr JS Watt

(Exploration & Mining)

Dr C Ryan

Dr SH Sie

(Applied Physics)

Dr MJ Kenny

Mr GR Baxter

Dr LS Wielunski

JAMES COOK UNIVERSITY, AINSE FELLOW

Mr D Mylrea

INSTITUTE OF GEOLOGICAL & NUCLEAR SCIENCES, NEW ZEALAND

Dr IC Vickridge

MONASH UNIVERSITY

Ms L Frick

RMIT

(Applied Physics)

Dr P Paterson

Dr P Johnston

Dr M Kijek

Prof J Miller

Dr S Russo

Dr I Bubb

Ms G Lee

Mr A Rubio

Mr S Walker

LIST OF PARTICIPANTS
(as at time of printing)

RMIT Cont'd

Mr W Studd
Mr P McMahon
Mr R Walker
Mr W Toye
Mr J McCallum
Prof D Sood
Mr K O-Rossiter
Dr R Manory
Mr P Gortmaker
Mr W Zhou
Mr L Jun
Mr S Bhansali
Mr LJ Lin
Prof J Miller

UNIVERSITY OF MELBOURNE

Dr S Praver
Dr KW Nugent
Dr MBH Breese
Dr A Saint
Dr M Cholewa
Dr W Piekarczyk
Dr VN Gurarie
Dr DN Jamieson
Mr A Orlov
Dr AD Dymnikov
Dr M Livett
Mr G Moloney
Mr JS Laird
Mr S Dooley
Mr MG Allen
Mr P Weiser
Mr AA Bettiol
Mr L Kostidis
Mr L Witham
Mr RA Bardos
Dr G Legge
Mr PM O'Brien
Ms L Mason
Mr S Reeves

LIST OF PARTICIPANTS
(as at time of printing)

UNIVERSITY OF NSW. AINSE FELLOW

Mr JW Martin

UNIVERSITY OF NEWCASTLE

Mr B Mitrovic

Mr J O'Connor

Mr C Fell

Mr S He

Mr H Hu

Ms L Ting

Mr Q Lu

Mr U Stein

Mr G Cotterill

Mr Y Shen

Mr F Zewei

Mr F Zhang

Mr BV King

Mr M Clark

Mr J Yao

Mr L Zhu

UNIVERSITY OF TASMANIA

Mr DW Russell

Dr JC Van Moort

Dr P McGoldrick

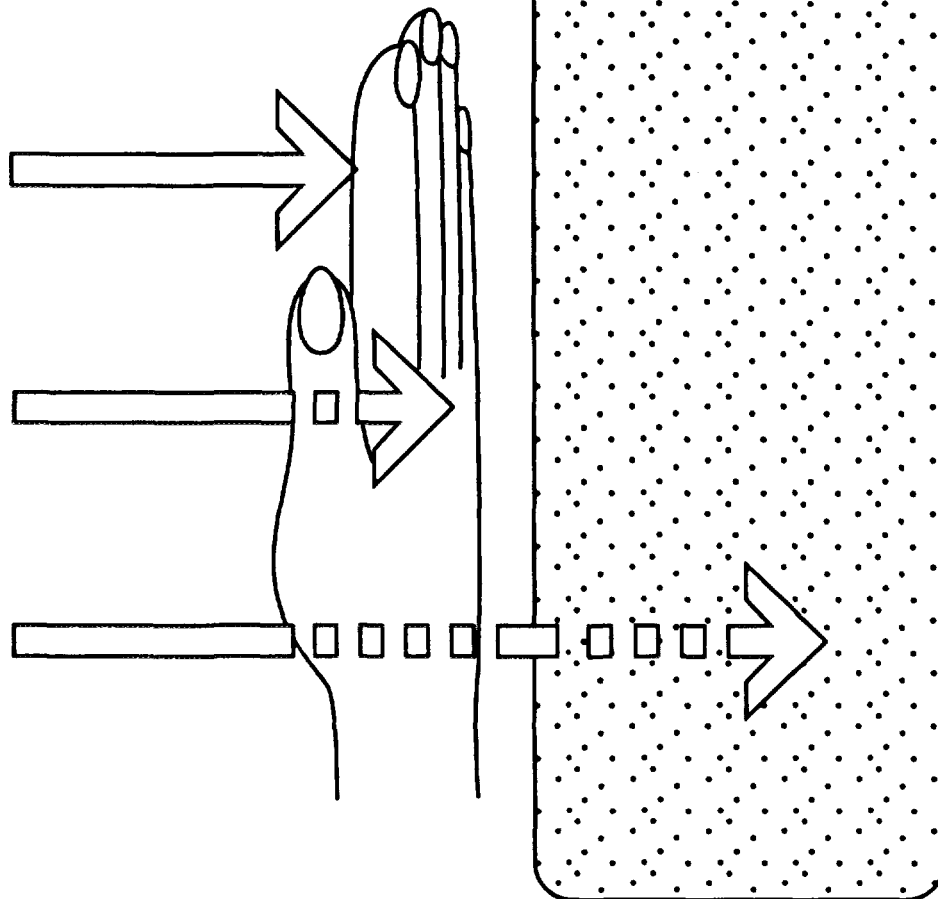
UNIVERSITY OF WESTERN AUSTRALIA

Prof A Nassibian

Dr B Nener

Dr S Teng Lai

Leaders in **RADIATION** TECHNOLOGY



DOSIMETER CORP
Pocket Dosimeters
Survey Meters

ALPHA NUCLEAR
Radon Monitoring

TELEDYNE ISOTOPES
TLD Systems
Scintillation Detectors

TENNELEC/THE NUCLEUS
NIM Modules, MCA's
Low background counters

N.E. TECHNOLOGY
Health Physics Equipment
Radiological Instruments

APTEC NUCLEAR
MCA's, Health Physics
Equipment

WELLHOFER KERNPHYSIK
Waterphantoms for
Radiotherapy

OXFORD SCIENTIFIC

39 Bridge Street, Rydalmere 2116
P.O. Box 232 Rydalmere 2116
Telephone: (02) 638 1244 Fax: (02) 638 0878